Improving Pyrometry of Advanced High Strength Steels During Intercritical Annealing

by
Fatima Kikelomo Suleiman

A thesis
presented to the University of Waterloo
in fulfillment of the
thesis requirement for the degree of
Doctor of Philosophy
in
Mechanical and Mechatronics Engineering

Waterloo, Ontario, Canada, 2025

© Fatima Kikelomo Suleiman 2025

Examining committee membership

The following served on the Examining Committee for this thesis. The decision of the Examining Committee is by majority vote.

External Examiner	Thomas Pierre Professor
Supervisor	Kyle J. Daun Professor
Internal Member	Mihaela Vlasea Associate Professor
Internal Member	Elliot Biro Associate Professor
Internal-external Member	Alexander Penlidis Professor

Author’s declaration

I hereby declare that I am the sole author of this thesis. This is a true copy of the thesis, including any required final revisions, as accepted by my examiners.

I understand that my thesis may be made electronically available to the public.

Abstract

Advanced high strength steels (AHSS) play a prominent role in the automotive industry due to their unique combinations of strength and ductility—essential material properties for manufacturing lightweight vehicles that meet global regulations for fuel economy, vehicle emissions, and passenger safety. Precise thermal control during intercritical annealing is crucial to achieving the mechanical properties of AHSS. Unfortunately, steel manufacturers report unacceptably high rejection rates for AHSS due to substandard mechanical properties. This problem is often attributed to temperature excursions during intercritical annealing of the AHSS, which can be caused by errors in the pyrometrically-inferred temperatures used to control the furnaces. Measuring the temperature of the steel strip through pyrometry requires detailed knowledge of the spectral emissivity of the steel strip, which is imperfectly known since it varies with wavelength, direction, temperature, surface roughness, and oxidation, the latter depending on alloy composition and processing conditions. Therefore, wavelength-dependent variations in the spectral emissivity of AHSS lead to errors in pyrometry measurements during intercritical annealing, which in turn affect the mechanical properties of the steel.

In pyrometry, a temperature estimate is typically obtained using spectral irradiance measured from the steel strip in combination with an emissivity compensation algorithm that assumes or prescribes an underlying emissivity relationship based on the number of detection wavelengths. While various emissivity compensation approaches have been developed for mitigating pyrometer errors caused by uncertain spectral emissivity, none have been specifically designed for AHSS. Hence, these methods do not adequately capture how the evolving surface state of annealing AHSS affects the spectral emissivity and thus the resulting pyrometrically-inferred measurements. Further, existing pyrometry algorithms only provide a point estimate of the surface temperature, making it impossible to assess the reliability of the estimates. To address these challenges, this dissertation aims to develop robust pyrometry methods for AHSS that provide accurate and precise temperature estimates with its associated uncertainties.

This thesis starts by presenting an empirical approach for modelling the spectral emissivity of advanced high strength steel based on response surface methodology (RSM). Using *ex situ* measurements on annealed dual-phase AHSS samples (DP980), variation in the spectral emissivity with respect to dew point, alloy composition, pre-annealed surface state, and wavelength is analyzed using full factorial designs. The significant main and interaction effects were found to vary across the spectral range, with the ratio of alloy components and pre-annealed surface state dominating at shorter and longer wavelengths, respectively. Furthermore, the factorial design of experiments was used to develop a novel multivariate emissivity model capturing the effects of dew point, alloy composition, pre-annealed surface state, and wavelength on the emissivity of dual-phase AHSS.

To extend the investigation to the high-temperature spectral emissivity variations during intercritical annealing, a laboratory-scale annealing simulator representative of the industrial furnace conditions was designed and fabricated to enable *in situ* pyrometry and emissivity measurements on AHSS samples. With lab-scale experiments that simulate the annealing and temperature control process of an industrial continuous galvanizing line (CGL), the *in situ* effect of process parameters, such as chemical composition, annealing temperature, and atmosphere dew point, on the radiative properties of AHSS was observed and modelled. Using *in situ* measurements from DP980 alloys heated in the annealing simulator, the suitability of existing pyrometry models for accurately predicting the surface temperature of AHSS was examined. By comparing the performance of several dual-wavelength (ratio) and multi-wavelength pyrometry algorithms, it was observed that both methods over-predict the surface temperature; however, the predictions of the multi-wavelength algorithm were generally superior.

Given that the spectral emissivity varies significantly with the surface properties of the AHSS coil and further evolves with surface oxidation during annealing, this thesis also investigated the effect of the annealing atmosphere on the radiative properties of dual phase AHSS (DP980) using *in situ* spectral emissivity measurements from samples annealed within a reducing N_2-H_2 atmosphere at dew points ranging from −45°C to +10°C, with an annealing schedule similar to that of industrial continuous galvanizing lines (CGLs). The analysis further explored the effect of variations in oxidation kinetics by comparing the radiative properties of DP980 replicates annealed with the same heating schedule and dew point. It was also discovered that low-

temperature oxidation of the native oxide of AHSS impacts the evolving spectral emissivity during intercritical annealing. In addition, a comparison of evolving spectral emissivity of dual-phase AHSS alloys against that of a standard EDDS grade IF steel showed that *in situ* emissivity measurements could potentially identify the formation of mixed/ternary oxides during annealing.

Furthermore, this thesis also evaluated the ability of *ex situ* measurements to capture temperature-dependent variations in emissivity due to electron mobility as described by the Drude model and the Hagen-Rubens theory. The *ex situ* radiative properties were found to underpredict the *in situ* spectral emissivity, especially at lower temperatures and at shorter wavelengths. This underprediction was also shown to significantly impact the accuracy of pyrometry estimates at those temperatures. The *ex situ* measurements were also used to validate the annealing simulator against an industry-standard galvanizing simulator.

Finally, with the ultimate objective of improving the robustness of pyrometrically-inferred temperature measurements, this dissertation presents a Bayesian pyrometry methodology in which all pyrometry variables including the measured spectral irradiance, spectral emissivity and inferred-temperature are expressed as random variables that obey probability density functions. Additional information about the spectral emissivity from *ex situ* characterization were first incorporated into the inference through maximum likelihood priors. The prior and measurement densities were propagated through Bayes' equation to obtain the posterior densities. The posterior densities provide the pyrometrically-inferred temperature and, crucially, its associated uncertainties. Compared to standard pyrometry methods that provide a point estimate of surface temperature, the Bayesian framework infers the measurement uncertainty via the posterior probability density, which will allow galvanizers to better assess the reliability of the pyrometrically-inferred temperature. The credibility interval of the temperature posterior was further narrowed by defining a multivariate *in situ* emissivity prior conditioned on the annealing dew point and the equivalent blackbody temperature.

Overall, by investigating the behaviour of the spectral emissivity of AHSS during processing, specifically how it evolves with material properties and processing parameters, this thesis presents a comprehensive empirical approach to developing emissivity compensation algorithms that improves the accuracy and reliability of pyrometric temperature predictions on AHSS during annealing.

Land and ancestral acknowledgement

I acknowledge that this research takes place on the traditional, unceded territory of the Attawandaron, Anishinaabeg, and Haudenosaunee peoples. The University of Waterloo's main campus is located on the Haldimand Tract, land promised to the Six Nations in the 1784 treaty but never fully honoured, covering 10 kilometers on each side of the Grand River. Of the original 950,000 acres, only 48,000 remain in Indigenous hands.

These lands are not just historical sites but living homelands that continue to hold deep meaning for Indigenous peoples, who maintain a profound and ongoing relationship with them. I recognize and respect the inherent rights of Indigenous Nations and the enduring effects of settler colonialism on their lands, knowledge systems, and stewardship. As a settler, I understand that acknowledgment alone is not enough; it must be accompanied by a sustained commitment to contributing to efforts for Indigenous justice and healing.

As a descendant of Meritah, the land known today as Africa, and specifically a Black West African born and raised on the continent, I carry the inheritance of ancestors shaped by colonialism, though not by the transatlantic slave trade. I am deeply grateful for the land-based wisdom and resilience passed down through generations, fully aware of the privilege of access to this ancestral memory. I extend my deepest respect to the legacy of resilience, survival, and resistance shared by all African peoples, especially those whose ancestors endured the violence of enslavement. Their strength and perseverance, which have shaped Black identity globally, are integral to my broader understanding of our collective inheritance.

This research is grounded in care for both the land and its people, with a commitment to mitigating climate change, promoting sustainability, and fostering social equity; it is carried out with deep respect for the land not only as a site of research, but as a living source of knowledge, material, and meaning. The resources that make this work possible, particularly iron, which forms the basis of steel and its advanced alloys, are gifts of the Earth, first discovered, respected and worked by the ancestors. I honour the deep knowledge of Indigenous peoples, whose enduring

relationship with the land reflects a profound understanding of natural materials and sustainable practices. This research also stands on a long continuum of African metallurgical knowledge, including the early iron-working traditions of the Nok culture in present-day Nigeria, one of West Africa's earliest known iron-smelting societies. Their legacy speaks to a continuity of knowledge, creativity, and a deep respect for the materials of the Earth.

I do not take for granted the gift of intellect, nor the understanding that all knowledge, including mine, rests on the foundations laid by those who came before. This includes elders, knowledge keepers, and ancestors who have shared their insights across generations and through diverse ways of knowing. The wisdom passed down, deeply rooted in the land, is a profound gift that complements the Western science that predominantly informs this research.

While grounded in the technical study of steel alloys, this research is ultimately an offering guided by a commitment to the wellbeing of the land and its people. It is my hope that it contributes, in its own small way, to the broader efforts to mitigate climate change and to strive for a more just and sustainable future—one that honours the land and its people in their resilience and interconnectedness.

I extend this acknowledgement with respect and gratitude, alongside a dedication to upholding the ethical responsibilities of research with care. If any oversight appears, it is unintentional and a reflection of my ongoing growth in wisdom. I continue to learn from teachers, elders and the land, understanding that this journey is one of humility and lifelong learning.

Acknowledgements

"*I come as one, but I stand as ten thousand.*" ― Maya Angelou

This quote speaks to the essence of my doctoral journey. While this thesis carries my name, it is the result of the collective support, wisdom, and guidance from a village of many—family, mentors, colleagues, friends, and even strangers. Though I cannot name them all, I owe so much to so many. Please forgive me if this acknowledgement becomes one of the lengthiest you may ever read, but the journey was long, the support network vast, and the gratitude deep.

To begin with, I would like to express my deepest gratitude to my supervisor, Professor Kyle Daun, whose guidance has far exceeded the bounds of academic mentorship. I cannot fully express the privilege of working with someone whose sharp intellect and brilliance, coupled with kindness, humour, and integrity, have shaped not only my research but also my values. From Professor Daun, I am learning that how you do one thing is how you do everything—that excellence in research is inseparable from being a good leader, an inspiring instructor, an interdisciplinary thinker, an effective writer, a compelling storyteller, and above all, a good human being. In a world shaped by "publish or perish," you give me hope that it is possible to be ambitious and successful without conforming to one narrow vision of academic worth. In response to your encouraging compliments on my work, I would often say, "It is all in the excellent supervision," and you would laugh—but the truth is, I owe more to that excellent supervision than I can ever fully express. Being your student has truly been a great honour. I really did win the supervisor lottery. Thank you, Kyle—truly.

I would like to thank the members of my examination committee—Prof. Mihaela Vlasea, Prof. Elliot Biro, Prof. Alex Penlidis, and Prof. Thomas Pierre—for generously offering their time, insights, and expertise in reviewing this thesis. A special thank you to Prof. Alex Penlidis, whose course on Response Surface Methodology one of the key chapters of this work. I would also like to express my gratitude to Distinguished Professor Emerita, Carolyn Hansson, who was originally part of my committee and whose guidance during my comprehensive exam were invaluable.

I would also like to extend my sincere thanks to Dr. Frank Goodwin, Ana Paula Domingos Cardoso, and the rest of the industry partners and researchers in the Galvanized Autobody Partnership (GAP) for fostering a collaborative, curiosity-driven research environment. Your support and engagement consistently made me feel that my work was both meaningful and appreciated. I am especially grateful to Professor Joe McDermid—not only for patiently answering what must have felt like an endless stream of metallurgy questions, but also for the many ways you have supported and encouraged my research. Your generosity and quiet vote of confidence have meant a great deal. Special appreciation to Bill Marr at Stelco, and Tom Larrick of Willamson Corporation for their considerable guidance towards the success of this project.

I would like to thank the outstanding technical staff—especially Charlie Boyle, Rick Forgett, Rob Kraemer, Mark Kuntz, Neil Griffett, Mark Whitney, and Matthew Hanna—who contributed their skills and expertise toward the design, development, and construction of the annealing chamber. Without your insight and commitment, there would be no *in situ* measurements to speak of, and therefore, no thesis. You turned conceptual ideas and technical drawings into a working system. Overcoming the countless challenges in this project would not have been possible without your exceptional troubleshooting and problem-solving skills.

Speaking of the chamber and the GAP project, I would like to extend my gratitude to my colleagues who worked alongside me on this project. Roger Tsang, thank you for introducing me to annealing experiments and providing a solid foundation for my work. Your steady support during the early, often chaotic phases of the chamber development made all the difference. Kaihsiang Lin, your depth of knowledge in electromagnetic wave theory continues to inspire me. Thank you for all the *ex situ* measurements and the Taiwanese tea and snacks—intellectual and nutritional support in perfect balance. Nishant Narayanan, your fluency in complex data analysis, statistical modelling and FTIR spectroscopy was always impressive. Thank you for being easy to work with, and for all the *ex situ* support. Michiyo Kagaya, thank you for sharing in the frustrations of annealing experiments and for inheriting the chamber. I aspire to your level of meticulousness—and your slide aesthetics. Ardhendu Bhattacharya, who got adopted into GAP project, your experimental expertise and knowledge of optics and radiative properties have been invaluable.

This acknowledgement would be incomplete without mentioning the rest of the WatLIT crew: Stephen Robinson-Enebeli, Arpan Singh, Jun Wang, Horace Looi, Rodrigo Miguel, Sina

Talebi Moghaddam, Stanislav Musikhin, Boxuan (Tom) Zhao, Cameron Klassen, Paule Lapeyre, Daniel Blackmore, Michael Nagorski, Halil Ibrahim Yazici, Ornel Padilla Estrada, Felipe Martinez Guarin, Alireza Kaveh, Avery Opalka, Mu-An Tsai, Francois Bechard-Cote, and Ned Zhou. Some notable alumni also contributed to my work: Paul Hadwin and Tim Sipkens. Thank you all for your camaraderie and intellectual contributions. Our meetings and get-togethers were frequent and never painful or dull, which says everything.

I would like to extend my gratitude to the many staff across departments on campus who supported my PhD journey, including Kristine Meier, Jian Zhou, Mitchell Forsyth amongst others. Special thanks to the advisors at the Writing and Communication Centre—particularly Jane Russwurm, Nadine Fladd, Sinem Ozkardas, Stephanie Florence, and Elise Vist—for their expansive support. Your guidance went beyond writing; the feedback you provided were pivotal in shaping my growth as a scholar. My thanks also go to my Career Leader team at the Centre for Career Development, especially my supervisor-turned-dear-friend, Lauren Broderick. The privilege to serve as a Career Leader remains one of the highlights of my UWaterloo experience.

My parents and siblings are the foundation of my strength. I am the daughter of an inspiring medical doctor, and a woman of many talents—nurse turned consummate entrepreneur. I also have the honour of being the first of three siblings.

Dad, Papa Shiii, thank you for being my rock, my best friend, and my confidant. You are always ready to listen and always steady. Thank you for your wisdom and your exemplary faith. You are the original Dr. Suleiman, the life-saving kind, and I am honoured to follow in your footsteps as Dr. Suleiman II—though my kind of doctor fixes more equations than people.

Mom, Adebimpe, the one and only Maman Fāṭima, thank you for always believing that your daughter is the best thing since sliced bread, even when I am more passionate about books than chores. Your pride in me has never wavered, and your sacrifices have made this possible.

To my siblings, Halima and Mubarak—I am beyond lucky to do life as the founding member of Mu-Hali-Fat; You make it a joy and an honour to be a big sister. You are both so incredibly good at what you do, and I am constantly inspired by your brilliance and drive.

To the extended Suleiman-Kazeem-Awoleye-Okupe-Adekale family, and to the many others who have become kin through love and care—your presence has been an integral part of the tapestry of this journey. While I cannot name everyone here, please know that you are remembered and deeply appreciated.

To my many uncles and aunties—thank you for your unwavering support. Uncle Deremi, I am deeply grateful for your generosity and kindness. Uncle Sandy, your unconditional support and encouragement since my childhood have shaped me into the person I am today. To my ever-inspiring Aunty Musili—thank you for being such a remarkable role model; your PA is forever grateful. To Mr. Akeem Kazeem, thank you for your unfailing support and encouragement.

To my mother, Mrs. Adekale, thank you for feeding both my body and soul with endless food, love, and care. To my cousin, Dr. Adun Okupe, thank you for blazing the trail to a PhD. To my darling Queen Zee, my ever-generous sugar mummy, thank you for letting this first daughter experience what it is like to have the best big sister in the world. To Aunty Dami, thank you for everything; you are the epitome of grace and rich aunty vibes. I hope to be you when I grow up.

To my PhD baby, Jamal, Aunty loves you dearly, JJ! Thank you for your enlightening innocence and the reminder that whether Grade 1 or a PhD, we are all students—and we all deserve to love learning.

To my dear friends: Akuvi, Dee, Dola, Farida, Ife, Ijeoma, Ummi, and Vanessa—thank you for ensuring that I have a life outside academia. Whether it has been decades or just shy of one, your friendship has added colour to my life in more ways than I can express here.

To my friends and comrades in the journey of being a Woman in Engineering, PhD edition: Blessing, Kelly, Mercy, Shaundell, Shina, and Xiaoye—thank you for the shared experiences.

Some people discovered coffee during grad school; I found fitness. Focusing on my body instead of my intellect reminded me that perfection is not required: progress, no matter how slow, is still progress. My heartfelt thanks to the instructors at Warrior Athletics and KO Yoga; your guidance helped me finish this journey stronger and saner than I began.

It would be remiss of me not to thank myself for believing I could, for putting in the work and for seeing this through. I do not know where the courage came from, but I am in awe of how it unfolded over time.

To my past, present, and future selves—may we always persevere, with grace.

Dedication

To the force greater than myself—

ever present, ever sustaining.

Table of contents

Examining committee membership ..... **ii**

Author's declaration ..... **iii**

Abstract ..... **iv**

Land and ancestral acknowledgement ..... **vii**

Acknowledgements ..... **ix**

Dedication ..... **xiii**

List of figures ..... **xx**

List of tables ..... **xxviii**

List of abbreviations ..... **xxx**

List of symbols ..... **xxxiii**

Latin characters xxxiii

Greek characters xxxiv

Operators and functions xxxv

Common subscripts and superscripts xxxvi

Chapter 1 Introduction: Pyrometry of AHSS **1**

1.1. Thesis objective and document overview 3

Chapter 2 Background and literature review: AHSS and pyrometry **7**

2.1. Advanced high strength steel (AHSS) alloys 7

2.1.1. Continuous galvanizing lines (CGLs) 10

2.1.2. Intercritical annealing of AHSS 12

2.1.3. Thermodynamic stability of AHSS oxides during annealing 15
2.2. Pyrometry measurement model 18
2.2.1. Emissivity models for pyrometry 21
2.2.1.1. Single wavelength pyrometry 23
2.2.1.2. Dual-wavelength pyrometry 24
2.2.1.3. Multi-wavelength pyrometry 26
2.2.2. Effect of temperature and oxidation on the radiative properties of AHSS 28
Chapter 3 Multivariate spectral emissivity model for advanced high strength steel 31
3.1. Sample preparation and processing 33
3.2. Response surface methodology (RSM): factorial design 35
3.3. Results and discussion 37
3.3.1. Spectral emissivity measurements 37
3.3.2. 2^3 full factorial design 41
3.3.3. General full factorial design 44
3.3.3.1. Regression analysis: spectral emissivity model 46
3.4. Conclusion 50
Chapter 4 Experimental apparatus for *in situ* radiative measurement 51
4.1. Features of the annealing simulator 52
4.2. Chamber 1: Box design 55
4.2.1. Prototype implementation 55
4.2.2. Upgraded implementation 56
4.3. Chamber 2: Vacuum-based design 59
Chapter 5 Impact of evolving spectral emissivity on pyrometry 63
5.1. Experimental procedure 64
5.2. Experimental results 65

5.2.1. *In situ* spectral emissivity 66
5.2.2. Pyrometrically-inferred temperature 68
5.2.3. Inferred spectral emissivity from the pyrometry models 71
5.3. Conclusion 72
Chapter 6 Bayesian approach to pyrometry of advanced high strength steel 73
6.1. Pyrometry noise model 75
6.2. Bayesian framework 77
6.2.1. Sample-based spectral emissivity prior 79
6.2.2. Calibration coefficient prior 81
6.2.3. Inferring the temperature 82
6.3. Pyrometer and *in situ* measurements 83
6.4. Quantifying uncertainty in pyrometrically-inferred parameters 85
6.5. Comparing the Bayesian approach with a multi-wavelength model 87
6.6. Conclusions 91
Chapter 7 Effect of dew point on the evolving radiative properties 92
7.1. Experimental and measurement procedure 93
7.2. Results and discussion 93
7.2.1. *In situ* time-resolved spectral emissivity measurement 95
7.2.2. Multi-wavelength pyrometry estimates 99
7.3. Conclusions 106
Chapter 8 *In situ* and *ex situ* investigation of the radiative properties 107
8.1. Impact of low-temperature oxidation thermodynamics 108
8.2. Experimental procedure 110
8.3. Effect of rolling direction on FTIR measurement 111
8.4. *In situ* spectral emissivity variation in the WAS simulator 113

8.5. *Ex situ* spectral emissivity of quenched WAS and MGS samples 115
8.6. Comparing *in situ* and *ex situ* temperature-dependent radiative properties 117
8.6.1. Pyrometry estimates with *in situ* versus *ex situ* spectral emissivity 120
8.7. Conclusions 121
Chapter 9 Conditional emissivity prior for improved temperature estimates 123
9.1. Bayesian pyrometry model 125
9.1.1. Conditional emissivity prior 126
9.2. Annealing experimental procedure 130
9.3. Variations in radiative properties 131
9.3.1. Pre-annealed radiative properties 131
9.3.2. *In situ* spectral emissivity variation 134
9.4. Bayesian pyrometric temperature estimate 138
9.4.1. Generating a conditional emissivity prior from *in situ* replicates 138
9.4.2. Temperature estimates with the conditional emissivity prior 142
9.4.3. Further validation on DP980 alloy annealed at other dew points 144
9.4.4. Application to *in situ* measurements on other steel grades 146
9.5. Conclusions 148
Chapter 10 Conclusions and future work 151
10.1. Key knowledge contributions 151
10.1.1. Multivariate *ex situ* spectral emissivity model 151
10.1.2. Annealing simulator for *in situ* radiative measurements 152
10.1.3. *In situ* spectral and temporal variation in radiative properties 152
10.1.4. Accuracy of existing emissivity compensation algorithms for AHSS 155
10.1.5. Bayesian pyrometry model for uncertainty estimation 155
10.2. Ongoing and future work 158

10.2.1. Expanding the spectral range of the *in situ* radiative measurements 158
10.2.2. Number of detection wavelengths for multiwavelength estimates 159
10.2.3. Response surface modelling of the *in situ* radiative properties 161
10.2.4. Stochastic prior design for improved temperature posterior estimate 161
10.2.5. Online pyrometry experiment on a CGL 162
10.3. Final remarks 163
References 165
Appendix A Thermodynamic analysis of the gas-metal oxidation reaction 181
A.1. Oxygen partial pressure of the annealing atmosphere 181
A.2. Oxygen partial pressure of the metal oxides 183
Appendix B Vacuum chamber design and implementation 185
B.1. Modular flange design 185
B.2. Vacuum feedthroughs 187
B.3. Atmosphere control 188
B.4. Quench system 190

List of figures

Figure 1.1. Graphical overview of the dissertation chapters and the key research question addressed in each chapter..... 6

Figure 2.1. Global formability diagram comparing the total elongation and ultimate tensile strength (UTS) for mild steels, conventional high strength steels, and advanced high strength steels (AHSSs) [25]. 8

Figure 2.2. Stress-strain curve comparing the mechanical properties of dual-phase steel, high strength low alloy (HSLA) steel and plain carbon [24]. 10

Figure 2.3. Schematic of a typical continuous galvanizing line showing an array of pyrometers in the annealing furnace. Adapted form Ref. [33]. 11

Figure 2.4. The iron-carbon (Fe-C) phase diagram showing the intercritical temperature region (red shaded area) for ferrite-austenite formation in steel. The pearlite phase consists of alternating layers of austenite and cementite. The A_1, A_2, A_3 and A_{CM} lines are the critical temperature boundaries for phase transformation where A_1 is the temperature at which the pearlite-to-austenite eutectoid transformation begins; A_2 is the curie temperature for magnetic transformation where the metal changes from ferromagnetic to paramagnetic; A_3 is the temperature at which the ferrite-austenite phase fully transforms into austenite in hypo-eutectoid steel while A_{CM} is the temperature at which the ferrite-cementite phase fully transforms into austenite in hyper-eutectoid steel. Adapted from Ref. [20]..... 13

Figure 2.5. Schematic of the annealing cycle for processing dual-phase alloys indicating the key temperatures and microstructure, where α is ferrite, γ is austenite and α′ is martensite. M_s is the martensite start temperature at which the austenite begins to transform into martensite and M_f is the martensite finish temperature at which the austenite becomes fully transformed into martensite. Adapted from Refs. [19, 27, 28, 39]. 15

Figure 2.6. Thermodynamic stability of Fe, Cr, Mn, Si oxides with respect to annealing temperature and oxygen partial pressure for two dew points (−30°C and +10°C) in a N_2-5%H_2 atmosphere. 17
Figure 2.7. Schematic diagram of a typical pyrometry measurement. 19
Figure 2.8. Spectral distribution of radiation emission from blackbody and real surfaces..... 22
Figure 2.9. Graphical illustration of the wedge vs normal pyrometry configuration [3]..... 24
Figure 3.1. Schematic illustration of the annealing schedule for the tested coupons. 34
Figure 3.2. Measured spectral emissivity, ε_λ, for (a) polished samples (b) as-received samples. 39
Figure 3.3. Scanning electron micrographs (SEM) of the annealed low Si/Mn ratio samples. The images on the right correspond to the white boxed regions in the images on the left. (a) Si/Mn=0.04, polished, annealed at −30°C, (b) Si/Mn=0.04, polished, annealed at +10°C (c) Si/Mn=0.04, as-received, annealed at −30°C, and (d) Si/Mn=0.04, as-received, annealed at +10°C. 40
Figure 3.4. Percent contributions of the main and interaction effects for the combination of the three factors, dew point (A), Si/Mn ratio (B), and surface state (C), at the following wavelengths: 1.2 μm, 1.6 μm, 2.1 μm, 2.4 μm, 2.8 μm, 3.2 μm, 3.6 μm, and 4.0 μm. 43
Figure 3.5. Residual analysis: (a) normal probability plot of residuals and (b) plot of residuals vs predicted spectral emissivity 48
Figure 3.6. Comparison of measured and predicted spectral emissivity, ε_λ, for (a) polished coupons and (b) as-received coupons..... 48
Figure 4.1. Schematic diagram of the annealing simulator..... 53
Figure 4.2. First iteration of the annealing simulator (Chamber 1 prototype) and (inset) of a heated coupon. 55
Figure 4.3. Upgraded implementation of Chamber 1 showing the mounted pyrometer and spectrometer optics, and (inset) a heated coupon. 56
Figure 4.4. Infrared thermal images of a black-painted AHSS sample showing the temperature uniformity for the equivalent measurement spot size (a) 600°C and (b) 850°C..... 57
Figure 4.5. The chamber back panel for the second design iteration (left – original) and third design iteration (right – updated), showing the modifications made to the bus bar feedthrough to improve airtightness. 58

Figure 4.6. Shell of the upgraded Chamber 1 showing the numerous holes that collectively contribute to the persistent infiltration problem..... 59
Figure 4.7. Vacuum-based implementation of the annealing simulator (Chamber 2): (a) the CAD model and (b) final implementation showing the mounted pyrometer and spectrometer optics, and (inset) a heated coupon. 60
Figure 4.8. *In situ* images of annealing AHSS coupons at 400°C, 500°C and 600°C showing differences in the temperature-dependent visible oxides obtained with (a) Chamber 1 (upgraded) and (b) Chamber 2. 62
Figure 4.9. *Ex situ* images of the AHSS coupons processed in (a) Chamber 1 (upgraded) showing the anomalous visible oxide formed on the steel surface after quenching, while samples annealed in (b) Chamber 2 do not have this oxide layer..... 62
Figure 5.1. Plot of spectral emissivity (ε_λ) vs wavelength (λ) for as-received DP980 at room temperature. 64
Figure 5.2. Thermocouple reading for the annealed DP980 sample showing the region of the observed oxidation..... 65
Figure 5.3. Images of the coupon surface during heating. The sample surface is clean at the start of the experiment (a), but an oxide layer begins to form at ~300°C (b), becomes thicker (c), and is fully formed by ~500°C (d). The oxide starts to clear at ~600°C (e) and cannot be seen at ~700°C (f)..... 66
Figure 5.4. Evolving spectral emissivity, ε_λ, of DP980 coupon measured using the NIR spectrometer. Dashed lines correspond to pyrometer detection wavelengths. 67
Figure 5.5. Plots of the spectral emissivity, ε_λ, as a function of (a) wavelength (λ) and (b) time (t) and temperature (T)..... 67
Figure 5.6. Pyrometrically-inferred temperature for (a) ratio pyrometry and (b) multi-wavelength pyrometry..... 70
Figure 5.7. Spectral emissivity for ratio pyrometry models compared with experimental data: (a) Ratio 1(1.6μm/2.4μm), (b) Ratio 2 (1.6μm/2.1μm), and (c) Ratio 3 (2.1μm/2.4μm)..... 71
Figure 5.8. Spectral emissivity for multi-wavelength pyrometry models compared with experimental data: (a) Model 1 (b) Model 2, and (c) Model 3. 72

Figure 6.1. Signal variance, σ_{Si}^2, plotted against the mean signal, $\overline{S_\lambda}$ at the three detection wavelengths: (a) 1.6 μm, (a) 2.1 μm, and (c) 2.4 μm. The solid red line corresponds to the sigmoid function while the dashed black line represents the linear fit. 77
Figure 6.2. Histograms and corresponding normal distribution for the sample-based spectral emissivity priors obtained from *ex situ* measurements for the three detection wavelengths: (a) 1.6 μm; (b) 2.1 μm; and (c) 2.4 μm. 79
Figure 6.3. Histograms and corresponding normal distribution for the pyrometer calibration coefficient prior at the three detection wavelengths: (a) 1.6 μm; (b) 2.1 μm; and (c) 2.4 μm. 82
Figure 6.4. *In situ* measurements with the associated thermocouple reading. (a) Pyrometer count measurement for the three detection wavelengths, and (b) *In situ* spectral emissivities obtained using the NIR spectrometer. 84
Figure 6.5. Marginalized posterior probability distributions for the hold period (800°C): (a) temperature; (b) $\varepsilon_{\lambda d1}$ at 1.6 μm; (c) $\varepsilon_{\lambda d2}$ at 2.1 μm; and (d) $\varepsilon_{\lambda d3}$ at 2.4 μm. The blue curves are the maximum *a posteriori* (MAP) distributions. The black curves indicate the *in situ* thermocouple (temperature) and NIR spectrometer (emissivity) measurement distributions. The solid lines are the mean values, and the shaded regions are 95% credibility intervals corresponding to two standard deviations of the mean. 86
Figure 6.6. Plot of the prior and *in situ* densities for the spectral emissivities at the detection wavelengths (a) $\varepsilon_{\lambda d1}$ at 1.6 μm; (b) $\varepsilon_{\lambda d2}$ at 2.1 μm; and (c) $\varepsilon_{\lambda d3}$ at 2.4 μm. The red curves are the maximum *a posteriori* (MAP) distributions. The black curves represent the NIR spectrometer (emissivity) measurement distributions. The solid lines indicate the distribution mean and the 95% credibility intervals (shaded area) are equivalent to two standard deviations of the mean. 87
Figure 6.7. MW estimates (solid red lines), MAP estimates (solid blue lines), i*n situ* estimates (dashed lines) and 95% credibility intervals for the parameters: (a) T, (b) $\varepsilon_{\lambda d1}$ at 1.6 μm, (c) $\varepsilon_{\lambda d2}$ at 2.1 μm, and (d) $\varepsilon_{\lambda d3}$ at 2.4 μm. The shaded areas represent 95% credibility bounds corresponding to two standard deviations of the mean or nominal values. 90
Figure 7.1. (a) Pre-annealed spectral emissivity, ε_λ, for the DP980 coupons. (b) Temperature measurements from the thermocouple attached to the samples during annealing. 94

Figure 7.2. Measured time-resolved spectral emissivity, ε_λ, for the target DPs: −30°C (a, d), −10°C (b, e), and +10°C (c, f). The white horizontal lines shown in (a) – (c) correspond to the wavelengths (1.2 μm, 1.6 μm, 2.1 μm, and 2.4 μm) plotted in (d) – (f). 96
Figure 7.3. Measured spectral emissivity for the three dew points as a function of the annealing temperature and time. (a) 400°C - 29.25 s, (b) 500°C - 37 s, (e) 600°C - 44.75 s, (d) 700°C – 52.5 s, (e) 800°C - 60 s (soak starts), (f) 800°C - 75 s (mid soak), and (g) 800°C - 90 s (soak ends).. 98
Figure 7.4. Pyrometry temperature predictions for Model #1 (red lines), Model #2 (blue lines), Model #3 (purple lines) and Model #4 (green lines) at the following target DPs: (a) −30°C, (b) −10°C and (c) +10°C. The dashed lines represent the thermocouple temperature measurements. 101
Figure 7.5. Pyrometry temperature predictions for the *ex situ* Gaussian prior (Model #5) showing the MAP estimates (solid blue lines), thermocouple temperature measurements (dashed lines) and 95% credibility intervals (shaded region) for the following target DPs: (a) −30°C, (b) −10°C, and (c) +10°C..... 101
Figure 7.6. The measurement error for the emissivity models (Model #1 − #5) compared against the uncertainty ($\pm 2\sigma$) obtained for stochastic emissivity prior (Model #5) at key temperatures for the following target DPs: (a) −30°C, (b) −10°C, and (c) +10°C. 103
Figure 7.7. Stochastic prior distributions at 2.1 μm with vertical lines representing the spectrometer emissivity measurements at the three dew points (−30°C, −10°C and +10°C). (a) Model #5 (*ex situ*-based prior) overlapped with spectral emissivity measurements at 400°C and (b) Model #5 (*ex situ*-based prior) overlapped with spectral emissivity measurements at 800°C. The shaded region represents 99.7% of the observations, which falls within 3 standard deviations of the mean (i.e., $\mu_\varepsilon \pm 3\sigma_\varepsilon$). 105
Figure 8.1. Logarithmic plot of the oxygen partial pressure (pO_2) as a function of process temperature. This shows the thermodynamic stability of the metallic oxides relative to oxygen potential of the annealing atmosphere at −30°C dew point. 109
Figure 8.2. Schematic of the annealing schedule showing the heating rate, peak annealing temperature (PAT), and quench rate. This schedule was used in both simulators. 110

Figure 8.3. Orientation-dependent variation in the near-normal directional-hemispherical spectral reflectance (ρ_λ) of cold-rolled DP980 measured with the integrating sphere. Error bars correspond to one standard deviation of the mean of the five samples. 112
Figure 8.4. (a) Contour of the evolving spectral emissivity, highlighting the *in situ* spectral and temporal variation of the DP980 alloy during annealing. (b) The spectral emissivity from (a) plotted at key annealing temperatures: 400°C (29.25 s), 500°C (37 s), 650°C (48.5 s), 750°C (56 s), 800°C (60 s - soak starts) and 800°C (90 s - soak ends). 113
Figure 8.5. Evolving spectral emissivity, ε_λ, measured *in situ* with the pyrometer and spectrometer at the three-detection wavelength versus (a) annealing time, *t*; and (b) annealing temperature, *T*. 114
Figure 8.6. *Ex situ* spectral emissivity at different annealing temperatures for samples processed in (a) Waterloo Annealing Simulator (WAS) and (b) McMaster Galvanizing Simulator (MGS). The pre-annealed emissivity represents the average of the 5 samples analyzed in Figure 8.3 (diagonal orientation only) with the measurement uncertainty excluded for clarity. 116
Figure 8.7. *Ex situ* spectral emissivity as a function of annealing temperature for the three detection wavelengths of the pyrometer: (a) 1.6 µm, (b) 2.1 µm, and (c) 2.4 µm. The red scatter represents the samples processed in the Waterloo Annealing Simulator (WAS), while the blue scatter is the samples processed in the McMaster Galvanizing Simulator (MGS). 117
Figure 8.8. Comparing the *in situ* and *ex situ* spectral emissivity for annealed DP980 at the following temperatures: (a) 200°C, (b) 300°C, (c) 400°C, (d) 650°C, (e) 750°C, and (f) 800°C (after 30s soak). The WAS_{spect} and WAS_{pyro} are the *in situ* spectrometer and pyrometer readings, respectively, from Figure 8.4 and Figure 8.5. The $WAS_{ex\ situ}$ and $MGS_{ex\ situ}$ are the *ex situ* FTIR spectrometer measurements on rapidly quenched samples, shown in Figure 8.6. 118
Figure 9.1. Pre-annealed spectral emissivity, ε_λ, for the AHSS and mild steel samples: DP980 (Samples #1 and #2), DP780 (Sample #3) and IF (Sample #4). 132
Figure 9.2. Optical micrographs and roughness parameters (S_q and S_q/τ) for the AHSS and mild steel samples: (a) DP980, DP780 and (c) IF. 133
Figure 9.3. Evolving spectral emissivity, ε_λ, measured *in situ* as a function of time, wavelength and temperature for the annealed steel samples at their respective dew points: (a, e) Sample #1: DP980 at −30°C DP; (b, f) Sample #2: DP980 at −45°C DP; (c, g) Sample #3: DP780 at −45°C

DP; and (d, h) Sample #4: IF at −30°C DP. The graphs on the right (e, f, g, and h) show the spectral emissivity at nominal temperatures relative to the pre-annealed values from Figure 9.1. 135
Figure 9.4. Temporal variations in the spectral emissivity at the pyrometry detection wavelengths: (a) 1.6 μm; (b) 2.1 μm; and (c) 2.4μm, highlighting the observed emissivity peaks. 136
Figure 9.5. Spectral emissivity as a function of temperature at the pyrometry detection wavelengths: (a) 1.6 μm, (b) 2.1 μm, and (c) 2.4μm. The temperature of the emissivity peaks falling within a 12°C range (693°C - 705°C). 137
Figure 9.6. *In situ* spectral emissivity of the DP980 sample (Sample #1) and replicates (Replicate #1 - #4) annealed at T_{dp1} = −30°C. (a) 1.6 μm, (b) 2.1 μm, and (c) 2.4μm. 139
Figure 9.7. Histogram and Gaussian distribution fit for the *in situ* general emissivity distribution conditional on T_{dp1}, i.e., $p(\varepsilon \mid T_{dp1})$, at the three detection wavelengths: (a) 1.6 μm, (b) 2.1 μm, and (c) 2.4μm. 140
Figure 9.8. Plot of the equivalent black body temperatures, $\mathbf{T}_{be}$, for the DP980 replicates annealed at T_{pd1}, showing the bin labels, r_j, and the predefined bin boundaries. 141
Figure 9.9. Histograms and Gaussian distributions for the conditional spectral emissivity prior, $p(\varepsilon \mid T_{dp1}, \mathbf{r}(\mathbf{T}_{be}))$, generated from *in situ* measurements on DP980 replicates annealed at the dew point, T_{dp1} = −30°C. 142
Figure 9.10. MAP estimates (solid lines) and 95% credibility interval (shaded area) for the pyrometrically-inferred temperatures computed on Sample #1 using the three emissivity priors: **(a)** *ex situ* emissivity prior, **(b)** *in situ* general emissivity prior, $p(\boldsymbol{\varepsilon} \mid T_{dp1})$, and **(c)** *in situ* conditional emissivity prior, $p(\boldsymbol{\varepsilon} \mid T_{dp1}, \mathbf{r}(\mathbf{T}_{be}))$. The dashed lines represent *in situ* nominal thermocouple measurements. 143
Figure 9.11. Posterior densities estimated with conditional emissivity prior for the DP980 samples annealed at **(a)** −45°C; **(b)** −30°C; and **(c)** −10°C. The solid lines indicate the posterior distribution mean and the 95% credibility intervals (shaded area) are equivalent to two standard deviations of the mean. The black dashed lines represent the *in situ* thermocouple measurements. 145
Figure 9.12. Posterior densities estimated with conditional emissivity prior for AHSS and mild steel grades annealed at various dew points: **(a)** DP780 annealed at −45°C; **(b)** DP980 annealed at −30°C; and **(c)** IF steel annealed at −30°C. The solid lines indicate the posterior distribution mean

and the 95% credibility intervals (shaded area) are equivalent to two standard deviations of the mean. The black dashed lines represent the *in situ* thermocouple measurements. 147
Figure 10.1. Multi-wavelength (MW) and dual-wavelength (DW) temperature posterior for a DP980 alloy (Si/Mn = 0.04) annealed at −30°C and −45°C showing the MAP estimates (solid lines); thermocouple temperature measurements (dashed lines) and error bounds corresponding to 95% credibility intervals (shaded region). Samples #1 and #2 are both −30°C replicates with varying oxidation kinetics impacting their spectral emissivity values [164]..... 159
Figure 10.2. Effect of increasing the number of detection wavelengths (between 1.2 − 2.5 μm) on the MAP and credibility intervals at the peak annealing temperature (PAT = 800°C) for a DP980 sample annealed at −30°C..... 160
Figure B.1. Images of the wet and mixing chamber designed for the humidification system in (a) Chamber 1 and (b) Chamber 2..... 188
Figure B.2. Piping and instrumentation diagram (P&ID) for the vacuum-based annealing simulator (Chamber 2). 189
Figure B.3. Comparing the anomalous visible oxide layer on (a) samples quenched in helium against (b) samples quenched with ultra-high purity nitrogen-hydrogen mixture..... 190

List of tables

Table 3.1. Nominal chemical composition of DP980 [103]. 34
Table 3.2. List of annealed coupons indicating the dew point of the annealing atmosphere, the ratio of alloy components, and the pre-annealed surface state. 35
Table 3.3. The uncoded and coded levels for the four factors: dew point (A), Si/Mn ratio (B), surface state (C), and wavelength (D)..... 37
Table 3.4. The 2^3 factorial design matrix and spectral emissivity responses for the combination of three factors: dew point (A), Si/Mn ratio (B), and surface state (C), at key wavelengths in the near-infrared region..... 42
Table 3.5. Statistically significant main and interaction effects contributing to the variations in spectral emissivity as identified from the F-test at 95% confidence interval. The check marks (✓) indicate the effects that are statistically significant. 43
Table 3.6. The general $2 \times 2 \times 2 \times 3$ factorial design and spectral emissivity responses for the combination of all four factors: dew point (A), Si/Mn ratio (B), surface state (C), and wavelength (D). 44
Table 3.7. ANOVA for the general ($2 \times 2 \times 2 \times 3$) factorial design 45
Table 3.8. Regression coefficients for the spectral emissivity model 47
Table 5.1. Spectral emissivity ratio (e-slope) measured from the as-received DP980 sample 68
Table 5.2. Multi-wavelength emissivity compensation algorithms 69
Table 5.3. Maximum absolute error and average relative error for pyrometry methods 70
Table 6.1. Coefficient of the sigmoid noise function modelled on the emission from a black body source at 350°C to 850°C..... 77
Table 6.2. Normality test results for the sample-based spectral emissivity priors at 95% confidence interval. 80

Table 6.3. MAP estimate, *in situ* estimate and their 95% credibility intervals for the temperature and spectral emissivities at 800°C (specifically the results corresponding to the measurements at the 90s). 85
Table 7.1. Dew point (DP) and oxygen concentration (O_2) of the annealing atmospheres. 94
Table 7.2. Summary of deterministic emissivity compensation algorithms (Models #1 − #4) and stochastic prior (Model #5). 100
Table 8.1. Pyrometry estimates (T_p) and the corresponding absolute error (AE) and relative error (RE) obtained with the *ex situ* spectral emissivity from both simulators (WAS_{exsitu} and MGS_{exsitu}) compared against the thermocouple temperatures (T) and the estimates inferred with the *in situ* spectrometer emissivity (WAS_{spect}). 120
Table 9.1. Silicon-to-manganese ratio (Si/Mn), coil extraction location and annealing dew point for the AHSS alloys annealed in this study. The alloy composition is measured using spark atomic emission spectrometry. 130
Table 9.2. Signed error (Error), relative error (RE) and the uncertainty (±2σ) obtained for pyrometric estimates on Sample #1 for the three priors; *ex situ* prior, *in situ* general prior and *in situ* conditional emissivity prior, at key temperatures (T) during the annealing cycle. 144
Table 9.3. Signed error (Error), relative error (RE) and the uncertainty (±2σ) obtained with the conditional emissivity prior at key temperatures (T) for DP980 samples annealed at the following dew points: −45°C, −30°C and −10°C. 146
Table 9.4. Signed error (Error), relative error (RE) and the uncertainty (±2σ) obtained with the conditional emissivity prior at key temperatures (T) for AHSS and mild steel grades annealed at various dew points: DP780 annealed at −45°C, DP980 annealed at −30°C, and IF mild steel annealed at −30°C. 148
Table A.1. Coefficients for the standard Gibbs energy of formation for each compound [74, 168]. 184
Table B.1. Summary of key functional, constraint and non-functional requirement for the vacuum-based annealing simulator. 185

List of abbreviations

This section lists common abbreviations used in this work.

Abbreviation	Definition
AC	Alternating Current
ADC	Analog-to-Digital Converter
AE	Absolute Error
AHSS(s)	Advanced High Strength Steel(s)
ANOVA	Analysis of Variance
ASTM	American Society for Testing and Materials
BH	Bake Hardening
CAD	Computer-Aided Design
CCD	Central Composite Design
CCT	Continuous Cooling Transformation
CF	ConFlat
CFRP	Carbon Fiber Reinforced Polymer
CGL	Continuous Galvanizing Line
CI	Confidence Interval
DC	Direct Current
DFF	Direct-Fired Furnace
DP	Dew point
DP	Dual-Phase
DW	Dual wavelength
EDDS	Extra Deep Drawing Steel
EDT	Electron Discharge Texturing
EM	Electromagnetic
Err	Error
FOV	Field of View
FTIR	Fourier Transform Infrared Spectroscopy
GA	Galvanneal
GAP	Galvanizers Autobody Partnership
GHG	Greenhouse Gas
GI	Galvanize

GOA	Geometric Optics Approximation
HRR	Hagen-Rubens Relation
HSLA	High Strength Low-Alloy
HSS	High Strength Steel
IF	Interstitial-Free
ISO	International Organization for Standardization
IZA	International Zinc Association
InGaAs	Indium Gallium Arsenide
KS	Kolmogorov-Smirnov Test
MAP	Maximum A Posteriori
MFC	Mass Flow Controller
MGS	McMaster Galvanizing Simulator
MIR	Mid-infrared
MRT	Multispectral Radiation Thermometry
MVN	Multivariate Normal
MW	Multi-wavelength
NIR	Near-infrared
NPP	Normal Probability Plot
OFHC	Oxygen-Free, High Conductivity
P&ID	Piping and Instrumentation Diagram
PAT	Peak Annealing Temperature
PCA	Principal Component Analysis
PDF	Probability Density Function
PID	Proportional-Integral-Derivative controller
PTFE	Polytetrafluoroethylene
RE	Relative Error
RMS	Root Mean Square
RMSE	Root Mean Square Error
RPV	Reactor Pressure Vessels
RSM	Response Surface Methodology
RTF	Radiant Tube Furnace
SEM	Scanning Electron Microscopy
SRI	Steel Recycling Institute
SRO	Short-Range Order
SSE	Sum of Squared Errors
SW	Single wavelength
TRACE	Thermometry Re-established by Automatic Compensation of Emissivity

TRIP	Transformation-Induced Plasticity
TS	Tensile Strength
TTT	Time-Temperature-Transformation
UHSS	Ultra High Strength Steels
UTS	Ultimate Tensile Strength
UV	Ultraviolet
VIS	Visible
WAS	Waterloo Annealing Simulator

List of symbols

This section presents the nomenclature and symbols used throughout the thesis. Given that the work draws on multiple bodies of literature, occasional conflicts in symbol usage arise. Where such conflicts occur, the "Section" column specifies the context in which a given definition applies. If no section is indicated, the definition is either applicable across the entire thesis or to all sections not covered by an alternative definition. The symbols are organized into two distinct lists: one for Latin characters and one for Greek characters. Commonly used subscripts and superscripts are provided in a separate list, while key operators and functions are presented in another list.

Latin characters

Symbol	Section	Definition
A_1	-	Eutectoid temperature
A_2	-	Curie temperature (magnetic transformation)
A_3	-	Upper critical temperature
A_{CM}	-	Temperature at which ferrite-cementite fully transforms into austenite
A_d	-	Detector area
a_0	-	Algorithm constant
B	-	Vector of blackbody intensities at the calibration temperature
C_1, C_2	-	Constants for the Planck distribution
d	-	Oxide film thickness
Err	-	Signed error
F	-	F-value
h	-	Planck's constant
I_λ	-	Spectral intensity
$I_{\lambda b}$	-	Blackbody spectral intensity
$I_{\lambda d}$	-	Spectral intensity at detection wavelength d
$I_{\lambda,ext}$	-	Extraneous radiation from additional surfaces in the pyrometer's FOV
$I_{\lambda,obs}$	-	Observed spectral intensity leaving the surface
$I_{\lambda,ref}$	-	Reflected intensity from surroundings

K	-	Vector for calibration constants
K_λ	-	Spectral calibration constant
L_S	-	Cholesky factorization of inverse measurement covariance
M	-	Metal element within steel
M_s	-	Martensite start temperature
M_f	-	Martensite finish temperature
M_xO_y	-	Metallic oxide of the element M within the steel
n	3	Number of factors
p	2, 5	Number of irradiance measurements
p	-	Partial pressure
R^2	-	Coefficient of determination: Adj. –Adjusted, Pred. –Predictive
R_λ	-	Spectral responsivity of the pyrometer
R_q	-	RMS roughness (line-based)
RE	-	Relative error
S	-	Vector of the spectral irradiance signals
S_λ	-	Spectral irradiance signal
S_q	-	RMS roughness (area-based)
S_q/τ	-	Surface slope
T	-	Surface temperature of the target
$\mathbf{T}_{be}$	-	Vector of the equivalent blackbody temperature
$T_{be\lambda d}$	-	equivalent blackbody temperature at a detection wavelength
T_p	-	Predicted pyrometry temperature
T_{TC}	-	Thermocouple temperature
T_{dp}	-	Atmosphere dew point
$\hat{y}$	-	Predicted response

Greek characters

Symbol	Section	Definition
α	2.1	Ferrite phase
α'	-	Martensite phase
γ	-	Austenite phase
α_λ	-	Spectral directional absorptivity
ϵ	-	Random error
ε	-	Spectral emissivity
ε_λ	-	Near-normal emissivity
$\varepsilon_{\lambda d}$	-	Spectral emissivity at detection wavelength

$\varepsilon_{\lambda dr}$	-	Emissivity ratio
$\varepsilon_{\lambda,n}$	-	Normal spectral emissivity
Γ_{ε}	-	Covariance of the spectral emissivity
Γ_{K}	-	Covariance of the calibration constant
Γ_{φ}	-	Covariance of the nuisance parameters
Γ_{S}	-	Covariance of the measurement noise
Γ_{SC}	-	Covariance of the calibration measurement noise
Γ_{POST}	-	Covariance of the temperature posterior probability density
λ	-	Wavelength
λ_{d}	-	detection wavelength
μ	-	mean
φ	-	Nuisance parameters vector
ϕ	2.2.1	Azimuthal angle
Φ	-	Incident radiant energy
θ	-	Polar angle
ρ_{λ}	-	Spectral directional-hemispherical reflectance
χ^2	-	Least square error
σ	2.2.2 7.2.1	Surface roughness
σ	-	Standard deviation
σ_{G}	-	Gaussian white noise

Operators and functions

Functions	**Definition**
chol(·)	Cholesky factorization
cov(·)	Covariance matrix
diag(·)	Diagonal matrix
ln(·)	Natural logarithm
mean(·), $\bar{\cdot}$	Mean, average
$\mathcal{N}(\cdot)$	Normal distribution
p(·)	Probability density function
var(·)	Variance
$(\cdot)^{-1}$	Inverse
$(\cdot)^{T}$	Transpose
$\lvert\cdot\rvert$	Determinant

Common subscripts and superscripts

Subscript (or superscript)	Section	Definition
be	-	Equivalent blackbody temperature
d	-	Detection-related
dp	-	Dew point
G (superscript)	-	Gaussian
i	-	Detection wavelength index
i	2.2.1	Incident direction
i	3	Factor index
j	3	Factor index
j	9	Categorical bins index
k	3	Factor index
λ	-	Wavelength
λd	-	Detection wavelength
λd1, λd2, λd3	-	Specific detection wavelengths
meas	-	Measurement
mod	-	Model
post	-	Posterior probability
P (superscript)	-	Poisson
pr	-	Prior probability
pr,CAL	-	Prior calibration probability
SC	-	Calibration-related
spect	-	Spectrometer
pyro	-	Pyrometer
MAP	-	Maximum A Posteriori estimate

Chapter 1
Introduction: Pyrometry of AHSS

With strict global regulations surrounding vehicle emission and crash performance, automotive manufacturers increasingly turn to lightweighting to improve fuel efficiency and reduce emissions from fossil-fuelled vehicles, and to extend the range of electric vehicles. One key material enabling this is Advanced High-Strength Steels (AHSS)—steel alloys with complex microstructures that provide the high strength-to-weight ratios and formability essential for automotive lightweighting. Compared to other expensive low-density materials, such as aluminium, magnesium, and carbon fiber composites, AHSS alloys may be used to develop automotive parts that meet crash safety standards while reducing vehicle weight by up to 39% and eliminating 50% to 70% of the carbon emissions produced over the life cycle of the vehicle [1, 2].

AHSSs derive their high yield strength and ductility through a highly engineered microstructure, which is achieved via a precisely controlled, alloy-dependent intercritical annealing process. Generally, the steel industry needs to control the intercritical annealing process within ±2 to ±4°C of the desired annealing temperature, especially for second and third generation AHSS grades. However, in recent times, steelmakers report AHSS rejection rate as high as 30% [3] due to substandard mechanical properties, both in terms of strength and zinc layer adhesion. Nonuniform heating has two potential origins. First, uncertain radiative properties lead to errors in the pyrometrically-inferred temperatures used to control the annealing furnaces. Second, uncertainty in the heating rate during intercritical annealing, potentially due to inefficient furnace design and operation, leads to non-uniform irradiation of the AHSS strip, which produces local variations in the temperature along the coil [4, 5]. The combination of these factors compounds into significant temperature excursions. The resulting substandard mechanical properties cost steelmakers millions of dollars annually, while impeding the development of vehicles with improved crashworthiness and fuel efficiency. This thesis will focus on a key cause for substandard AHSS properties—namely, errors in the pyrometer measurements.

Accurate pyrometry estimates are challenging due to the lack of detailed knowledge on the radiative properties of AHSS, specifically, the spectral emissivity, which defines the efficiency with which a material emits thermal radiation as a function of wavelength, temperature, and direction. The spectral emissivity of AHSS is imperfectly known as it varies with the as-received properties of the steel—specifically alloy composition and surface roughness— and further evolves during annealing due to temperature, dew point, and other process parameters. These uncertain wavelength-dependent variations in spectral emissivity cause errors in pyrometrically-inferred temperatures, which, in turn, can induce thermal excursions during processing and deficient mechanical properties in the steel. Further, current pyrometry methods only provide a point estimate of the surface temperature, making it impossible for steelmakers to assess the reliability of the estimates.

In pyrometry, the unknown spectral emissivity is usually inferred simultaneously with the steel temperature using intensities measured at one or more wavelengths, typically by assuming or prescribing an underlying emissivity relationship based on the number of detection wavelengths. This relationship, often referred to as an emissivity compensation algorithm, can either be a constant, in the case of the single-wavelength pyrometry, or an emissivity ratio or function for dual-, and multi-wavelength pyrometers [6]. Several studies have developed emissivity compensation approaches for dual- and multi-spectral pyrometry methods on metals, in order to mitigate pyrometer errors caused by uncertain spectral emissivity [7-16]. However, none of these methods adequately addresses how the spectral emissivity of automotive AHSS alloys varies with interdependent material properties and processing conditions. Thiessen et al. [17] showed that using a quotient pyrometer (i.e., dual-spectral/ratio pyrometry method with greybody approximation) on transformation induced plasticity (TRIP) AHSS alloys produced temperature deviations of up to 52 K due to the emissivity fluctuations caused by an oxide layer that forms on the steel surface during annealing. Thermal excursions caused by pyrometry errors impact the microstructure and mechanical properties of advanced high-strength steels (AHSS) significantly. Mosser et al. [18] showed that, for an annealed dual-phase (DP980) AHSS alloy, temperature deviations of 50K below the nominal temperature negatively impacted the yield strength of the steel, while deviation of 50K above the nominal temperature compromises the elongation at failure, affecting the ductility of the steel.

To address the lack of a pyrometry approach tailored specifically to the complex interdependent properties of AHSS, the International Zinc Association (IZA)'s Galvanized Autobody Partnership (GAP) program, a global consortium of steel producers, automakers, and equipment manufacturers, commissioned this research project with the goal of developing robust pyrometry methods that minimize the thermal excursions caused by inaccurate estimates, thus, increasing the production of prime, high-quality AHSS materials.

1.1. Thesis objective and document overview

This thesis focuses on developing a robust pyrometry method that accounts for how the spectral emissivity of AHSS varies with temperature, interdependent material properties (including alloy composition, surface roughness, oxide film thickness), and annealing process parameters (such as dew point and atmospheric temperature). More importantly, this research aims to combine this robust emissivity model with an uncertainty estimation technique that quantifies the measurement uncertainty associated with the pyrometrically-inferred temperatures. While this thesis focuses on intercritical annealing of dual-phase AHSS alloys (DP980), the methods developed in this work can be extended to any AHSS grades and other materials requiring infrared temperature estimates, thereby enhancing pyrometry applications beyond AHSS.

Figure 1.1 gives an overview of the content of this dissertation, highlighting the primary research question addressed in each chapter. This thesis consists of eight core chapters, excluding the introduction and concluding chapters:

- **Chapter 2** provides background knowledge required to understand the complex interdependent relationship between alloy chemical composition and annealing process parameters influencing accurate pyrometry of AHSS. This chapter starts with an overview of AHSS alloys, their properties, and the intercritical annealing process employed in continuous galvanizing lines to impart the desired mechanical properties. This is followed by a review of the principles of pyrometry, and a summary of existing methods typically used to compensate for variations in the spectral emissivity of metals.
- **Chapter 3** presents a new multivariate emissivity model that elucidates the interdependent relationship between the surface state and radiative properties of AHSS. This leverages factorial design of experiments to capture the parametric effects of dew point, alloy

composition, pre-annealed surface state, and wavelength on the *ex situ* normal emissivity of dual-phase AHSS alloys.

- **Chapter 4** introduces the features and design of the chamber used to conduct *in situ* pyrometry and radiative measurements, simulating the industrial intercritical annealing process.
- **Chapter 5** looks at *in situ* time-resolved spectral emissivity and pyrometry measurements carried out on dual phase AHSS alloy (DP980) heated in the annealing chamber. It provides crucial insights into the temperature-dependent effects that takes place during annealing, specifically how the evolving surface influences the radiative properties and consequently, the pyrometrically-inferred temperature.
- **Chapter 6** proposes the Bayesian framework for estimating the pyrometrically-inferred temperature and, crucially, its associated uncertainties. Spectral emissivity measurements obtained through *ex situ* characterization are incorporated into the inference through maximum likelihood priors that describe the expected variations in radiative properties. Existing pyrometry methods only provide a point estimate of surface temperature; however, inferring the posterior probability density with the Bayesian framework will allow galvanizers to better assess the reliability of the pyrometrically-inferred temperature.
- **Chapter 7** examines the effect of internal and external selective oxidation on the radiative properties of DP980 alloy by varying the oxidation potential (i.e., dew point) of the annealing atmosphere. This chapter provides an *in situ* analysis of the interdependent effect of dew point, temperature, and time on the spectral emissivity of a DP980 AHSS alloy, and how they impact the pyrometry estimates. Using the Bayesian pyrometry framework, this chapter examines the feasibility of having a single pyrometry model that compensates for spectral emissivity variations across different AHSS processing conditions.
- **Chapter 8** is a comparative analysis of the *ex situ* and *in situ* radiative properties of annealed DP980 alloy. Investigating the difference between the temperature-dependent variations in spectral emissivity observed *in situ* and *ex situ* provides insight into the impact of low temperature oxidation on the radiative properties of AHSS. Comparing pyrometry error resulting from the difference between the *ex situ* and *in situ* emissivity measurements highlights why accurate pyrometry needs to account for temperature-dependent variations in the optical properties of the composite metal-oxide AHSS surface.

- **Chapter 9** presents a conditional stochastic prior for the imperfectly known spectral emissivity that explicitly incorporates the covariate dependence of the radiative properties on the annealing dew point and the equivalent blackbody temperature. The narrower credibility interval obtained with this approach significantly improves the accuracy of the temperature posterior. In addition, this chapter highlights the impact of selective oxidation and pre-annealed surface topography on the radiative properties of AHSS by comparing the *in situ* emissivity of two dual phase alloys (DP980 and DP780) against a standard EDDS grade IF steel.

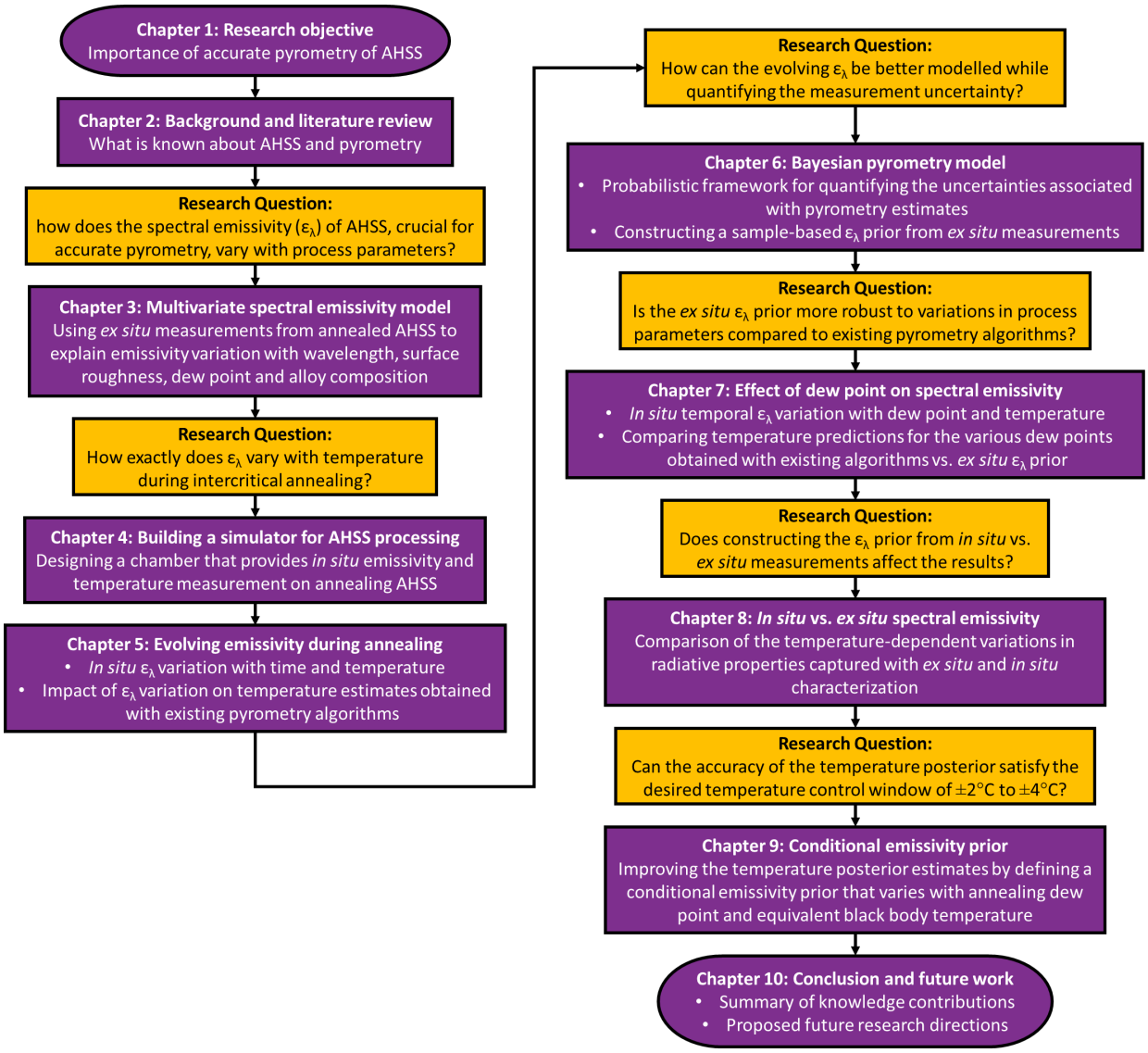


Figure 1.1. Graphical overview of the dissertation chapters and the key research question addressed in each chapter.

Chapter 2
Background and literature review: AHSS and pyrometry

This literature review chapter consists of two main sections. The first section describes the continuous galvanizing line and the intercritical annealing process used to produce AHSS. The effect of the annealing atmosphere on the selective oxidation of AHSS and thus its spectral emissivity is also discussed. The second half of this chapter introduces the equations that govern pyrometry and the passive emissivity compensation techniques that have been developed to improve the accuracy of pyrometry measurements on metals.

2.1. Advanced high strength steel (AHSS) alloys

Advanced high strength steels (AHSSs) are steel grades with complex multiphase microstructure produced by specific chemical composition and a precise thermomechanical process [1]. AHSSs contain iron and carbon with varying amount of alloying elements, such as manganese, silicon, chromium, nickel, and molybdenum, which allows the formation of the complex microstructure of multiple phases, including ferrite (α), austenite (γ), martensite (α′), cementite (Fe_3C), pearlite (lamellar α+Fe_3C), bainite (non-lamellar α+Fe_3C), and retained austenite, in carefully selected combinations to deliver strength and formability. Although some mild steels and conventional high strength steel (HSS) grades, including interstitial-free (IF) steel, high-strength low-alloy steel (HSLA) and bake hardening (BH) steels, also contain alloying elements, they are in minimal quantities and the tensile strength (TS) of these steels are typically below 700MPa, or yield strengths (YS) below 550MPa [19]. AHSSs typically contain higher amounts of alloying elements, which gives them higher tensile strengths and ductility as shown in Figure 2.1. The distinction between the different grades of specific AHSS and HSS alloys are not always clear cut as steel manufacturers use different classification for their alloys either in terms of yield strength (i.e., maximum stress beyond which the steel alloy begins to permanently deform), tensile strength (i.e., maximum stress beyond which the steel alloy fails and fractures) and/or total elongation (i.e., total

strain experienced by the steel alloy at the point of failure) [19, 20]. However, ASTM's steel standards [21-23] provide mandatory guidelines and requirement for the chemical composition, mechanical and metallurgical properties of the various grades of mild and high strength steel alloy.

In terms of weight per gauge, the density of AHSSs is similar to that of traditional steels, but their higher specific strength-to-weight ratio means that automobile manufacturers can achieve the required structural strength and integrity with thinner gauges to reduce the overall vehicle weight, which is called "down gauging" [19]. Therefore, AHSSs are the often viewed as the most affordable high performing material for automotive lightweighting, especially when compared to other ferrous, nonferrous or composite low-density materials, such as cast iron, aluminium alloys, magnesium alloys, titanium alloys, polymers, and carbon fiber composites [19, 24].

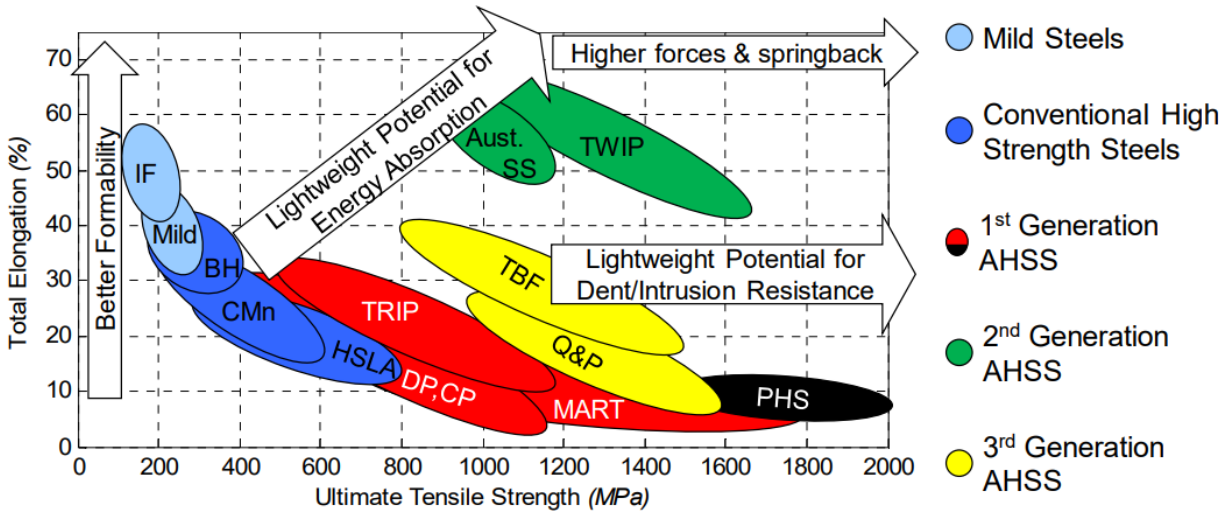


Figure 2.1. Global formability diagram comparing the total elongation and ultimate tensile strength (UTS) for mild steels, conventional high strength steels, and advanced high strength steels (AHSSs) [25].

AHSSs are generally classified into grades and generations based on their mechanical properties and the microstructure in terms of the phase of the steel [19]. First generation AHSSs have a ferrite-based microstructure that provides them with increased strength relative to mild or conventional steel, but very limited formability as seen in Figure 2.1. Second generation AHSSs exhibit a fully stable austenitic microstructure due to the addition of high amounts of alloying elements (e.g. Mn, C, Ni, Al, Si). Consequently, second generation AHSSs offer significantly improved strength and ductility, making them more formable than first generation AHSSs.

However, their high production costs and low manufacturing yields have limited their widespread adoption. The shortcomings of the second generation AHSSs resulted in the ongoing development of third generation AHSSs (3G-AHSSs) with the goal of offering high strength and enhanced ductility at a reasonable cost [19, 26].

These grades of AHSSs play an important role in reducing greenhouse gas (GHG) emissions in the automotive industry. Vehicle lightweighting with AHSS leads to improved fuel efficiency during use, thereby reducing overall GHG emission over the entire vehicle life cycle. The material average GHG emissions from the primary production of steel can be 7 to 20 times less than that of other low-density materials, such as aluminium, magnesium, and carbon fiber reinforced polymers (CFRP) composites [1]. A study by the Steel Recycling Institute showed that vehicles made with AHSS produced a lower total life cycle GHG emissions than those made from aluminium for every class of vehicle tested [2]. The study also showed that vehicles made with AHSS components produce a 30-60% reduction in pollutant emission in comparison to vehicles lightweighted with aluminium (a popular alternative to steel), depending on the vehicle type i.e., sedans, pickups, SUVs, or HEVs.

This thesis will focus on dual-phase (DP) steels, the most widely used AHSS grade in the automotive industry [24, 26, 27]. This first-generation AHSS has a duplex microstructure consisting of soft ferrite matrix interspersed with islands of hard martensite [19, 28]. DP steel provides an excellent combination of high strength, lower yield strength to tensile strength ratio, continuous yielding (i.e., smooth transition from elastic deformation to elastic-plastic deformation [29]) and improved ductility, especially when compared to HSLA steel of the same tensile strength, as shown in Figure 2.2 [24, 28, 30]. Dual-phase AHSS, due to its high work hardening rate, provides excellent fatigue strength and crash energy absorption, making it a critical material for improving crash safety performance in the crumple zones and safety cage components of vehicles [1, 31, 32].

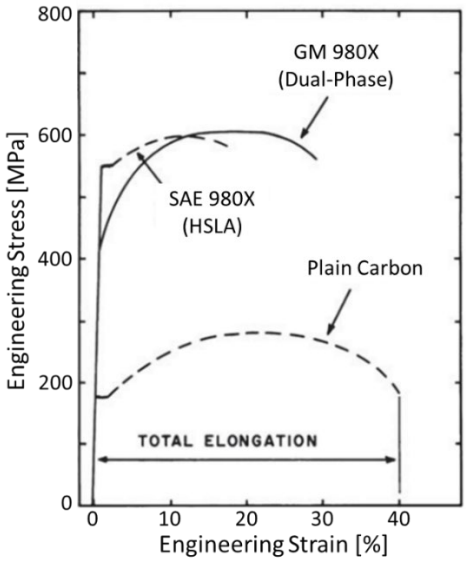


Figure 2.2. Stress-strain curve comparing the mechanical properties of dual-phase steel, high strength low alloy (HSLA) steel and plain carbon [24].

2.1.1. Continuous galvanizing lines (CGLs)

Industrially, cold-rolled and hot-dipped AHSS products are produced using continuous galvanizing lines (CGLs) like the schematic shown in Figure 2.3. The original continuous hot dip galvanizing process was developed and patented by Tadeusz Sendzimir in 1934 [33, 34]. First, incoming full hard cold-rolled coils from the cold reduction mill introduced at the line entry are uncoiled and welded to existing coils so the process remains continuous. The welded steel strip undergoes alkaline cleaning to remove dirt and surface contaminants. Next, the strip is heat treated in the furnace based on prescribed heating schedule to obtain the desired mechanical properties. The furnace section of the CGL can either be fired directly using a Direct-Fired Furnace (DFF) or indirectly using a Radiant Tube Furnace (RTF), depending on the target temperature and the heating schedule [34]. The heat treatment furnace is filled with a dew point-controlled mixture of nitrogen and hydrogen to create a reducing atmosphere to control the oxidation of the steel during intercritical annealing.

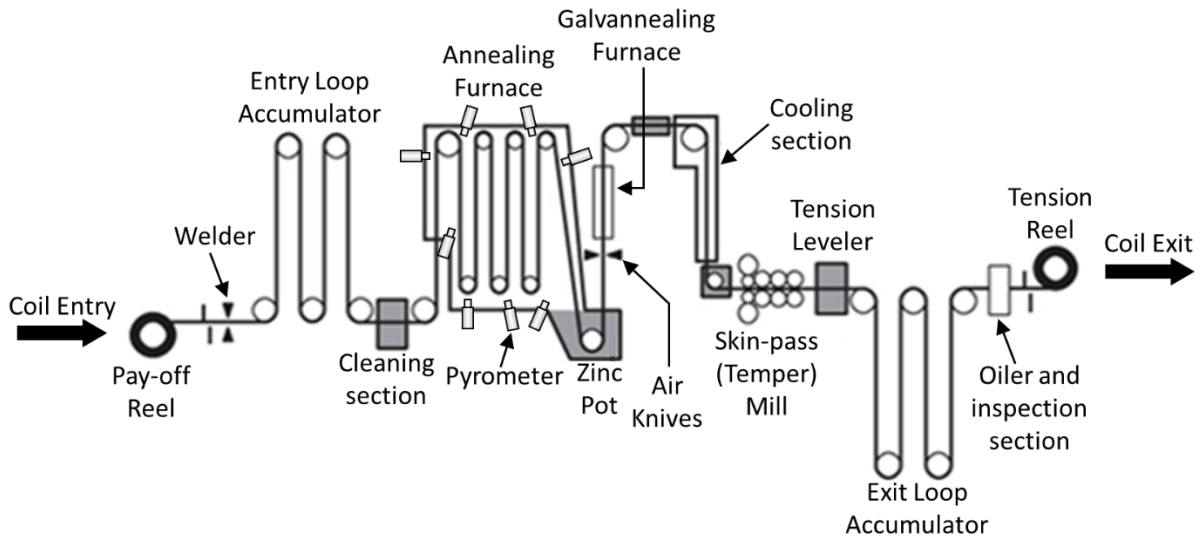


Figure 2.3. Schematic of a typical continuous galvanizing line showing an array of pyrometers in the annealing furnace. Adapted from Ref. [33].

Upon exiting the annealing furnace, the steel is cooled from the peak annealing temperature at a carefully controlled cooling rate to obtain the desired hard-phase microstructure. The steel strip is then introduced into a molten zinc pot via a "snout" when it is at or slightly above the melting point of the zinc alloy, typically by 2 to 3°C [34]. The zinc pot is typically maintained at a temperature corresponding to the melting point of the zinc alloy, which generally ranges from 450°C to 470°C [35]. Accurate pyrometry is also required to ensure that the steel strip is introduced into the zinc pot at the right temperature, as otherwise a significant temperature mismatch between the strip and the zinc pot prevents proper zinc layer adhesion to the substrate steel, leading to poor corrosion performance. Air knives are located at the exit of the zinc pot to control the coating weight on both sides of the steel strip as the steel heads to the final cooling section to solidify the coating on the steel surface. For some applications, the zinc-coated steel is further heated in a galvannealing furnace, immediately following the air knives, to produce a zinc-iron intermetallic coating. The zinc-coated AHSS products are known as galvanized (GI), while AHSS alloys with the zinc-iron intermetallic coating are referred to as galvannealed (GA). Other coating variations such as galfan and galvalume are also produced on the CGL by increasing the aluminium of the zinc bath to 5 wt.% and 55 wt.% respectively, which is significantly higher than the <0.3 wt.% Al content found in a typical galvanized zinc bath [36]. These coatings are important for corrosion

resistance of the steel with the GA coating offering other benefits including enhanced formability, paint adhesion and weldability [37]. After cooling, the coated steel goes through post-processing sections, which includes the skin-pass/temper mill, tension leveler, chemical treatment, oiler, and recoiler, before it finally exits the CGL.

2.1.2. Intercritical annealing of AHSS

Transformational strengthening is the primary mechanism for modifying the mechanical properties of AHSS and therefore, precise thermomechanical processing of AHSS is crucial to achieving the desired microstructure and mechanical properties [1, 19]. The strength of dual-phase AHSS depends on the martensitic volume fraction of the steel, and a carefully controlled heating and cooling process is required to transform unprocessed (as-received) steel from its ferrite-cementite (α+Fe_3C) structure to a martensite containing multiphase structure [19, 38].

The heating process for AHSS is referred to as intercritical annealing, as the steel strip is heated to and held at a temperature in the intercritical region between A_1 (eutectoid temperature) and A_3 (upper critical temperature) to achieve a mixed ferrite-austenite (α+γ) microstructure [19]. The iron-carbon phase diagram indicating the intercritical annealing temperature region is shown in Figure 2.4. In the intercritical region, there is a stable mix of ferrite and austenite depending on the carbon content of the steel and temperature. Annealing the AHSS strip at high intercritical annealing temperature, closer to the A_3 line, produces high austenite fractions of decreased average carbon content compared to austenite formed at lower intercritical temperatures, because the available carbon is distributed over a larger volume of austenite. This results in a higher amount of austenite available for further transformations, but the lower carbon content in the austenite would result in non-homogenous distribution of hardness after quenching especially if the carbon is not uniformly distributed within the austenite, i.e., poor hardenability due to localized differences in hardness [19]. On the other hand, a lower intercritical annealing temperature closer to the A_1 line produces low austenite fractions with high carbon content, which improves hardenability, but only a small amount of austenite would be available for further transformations into hard phases like bainite or martensite upon cooling. For this reason, accurate pyrometry is required to carefully control the steel temperature within the intercritical region to achieve the right trade-off between austenite fraction and carbon content.

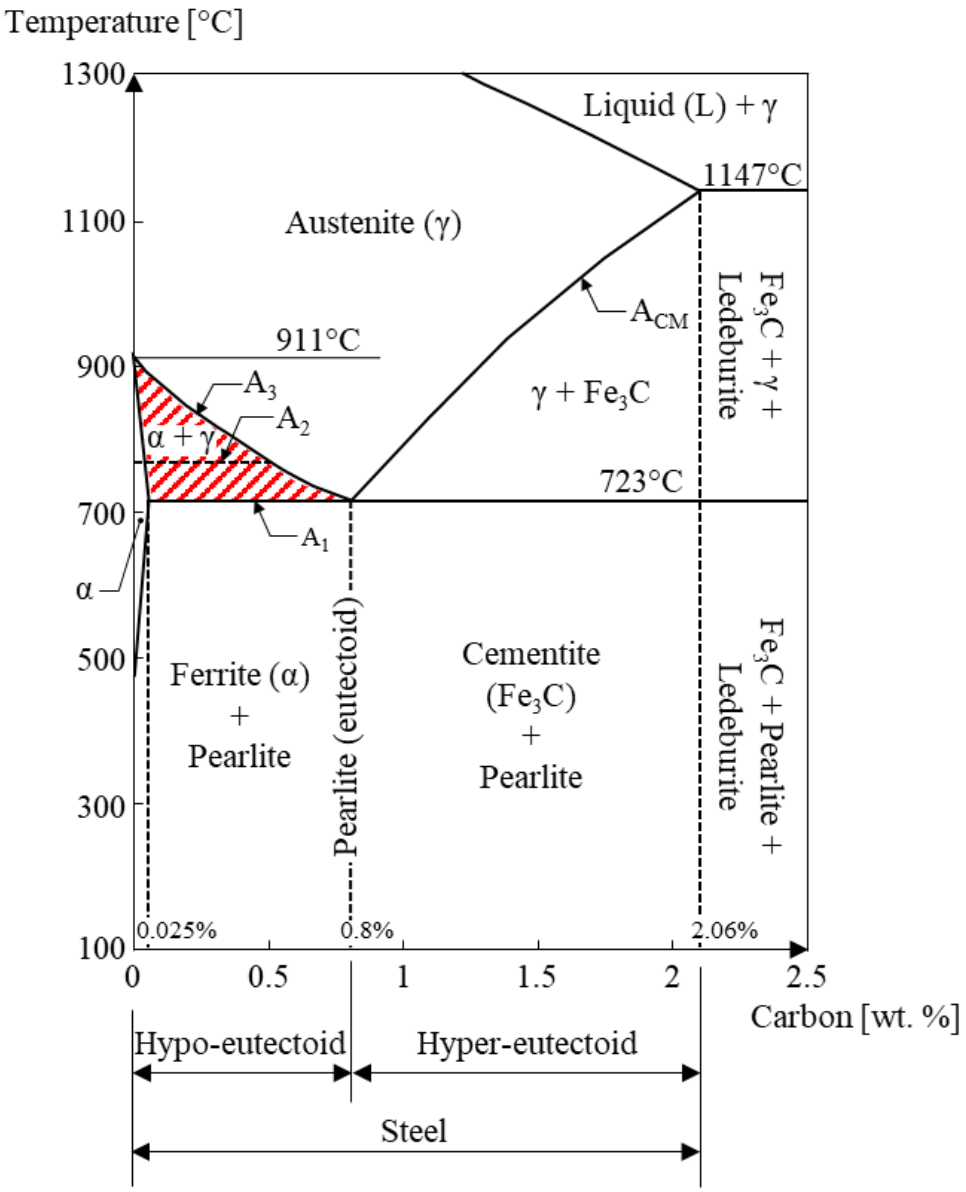


Figure 2.4. The iron-carbon (Fe-C) phase diagram showing the intercritical temperature region (red shaded area) for ferrite-austenite formation in steel. The pearlite phase consists of alternating layers of austenite and cementite. The A_1, A_2, A_3 and A_{CM} lines are the critical temperature boundaries for phase transformation where A_1 is the temperature at which the pearlite-to-austenite eutectoid transformation begins; A_2 is the curie temperature for magnetic transformation where the metal changes from ferromagnetic to paramagnetic; A_3 is the temperature at which the ferrite-austenite phase fully transforms into austenite in hypo-eutectoid steel while A_{CM} is the temperature at which the ferrite-cementite phase fully transforms into austenite in hyper-eutectoid steel. Adapted from Ref. [20].

Following intercritical annealing, the final multi-phase structure of the AHSS grade is obtained by controlled cooling/quenching from the intercritical annealing temperature. Depending on the cooling rate, the austenite microstructure formed during intercritical annealing can decompose into pearlite, bainite, or martensite if the steel is slow-cooled, moderately-cooled or rapidly-cooled, respectively [19]. The time-temperature transformation (TTT) and continuous cooling transformation (CCT) diagrams of the steel can be used to the predict the final microstructure of the decomposed austenite based on the cooling time and temperature [19].

Figure 2.5 shows a general schematic of the thermal processing cycle for dual-phase AHSS alloys. The incoming cold-rolled strip is transformed into ferrite-austenite ($\alpha+\gamma$) microstructure by heating to and soaking at an intercritical annealing temperature above A_1, but below A_3. Prior to the rapid quench required to transform the austenite to martensite, the steel can be slow-cooled briefly, shifting the phase balance to increase the ferrite fraction while reducing the austenite content [19, 39]. The steel is then quenched rapidly to a temperature below the martensite start temperature (M_s) to prevent the formation of pearlite and bainite intermediate phases [27, 28]. It is important to note that the actual value for the temperatures, A_1, A_3, and M_s, depend on alloy composition and the phase equilibrium at the intercritical annealing temperature. As a result, AHSS alloys with varying alloying content can have different phase transformation behaviors due to their unique equilibrium phase boundaries, and CCT and TTT diagram. Therefore, accurate pyrometry is essential to control and optimize the annealing temperatures and heating and cooling rates that govern the phase transformation of the alloy.

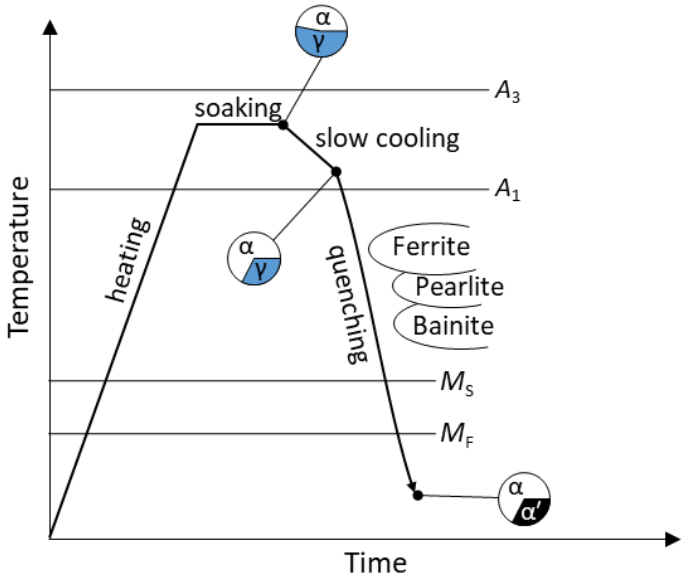


Figure 2.5. Schematic of the annealing cycle for processing dual-phase alloys indicating the key temperatures and microstructure, where α is ferrite, γ is austenite and α′ is martensite. M_s is the martensite start temperature at which the austenite begins to transform into martensite and M_f is the martensite finish temperature at which the austenite becomes fully transformed into martensite. Adapted from Refs. [19, 27, 28, 39].

2.1.3. Thermodynamic stability of AHSS oxides during annealing

During annealing, high-temperature oxides are formed when the alloy elements within the AHSS react with an oxidant (e.g., oxygen, water vapor, or carbon dioxide) in the furnace atmosphere. In a multi-oxidant gas atmosphere, the overall oxygen partial pressure experienced by the metal also depends on the partial pressure ratio of CO and CO_2 (i.e., P_{CO}/P_{CO_2}) and the partial pressure ratio of H_2 and H_2O (i.e., P_{H_2}/P_{H_2O}). At constant pressure and temperature, the thermodynamic stability of oxides is determined by the overall standard Gibbs free energy change for the metal oxidation reaction. For most pure metals, the Ellingham diagram (a plot of standard Gibbs energies of formation of oxides vs temperature) is typically used to determine whether the metal would form an oxide at a given temperature based on the partial pressure of O_2, and/or the pressure ratios of CO/CO_2 and H_2/H_2O in the annealing atmosphere [40, 41].

AHSS alloys, specifically, are annealed in a single oxidant environment, usually water vapour. The annealing atmosphere is a dew point (DP) controlled nitrogen-hydrogen gas mixture, i.e., N_2– (5 to 20 vol.%) H_2, to prevent the oxidation of the steel surface via the reaction:

$$M_xO_y + yH_2 \rightarrow xM + yH_2O \quad (2.1)$$

where M denotes a metal element within the steel and M_xO_y is the corresponding metallic oxide. Alloying elements such as Mn, Si, Al, and Cr readily segregate from the bulk material toward the surface (external oxidation) and subsurface (internal oxidation) to form oxides in these locations during annealing. The ability of these alloying elements to form stable oxides in the presence of an N_2-H_2 atmosphere that is reducing to the native iron oxides of the steel is known as *selective oxidation* [42]. The presence of these oxides on the steel surface prior to immersion in the molten zinc bath can cause poor wettability and coating adhesion, which impacts the corrosion resistance of the steel [43, 44]. Also, given that emissivity is a surface property, the formation of surface oxides during annealing will produce spectral emissivity variations that influence the accuracy of the pyrometrically-inferred temperature. Therefore, understanding the thermodynamic stability of the equilibrium between the various metal species in the AHSS alloy and their oxides with respect to the annealing atmosphere is critical towards understanding the radiative properties and pyrometry of AHSS.

Figure 2.6 shows the oxygen partial pressure as a function of process temperature for Cr, Fe, Mn, Al and Si oxides annealed within a 5% H_2 reducing atmosphere at two dew points (−30°C and +10°C). The oxygen partial pressures at equilibrium were obtained from standard Gibbs free energies for water vapor and the oxide compounds as outlined in Appendix A. The oxygen partial pressure (pO_2) of the annealing atmosphere at a given dew point and temperature is a measure of the oxidation potential of the atmosphere and does not physically translate into the number of O_2 molecules in the atmosphere [45]. If the oxygen partial pressure of the atmosphere is higher than the equilibrium oxygen partial pressure of the metal oxide, the metal will oxidize. Likewise, when the oxygen partial pressure of the atmosphere is lower than that of metal oxide, the oxide will be reduced. As expected, the stable selective oxides are predicted to form during annealing since the equilibrium oxygen partial pressure curve for these oxides (MnO, SiO_2, Al_2O_3 and Cr_2O_3) fall well below the oxygen partial pressure curves for the annealing atmosphere at both dew points.

For the oxygen potential curves in Figure 2.6, the activity of all the metal species is assumed to be unity, i.e., the metallic oxides will exist in their pure condensed phase. In practice, however, the alloying element activity would be obtained from the actual atomic or mole fraction of the individual elements in the AHSS alloy, which would result in very small activity values for

these alloying elements (≤0.05) [46-48]. The lower activity values for the alloying elements (i.e., Mn, Si, Cr, Al) increases the equilibrium oxygen partial pressure of their selective oxides which means that these oxides would be reduced at higher annealing temperatures and lower dew points.

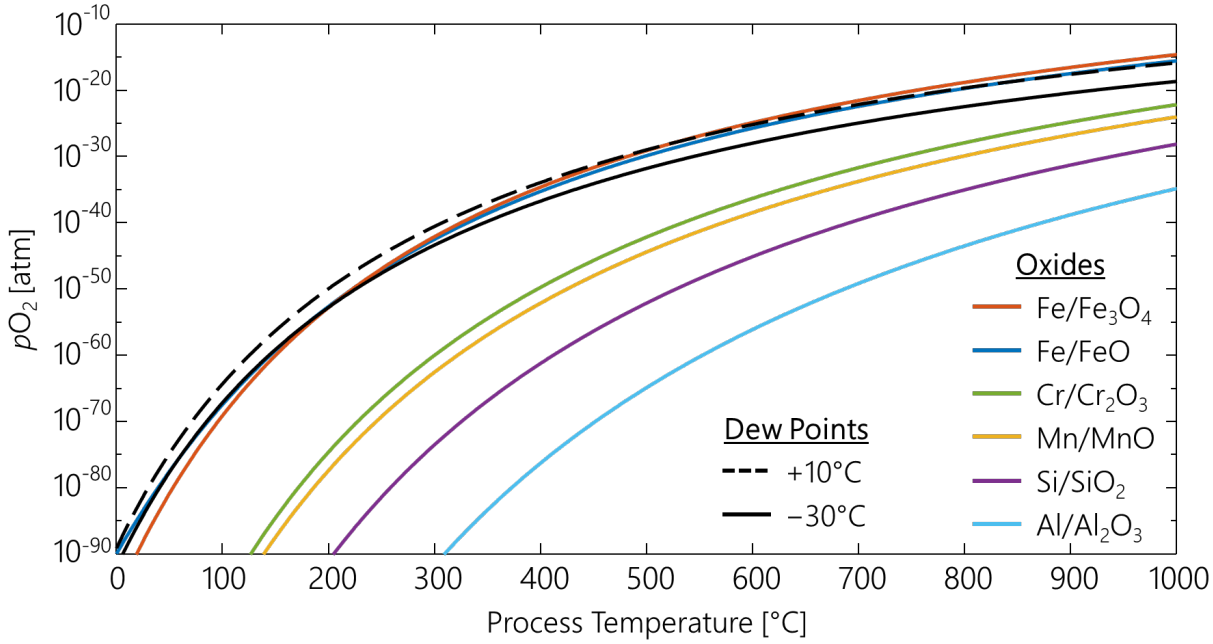


Figure 2.6. Thermodynamic stability of Fe, Cr, Mn, Si oxides with respect to annealing temperature and oxygen partial pressure for two dew points (−30°C and +10°C) in a N_2-5%H_2 atmosphere.

An important observation from Figure 2.6 is that the 5% H_2 annealing atmosphere is only slightly reducing for the native iron oxides (FeO and Fe_3O_4) at temperatures below ~300°C and ~600°C for the −30°C and +10°C dew points, respectively. For the higher dew point (+10°C), the equilibrium oxygen potential curves for the iron oxides coincide with the oxygen partial pressure of the annealing atmosphere at high temperatures, which suggests that the formation of iron oxides are thermodynamically favorable even with increasing process temperature. This indicates that the surface oxides that may influence pyrometry estimates during annealing are not limited to selective oxides, especially at lower temperatures.

Although the oxidation potential diagram indicates the tendency of the alloying elements to oxidize under equilibrium conditions, it provides no information about the kinetics of the oxidation reaction. The rate and extent to which the AHSS will form internal or external oxides depend on the combination of the annealing temperature, dew point and oxygen partial pressure,

surface preparation, pretreatment of the metal, concentration of alloying element, existing peroxidation on the metal surface, annealing duration, among other factors [49]. External selective oxidation is favorable at lower dew points (i.e., lower oxygen partial pressure) due to the greater outward flux of less noble alloying elements compared to the inward flux of oxygen. The oxidation process for AHSS alloys is even more complicated than the pure-metal oxidation scenario for several reasons [41]. Each element in an AHSS alloy has unique diffusivity in the bulk metal and tendency to oxidize as described by the Ellingham diagram. Also, in addition to binary oxides, the alloying elements can form ternary or higher oxides with each of these oxides having varying degrees of solubility [41, 50].

2.2. Pyrometry measurement model

Pyrometry, also known as radiation thermometry, refers to the remote sensing (non-contact) measurement of the temperature of a target material by processing the radiant flux emitted from the material. Steel manufacturers rely on temperature measurements from pyrometers to control and maintain the desired thermal cycle within the annealing furnace and at other critical process locations along the continuous galvanizing line (CGL). Due to their non-contact and non-destructive nature, pyrometers can accommodate rapid line movements and strip vibrations without scarring the materials [51]. Generally, the temperature range of interest is between 100°C and 1500°C [52]; intercritical annealing temperatures for AHSS grades typically range from 600°C to 850°C [47, 53].

Figure 2.7 shows the schematic of a typical pyrometry measurement. Most pyrometers are equipped with a photonic detector (e.g., InGaAs) that releases electrons in proportion to incident radiation intensity. The generated electrons are counted over a defined measurement interval and then processed by the analog-to-digital converter (ADC) into a signal that can be analyzed by the pyrometry algorithm.

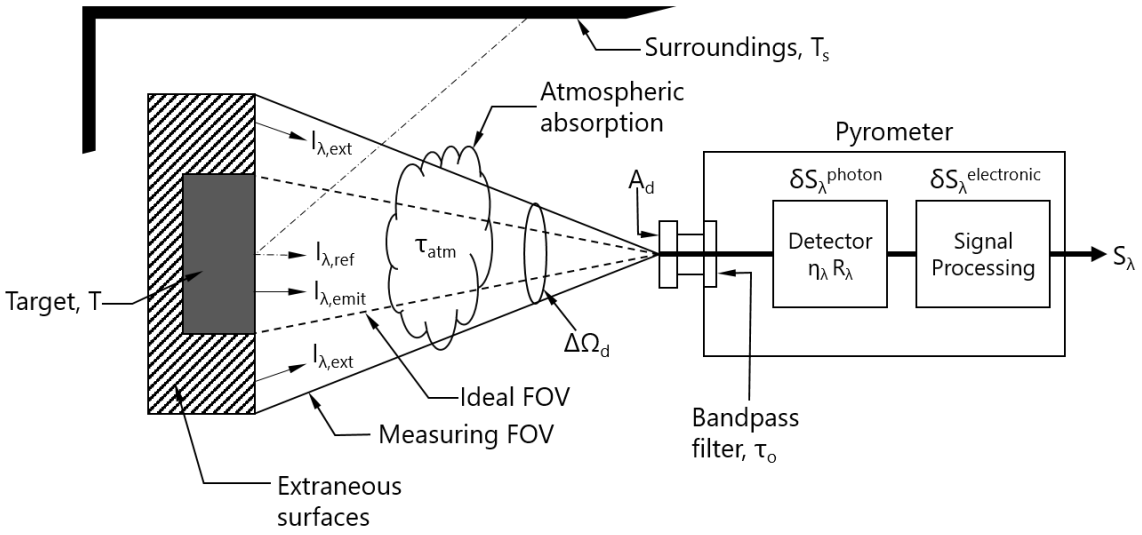


Figure 2.7. Schematic diagram of a typical pyrometry measurement.

In the absence of measurement noise, the signal (counts), S_λ, generated by a pyrometer at a given wavelength is proportional to the radiant intensity incident on the device [52], such that

$$S_\lambda = R_\lambda \Phi_\lambda = \Delta\Omega_d A_d \cdot \int_{\Delta\lambda} \tau_o(\lambda) \cdot \tau_{atm}(\lambda) \cdot R_\lambda(\lambda) \cdot I_{\lambda,obs} d\lambda \tag{2.2}$$

where R_λ is the spectral responsivity of the pyrometer, which directly relates the output (counts) to incident radiant energy, Φ_λ; A_d and $\Delta\Omega_d$ are the detector area and detection solid angle, respectively; τ_o is the transmittance of the spectral bandpass filter; τ_{atm} is the atmospheric transmittance, accounting for the presence of participating media (steam, flames, combustion gasses, etc.) in the device's optical path; and $I_{\lambda,obs}$ is the spectral intensity leaving the surface. The spectral responsivity, R_λ, also accounts for the efficiency and configuration of the collection optics.

This observed intensity, $I_{\lambda,obs}$, includes the reflected intensity, $I_{\lambda,ref}$, from the surroundings as well as any extraneous radiation, $I_{\lambda,ext}$, from additional surfaces in the pyrometer's field-of-view (FOV) due to misalignment or obstructions

$$I_{\lambda,obs} = I_{\lambda,emit} + I_{\lambda,ref} + I_{\lambda,ext} = \varepsilon_\lambda(\lambda,T,\theta) \cdot I_{\lambda b}(\lambda,T) + \left[1 - \varepsilon_\lambda(\lambda,T,\theta)\right] \cdot I_{\lambda b}(\lambda,T_s) + I_{\lambda,ext} \tag{2.3}$$

where T is the surface temperature of the target, T_s is the temperature of the surrounding surfaces, ε_λ (λ, T, θ) is the directional spectral emissivity of the target surface, and θ is the angle formed between the optical axis of the pyrometer and the surface normal of the steel strip. For surfaces in the presence of high temperature surroundings, as is the case in annealing furnaces, reflected

irradiation represents a significant portion of the pyrometer signal but can be accounted for if T_s is known. The extraneous radiant energy, $I_{\lambda,ext}$, is only relevant for applications involving small or moving targets as they tend to result in a partially filled field-of-view. The focal distance of the pyrometer can typically be adjusted to reduce the viewing diameter, thus eliminating the extraneous radiation. For this research, it is assumed that the signal generated by the pyrometer is solely due to irradiance of the target surface. This is also a valid assumption for industrial pyrometers as the detector wavelengths, aperture diameter, focal distance, alignment, and device location along the CGL are all selected to ensure that the radiation incident on the pyrometer is coming solely from the steel. Therefore, in the absence of additional radiant flux originating from the surrounding or atmospheric absorption in the optical path the device, Eq. (2.3) can be reduced to

$$S_\lambda = R_\lambda \cdot \Delta\Omega_d A_d \cdot \int_{\Delta\lambda} \tau_o(\lambda) \cdot \varepsilon_\lambda(\lambda, T, \theta) \cdot I_{\lambda b}(\lambda, T)\, d\lambda \tag{2.4}$$

Typically, for high temperature pyrometry, the spectral width of the band pass filter is sufficiently narrow such that the signal can be modelled by

$$S_\lambda = \underbrace{\Delta\Omega_d A_d \cdot \tau_o(\lambda_d) \cdot R_\lambda(\lambda_d)}_{K_\lambda(\lambda_d)} \cdot \varepsilon_\lambda(\lambda_d, T, \theta) \cdot I_{\lambda b}(\lambda_d, T)\, \Delta\lambda \tag{2.5}$$

where λ_d is the center wavelength and K_λ is the calibration constant that describes the photoelectric efficiency of the detector and detector optics [54]. The pyrometer is initially calibrated using a blackbody reference source prior to installation on a CGL, and it is subsequently removed at regular intervals for recalibration to ensure measurement accuracy during annealing.

At sufficiently small values of λT, the blackbody spectral intensity, $I_{\lambda b}$, is given by Wien's approximation to the Planck distribution:

$$I_{\lambda b}(\lambda, T) = \frac{C_1}{\lambda_d^5 \left[\exp\left(\frac{C_2}{\lambda_d T} \right) - 1 \right]} \approx \frac{C_1}{\lambda_d^5 \left[\exp\left(\frac{C_2}{\lambda_d T} \right) \right]} \tag{2.6}$$

with $C_1 = (2hc_0^2) = 1.191 \times 10^8$ W·μm^4·m^{-2}sr^{-1} and $C_2 = (hc_0/k_B) = 1.439 \times 10^4$ μm·K, h and k_B are the Planck and Boltzmann constants, respectively, and c_0 is the speed of light in vacuum.

For pyrometry measurements at two or more wavelengths, the signals/counts at all detection wavelengths can be combined into a vector, $\boldsymbol{S}_\lambda$. The method used to infer T from S_λ (or $\boldsymbol{S}_\lambda$) depends on the number of measurement wavelengths as well as the *a priori* knowledge available about the spectral emissivity of the target material. Section 2.2.1 provides a literature review of the general emissivity modelling approaches used to represent *a priori* knowledge about the spectral emissivity, ε_λ, of metal surfaces. While this thesis focuses primarily on spectral emissivity variations of AHSS in the near-infrared range of 1.2 μm to 2.5 μm, the pyrometrically-inferred temperature estimates will only be evaluated from a combination of intensity measurements recorded at three wavelengths: 1.6 μm, 2.1 μm, and 2.4 μm. These three wavelengths correspond to the detection channels of a commercial multi-wavelength pyrometer (Williamson PRO MWX-ST-17) typically used in continuous galvanizing lines.

2.2.1. Emissivity models for pyrometry

Emissivity is the surface radiative property describing the thermal radiation emitted from a real surface compared to the emission from a blackbody at the same temperature. In addition to its dependence on surface temperature, T, the emitted intensity (and thus emissivity) of real surfaces varies with wavelength, λ, and direction of emission as specified by the polar angle from the surface normal (θ) and azimuthal angle (ϕ) because real surfaces are not diffuse emitters. A blackbody, on the other hand, describes the ideal diffuse emitter and therefore the emitted radiation from a blackbody does not vary with direction (i.e., isotropic) but it does vary with wavelength as seen from Planck's distribution curve in Figure 2.8.

Specifically, the spectral directional emissivity, $\varepsilon_\lambda(\theta, \phi, T)$, which is crucial for pyrometry defines the radiant intensity emitted from a real surface, $I_{\lambda,\text{obs}}$, in a given direction, relative to the emitted radiation from a blackbody, $I_{\lambda\text{b}}$, at the same temperature [54]:

$$\varepsilon_\lambda\left(\theta,\varphi,T\right)=\frac{I_{\lambda,\text{obs}}\left(\theta,\varphi,T\right)}{I_{\lambda\text{b}}\left(T\right)} \tag{2.7}$$

Kirchhoff's law states that at thermal equilibrium, the energy emitted by a surface must be equal to the energy absorbed [54], therefore, the spectral directional emissivity can be related to the spectral directional absorptivity, $\alpha_\lambda(\theta_i, \phi_i, T)$, for a given incident direction (θ_i, ϕ_i), such that:

$$\varepsilon_\lambda\left(\theta,\varphi,T\right)=\alpha_\lambda\left(\theta_{\text{i}}=\theta,\varphi_{\text{i}}=\varphi,T\right) \tag{2.8}$$

Given that metals are opaque real surfaces, incident radiation must either be reflected or absorbed. Therefore, the spectral directional emissivity can be related to the spectral directional-hemispherical reflectivity, $\rho_\lambda(\theta_i, \phi_i, T)$ to give

$$\varepsilon_\lambda(\theta,\varphi,T) = \alpha_\lambda(\theta_i = \theta, \varphi_i = \varphi, T) = 1 - \rho_\lambda(\theta_i = \theta, \varphi_i = \varphi, T)$$
$$\therefore \varepsilon_\lambda(\theta,\varphi,T) = 1 - \rho_\lambda(\theta,\varphi,T) \tag{2.9}$$

For most pyrometry applications, the emissivity of interest is the normal spectral emissivity, $\varepsilon_{\lambda,n}(T)$, i.e., the spectral (wavelength-dependent) emissivity measured in the normal direction ($\theta = 0$). The azimuthal angle of the pyrometry measurement is typically ignored as it is assumed that the radiative properties of the target surface at a given normal angle is uniform in all azimuthal directions. However, in practice, if significant rolling artefacts and directional features are imparted on the cold-rolled AHSS prior to annealing, the azimuthal angle can influence the measured spectral emissivity. Some hybrid (polarization) pyrometry methods have also been explored that exploit the directional variability of the emissivity to improve temperature predictability [10, 52, 55-57]. Additionally, some materials under specific conditions have approximately wavelength-independent properties over a particular wavelength range. This is called the greybody approximation.

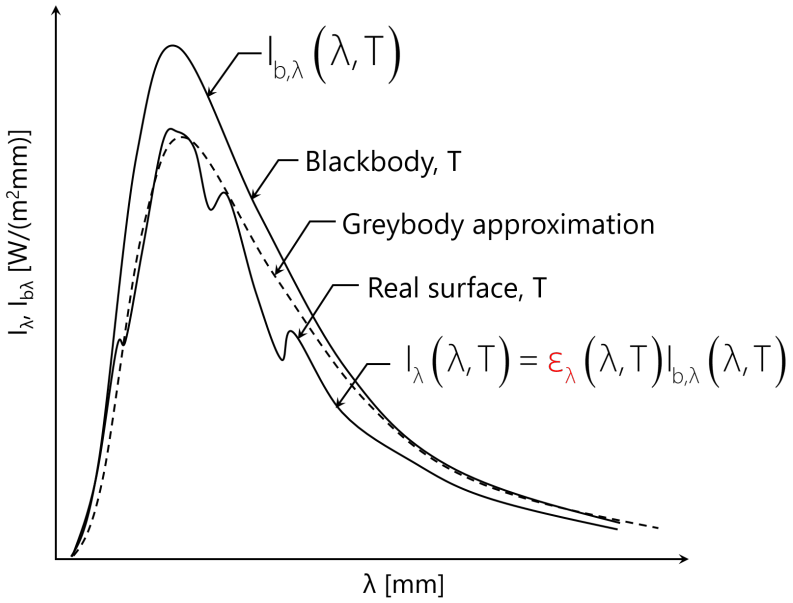


Figure 2.8. Spectral distribution of radiation emission from blackbody and real surfaces.

In pyrometry, the unknown spectral emissivity of a target material is usually inferred simultaneously with the steel temperature using radiances measured at one or more wavelengths, typically by assuming or prescribing an underlying emissivity relationship based on the number of detection wavelengths. The assumed emissivity relationship, often referred to as an emissivity compensation algorithm, can either be a constant, in the case of single-wavelength pyrometry, or an emissivity ratio or function for dual-, and multi-wavelength pyrometers. The scheme used to infer temperature from the measured irradiance depends on the approach used to model the spectral emissivity of the target material and consequentially, the number of detection wavelengths at which the spectral irradiance is measured. Subsections 2.2.1.1 to 2.2.1.3 briefly review single-, dual-, and multi-wavelength pyrometry, which are all used in the manufacture of AHSS. In depth discussions on the history and other applications of these methods can be found in other studies [58].

2.2.1.1. Single wavelength pyrometry

Single wavelength (SW) pyrometry utilizes the spectral radiance measurement at one detection wavelength, λ_d, to infer the temperature of the surface. It is most suitable for stable materials [11] as it assumes that the target surface has a constant and known spectral emissivity. The SW pyrometry temperature is obtained by inverting Eq. (2.5)

$$T = \frac{C_2}{\lambda_d \ln\left[\frac{\varepsilon_{\lambda_d} K_{\lambda d}}{\lambda_d^5 S_\lambda}\right]} \tag{2.10}$$

Correctly inferring the AHSS strip temperature using SW pyrometry is difficult because ε_λ usually varies with temperature, surface roughness, and oxide formation as the steel is being annealed. For this reason, this approach can only be applied in “wedge” type configurations, in which the pyrometer is aimed precisely at the center of the notch formed between the steel strip and the roll, where the spectral emissivity is close to unity due to the blackbody cavity effect [7, 59]. The wedge pyrometer orientation is illustrated in Figure 2.9. Any misalignment in the field-of-view of a wedge pyrometer reduces the spectral emissivity from the blackbody conditions, which in turn, influences the accuracy of the inferred temperature. In addition to the geometry and

alignment, the single wavelength temperature reading obtained from a wedge pyrometer is highly sensitive to any temperature difference between the strip and the roll.

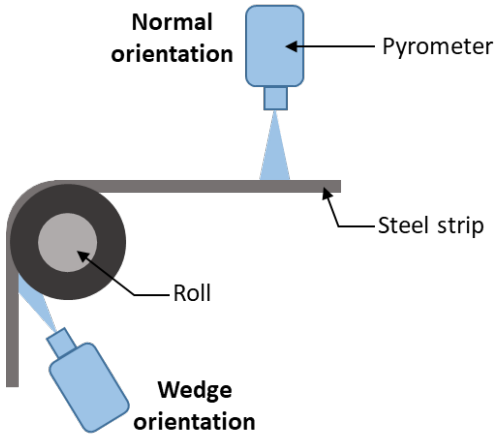


Figure 2.9. Graphical illustration of the wedge vs normal pyrometry configuration [3].

2.2.1.2. Dual-wavelength pyrometry

Dual wavelength (DW) pyrometry utilizes the spectral irradiance measured at two distinct wavelengths, λ_{d1} and λ_{d2} to estimate surface temperature. Although dual wavelength pyrometry can be used in applications with unknown spectral emissivity, it still requires *a priori* knowledge of the relationship between the spectral emissivity at the two wavelengths. The spectral emissivity at one wavelength is typically expressed as a reciprocity function of the other, i.e., $\varepsilon_{\lambda d1} = f(\varepsilon_{\lambda d2})$ [8, 11]. Dual-wavelength pyrometry is more robust to errors caused by atmospheric absorption and partially filled fields-of-view as the ratio of the measured spectral irradiances cancels out these effects.

The most common subset of DW pyrometry is the *ratio (or two-color) pyrometry* in which the measured irradiance is expressed as a ratio and the temperature is estimated by

$$T = \frac{C_2\left[\frac{1}{\lambda_{d2}} - \frac{1}{\lambda_{d1}}\right]}{\ln\left[\frac{\varepsilon_{\lambda d2}}{\varepsilon_{\lambda d1}}\left(\frac{\lambda_{d1}}{\lambda_{d2}}\right)^5 \frac{S_{\lambda 1}}{S_{\lambda 2}}\right]} \tag{2.11}$$

To obtain accurate temperature estimate with ratio pyrometry, the ratio of the emissivity values, $\varepsilon_{\lambda dr}$, often called the "e-slope", has to be a known constant independent of temperature and surface conditions, i.e.,

$$\varepsilon_{\lambda dr} = \frac{\varepsilon_{\lambda d2}}{\varepsilon_{\lambda d1}} = \text{constant} \tag{2.12}$$

For surfaces that can be approximated as gray, $\varepsilon_{\lambda dr}$ is unity. If the emissivity assumption is valid, the ratio temperature estimate becomes more resilient to measurement error as the detection wavelengths move further apart [60]. On the other hand, if $\varepsilon_{\lambda dr}$ does not depend on the evolving surface state, the use of wavelengths that are spectrally far apart increases the error.

Zentner et al. [51, 61] applied a linear reciprocal function (λ_{d1} = 2.18μm or 2.2μm and λ_{d2} = 2.4μm) to infer the surface temperature of zinc-coated steel samples during the galvannealing process. It was found that the error on the temperature estimates was up to ±20K when the function coefficients ware assumed to be fixed irrespective of the annealing temperature. These constant coefficient values were obtained from a regression analysis of the spectral emissivity measurements obtained from laboratory experiments. On the other hand, when different coefficient values were used at each of the galvannealing temperatures, the error on the inferred temperatures was reduced to ±10K.

Tanaka and Dewitt [10, 11] and Tanaka et al. [62, 63] reported a reciprocal f-function between two spectral emissivities called TRACE (Thermometry Re-established by Automatic Compensation of Emissivity). The TRACE f-function represents *a priori* emissivity knowledge obtained experimentally using a set of spectral irradiance measurements and the true target temperature. Tanaka and Dewitt [11] applied this method to cold-rolled carbon steel and galvannealed steel at wavelengths of 1.6μm and 3μm for temperatures ranging from 700K to 900K (427°C to 627°C). The temperature estimates obtained with the TRACE method showed good agreement with the true target temperature, especially when compared with the values obtained from the single wavelength and ratio pyrometry methods. In terms of specific dual-wavelength pyrometry measurement on AHSS alloys, Thiessen et al. [17] applied the ratio method to different alloys of transformation induced plasticity (TRIP) assisted steel with the assumption that the surfaces are approximately grey. The results show that for TRIP steel heated up to 850°C, the ratio pyrometry method over-predicts the true surface temperature with the expected deviation ranging from 26°C to 52°C depending on the alloy composition of the steel.

2.2.1.3. Multi-wavelength pyrometry

Multi-wavelength (MW) or multispectral pyrometry refers to pyrometry systems that infer the surface temperature from the spectral irradiance measured at three or more discrete wavelengths along with an emissivity compensation algorithm/function. Increasing the number of detection wavelengths provides more degrees of freedom to capture the complex spectral emissivity relationships, while allowing for the statistical reduction of errors caused by measurement noise [64]. Emissivity compensation algorithms for MW pyrometry are usually polynomial functions derived by empirical or theoretical analysis to model how the spectral emissivity varies with the underlying parameters such as wavelength, roughness, steel temperature and equivalent blackbody temperature [6, 58, 65, 66]. Typically, the coefficients of the compensation algorithms are inferred simultaneously with the unknown temperature. That is, if the underlying emissivity function has n unknown coefficients, there will be n+1 unknowns in total including the unknown temperature.

The multi-wavelength pyrometry method can be solved either by exact or least-squares methods [58, 66]. To solve for temperature from p irradiance measurements by the exact method, the emissivity model should have $p-1$ unknown coefficients, while the least-squares method requires an emissivity model with $p-2$ unknown coefficients, i.e., to infer the surface temperature for a three-wavelength model, the maximum number of unknown coefficients in the emissivity polynomial should be two for the exact method and one for the least squares method. While the exact method allows the use of more polynomial coefficients to capture the complex emissivity relationship given a limited number of detection wavelengths, previous investigations into solving emissivity compensation models by the exact method shows that this approach tends to result in large errors and overfitting for pyrometers with more than three detecting wavelengths [65]. Using the least-squares method, on the other hand, will reduce the large errors as it finds the optimum temperature and coefficients values that minimizes the sum-of-squares residuals. The objective function of the least-squares method in terms of the raw counts is therefore given by

$$\chi^2 = \sum_{i=1}^{p} [S_{\lambda,\mathrm{meas},i} - S_{\lambda,\mathrm{mod},i}]^2 \tag{2.13}$$

where $S_{\lambda,\mathrm{meas},i}$ is the measured spectral counts and $S_{\lambda,\mathrm{mod},i}$ is the modelled spectral count that minimizes the sum of squared errors for a prescribed emissivity compensation algorithm. The variable i denotes the detection wavelength, i =1,2…, p.

For compensation algorithms in exponential form, the objective function is defined as

$$\chi^2 = \sum_{i=1}^{p} [\ln(S_{\lambda,\text{meas},i}) - \ln(S_{\lambda,\text{mod},i})]^2 \tag{2.14}$$

Several experimental and theoretical studies have been conducted to understand and develop multi-wavelength emissivity compensation algorithms [12-14, 58]. Duvaut et al. [12] compared the performance of several mathematical and physical emissivity compensation algorithms for steel, aluminium, tantalum, and titanium at 573 K, and wavelengths between 2 to 10 micrometers. They considered linear and fractional wavelength-dependent models, as well as relationships developed from the Maxwell and Fresnel's equations. Pellerin et al. [58] produced an emissivity compensation algorithm for aluminium alloys based on the Hagen-Rubens Relation (HRR) [67] to explicitly account for both wavelength- and temperature-dependent variations. Khan et al. [13, 14] used linear and log-linear polynomials to develop wavelength-dependent emissivity models for platinum, chromium, molybdenum and iron, based on experimental data extracted from the existing literature. Wen et al. [9, 64, 68] has also extensively evaluated several emissivity compensation models to improve pyrometry accuracy for aluminium alloys and steel. MW emissivity compensation algorithms are robust for uncontaminated surfaces, but they can be unreliable for materials whose emissivity varies significantly with factors other than wavelength and temperature, e.g., surface roughness or the formation of a surface oxide [11].

It is important to note that some of the emissivity compensation approaches described as dual- and multi-wavelength pyrometry so far in this thesis can sometimes be interchanged depending on the application. For example, Tsai et al. [69] conducted a comprehensive analysis of the use of linear and non-linear compensation functions for dual-wavelength pyrometry measurements on aluminium alloys. Ratio pyrometry has also been extended to applications with spectral irradiance measured at three and four wavelengths [6]. This multi-wavelength ratio-based method is sometimes referred to as multicolor pyrometry [13, 70], even though a compensation function is not used in obtaining the surface temperature. Reynolds [70] reviewed the principle of two- and three-color pyrometers and their application to non-ferrous materials. Khan et al. [13] extended this analysis further by looking at a four-color pyrometer where the measured spectral irradiance is grouped together to form three two-color ratios and the emissivity at the three wavelengths is expressed as a constant ratio.

2.2.2. Effect of temperature and oxidation on the radiative properties of AHSS

Prior to the CGL, the full-hard (i.e., unannealed and cold-rolled) AHSS surface is best described as a rough but uncontaminated metallic surface, with its radiative properties mainly varying with surface topography imparted by upstream processing, which includes cold-rolling and pickling. In the near-infrared range crucial for pyrometry, the spectral emissivity of most metals, including AHSS, decreases with increasing wavelength due to increased back-scattering of electromagnetic wave by the free electrons of the metal at longer wavelengths. Moreover, as wavelength increases, surfaces become more optically smooth ($\sigma/\lambda << 1$) for a given surface roughness (σ) and therefore more reflective (less emissive) as wavelength increases [54]. During annealing, the formation of selective oxides further changes the topography of the AHSS surface, contributing to the overall temperature-and wavelength-dependent variations in emissivity. Therefore, the radiative properties of the AHSS during annealing varies with the composition and morphology of the surface oxides, which depends on alloy composition, atmosphere, and heating schedule.

The radiative properties of an interface depends on the optical properties (e.g., complex refractive index) of the material as well as surface topography. For most smooth, homogenous metallic surfaces ($\sigma/\lambda << 1$), the Drude free electron theory and the Hagen-Reubens theory elucidate how increased electron scattering at higher temperatures produce changes in optical properties that increase the spectral emissivity of the pure metal surface [52, 54, 71]. For polished metallic surfaces, Hagen-Rubens theory predicts that spectral emissivity should increase with temperature at wavelengths longer than the crossover or "X" point and decrease with increasing temperature at wavelengths shorter than this point. For most metals, the crossover point is in the visible or near-infrared spectrum.

However, for a non-smooth metallic surface with an oxide layer, as in the case of an AHSS alloy, the temperature-dependent changes in the optical properties of the material are complex and depend on many variables. In addition to increased electron scattering at high temperatures for the metallic substrate, several studies [57, 72-77] have shown that the roughness of metallic surface combined with the oxide layer features (composition, morphology, uniformity, and thickness) all contribute to variations in the complex refractive indices of the metal substrate and oxide layer. The morphology of the surface oxides formed during intercritical annealing of AHSS can range from a thin film-like oxide layer to a grainy/nodular-like oxide layer. Samples annealed at higher

dew points are more likely to form nodular oxides while sample processed at lower dew points tend to have thin film-like oxides [75, 77]. Both film-like and nodular-like oxides can occur simultaneously on the oxidized AHSS surfaces with each of these morphologies having different effects on the EM wave interactions. Due to the dielectric nature of oxide materials combined with the thinness of the oxide layers (40 nm $\leq d \leq$320 nm [78]), it is assumed that the oxide layer is non-absorbing. At shorter wavelengths where the film thickness (d) is smaller than the pyrometry wavelength ($d \leq \lambda$), the formation of a thin film-like oxide layer results in the thin-film interference effects whereby the radiation reflected from the top and bottom interfaces of the oxide film are phase-shifted, producing constructive and destructive interference patterns [54]. The lower the refractive index of a uniform oxide film, the more pronounced the thin-film interference effect, thus the higher the spectral emissivity of the AHSS surface [54]. Typically, the AHSS surface consists of non-uniform and discontinuous oxide film interspersed with nodular-like oxides which produces weaker interference effects [75]. At wavelengths larger than the oxide thickness (i.e., $\lambda >> d$), the radiative properties of the AHSS surface are dominated by the roughness effect due to the pre-annealed surface roughness and the oxide nodules. In this case, the EM wave interacting with the optically rough AHSS surface is randomly scattered producing multiple reflections (and thus more energy absorption) that increases the spectral emissivity of the surface. These surface roughness effects can be modelled using geometric optics approximation (GOA) ray-tracing [79].

Several studies (e.g., [43, 44, 80-87]) have investigated how selective oxidation affects the mechanical properties, reactive wetting, and zinc layer adhesion of AHSS, but very few have looked at the effect of selective oxidation on the spectral emissivity and pyrometry of AHSS. In a comparison of TRIP and oxide-free IF steel, Ham et al. [77, 88] studied the correlation between the emissivity of these AHSS grades annealed within reducing atmospheres of various dew points. Ham et al. demonstrated that due to the selective oxidation of Mn and Al, the global emissivity of the TRIP steel varied with the dew point of the annealing atmosphere while the emissivity of the non-oxidizing IF steel remained constant [77]. Somveille et al. [89] analyzed the effect of surface oxidation on the spectral emissivity of dual-phase AHSS alloys (DP780 and DP980) quenched at intervals during the heat treatment cycle. The *ex situ* characterized emissivity measurements showed that variations in the radiative properties of the alloy are linked to their alloy composition. The DP780 alloy, with a higher manganese-content (lower Si/Mn ratio), exhibited higher spectral

emissivity due to oxide layer growth during heat treatment. On the other hand, the DP980 alloy with the higher Si/Mn ratio exhibited minimal variations in the *ex situ* spectral emissivity measurements. Lin et al. [74, 75] specifically showed that the radiative properties of dual-phase AHSS alloys (DP780 and DP980) are dependent on the surface roughness effect imparted pre-annealing in addition to the thin-film interference effect of the selective oxides formed during annealing.

For other metals and alloys, studies also show that surface oxidation impacts the varying spectral emissivity and the accuracy of pyrometry measurement. Cao et al. [90, 91] and King et al. [92] studied the effect of air-induced oxidation on the emissivity of candidate alloys for high-temperature reactor pressure vessels. Cao et al. found the spectral emissivity of the alloys to vary with oxide layer thickness, with thinner oxide producing lower spectral emissivity values [91]. Cao et al. also linked the thickness of the oxide layer to the chromium content of the alloys [91] while del Campo et al. [93] and Zhao et al. [94] evaluated how the spectral emissivity of nickel-based alloys varies with the growth of an oxide film due to the interference effects. It is important to note that for a film-like oxide layer, the interference effect depends on the refractive indices of the dielectric oxide and thickness of the oxide film relative to the wavelength of the incident radiation [54]. Weng and Wen [95] examined the effects of surface oxidation on the spectral emissivity of aluminium alloys and the accuracy of several multispectral radiation thermometry (MRT) models in predicting the temperature for oxidized and unoxidized alloys. Hagqvist et al. [96] proposed an additive emissivity model for Ti-6Al-4V alloy that considers the oxide layer thickness as a variable, in order to qualitatively account for the effect of oxidation on pyrometry measurements. Iuchi et al.[57] derived an emissivity model that considers oxide film growth on metal surfaces by expressing the directional and polarized emissivities as functions of direction, oxide film thickness, and optical constants of the metal and the oxide film. Wen [68] used the Agababov roughness function [97] to update four existing compensation algorithms to model the effects of surface roughness on the spectral emissivity of aluminium alloys. King et al. [98] and Jo et al. [72] used a modified geometric optics approximation (GOA) to obtain directional spectral emissivity models for metal surfaces that account for dependencies on temperature, composition, and roughness. Generally, these works show that the emissivity of a metal or an alloy increase in the presence of an oxide layer, which leads to increased uncertainty in the inferred temperature.

Chapter 3
Multivariate spectral emissivity model for advanced high strength steel[1]

The preceding chapter highlighted that existing emissivity compensation models do not accurately capture how the spectral emissivity of AHSS alloys varies with interdependent material properties and processing conditions. Furthermore, despite the known effects of surface roughness, alloy composition, dew point, and oxide film thickness on spectral emissivity of AHSS [77, 99] and other metal and alloys [92, 93, 95, 100], only a few studies have reported multivariable emissivity relationships that account for these additional parameters. Iuchi et al. [57] derived an emissivity model that considers oxide film growth on metal surfaces by expressing the directional and polarized emissivities as functions of direction, oxide film thickness, and optical constants of the metal and the oxide film. Wen [68] used the Agababov roughness function [97] to update four existing compensation algorithms to model the effects of surface roughness on the spectral emissivity of aluminium alloys. King et al. [98] and Jo et al. [72] used a modified geometric optics approximation (GOA) to obtain directional spectral emissivity models for metal surfaces that account for dependencies on temperature, composition, and roughness. Lin and Daun [101] applied the Davies' model [102] to investigate the relationship between surface roughness and spectral emissivity for dual-phase AHSS alloys.

Building on these studies, this chapter proposes the factorial design of experiments as a statistical tool for modelling the interdependent effects of wavelength, alloy composition (Si/Mn ratio), annealing atmosphere (dew point), and pre-annealed surface state on the spectral emissivity

[1] The content of this chapter has been published as:

F. K. Suleiman, K. Lin, and K.J. Daun, 2021, "Development of a multivariate spectral emissivity model for an advanced high strength steel alloy through factorial design-of-experiments," J. Quant. Spectrosc. Radiat. Transfer, 271, 107693 (13pp). doi: 10.1016/j.jqsrt.2021.107693.

of AHSS alloys. To the best of the author's knowledge, this work is the first time factorial designs have been used to develop spectral emissivity models for pyrometry during metallurgical processing. The analysis considers coupons cut from coils of two different cold-rolled DP980 alloys, with silicon-to-manganese (Si/Mn) ratios of 0.23 and 0.04, respectively. Coupons are either left in their as-received state or polished mechanically. The coupons are then annealed in a 95% N_2/5% H_2 atmosphere at dew points of −30°C or +10°C, within a galvanizing simulator. The spectral emittance of each sample is obtained from reflectance measurements made with a Bruker Invenio-X FTIR spectrometer (1.2 μm – 25 μm), but only the measurements for the infrared pyrometry range of 1.2 μm – 4.0 μm is analyzed in this thesis.

The most significant main and interaction effects were determined through an analysis of variance (ANOVA) procedure. The pre-annealed surface state of the steel is the most dominant effect at longer wavelengths, while alloy composition dominates at shorter wavelengths. Also, while the annealing atmosphere dew point does not strongly affect emissivity, its interaction effect with alloy composition contributes significantly to the observed variations, especially for wavelengths below 3 μm. These effects were then incorporated into a bilinear model with parameters derived through regression to the experimental data. The fitted linear regression model obtained for a three-wavelength pyrometer (1.6 μm, 2.1 μm, 2.4 μm) provides a good approximation of the experimental measurements ($R^2 = 0.98$).

The results demonstrate how factorial designs provides key insights into the relationship between the surface state and radiative properties of the steel strip and may be used to develop multivariable emissivity compensation algorithms for pyrometry. While this thesis focuses on intercritical annealing of dual-phase steels, the methodology described here applies to characterizing the variables influencing radiative property variations in a wide range of materials encountered in pyrometry or remote sensing applications.

3.1. Sample preparation and processing

Coupons were cut from two different cold-rolled DP980 AHSS alloys having compositions that conform to ASTM A1079-17 [103] as detailed in Table 3.1. Although the exact composition of the alloys is proprietary, their Si/Mn mass ratios, which have the most pronounced effect on oxide composition, are 0.04 and 0.23, as measured by spark atomic emission spectrometry. In order to investigate the influence of the pre-annealed surface state on the spectral emissivity, half of the coupons were polished using a series of polishing wheels with progressively finer grit and particle size (240 grit SiC, 320 grit SiC, 400 grit SiC, 600 grit SiC), producing a mirror-like finish. The root-mean-square (RMS) roughness for all the samples was measured using an optical profilometer (WYKO NT1100). The sub-group of polished surfaces has an RMS roughness of R_q = 0.15 μm, while the as-received subgroup has an RMS roughness of R_q = 0.65 μm. All the samples were annealed within a galvanizing simulator (MGS, Iwatani-Surtec, Japan) [104] with a 95%/5% N_2/H_2 atmosphere according to the heating schedule illustrated in Figure 3.1. Although the samples are processed in a galvanizing simulator, the treatment involved only annealing and did not include the zinc coating step. At the end of the annealing cycle, the samples were rapidly quenched to freeze their high-temperature surface state for *ex situ* characterization of the corresponding radiative properties. Given that spectral emissivity is primarily a surface property, the rapid quench ensures that *ex situ* measurements are an approximate representative of the samples' high-temperature surface state. Similarly, previous pyrometry studies on steel alloys [69] indicate that observed variations in emissivity at high temperatures are significantly influenced by the changes in surface properties due to oxidation and the resulting interference effect. Nevertheless, potential variations in emissivity due to temperature-dependent changes in electrical conductivity are also discussed later in this chapter. The annealing dew point used for each sample is listed in **Table 3.2**. Two coupons were processed for each experimental condition in order to provide a measure of repeatability. All samples were cleaned and rinsed with ethanol and acetone before annealing and again prior to making radiative measurements post-annealing.

The near-normal directional-hemispherical spectral reflectance, ρ_λ, of each annealed coupon was measured using a Bruker Invenio-R FTIR spectrometer (1.2 μm - 25 μm), but only the measurements in the infrared pyrometry range of 1.2 μm - 4 μm are used for this study. The FTIR has a calibration uncertainty of ±2% and a repeatability accuracy of less than ±1% based on

reflectance measurements over the entire spectrum. The near-normal emissivity, ε_λ, was then inferred using Kirchhoff's law [105]

$$\varepsilon_\lambda = 1 - \rho_\lambda \tag{3.1}$$

The spectral emissivity measurements from the annealed coupon are then combined with the pre-annealed material properties (Si/Mn ratio and surface state) and the process parameter (dew point) to develop a multivariate emissivity compensation relationship using the response surface methodology described in the next section.

Table 3.1. Nominal chemical composition of DP980 [103].

Constituents	C	P	S	Mn+Al+Si	Cu	Ni	Cr+Mo	V+Nb+Ti
%mass max	0.23	0.08	0.015	6.00	0.20	0.50	1.40	0.35

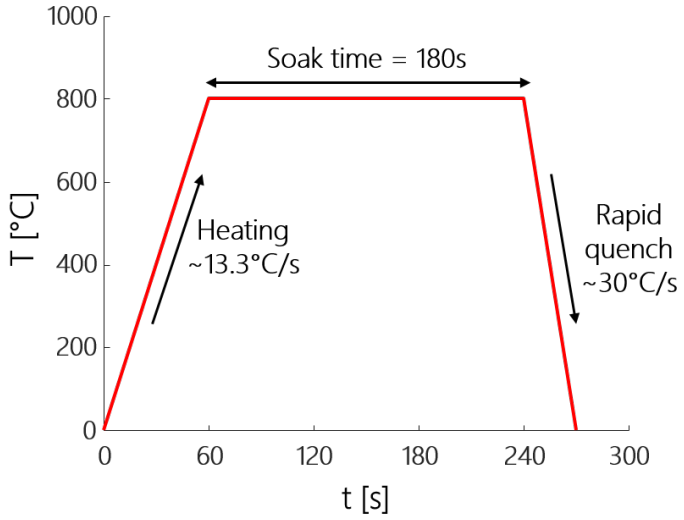


Figure 3.1. Schematic illustration of the annealing schedule for the tested coupons.

Table 3.2. List of annealed coupons indicating the dew point of the annealing atmosphere, the ratio of alloy components, and the pre-annealed surface state.

Sample/Run No.	Dew Point	Si/Mn Ratio	Surface State
1	−30°C	0.04	Polished
2	−30°C	0.04	As-received
3	−30°C	0.23	Polished
4	−30°C	0.23	As-received
5	+10°C	0.04	Polished
6	+10°C	0.04	As-received
7	+10°C	0.23	Polished
8	+10°C	0.23	As-received

3.2. Response surface methodology (RSM): factorial design

In the response surface methodology, variations in the response variable, or a set of response variables, can be related to the combined influence of several independent variables. These independent variables are called *factors* [106]. A common RSM technique is the factorial design of experiments, where all levels of one factor are combined with all levels of the other factors [107]. The *level* of a factor refers to the value held by the independent variable during an experiment. Factorial designs provide an estimate of the main and interaction effects, which are important when investigating how the joint effects of the process factors contribute to the observed changes in the response (dependent variable). The *effect* of a factor refers to the change in the response variable due to a change in the level of the factor [106]. A *main effect* describes the influence of a factor on the response irrespective of the levels of the other factors, while an *interaction effect* considers the influence a factor has on the response variable in the context of the level of another factor [106]. An interaction effect becomes significant when the effect of one factor on the dependent variable varies with the level of another factor.

The observations from a factorial design can be modelled by a fixed effects model if the levels of the factors (i.e., values of the independent variables) are assumed to be constant [106]. Once the model structure is defined, an analysis of variance (ANOVA) procedure is carried out to identify the factors and factor interactions that have the most significant effects on the response.

ANOVA models can be explicitly translated into an equivalent linear regression model [106, 108-110], so a factorial design analysis also produces functions that elucidate the relationship between the factors and their response.

In this study, factorial designs are used to analyze the spectral emissivities of the annealed samples in two stages. First, individual 2^3 full factorial designs are used to evaluate the spectral emissivity of all samples at discrete pyrometry detection wavelengths of 1.2 μm, 1.6 μm, 2.1 μm, 2.4 μm, 2.8 μm, 3.2 μm, 3.6 μm, and 4.0 μm. This is done to investigate how the dew point, Si/Mn ratio, and pre-annealed surface state (polished vs. unpolished), labelled "A", "B", and "C", respectively, interact to produce variations in the radiative properties without considering the role of wavelength. These factors each have two levels, as shown in Table 3.3. In the second stage, a general full factorial design is carried out by adding a factor for wavelength ("D"), which accounts for the spectral variation of the properties. Factor D has three-levels: 1.6 μm, 2.1 μm, and 2.4 μm; corresponding to the detection wavelengths for a commercial multi-wavelength pyrometer (Williamson PRO MWX-ST-17).

To facilitate comparison of the main and interaction effects, the factor levels are converted to dimensionless coded values using Eq. (3.2) [106]:

$$\text{coded level} = \frac{2 \times \left(\text{uncoded level} - \text{mean} \right)}{\text{range}} \tag{3.2}$$

The significance of the effects of dew point, Si/Mn ratio, surface state, wavelength, and their interactions on the spectral emissivity of the DP980 steel is determined using an ANOVA procedure at a 95% confidence interval (CI). The regression model for predicting the spectral emissivity is then constructed using only the statistically significant model terms identified from the ANOVA results for the general factorial design.

Table 3.3. The uncoded and coded levels for the four factors: dew point (A), Si/Mn ratio (B), surface state (C), and wavelength (D).

Factors	Uncoded Levels	Coded Levels
Dew Point (A)	−30°C	-1
	+10°C	+1
Si/Mn Ratio (B)	0.04	-1
	0.23	+1
Surface State (C)	Polished (R_q = 0.15 μm)	-1
	As-received (R_q = 0.65 μm)	+1
Wavelength (D)	1.6 μm	-1.083
	2.1 μm	0.166
	2.4 μm	0.917

3.3. Results and discussion

3.3.1. Spectral emissivity measurements

Figure 3.2 shows the spectral emissivity of the annealed DP980 alloys. Each curve represents the average of the two measurements from replicate samples. The standard deviation between the measurements from the two replicates ranges between 8.4×10^{-8} and 0.02, with a mean value of 0.005 (i.e., a mean relative standard deviation of 1.3%), demonstrating that the measurements are repeatable. Generally, the spectral emissivity for all samples decreases with increasing wavelength as expected for metals within the infrared spectrum.

The spectral emissivity for the polished samples in Figure 3.2 (a) shows greater variability in comparison to the as-received samples in Figure 3.2 (b). Typically, the spectral emissivity of a material increases with increasing roughness in the context of EM wave scattering theory [105, 111] but from the polished samples in Figure 3.2 (a), it is observed that for the shorter wavelengths

(<~2 μm), the emissivity values are higher than their as-received counterparts in Figure 3.2 (b). This contrary relationship between surface roughness and spectral emissivity is attributed to the interference effect of coherent reflection in the presence of a uniform oxide layer on the annealed surfaces [112]. The absence of large scale roughness on the polished surfaces allows for a more uniform oxide layer to form during the annealing process [113]. The spectral emissivity at shorter wavelengths is influenced by the structure and uniformity of the oxide layer formed during the annealing process, which depends on the pre-annealed surface state of the steel.

References [74] and [75] provide a detailed analysis of the oxide structure that contribute to the varying radiative properties for both alloys under the different procession conditions. However, the analysis in this work will focus on the low Si/Mn ratio samples, which are the primary focus of this dissertation. Accordingly, Figure 3.3 shows the scanning electron micrographs (SEM) of only the annealed low Si/Mn ratio coupons. Figure 3.3 (a) and (b) reveal that a uniform fully developed oxide layer is formed on the polished samples. For the polished specimen annealed at −30°C, shown in Figure 3.3 (a), the oxide layer appears homogenous, while the polished sample annealed at the higher dew point (Figure 3.3 (b)) shows a thicker oxide layer with a few oxide nodules. On the other hand, Figure 3.3 (c) and (d) show that the as-received samples form isolated oxide nodules instead of a continuous oxide layer. The amount of oxide nodules formed on the as-received surfaces appears to increase with increasing dew point, as seen in Figure 3.3 (d). The lack of a visible oxide layer on the as-received samples is most probably due to the fracture artifacts introduced by the cold-rolling process. The removal of these artifacts, pre-annealing, appears to promote the formation of a fully developed, homogeneous oxide layer on the polished samples.

Figure 3.2 (a) and (b) also show that samples with lower Si/Mn ratios generally have higher spectral emissivity values. Increasing the dew point causes the emissivity to increase for samples with the lower Si/Mn ratio, while the opposite effect is observed for the higher Si/Mn ratio. The former effect is caused by the segregation of alloying elements from the bulk material to form selective oxides on the surface during annealing. Changes in the surface topography caused by these oxides lead to variations in the spectral emissivity [18, 77, 99]. The Ellingham diagram indicates that the most likely oxides to form are MnO, SiO_2, $MnSiO_3$, Mn_2SiO_4 [114], but given the higher solubility of MnO in austenite (7.2 $(ppm)^2$) relative to the solubility of the other oxides

($SiO_2 = 3.1 \times 10^{-5}$ (ppm)^3, $MnSiO_3 \approx Mn_2SiO_4 = 7.6 \times 10^{-6}$ (ppm)^7) [78] combined with the lower Si/Mn ratio, and higher oxygen pressure, for the alloys considered here, the oxides are expected to be almost exclusively MnO [42]. This means that samples with more manganese content (i.e., lower Si/Mn ratio) are more likely to exhibit higher spectral emissivity during annealing because they have a greater tendency to oxidize externally. Overall, these results indicate that the radiative properties of dual-phase alloys depend not only on annealing atmosphere and alloy composition but also on their pre-annealed surface states.

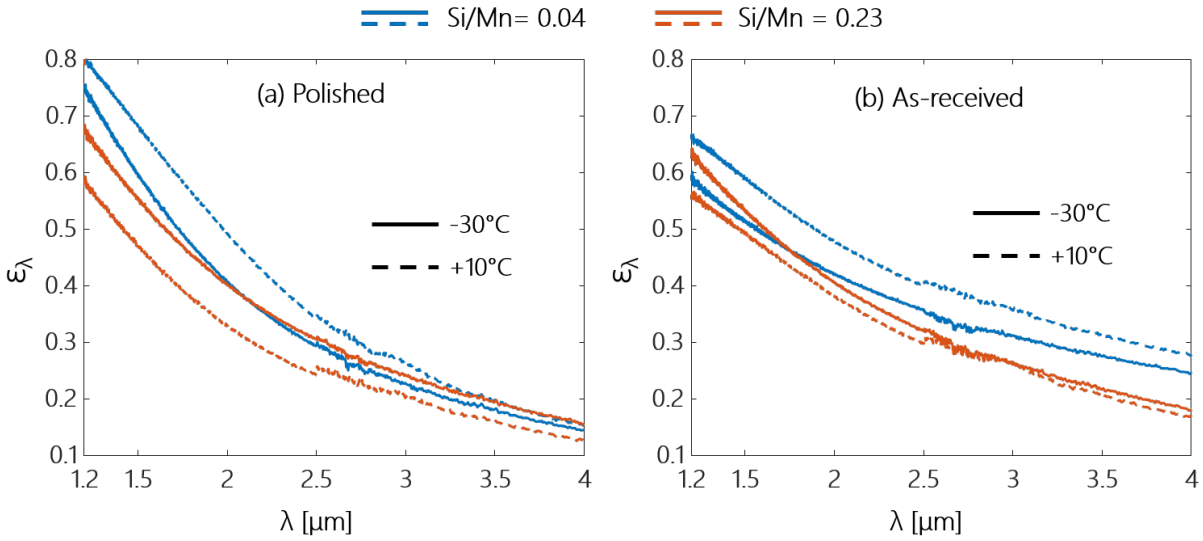


Figure 3.2. Measured spectral emissivity, ε_λ, for (a) polished samples (b) as-received samples.

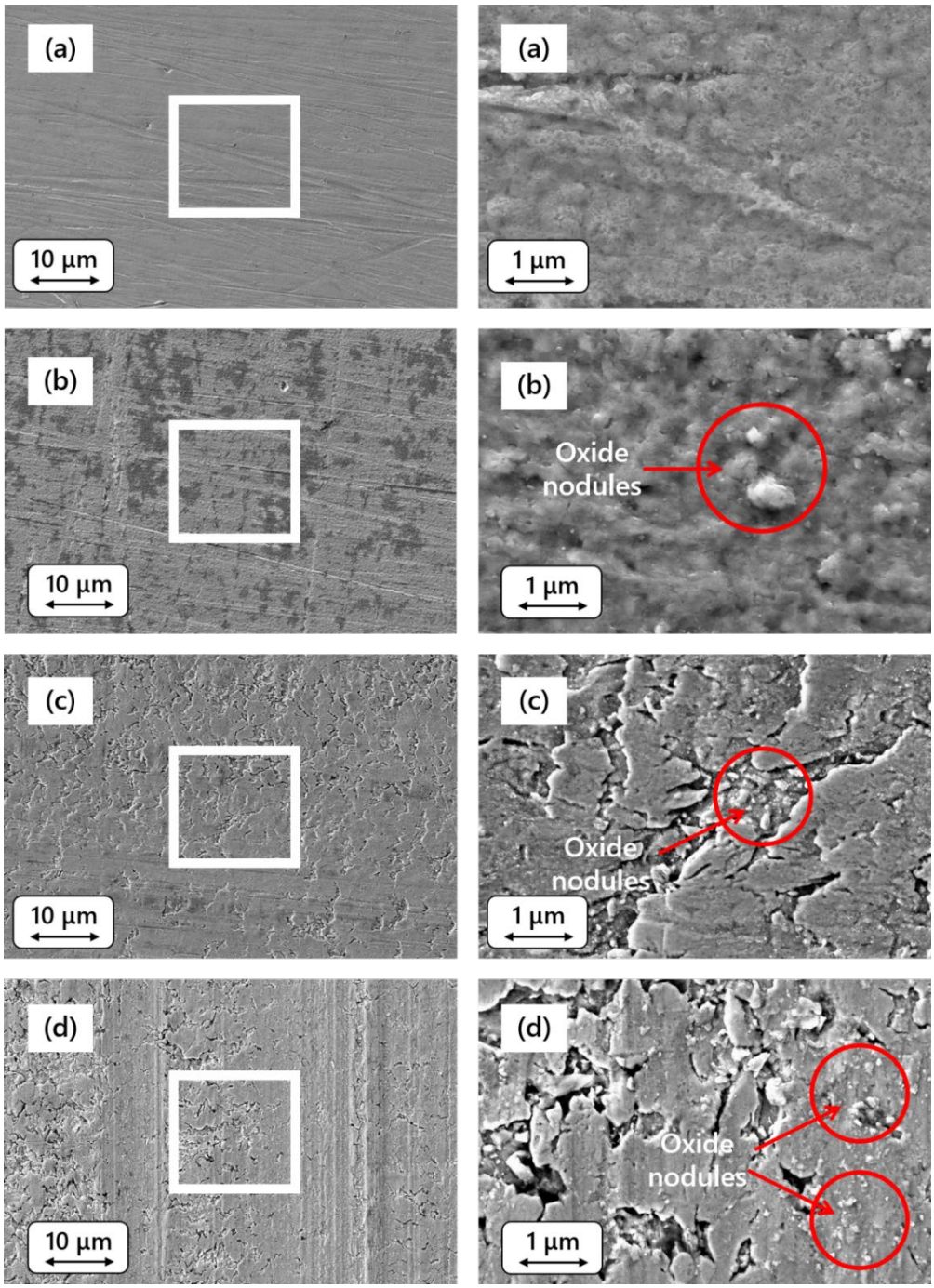


Figure 3.3. Scanning electron micrographs (SEM) of the annealed low Si/Mn ratio samples. The images on the right correspond to the white boxed regions in the images on the left. (a) Si/Mn=0.04, polished, annealed at −30°C, (b) Si/Mn=0.04, polished, annealed at +10°C (c) Si/Mn=0.04, as-received, annealed at −30°C, and (d) Si/Mn=0.04, as-received, annealed at +10°C.

3.3.2. 2^3 full factorial design

The 2^3 factorial design matrix and the spectral emissivity measurements from both replicates are shown in Table 3.4. The run order of the experiment was randomized to protect the analysis from serially correlated errors as well as the effects of unknown nuisance variables.

The ANOVA procedure is applied to determine not only the factors and interactions that are significant but also the magnitude of these effects as expressed by the percentage contribution of their sum-of-squares residual relative to the total sum-of-squares residual. This provides an approximate quantitative measure of the main and interaction effects responsible for the varying spectral emissivity. Figure 3.4 summarizes the percent contribution of effects across the spectral range, while detailed ANOVA results at each of the eight wavelengths are included as supplemental material in Ref. [115]. The contributions of the main and interaction effects vary significantly with different trends across the wavelengths. The main effect of Si/Mn ratio (B) dominates at shorter wavelengths ($\lambda <$ ~2.6 μm), accounting for up to 51% at its peak wavelength of 2.1 μm, whereas the main effect of surface state (C) dominates at the longer wavelengths. The results also indicate that the emissivity is insensitive to the main effect of dew point, accounting for a maximum of 1.24% of the variability at 2.1 μm. However, the interaction between dew point and Si/Mn ratio (AB) is the most significant interaction effect, meaning that the impact of dew-point depends strongly on the alloy composition of the steel. The most prominent effects over this spectral range are, in order of importance: Si/Mn ratio (B), surface state (C), dew point-Si/Mn ratio (AB) interaction, and Si/Mn ratio-surface state (BC) interaction. These four effects combined account for over 93% of the total variability observed in the spectral emissivity.

A statistical F-test is carried out to evaluate the significance of the effects at a level of 0.05, corresponding to a 95% confidence interval (F-value > $F_{(0.05,1,8)}$ = 5.32). The results of this test, summarized in Table 3.5, shows that the four factors identified via the magnitude of their percent contributions are significant at all wavelengths. Some of the main and interaction effects with minimal contributions to the total variability (less than 4%) were identified to be statistically significant via the F-test. All main and interaction effects were found to be statistically significant at 1.6 μm, while the specific significant effects vary across the other pyrometry wavelengths. However, the main effects, B and C, and the interaction effects, AB and BC, were significant at all the wavelengths. A detailed analysis of the main effects and interaction effects at the selected

pyrometry wavelengths is provided in Appendix A and Appendix B of Ref. [115], respectively. Overall, both the estimated percent contributions and the F-test results show that the key main and interaction effects that contribute to the change in spectral emissivity vary with wavelength. This observation provides a foundation for analyzing and optimizing wavelength combinations for improving the reliability of pyrometry estimates. For future pyrometer design, the RSM process can be used to estimate the sensitivity of selected wavelengths to key process effects and to understand how this sensitivity varies among the wavelengths. Applying this procedure will facilitate the selection of wavelengths that will provide the most sensitivity to the varying emissivity and thus minimize the error in the pyrometrically-inferred temperature.

Table 3.4. The 2^3 factorial design matrix and spectral emissivity responses for the combination of three factors: dew point (A), Si/Mn ratio (B), and surface state (C), at key wavelengths in the near-infrared region.

Std. No.	Run No.	Coded Factors			Wavelength [μm]							
					1.2	1.6	2.1	2.4	2.8	3.2	3.6	4.0
		A	B	C	Replicate I: Spectral emissivity, ε_λ							
1	1	-1	-1	-1	0.754	0.547	0.375	0.308	0.249	0.205	0.172	0.147
2	5	1	-1	-1	0.808	0.644	0.461	0.370	0.284	0.231	0.188	0.154
3	3	-1	1	-1	0.670	0.527	0.385	0.326	0.267	0.224	0.188	0.160
4	7	1	1	-1	0.586	0.438	0.311	0.258	0.218	0.178	0.148	0.123
5	2	-1	-1	1	0.588	0.485	0.398	0.361	0.315	0.289	0.266	0.242
6	6	1	-1	1	0.662	0.561	0.455	0.408	0.370	0.332	0.300	0.270
7	4	-1	1	1	0.621	0.502	0.382	0.333	0.285	0.241	0.212	0.183
8	8	1	1	1	0.552	0.465	0.359	0.306	0.277	0.236	0.198	0.168
					Replicate II: Spectral emissivity, ε_λ							
1	1	-1	-1	-1	0.752	0.557	0.383	0.312	0.249	0.202	0.168	0.142
2	5	1	-1	-1	0.803	0.638	0.456	0.365	0.287	0.228	0.185	0.152
3	3	-1	1	-1	0.663	0.511	0.371	0.313	0.259	0.213	0.181	0.153
4	7	1	1	-1	0.570	0.431	0.302	0.253	0.221	0.185	0.150	0.125
5	2	-1	-1	1	0.583	0.499	0.412	0.375	0.330	0.299	0.271	0.251
6	6	1	-1	1	0.661	0.571	0.464	0.416	0.379	0.342	0.311	0.279
7	4	-1	1	1	0.627	0.506	0.386	0.335	0.278	0.237	0.204	0.178
8	8	1	1	1	0.560	0.476	0.366	0.315	0.269	0.231	0.194	0.164

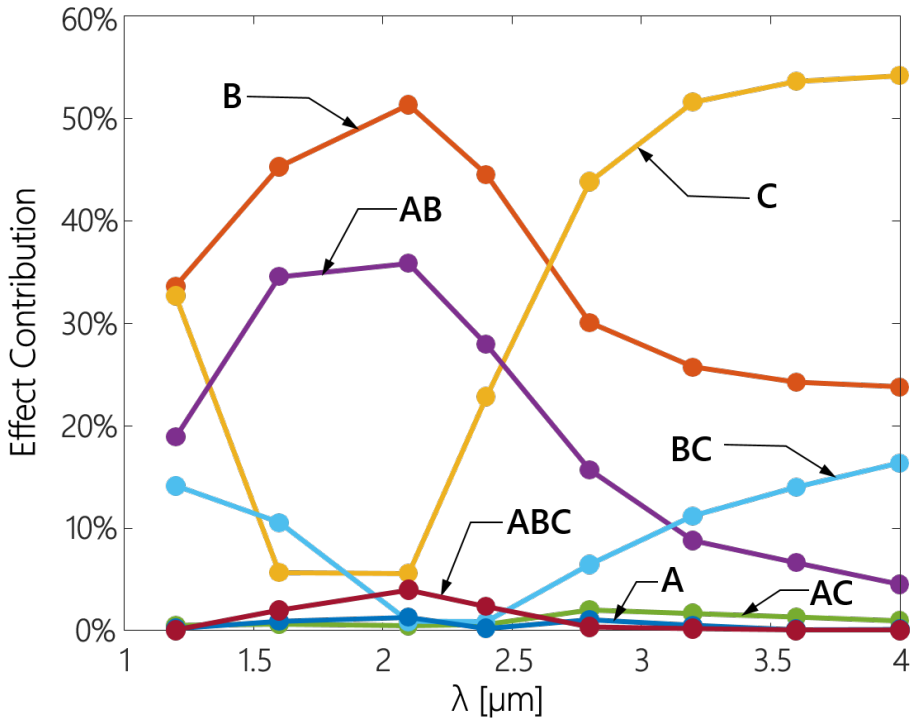


Figure 3.4. Percent contributions of the main and interaction effects for the combination of the three factors, dew point (A), Si/Mn ratio (B), and surface state (C), at the following wavelengths: 1.2 μm, 1.6 μm, 2.1 μm, 2.4 μm, 2.8 μm, 3.2 μm, 3.6 μm, and 4.0 μm.

Table 3.5. Statistically significant main and interaction effects contributing to the variations in spectral emissivity as identified from the F-test at 95% confidence interval. The check marks (✓) indicate the effects that are statistically significant.

Source of variation	Wavelength							
	1.2 μm	1.6 μm	2.1 μm	2.4 μm	2.8 μm	3.2 μm	3.6 μm	4.0 μm
A	✓	✓	✓	-	✓	✓	-	-
B	✓	✓	✓	✓	✓	✓	✓	✓
C	✓	✓	✓	✓	✓	✓	✓	✓
AB	✓	✓	✓	✓	✓	✓	✓	✓
AC	✓	✓	-	-	✓	✓	✓	✓
BC	✓	✓	✓	✓	✓	✓	✓	✓
ABC	-	✓	✓	✓	-	-	-	-

3.3.3. General full factorial design

The experiment matrix containing coded factors and spectral emissivity measurements for the general (2 × 2 × 2 × 3) factorial is shown in Table 3.6, while the ANOVA results are presented in Table 3.7. The general design is used to develop a mathematical model that specifically describes how the spectral emissivity varies over the detection wavelengths (1.6 μm, 2.1 μm, and 2.4 μm) of a commercial multi-wavelength pyrometer (Williamson PRO MWX-ST-17).

Table 3.6. The general 2 × 2 × 2 × 3 factorial design and spectral emissivity responses for the combination of all four factors: dew point (A), Si/Mn ratio (B), surface state (C), and wavelength (D).

Std. No.	Run No.	Coded Factors				Spectral emissivity, ε_λ	
		A	B	C	D	Replicate I	Replicate II
1	1	-1	-1	-1	-1.083	0.547	0.557
2	5	1	-1	-1	-1.083	0.644	0.638
3	3	-1	1	-1	-1.083	0.527	0.511
4	7	1	1	-1	-1.083	0.438	0.431
5	2	-1	-1	1	-1.083	0.485	0.499
6	6	1	-1	1	-1.083	0.561	0.571
7	4	-1	1	1	-1.083	0.502	0.506
8	8	1	1	1	-1.083	0.465	0.476
9	1	-1	-1	-1	0.167	0.375	0.383
10	5	1	-1	-1	0.167	0.461	0.456
11	3	-1	1	-1	0.167	0.385	0.371
12	7	1	1	-1	0.167	0.311	0.302
13	2	-1	-1	1	0.167	0.398	0.412
14	6	1	-1	1	0.167	0.455	0.464
15	4	-1	1	1	0.167	0.382	0.386
16	8	1	1	1	0.167	0.359	0.366
17	1	-1	-1	-1	0.917	0.308	0.312
18	5	1	-1	-1	0.917	0.370	0.365
19	3	-1	1	-1	0.917	0.326	0.313
20	7	1	1	-1	0.917	0.258	0.253
21	2	-1	-1	1	0.917	0.361	0.375
22	6	1	-1	1	0.917	0.408	0.416
23	4	-1	1	1	0.917	0.333	0.335
24	8	1	1	1	0.917	0.306	0.315

The percent contributions listed in the ANOVA (Table 3.7) indicate that the main effect of wavelength (D) is the most dominant, accounting for 69.8% of the total variability, followed by the Si/Mn ratio (B) and the dew point-Si/Mn (AB) interaction, which account for 13.7% and 9.6%, respectively. The combination of these three effects accounts for over 93% of the variations in the spectral emissivity. In addition, F-tests at 95% confidence interval (F-value > $F_{(0.05,1,32)}$ = 4.15) indicate that 12 out of the 15 effects are statistically significant.

Table 3.7. ANOVA for the general (2 × 2 × 2 × 3) factorial design

Source of variation	Sum of Squares ($\times 10^{-3}$)	Degree of Freedom	Mean Square ($\times 10^{-3}$)	F-value	p-value ($\times 10^{-3}$)	Percent Contribution	Significance at 95% CI
A	0.857	1	0.857	8.69	5.94	0.20	✓
B	57.83	1	57.8	585.94	3.84×10^{-19}	13.69	✓
C	1.77	1	1.77	17.98	0.178	0.42	✓
D	295	1	295	2987.95	3.55×10^{-30}	69.83	✓
AB	40.6	1	40.6	411.36	7.86×10^{-17}	9.61	✓
AC	0.643	1	0.643	6.51	15.7	0.15	✓
AD	0.1002	1	0.1002	1.02	321	0.02	
BC	2.07	1	2.07	20.95	0.0677	0.49	✓
BD	0.906	1	0.906	9.18	4.82	0.21	✓
CD	10.62	1	10.62	107.59	9.2×10^{-9}	2.51	✓
ABC	3.22	1	3.22	32.59	2.53×10^{-3}	0.76	✓
ABD	1.099	1	1.099	11.14	2.16	0.26	✓
ACD	0.0142	1	0.0142	0.14	707	3.37×10^{-3}	
BCD	4.53	1	4.53	45.87	1.18×10^{-4}	1.07	✓
ABCD	0.0123	1	0.0123	0.12	726	2.92×10^{-3}	
Error	3.16	32	0.0987			0.75	
Total	422	47					

3.3.3.1. Regression analysis: spectral emissivity model

The general expression for a linear regression model with interactions is given by

$$\hat{y} = \beta_0 + \sum_{i=1}^{n} \beta_i x_i + \sum_{i=1}^{n-1} \sum_{j=2}^{n} \beta_{ij} x_i x_j + \sum_{i=1}^{n-2} \sum_{j=2}^{n-1} \sum_{k=3}^{n} \beta_{ijk} x_i x_j x_k + \cdots + \epsilon \tag{3.3}$$

where $\hat{y}$ is the predicted response; n is the number of factors; β_0, β_i, β_{ij}, and β_{ijk} are the unknown coefficients; x_i, x_j, and x_k are the factors (independent variables); and ϵ is the random error.

The full spectral emissivity model with all the independent variables and their two-, three-, and four-factor interactions is

$$\begin{aligned} \hat{\varepsilon}_\lambda = {} & \beta_0 + \beta_1 A + \beta_2 B + \beta_3 C + \beta_4 D + \beta_{12} AB + \beta_{13} AC + \beta_{14} AD + \beta_{23} BC + \beta_{24} BD \\ & + \beta_{34} CD + \beta_{123} ABC + \beta_{124} ABD + \beta_{134} ACD + \beta_{234} BCD + \beta_{1234} ABCD \end{aligned} \tag{3.4}$$

Table 3.8 shows the values of the coded regression coefficients, their standard error, and 95% confidence interval estimates for the full model. The standard errors for all model coefficients are dissimilar because the design is not orthogonal at the wavelength factor (D) due to the non-uniform spacing between the three detection wavelengths, as seen in Table 3.8. The uncoded coefficient values provided in Table 3.8 are obtained by substituting Eq. (3.2) for each factor associated with the model terms.

The model closely matches the experimental observations based on the small values of the sum-of-squares error and root-mean-square error, summarised in Table 3.8, as well as the adjusted R^2 of 0.989. Furthermore, the predictive ability of the model when faced with new factor levels is indicated by the prediction R^2 parameter; in this case, the prediction R^2 is equivalent to its adjusted R^2, which indicates good predictability for new observations within the current range of the factors.

Table 3.8. Regression coefficients for the spectral emissivity model

Model Term	Coefficient	Value	Standard Error	95% CI Low	95% CI High	Uncoded Coefficient Values
Intercept	β_0	0.41626	0.00143	0.41334	0.41918	1.32994
A	β_1	0.00423	0.00143	0.00131	0.00715	0.00554
B	β_2	-0.03471	0.00143	-0.03763	-0.03179	-2.16905
C	β_3	0.00608	0.00143	0.00316	0.00900	-0.73785
D	β_4	-0.09501	0.00174	-0.09856	-0.09147	-0.40820
AB	β_{12}	-0.02908	0.00143	-0.03200	-0.02616	-0.04035
AC	β_{13}	0.00366	0.00143	0.00074	0.00658	-0.00181
AD	β_{14}	-0.00175	0.00174	-0.00529	0.00179	-0.00129
BC	β_{23}	0.00656	0.00143	0.00364	0.00948	3.03408
BD	β_{24}	0.00527	0.00174	0.00173	0.00881	0.72351
CD	β_{34}	0.01803	0.00174	0.01449	0.02157	0.34865
ABC	β_{123}	0.00819	0.00143	0.00526	0.01111	0.02381
ABD	β_{124}	0.00580	0.00174	0.00226	0.00934	0.00893
ACD	β_{134}	-0.00066	0.00174	-0.00420	0.00288	0.00011
BCD	β_{234}	-0.01177	0.00174	-0.01531	-0.00823	-1.27151
ABCD	B_{1234}	-0.00061	0.00174	-0.00416	0.00293	-0.00323
Goodness-of-fit statistics						
SSE= 0.003158		RMSE = 0.009935		R^2 = 0.992	Adj. R^2 = 0.989	Pred. R^2 = 0.984

The adequacy of the spectral emissivity model in Eq. (3.4) is further validated by analyzing the model residuals. The normal probability plot in Figure 3.5 (a) shows that the residual distribution is approximately normal with a slight skewness on the right tail. Although the residual vs predicted value plot in Figure 3.5 (b) does not have a pronounced non-random pattern, the distribution is not uniform around the zero-residual line. This could be due to heteroscedasticity (non-constant variance in the measurement) or a significant nonlinear term missing from the model. The plot of the measured and predicted ε_λ at 1.6 μm to 2.4 μm in Figure 3.6 suggests that

the trend in the residual is most probably due to a quadratic relationship that was not accounted for. The slight curvature in the data can be better modelled by fitting a second-order model obtained with either a 3^k factorial design, central composite design (CCD), or the Box-Behnken design [106].

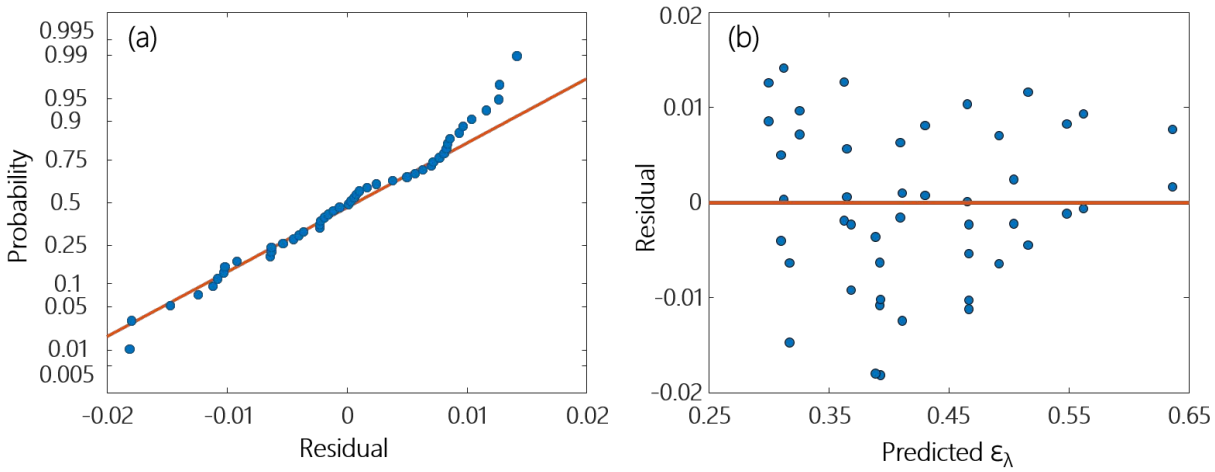


Figure 3.5. Residual analysis: (a) normal probability plot of residuals and (b) plot of residuals vs predicted spectral emissivity

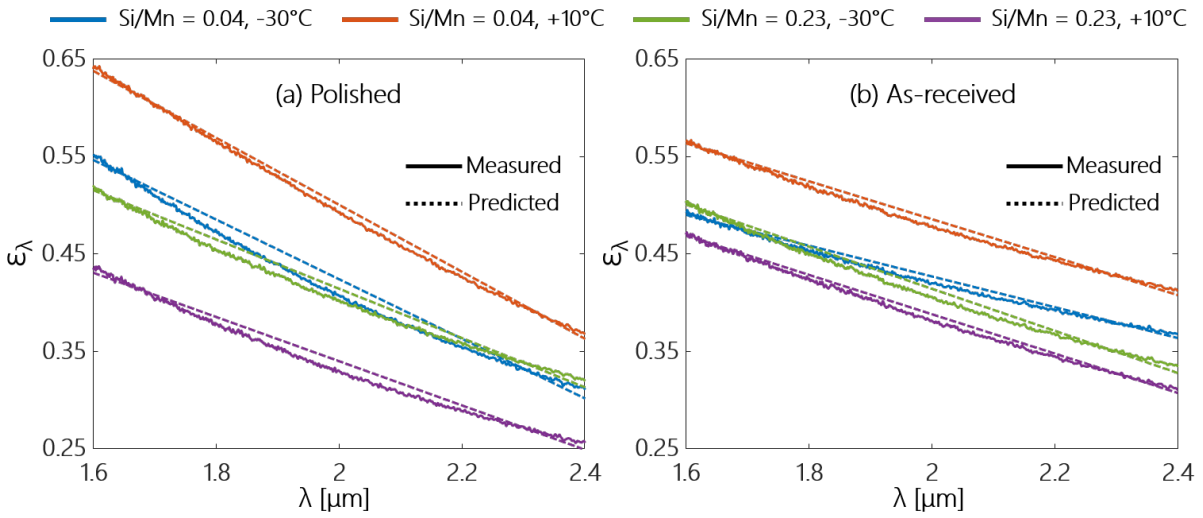


Figure 3.6. Comparison of measured and predicted spectral emissivity, ε_λ, for (a) polished coupons and (b) as-received coupons.

Finally, we consider how the accuracy of the proposed model may be affected if the AHSS samples experience temperature-dependent emissivity variations associated with changing electron mobility at high temperatures. Typically, the Hagen-Rubens relation is used to predict how the radiative properties of metals might increase with temperature via its electrical conductivity [52, 71, 105]. However, the Hagen-Rubens relation is only valid for low-resistivity metals at longer wavelengths in the infrared region ($\lambda >> 5\mu m$) (24, 38). Also at shorter wavelengths, metals exhibit a "crossover wavelength" or "X-point" over which the sensitivity of emissivity to temperature is reversed, and the spectral emissivity decreases as temperature increases [71, 105]. These factors, coupled with the effects of near-surface oxidation, make it difficult to predict or isolate temperature-dependent emissivity variations for metal alloys observed at the shorter wavelengths critical to pyrometry. Metals exposed to high-temperature oxidizing environments, such as the annealing furnace, generally have radiative properties similar to those of their oxide layer, because most of the thermal emission is predominantly at shorter wavelengths where the interference effect of the oxide layer is even more significant [71, 105]. Previous pyrometry studies on steel alloys [6, 58] that have used *in situ* spectral emissivity measurements to determine the effect of temperature also indicate that variations observed at high temperatures are significantly influenced by the changes in surface properties due to oxidation. Given that our current *ex situ* characterization technique considers temperature-induced surface variations, additional *in situ* temperature-dependent emittance measurements will be required to accurately determine how the proposed AHSS spectral emissivity model performs with high-temperature pyrometry measurements. In addition to elucidating the temperature-dependence associated with changing electrical conductivity in the metal, further analysis will ensure that the derived model is directly applicable to industrial conditions.

3.4. Conclusion

To reduce the temperature-excursions produced by pyrometry errors during intercritical annealing, emissivity compensation algorithms must be derived that accurately represent how the spectral emissivity varies with material properties and annealing process parameters. This chapter uses the response surface methodology (RSM) to analyze and model spectral emissivity variations for dual-phase AHSS alloys in terms of dew point, silicon-to-manganese (Si/Mn) ratio, pre-annealed surface state, and wavelength. First, a 2^3 design shows how dew point, Si/Mn ratio and surface state interact to produce variations in the spectral emissivity at specific wavelengths between 1.2 μm – 4.0 μm. To develop a multivariate spectral emissivity model for multi-wavelength pyrometry measurements, these three factors are combined with wavelengths (1.6 μm, 2.1 μm, and 2.4 μm) in a general ($2 \times 2 \times 2 \times 3$) factorial design.

ANOVA results for the 2^3 design identify the Si/Mn ratio (B), surface state (C), dew point-Si/Mn ratio interaction (AB), and Si/Mn ratio-surface state interaction (BC) to be statistically significant at each of the selected wavelengths. Their combined effect accounts for at least 93% of the total variability observed in the emissivity at these wavelengths. The main and interaction plots from this two-level design also indicate that polished samples have large emissivities at the shorter wavelengths ($\lambda = 1.2$ μm and $\lambda = 1.6$ μm), especially in the presence of the lower Si/Mn ratio.

Based on these results, a linear spectral emissivity model is then derived through regression analysis. The fitted model consists of all four main effects, five two-factor interactions, and three three-factor interactions. While the model closely interpolates the emissivity measurements, an analysis of the model residuals suggests the presence of one or more second-order effects that are not accounted for with the current model. A second-order emissivity model can easily be obtained using other RSM experiment designs such as 3^k factorial design, central composite design (CCD), or the Box-Behnken design [106], provided more samples are evaluated.

The response surface methodology introduced in this chapter provides key insights into how the evolving spectral emissivity of advanced high strength steels is influenced by process parameters during intercritical annealing, and the model derived from the RSM analysis will be used to provide more robust pyrometric temperatures, which are essential for the latest high-performance alloys.

Chapter 4
Experimental apparatus for *in situ* radiative measurement[2]

Given that the objective of this research is to improve the accuracy of pyrometry estimates during intercritical annealing, an experimental apparatus is needed to simulate how the radiative properties of DP steel change as the steel is heated, and how these changes impact the accuracy of emissivity compensation algorithms. The previous phase of this project studied the effect of temperature on the radiative properties of AHSS exclusively through *ex situ* analysis of rapidly quenched coupons processed within the galvanizing simulator at McMaster University [76, 89, 116, 117]. Unfortunately, the McMaster galvanizing simulator does not provide optical access to the coupons, making it difficult to observe how the radiative properties evolve with process time. As discussed in Chapter 2, the steel experiences increased electron scattering at higher temperatures, resulting in changes in radiative properties of the surface. Therefore, *ex situ* measurements made at room temperature do not account for the temperature-dependent variations in emissivity that occur during annealing. Moreover, the radiative properties of the AHSS depends on the oxides that form on the steel surface during heating, and these oxides may undergo morphological changes during quenching which would cause the radiative properties of extracted coupons to differ from the conditions within the chamber before quenching.

[2] The prototype design and implementation for Chamber 1 was carried out by Mr. Simon Trivett, a former MASc student at the Waterloo Laboratory for Inverse Analysis and Thermal Sciences (WatLIT), University of Waterloo. The upgraded implementation of Chamber 1 was led by Mr. Roger Tsang (Research Engineer, WatLIT), in collaboration with the author and with assistance from two undergraduate research assistants at WatLIT, Mr. Nick Ho and Ms. Daphne Patterson. Chamber 2 (vacuum annealing chamber) was solely designed and assembled by the author with machining/fabrication contracted to the Engineering Machine Shop at the University of Waterloo.

In an initial attempt to obtain *in situ* temperature-dependent measurements during the previous phase of the GAP emissivity project, Somveille [3] conducted some preliminary annealing experiments using a Gleeble® 3500 simulator, following the same process used by Shi et al. [118] to measure the radiative properties of Al-Si coated ultra high strength steels (UHSS). Specimens of two types of dual-phase AHSS alloy (DP980 and DP780) were annealed with the Gleeble® sample chamber filled with ultrahigh purity argon (99.999% purity, $O_2 \leq 2$ ppm) [3]. The spectral emissivities were inferred as the ratio of the near-normal spectral incandescence measured as the sample heated to the spectral incandescence emitted from a blackbody source. Unfortunately, the atmospheric control within the Gleeble® was inadequate to prevent oxidation of the samples, so the results were not representative of an industrial galvanizing line. To fully address these shortcomings, it was concluded that a stand-alone annealing simulator similar to the apparatus described by Ham et al. [77, 88] would be built at the University of Waterloo.

The rest of this chapter describes the annealing simulator components, design, installation, and the modifications necessary to make the annealing chamber functional in terms of temperature and heating schedule control, annealing atmosphere control and radiative measurements.

4.1. Features of the annealing simulator

A schematic of the experimental annealing simulator is shown in Figure 4.1. The chamber is designed to anneal steel coupons according to a specified heating schedule while measuring irradiance from the surface using various sensing techniques. Each coupon is mounted between two copper electrodes, which are connected to a programmable DC power supply. The coupon temperature is PID controlled with feedback from a K-type thermocouple (0.25 mm wire diameter) spot-welded to the back of the sample. A direct current (DC) power supply was chosen instead of an alternating current (AC) power supply to minimize the measurement errors caused by induction in the thermocouple wires.

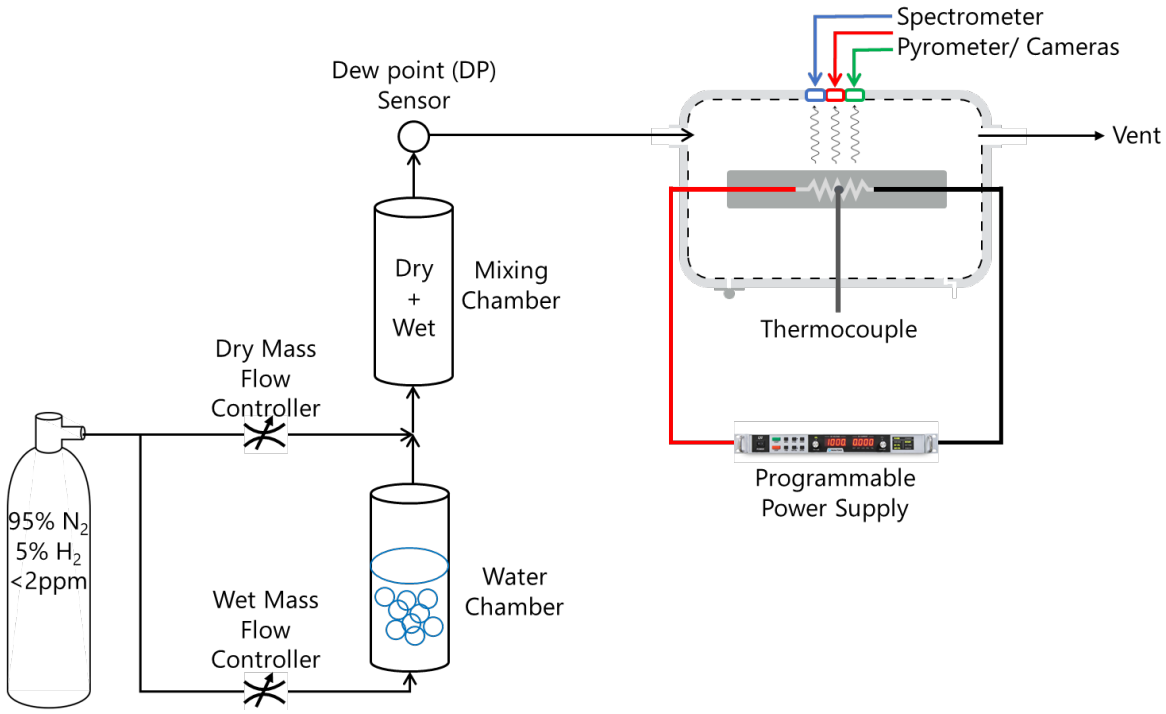


Figure 4.1. Schematic diagram of the annealing simulator

Typically, before the coupon is heated, the thermal processing chamber is continuously purged with 95% N_2/5% H_2 (certified ultrahigh purity mixture with < 2ppm O_2) for at least 20 minutes at a flow rate ≥8 standard litres per minute (slpm). The chamber exhaust includes a check valve to prevent back-flow into the system. To obtain the desired annealing dew point, a portion of the incoming gas is diverted through a tank of deionized water to create a wet flow and then recombined downstream with the dry flow in a mixing chamber. Two Sierra SmartTrak® 50 mass flow controllers (MFC) control the proportion of the wet flow (0-5 slpm range) and dry flow (0-15 slpm range) required to achieve the desired dew point. The dew point of the mixed gas is monitored using a Michell EA2-TX-100-HD dew point transmitter (hygrometer). The initial plan was to use a PID controller to automatically control the process dew point; however, it was difficult to accurately tune the PID constants for the required range of dew points, so the dry and wet MFC flow rates were manipulated manually instead. After annealing, the samples are quenched using a resident gas nozzle in order to suspend the surface state at the centre of the sample.

In terms of optical measurements, the chamber accommodates a Williamson PRO MWX-ST-17 multi-wavelength pyrometer, an OceanOptics NIRQuest512 spectrometer, a FLIR T400 infrared camera, and a visible camera. The pyrometer is equipped with a filter wheel that houses the bandpass filters centered on the following wavelengths: 1.6 μm (1.505 μm−1.790 μm), 2.1 μm (2.025 μm−2.23 μm), and 2.4 μm (2.250 μm−2.45 μm). The pyrometer is aimed through a 5.08 cm (2″) diameter calcium fluoride (CaF_2) window at a focal distance of 350 mm. The spectrometer is connected by optical fiber to a hard-mounted collimating lens that views the coupon at an oblique angle. The spectrometer is sensitive over 0.9μm − 2.5μm; however, due to low signal-to-noise ratio at the shorter wavelengths, only measurements over 1.2 μm are used for *in situ* pyrometry analysis. An absolute intensity calibration is carried out on the spectrometer using a blackbody source (Infrared Systems IR-563/301). The pyrometer and spectrometer measurement spot sizes are coincident on the center of the AHSS coupon with a diameter of approximately 2.5 cm. The FLIR camera is employed to check the temperature distribution in the center spot of the sample, while the visible camera is used to track any visible oxide evolution on the steel surface during annealing. The spectrometer has a fixed location since it is mounted at an angle but the pyrometer, FLIR camera and visible camera all use the CaF_2 view port so only one of these three devices can be used at a time.

The actual implementation and embodiment of these features took several iterations and numerous modifications to obtain reliable annealed samples, primarily due to challenges with oxygen infiltration and atmosphere control. The following subsections will discuss the design process for two main versions of the annealing simulator: Chamber 1 and Chamber 2. While the features and mode of operation of the annealing simulator do not change across the versions of the chamber, there are key design variations in the ways these features are embodied. The experimental results analyzed in Chapter 5 and Chapter 6 are based on Chamber 1, while the results from Chamber 2 are discussed in Chapter 7 and Chapter 8. The motivation behind the detailed design discussion in this chapter is to establish validity for the *in situ* emissivity and temperature measurements that will be introduced in the rest of this thesis, and more importantly, to provide guidance to future researchers about the challenges and best practices for constructing a thermal processing apparatus for similar applications.

4.2. Chamber 1: Box design

4.2.1. Prototype implementation

The first implementation of the annealing simulator is shown in Figure 4.2. The AHSS coupons were initially designed to bolt to two water-cooled copper electrodes, which were connected to a 30V, 170A DC power supply. The electrodes were water-cooled to minimize the amount of heat conducted from the hot steel sample to the copper electrodes. While this prototype had a functioning chamber that could heat steel coupons, making it an effective proof-of-concept, it also had many drawbacks. First, during the testing phase, it was discovered that the selected DC power supply did not provide the amount of current needed to heat a full-sized coupon at a ramp rate representative of a standard heat treatment furnace or a Gleeble®. The prototype also did not have a functioning atmosphere control system, although most of the hardware for the gas manifold systems had been constructed. Additionally, the original quench system design was a hole array aimed at the bottom edge of the sample, which only exposed a narrow surface area to the cooling gas which would produce a slow quenching rate, making it difficult to freeze the coupon surface for *ex situ* characterization. More importantly, the optics and filter windows were not incorporated in this implementation, so the chamber door needed to be left open during experiments to obtain any radiative measurements.

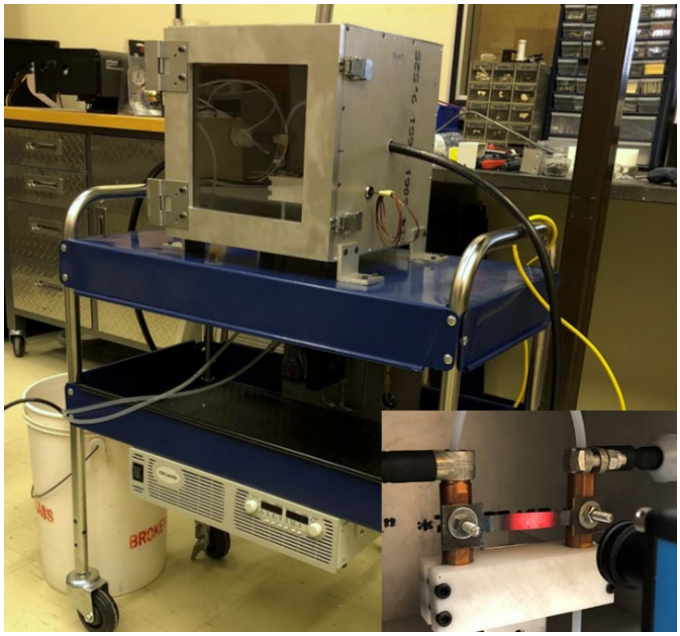


Figure 4.2. First iteration of the annealing simulator (Chamber 1 prototype) and (inset) of a heated coupon.

4.2.2. Upgraded implementation

To address the issues identified with the prototype, a second iteration of the chamber was developed as shown in Figure 4.3. Although the second version kept the main cube chamber from the prototype, several of the components were modified. First, the TDK-Lambda 30V, 170A DC power supply was upgraded to a TDK-Lambda, 8V, 600A, DC power supply. The existing power cable (00 AWG copper cables with 250A typical rating) was upgraded to a tinned copper bus bar (nVent ERIFLEX Flexibar 640A typical rating). The chamber was also transferred from the cart to an electronic rack for improved ergonomics and safety. The optical instruments and software for *in situ* measurements were also installed during this iteration. Both the CaF_2 optical window for the pyrometer and the 25° angular port for the spectrometer-collimating lens assembly were mounted on the chamber front door. An independent quench nozzle was installed and aimed at the back of the sample. The nozzle tip was covered in reflective foil to prevent heat damage from its proximity to the annealing sample. The PID controller was implemented in LabVIEW to control the heating schedule of the samples during annealing.

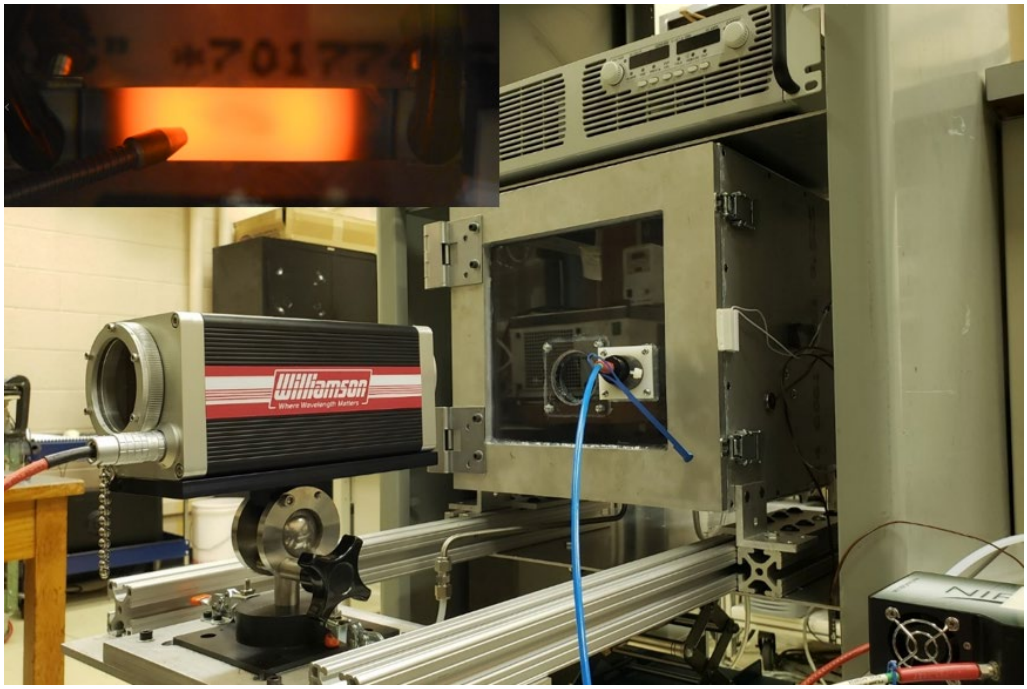


Figure 4.3. Upgraded implementation of Chamber 1 showing the mounted pyrometer and spectrometer optics, and (inset) a heated coupon.

These upgrades allowed for AHSS thermal processing under acceptable atmospheric conditions, making it possible to refine the temperature control and emissivity data collection process. During this step, it was discovered that new thermocouple wires needed to be used for each run/experiment to prevent aging and drift in the temperature measurements due to short-range ordering (SRO) of the crystal structure in the chromel conductor of the K-type thermocouple. It is important to note that the use of a DC power supply to heat the sample will lead to ohmic offset error in the temperature measurement if both thermocouple wires are not placed at an equipotential location along the length of the sample [119]. Therefore, to prevent the ohmic offset voltage error, the thermocouple wires were first welded together to form an intrinsic bead junction before welding onto the steel sample.

In addition, the temperature uniformity of the measurement spot was investigated using infrared thermal imaging on a black-painted sample ($\varepsilon_\lambda \approx 0.94$). Figure 4.4 shows that the measurement spot at the centre of the sample has a temperature uniformity of approximately ±5°C and ±10°C at 600°C and 850°C, respectively. Moreover, based on the ASTM E230 standard, the uncertainty for the thermocouple estimates is ±2.2°C or 0.75%, depending on which is greater over the temperature range [120].

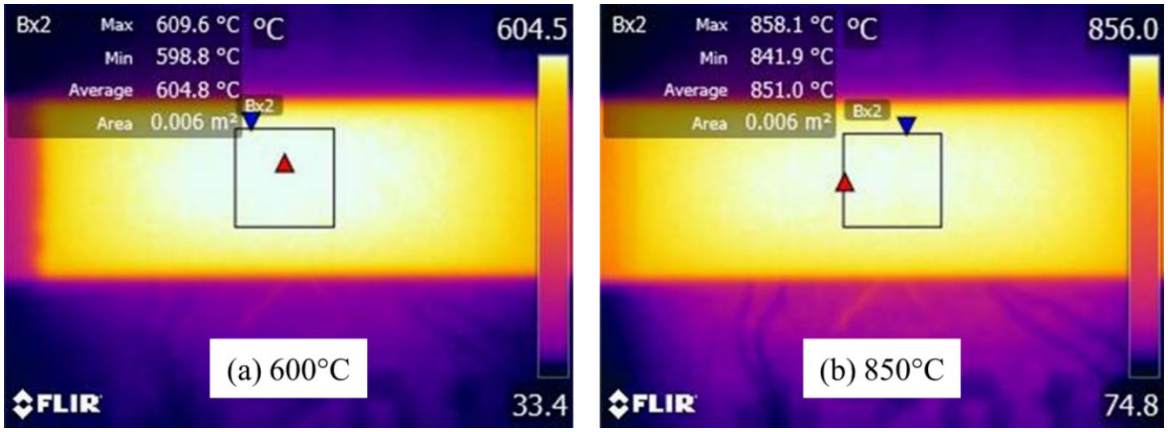


Figure 4.4. Infrared thermal images of a black-painted AHSS sample showing the temperature uniformity for the equivalent measurement spot size (a) 600°C and (b) 850°C.

Although the upgraded version of the box design provided *in situ* temperature and spectral intensity measurements on annealed AHSS (Chapter 5 and Chapter 6), the heated samples showed visible signs of oxidation during heating and after quenching irrespective of the low dew point of

the H_2-N_2 gas mixture. On further analysis, it was concluded that the observed oxidation could be due to either oxygen infiltration during the annealing process or residual oxygen within the chamber despite the extended purging time. First, a makeshift baffle was placed around the gas inlet within the chamber to promote mixing and avoid any stagnation issues. Next, potential infiltration areas (leaks) were identified around the chamber using a handheld hydrogen gas sensor. The first attempt to seal these leaks involved the use of silicone caulk along every seam and opening. This slightly reduced the amount of observed oxidation, but the sealant deteriorated easily after one or two runs, especially at the back of the chamber due to movements in the bus bar slots and door hinge. This led to a redesign of the bus bar mode of connection, as shown in Figure 4.5. The original gasket was replaced with a vacuum-grade Teflon feedthrough with a copper insert that connected to bus bar on both sides, thereby eliminating the large gap resulting from having a continuous bus bar piece. The front door system of the chamber was also modified with an O-ring and the hinges were replaced with a latch system with two latches on each side of the box (8 latches in total) to create a uniform seal around the door. Vacuum grease was also applied to the door before each experiment to improve the seal and minimize the leaks.

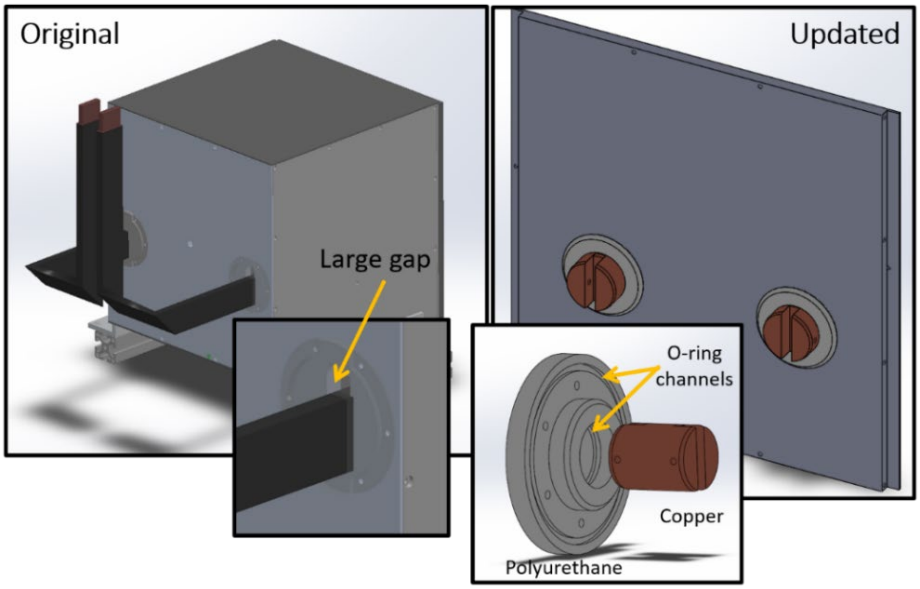


Figure 4.5. The chamber back panel for the second design iteration (left – original) and third design iteration (right – updated), showing the modifications made to the bus bar feedthrough to improve airtightness.

While these modifications eliminated the significant leaks around the bus bars connections and the front door, samples processed after the modifications continued to show extensive surface

oxidation, indicative of oxygen infiltration. Further leak tests with the N_2/H_2 gas and a hydrogen detector showed that while the modification improved some areas of the chamber, additional leak sources were introduced during the modification process, especially on the chamber side panels where new holes were created to accommodate the modified door latch system. In addition, some of the existing screw holes became redundant from changing out the front and back panels, contributing to increased leaks. Figure 4.6 shoes the chamber shell with the new and redundant holes, which contributed to the overall increase in leaks.

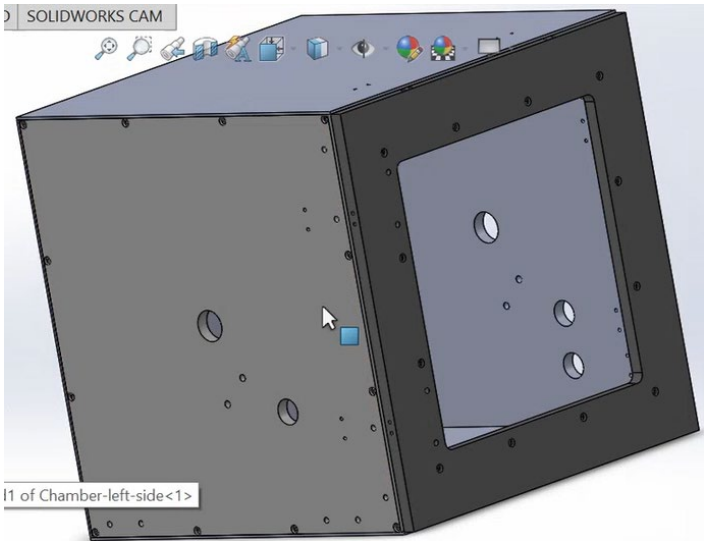


Figure 4.6. Shell of the upgraded Chamber 1 showing the numerous holes that collectively contribute to the persistent infiltration problem.

4.3. Chamber 2: Vacuum-based design

The persistent leaks and the sensitivity of the AHSS samples to oxygen infiltration necessitated the design of an entirely new vacuum-grade chamber. The high AHSS alloy content and its affinity for oxygen were not fully understood when the original chamber was designed; even the choice of aluminium for the chamber walls proved inappropriate for this application, given that aluminium is an oxygen-getter material that emits oxygen when it becomes saturated. This, and many other lessons learned from Chamber 1, were incorporated into the design of the vacuum-based Conflat flange annealing setup shown in Figure 4.7. Detailed engineering drawings are included in Appendix B. Although the chamber can hold vacuum, the samples are heated and quenched under slightly positive atmosphere pressure. The goal of using a vacuum chamber is to allow for pumping down the annealing environment to remove all oxidants (e.g., oxygen, water vapor, and carbon

dioxide) before refilling the chamber with the desired atmosphere, while simultaneously preventing any leakage or infiltration.

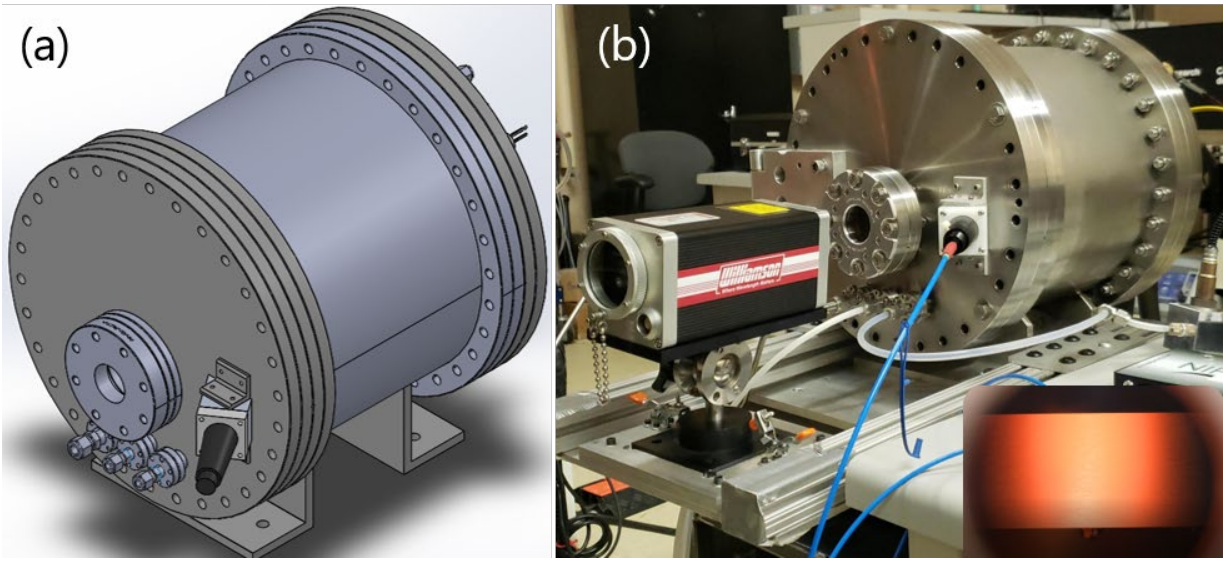


Figure 4.7. Vacuum-based implementation of the annealing simulator (Chamber 2): (a) the CAD model and (b) final implementation showing the mounted pyrometer and spectrometer optics, and (inset) a heated coupon.

Experiments begin by evaluating the chamber using a Varian DS 402 pump to a medium vacuum pressure between 28-100 Pa, as measured with a vacuum gauge at the exit. While the chamber can achieve 100 Pa within two hours of pumping, the chamber and gas lines are usually pumped overnight (≥ 12 hours) to promote gas desorption from the surfaces within the chamber (i.e., outgassing). In addition to the vacuum gauge placed at the outlet, a zirconia oxygen sensor (Rapidox 2100 Oxygen Analyser) is also installed to monitor oxygen content within the chamber. The oxygen content after pumping usually ranges from 5 ppm to 20 ppm. The vacuum gauge and oxygen analyzer serve as diagnostic tools since failure to reach these values during pumping indicates an imperfect seal on the chamber door or infiltrations along the gas or quench lines. After achieving the desired pressure and oxygen concentration for the vacuum, the chamber is first pre-purged with regular high purity N_2 ($\leq$ 5 ppm O_2) before switching over to the ultra-high purity N_2-H_2 mixture (certified $\leq$ 2 ppm O_2). The O_2 concentration reading during the nitrogen pre-purge is usually less than 2 ppm. Having a two-step purging process serves two purposes: (1) it extends the purging time to get rid of lingering oxidants without wasting the expensive nitrogen-hydrogen

mixture; and (2) it allows for a final oxygen infiltration check in the gas lines as the O_2 concentration drops to very low values (<10-20 ppm) in the presence of the reducing atmosphere. The chamber redesign process successfully eliminated the visible oxidation problems as shown in Figure 4.8 (*in situ*) and Figure 4.9 (*ex situ* after quench). The water and mixing vessels for the atmosphere and dew point control system were also redesigned as vacuum chambers to provide leak-free dew point control for the annealing process. Additionally, an SF72 dew-point transmitter compatible with the Rapidox oxygen analyzer is installed at the exit to confirm that the dew point within the chamber matches the dew point at the inlet mixing chamber. The O_2 concentration is continuously monitored throughout the course of the annealing experiment. Having an oxygen sensor in addition to the dew point sensors in this annealing setup is extremely important to estimate the overall oxidation potential of the annealing atmosphere. Dew point measurements only indicate the oxidation potential of the annealing atmosphere due to water vapour with no insight into the contributions of other oxidants on the oxidation potential of a mixed atmosphere, such as when the oxygen infiltration scenarios encountered with Chamber 1.

The key decisions that led to this successful redesign are summarized in Appendix B, along with detailed engineering drawings. AHSS coupons annealed in Chamber 2 were further validated by comparing them against samples processed in the McMaster galvanizing simulator, which is the benchmark laboratory setup for simulating industrial annealing processes. The results of this comparison will be discussed in Chapter 8.

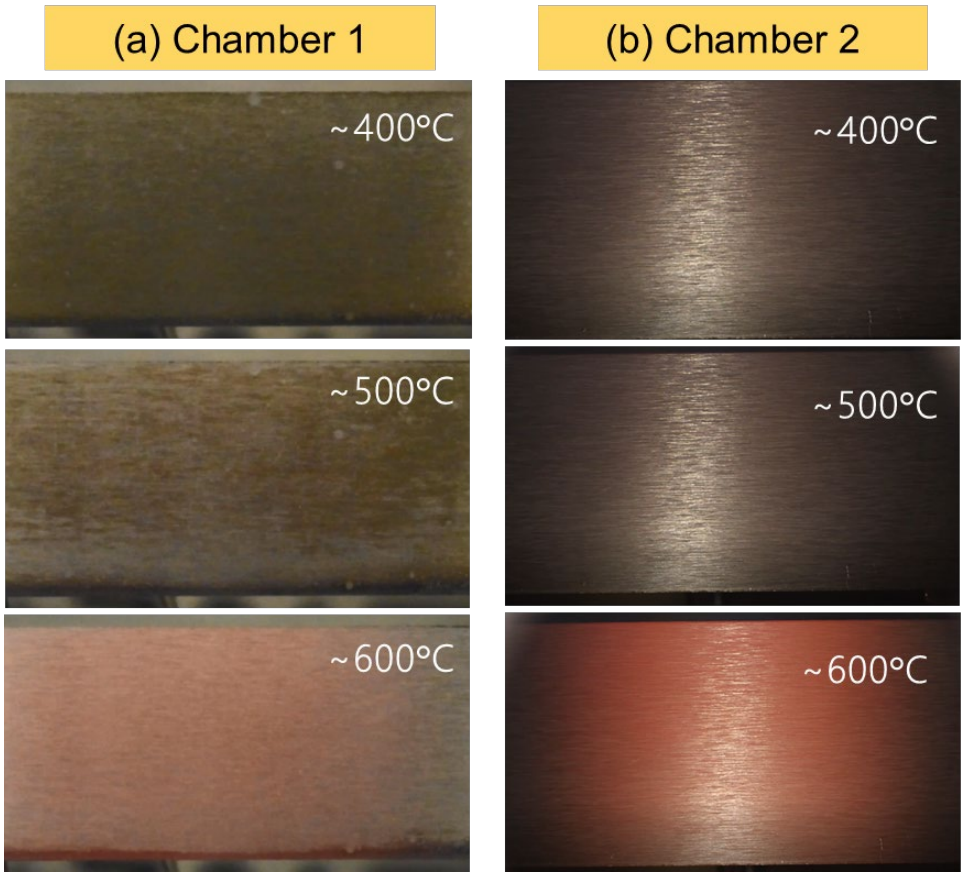


Figure 4.8. *In situ* images of annealing AHSS coupons at 400°C, 500°C and 600°C showing differences in the temperature-dependent visible oxides obtained with (a) Chamber 1 (upgraded) and (b) Chamber 2.

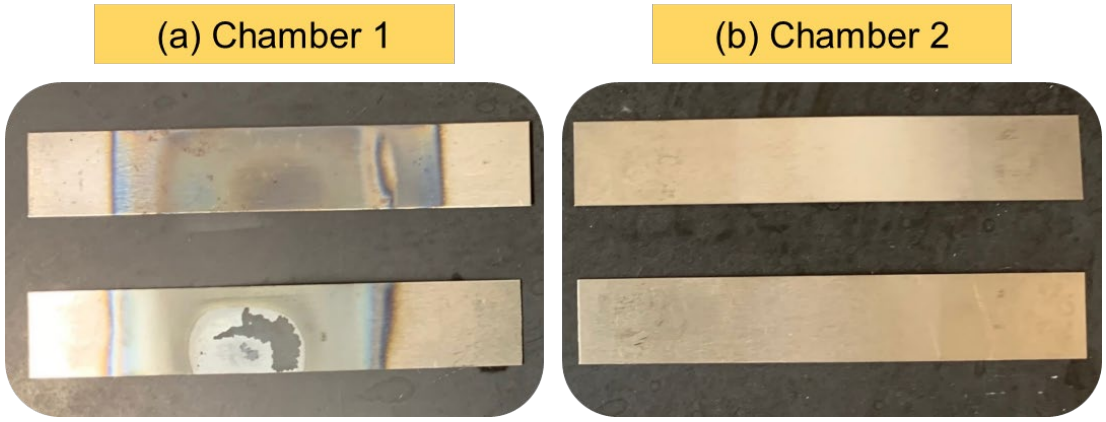


Figure 4.9. *Ex situ* images of the AHSS coupons processed in (a) Chamber 1 (upgraded) showing the anomalous visible oxide formed on the steel surface after quenching, while samples annealed in (b) Chamber 2 do not have this oxide layer.

Chapter 5
Impact of evolving spectral emissivity on pyrometry[3]

This chapter examines how the evolving surface state of dual-phase steel (DP980) affects the spectral emissivity of the material and pyrometrically inferred temperature during annealing. While temperature is the main quantity-of-interest, many experiments have also investigated how the spectral emissivity of metals and alloys changes during heating. Shi et al. [118] investigated how coating evolution and different heating atmospheres (argon and air) affected the spectral emissivity of Al-Si coated 22MnB5 steel. González-Fernández et al. [121] studied how thermal cycling and surface roughness impacts the spectral emissivity of Ti–6Al–4V alloy between 500 and 1150 K in the mid-infrared spectrum (2.5μm − 22μm). Teodorescu et al. [122-124] studied the spectral emissivity of nickel, titanium, alumina and zirconium heated under ultra-high vacuum conditions at temperatures ranging from 823 K and 1650 K. Comparatively few studies have focused on the relationship between the evolving surface state and the spectral emissivity of uncoated AHSS, with the exception of the works by Ham et al. [77, 88], Somveille et al. [116], and Lin and Daun [74-76, 116, 117], as described in Section 2.2.2.

In this chapter, *in situ* spectroscopic measurements made on DP980 coupons annealed within the Waterloo annealing chamber are used to explore the connection between the evolving surface state and the spectral emissivity, and thus the pyrometrically-inferred temperature. Coupons are heated within a controlled reducing atmosphere of 95% N_2/5% H_2 and a dew point of -40°C. Spectral irradiance is measured simultaneously with a near-infrared spectrometer (0.9μm − 2.5μm) and a multi-channel pyrometer (1.6μm, 2.1μm, and 2.4μm). The visible change in the

[3] The content of this chapter has been disseminated in a conference paper as:

F.K. Suleiman, K. Lin, R. Tsang, T.F. Larrick, and K. J. Daun, 2019, "Impact of evolving spectral emissivity on pyrometry during intercritical annealing," Proceedings of the 111th Galvanizers Association Meeting, Charleston, South Carolina, USA.

appearance of the steel surface is related to the variation in spectral emissivity. The performance of ratio and multi-wavelength pyrometry methods for estimating the surface temperature of AHSS is also examined.

5.1. Experimental procedure

The 152.4 mm × 25.4 mm ×1.5 mm coupons were cut from a coil of cold-rolled DP980. The elemental composition of the steel conforms to ASTM A1079-17 standard as detailed in Table 3.1. Although the exact composition of the coupon used in this experiment is proprietary, the Si/Mn mass ratio measured by spark atomic emission spectrometry is 0.04. Figure 5.1 shows the near-normal directional-hemispherical spectral emissivity of the as-received coupons measured with a Bruker Invenio-X FTIR spectrometer. All samples are cleaned with ethanol to remove oil and surface contaminants before annealing.

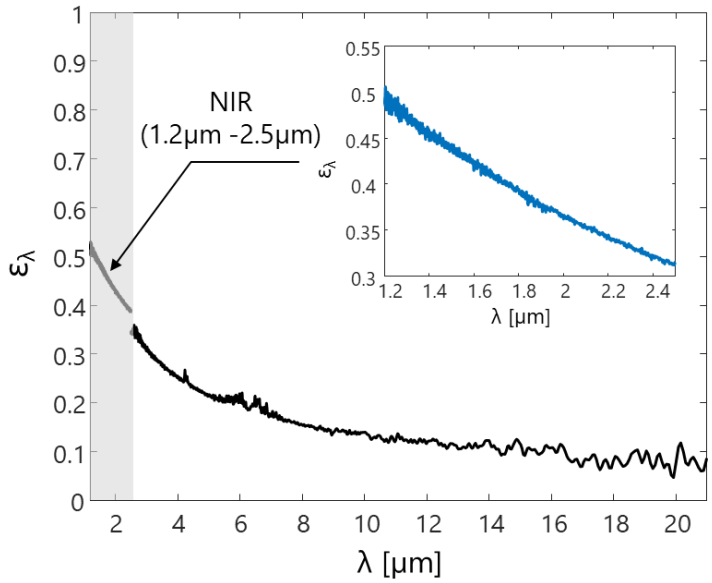


Figure 5.1. Plot of spectral emissivity (ε_λ) vs wavelength (λ) for as-received DP980 at room temperature.

The DP980 coupon is heated in the chamber described in the chamber described in Section 4.2.2. Before the coupon is heated, the thermal processing chamber is continuously purged with 95% N_2/5% H_2 at a rate of 8 standard liters per minute for at least 20 minutes. All tests described in this chapter were carried out with the gas mixture at a dew point of −40°C. The coupon is heated to 800°C according to a linear ramp rate over 60s (13.33°C/s), soaked at 800°C for 30s, and then quenched with the process gas. *In situ* measurements are conducted only during the sample heating

process, so the quench rate is uncontrolled. The spectrometer collects spectra every 0.25 s during the sample heating schedule. The pyrometer data acquisition time interval is set to 0.1 s for these experiments. The spectrometer data is further smoothed with a first-order, three-frame Savitzky-Golay filter.

5.2. Experimental results

The actual temperature reported by the thermocouple attached to the steel coupon is shown in Figure 5.2. A straw-colored oxide layer begins to form when the sample approaches 300°C and appears fully formed by the time the steel heats up to 500°C. This indicates some amount of residual oxygen in the chamber. The oxide begins to dissipate as the sample temperature increases further and appears to be completely gone as the sample reaches 700°C. The shaded region in Figure 5.2 corresponds to the presence of the oxide and the stages of the oxide layer formation are also shown in Figure 5.3.

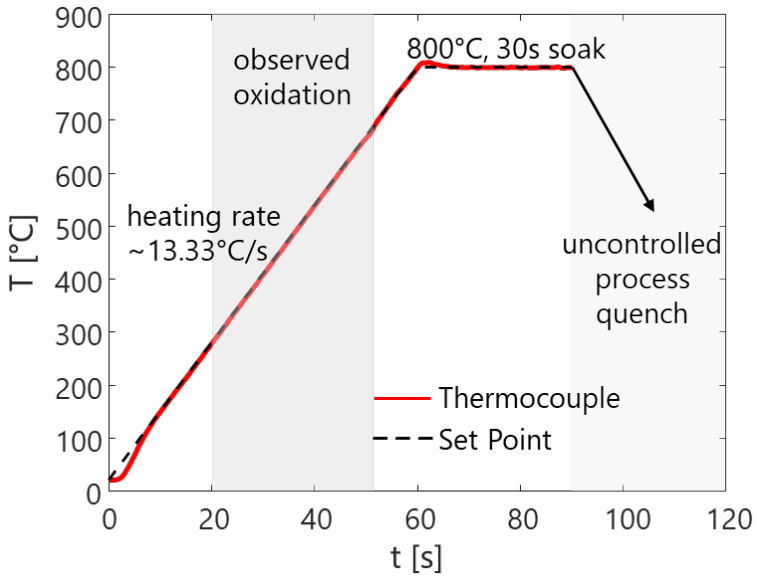


Figure 5.2. Thermocouple reading for the annealed DP980 sample showing the region of the observed oxidation.

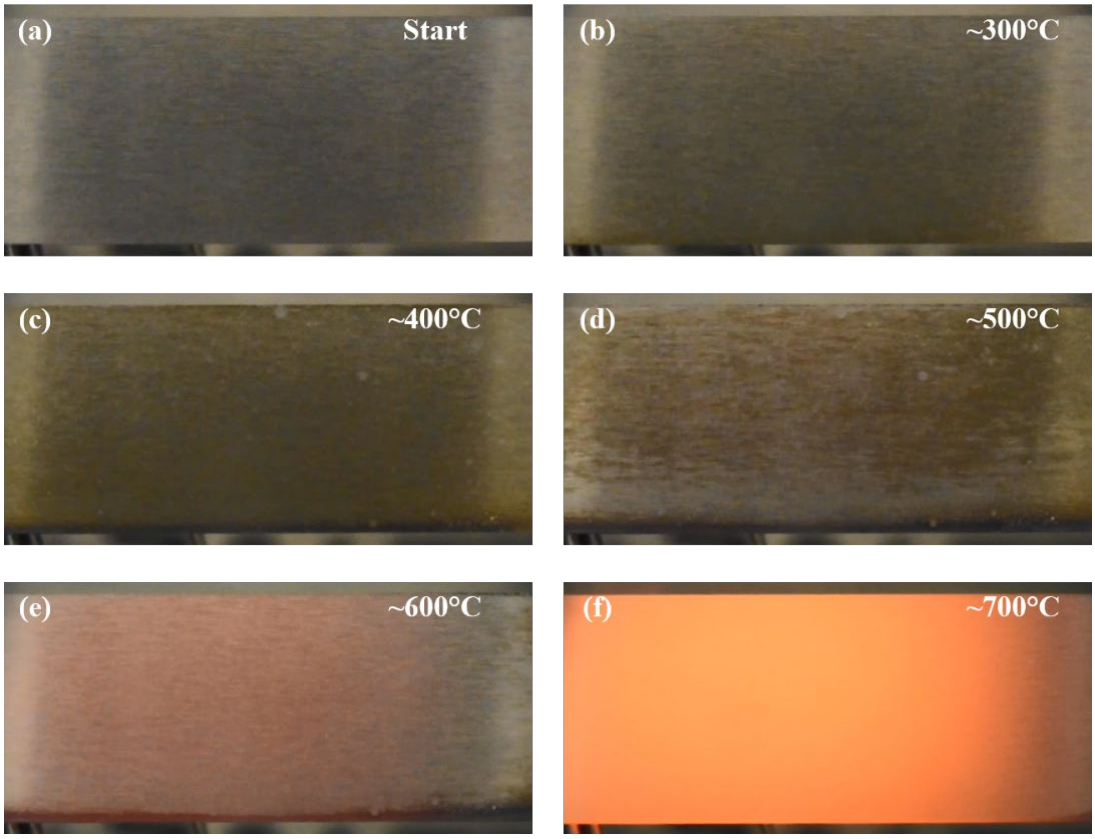


Figure 5.3. Images of the coupon surface during heating. The sample surface is clean at the start of the experiment (a), but an oxide layer begins to form at ~300°C (b), becomes thicker (c), and is fully formed by ~500°C (d). The oxide starts to clear at ~600°C (e) and cannot be seen at ~700°C (f).

5.2.1. *In situ* spectral emissivity

The normal spectral emissivity, ε_λ, is calculated from the intensity measured by the spectrometer, such that, $\varepsilon_\lambda(\lambda, T) = I_\lambda(\lambda, T) / I_{\lambda b}(\lambda, T)$, where λ is the measurement wavelength; T is the sample temperature given by the thermocouple; I_λ is the spectral intensity recorded with the spectrometer; and $I_{\lambda b}$ is the blackbody spectral intensity at the sample temperature. The time-and temperature-dependent spectral normal emissivity for the DP980 sample is plotted in Figure 5.4 and Figure 5.5 for temperatures ranging from 400°C – 800°C. The higher spectral emissivity observed during the heating coincides with the formation of the oxide film illustrated in Figure 5.3. Alloying elements such as Mn, Al, Si, and Cr segregate from the bulk material toward the surface and form selective oxides during annealing. The change of surface topography caused by these oxides will also lead to variation in the spectral emissivity [18, 99]. Under the conditions of this experiment, based on

the Ellingham diagram [114] one would expect to see manganese or chromium oxide form on the surface.

The spectral emissivity plotted in Figure 5.4 and Figure 5.5 decreases with increasing wavelength, which is typical for metals over infrared wavelengths. The spectral emissivity is highest at 400°C due to the oxide formation but decreases as the temperature increases and the oxide clears. The radiative properties at shorter wavelengths (< 2μm) are more impacted by oxide formation compared with those at longer wavelengths. The spectral emissivity remains stable once the surface reaches 800°C, and the values of ε_λ at the beginning and end of the soak period are indistinguishable from each other.

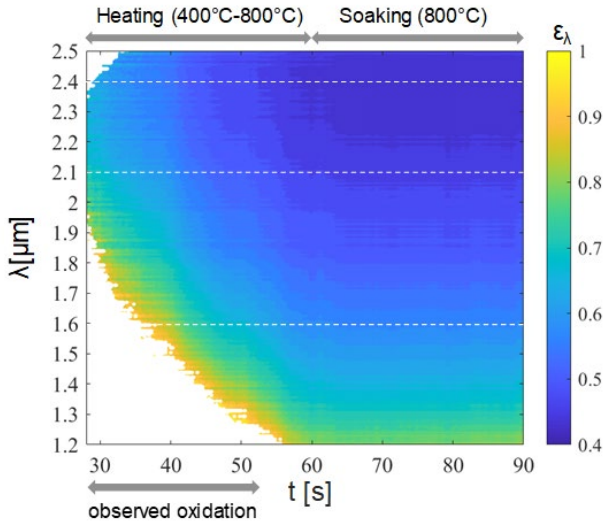


Figure 5.4. Evolving spectral emissivity, ε_λ, of DP980 coupon measured using the NIR spectrometer. Dashed lines correspond to pyrometer detection wavelengths.

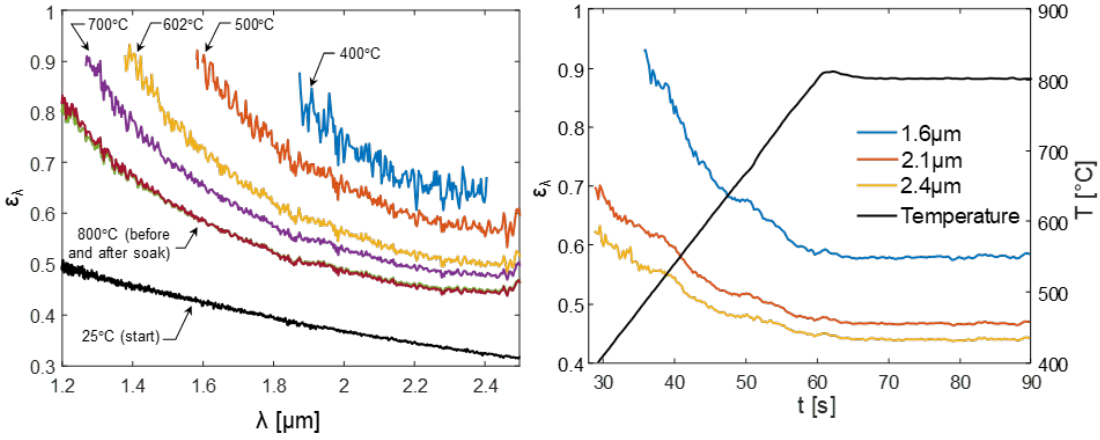


Figure 5.5. Plots of the spectral emissivity, ε_λ, as a function of (a) wavelength (λ) and (b) time (t) and temperature (T).

5.2.2. Pyrometrically-inferred temperature

This section investigates how the varying spectral emissivity affects the pyrometrically-inferred temperature by evaluating the accuracy of the DW (ratio) and MW pyrometric temperature estimated for the steady-state condition, i.e., the soaking period, where the effect of the surface oxide is minimized. In the case of ratio pyrometry, the emissivity ratio, $\varepsilon_{\lambda r}$ for the wavelength combinations indicated in Table 5.1 is obtained from the spectral emissivity of the as-received sample at room temperature shown in Figure 5.1. The inferred dual-wavelength temperature is then calculated using Eq. (2.11), i.e.,

$$T = \frac{C_2\left[\frac{1}{\lambda_{d2}} - \frac{1}{\lambda_{d1}}\right]}{\ln\left[\frac{\varepsilon_{\lambda d2}}{\varepsilon_{\lambda d1}}\left(\frac{\lambda_{d1}}{\lambda_{d2}}\right)^5 \frac{S_{\lambda 1}}{S_{\lambda 2}}\right]} \tag{5.1}$$

Table 5.1. Spectral emissivity ratio (e-slope) measured from the as-received DP980 sample

	Wavelength Combination	Emissivity Ratio, $\varepsilon_{\lambda r}$
Ratio 1	1.6 μm/2.4 μm	1.296
Ratio 2	1.6 μm/2.1 μm	1.178
Ratio 3	2.1 μm/2.4 μm	1.100

For the multi-wavelength approach, several emissivity compensation algorithms from literature were evaluated and the three exponential emissivity compensation algorithms listed in Table 5.2 were found to give the highest accuracy. For the equations in Table 5.2, a_0 is the algorithm constant and T_λ is spectral radiance temperature, i.e., the equivalent blackbody temperature calculated using the measured spectral irradiance. The irradiance measured by the pyrometer at the three detection wavelengths (p = 3) is solved simultaneously using non-linear least-squares regression to minimize the sum of squared errors given by

$$\chi^2 = \sum_{i=1}^{p} [\ln(S_{\lambda,\text{meas},i}) - \ln(S_{\lambda,\text{mod},i})]^2 \tag{5.2}$$

where $S_{\lambda,\mathrm{meas},i}$ is the measured spectral irradiance and $S_{\lambda,\mathrm{mod},i}$ is the modelled spectral irradiance that minimizes the sum of squared errors using the emissivity compensation algorithm. The equation for $S_{\lambda,\mathrm{mod},i}$ is obtained by combining Eqs. (2.5) and (2.6) to give

$$S_{\lambda,gen,i} = \frac{K_{\lambda\mathrm{d},i}\varepsilon_{\lambda\mathrm{d},i}\left(\lambda_{\mathrm{d},i},T\right)C_1}{\lambda_{\mathrm{d},i}^5\left[\exp\left(\frac{C_2}{\lambda_{\mathrm{d},i}T}\right)\right]} \tag{5.3}$$

The calibration constant, $K_{\lambda\mathrm{d},i}$, is determined through a blackbody calibration process, Planck's distribution constants, C_1 and C_2, are provided in Section 2.2, and the emissivity models listed in Table 5.2. are substituted in place of $\varepsilon_{\lambda\mathrm{d},i}(\lambda_{\mathrm{d},i}, T)$ for each model estimate.

Table 5.2. Multi-wavelength emissivity compensation algorithms

Emissivity Model	Mathematical Representation
Model 1	$\varepsilon_{\lambda d} = \exp\left(a_0\lambda_d\right)$
Model 2	$\varepsilon_{\lambda d} = \exp\left(a_0\frac{\lambda_d}{T_{\lambda d}}\right)$
Model 3	$\varepsilon_{\lambda d} = \exp\left(a_0\frac{\sqrt{\lambda_d}}{T_{\lambda d}}\right)$

The inferred temperature obtained as a function of time for both the ratio and multi-wavelength (MW) methods is displayed in Figure 5.6 and Table 5.3 summarizes the performance of the pyrometry methods in terms of the maximum absolute error and the average relative error. The best estimator overall for the soaking period is MW Model 2. Although both methods over-predict the surface temperature, the multi-wavelength method provides a better estimate of the surface temperature in comparison to the ratio method. A similar analysis of the pyrometrically-inferred temperature for TRIP steel heated up to 850°C also showed over-prediction of the true surface temperature [17].

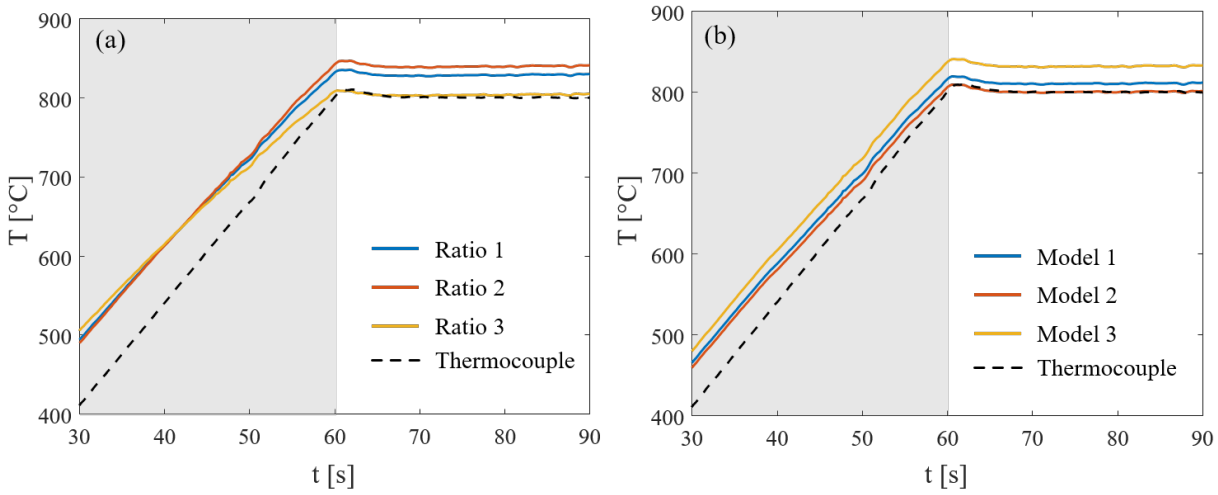


Figure 5.6. Pyrometrically-inferred temperature for (a) ratio pyrometry and (b) multi-wavelength pyrometry.

Table 5.3. Maximum absolute error and average relative error for pyrometry methods

Pyrometry Method	Model	Max Abs. Error Soaking (°C)	Avg. Relative Error Soaking (%)
Ratio	Ratio 1	32.4	3.57
	Ratio 2	42.3	4.86
	Ratio 3	8.5	0.45
Multi-wavelength	Model 1	16.8	1.37
	Model 2	6.3	0.12
	Model 3	37.9	3.99

For the ratio pyrometry methods, the best approximation during the soaking period was obtained for Ratio 3 (2.1 µm/2.4 µm). The greater precision observed for the 2.1 µm and 2.4 µm wavelength combination is most likely due to the proximity of the spectral bands to the region of emissivity consistency. As seen in Figure 5.4 and Figure 5.6 (a), the emissivity at wavelengths longer than 2µm experience the least variation with changing temperature and surface oxide condition. Tsai et al. [69] also noted that among five detection bands centred at 1.8 µm, 2.18 µm,

2.4 µm, 3.5 µm, and 4.5 µm, the bands at 2.18 µm and 2.4 µm produced the most accurate results for ratio pyrometry.

5.2.3. Inferred spectral emissivity from the pyrometry models

The accuracy of the pyrometry algorithm depends on the accuracy of the corresponding emissivity model. Figure 5.7 compares the ε_λ measured by the spectrometer to the values assumed by the ratio pyrometry models, which are obtained by substituting the inferred temperature into Eq. (5.3). The plots show that ratio pyrometry models do not fully capture how ε_λ changes with the evolving surface state. The MW models give a better approximation of ε_λ, as shown in Figure 5.8. For the MW models, the spectral emissivity was obtained by substituting the values of a_0 found by nonlinear regression, i.e., Eq. (5.2), into the emissivity models in Table 5.2. The significant difference between emissivities predicted using Model 2 and Model 3 suggests that the spectral emissivity for DP980 is best described by an exponential of linear first-order function of λ. Model 2 outperforms Model 1 because the former model accounts for the effect of the changing temperature in addition to wavelength.

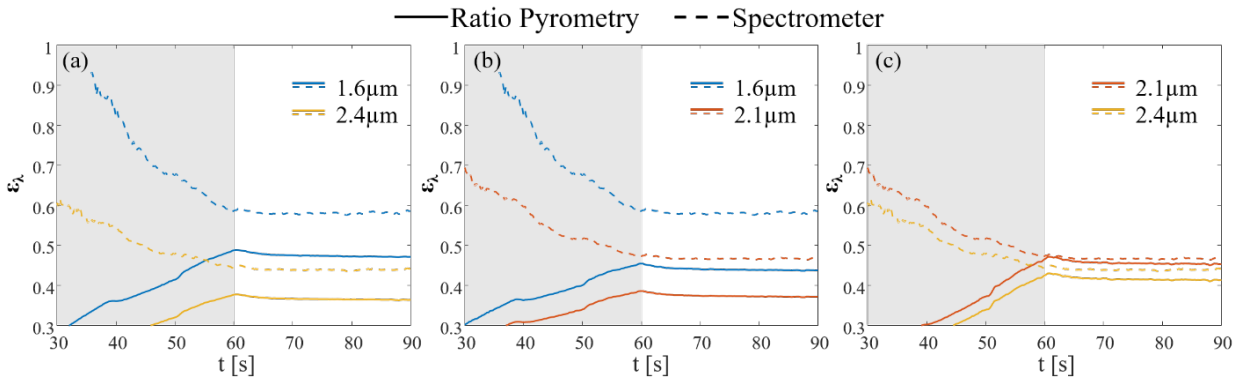


Figure 5.7. Spectral emissivity for ratio pyrometry models compared with experimental data: (a) Ratio 1(1.6µm/2.4µm), (b) Ratio 2 (1.6µm/2.1µm), and (c) Ratio 3 (2.1µm/2.4µm).

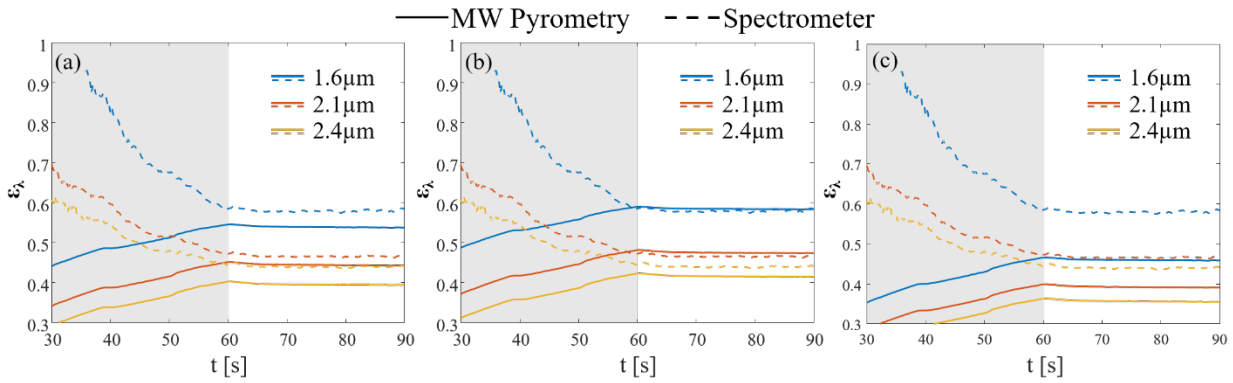


Figure 5.8. Spectral emissivity for multi-wavelength pyrometry models compared with experimental data: (a) Model 1 (b) Model 2, and (c) Model 3.

5.3. Conclusion

This chapter investigated the spectral emissivity for DP980 steel coupons annealed in 95% N_2/5% H_2 at a dew point of −40°C. Time-resolved spectral emissivity measurements are made *in situ* using a near-infrared spectrometer and then compared to values inferred from a multi-wavelength pyrometer and a range of ratio and multi-wavelength pyrometry algorithms. The algorithms are also assessed for their ability to predict the coupon temperature. The spectral emissivity of the steel coupon varies strongly with the formation and dissolution of an oxide layer on the steel surface, especially at wavelengths less than 2μm. The most accurate ratio pyrometry predictions are obtained at the longest measurement wavelengths, 2.1 μm and 2.4 μm. The temperature and emissivity measurements found with the multi-wavelength algorithms are generally superior. These results highlight the fact that accurate pyrometry relies on an accurate emissivity model.

Chapter 6
Bayesian approach to pyrometry of advanced high strength steel[4]

While several deterministic emissivity compensation approaches have been developed to mitigate pyrometer errors caused by uncertain spectral emissivity, none of these methods have yet to accurately capture how the spectral emissivity of automotive AHSS alloys varies with interdependent material properties and processing conditions.

In Chapter 5, we saw that uncertain wavelength-dependent variations in spectral emissivity makes it difficult for emissivity compensation algorithms to truly capture how the spectral emissivity of AHSS varies with the evolving surface state of the steel strip during thermal processing. Additionally, Thiessen et al. [17] showed that using a quotient pyrometer (i.e., dual-spectral/ratio pyrometry method with greybody approximation) on transformation induced plasticity (TRIP) AHSS alloys produced temperature deviations of up to 52 K due to the emissivity fluctuations caused by an oxide layer that forms on the steel surface during annealing. Thermal excursions caused by pyrometry errors may impact the microstructure and mechanical properties of advanced high-strength steels (AHSS) significantly. Mosser et al. [18] showed that, for an annealed dual-phase (DP980) AHSS alloy, temperature deviations of 50 K below the nominal temperature negatively impacted the yield strength of the steel while deviations of 50 K above the nominal temperature compromise the elongation at failure, affecting the ductility of the steel.

All pyrometry algorithms employ some *a priori* knowledge of the spectral emissivity of the target material, which is imperfectly known at best and inevitably leads to significant

[4] The content of this chapter has been published as:

F.K. Suleiman, K. Lin, R. Tsang and K. J. Daun, 2022, "Bayesian approach to pyrometry during intercritical annealing of advanced high strength steel," Meas. Sci. Technol., 33, 115012 (16pp). doi: 10.1088/1361-6501/ac849e.

uncertainties in the inferred temperatures [17, 125-127]. Nevertheless, very few studies have attempted to address this problem in a statistically rigorous manner. Araújo and Martins [128] applied Monte Carlo simulation to evaluate the uncertainty in dual-band pyrometry measurement using the grey surface approximation at ambient temperature by accounting for the uncertainty of the detectors, emissivity of the target surface, background temperature of the surrounding surfaces, and spectral characteristics of the detectors. Saunders [129] used sensitivity coefficients and the ISO-standard [130] propagation of uncertainty to derive analytical expressions for the uncertainty introduced by the dependent and independent calibration points for a three-parameter non-linear pyrometry calibration equation, solved by both exact fitting and least-squares methods.

This chapter proposes a Bayesian framework for estimating the pyrometrically-inferred temperature and, crucially, its associated uncertainties. In this approach, all variables (measurements, calibration coefficients, spectral emissivity, and inferred temperature) are treated as random variables that obey probability density functions (pdfs) related through Bayes' equation. Although Bayesian inference has been used to provide robust temperature estimates for niobium and AISI 52100 alloy steel [131] and other inverse problems and remote sensing applications [132-135], to the best of the author's knowledge, this is the first time that Bayesian inference has been used to carry out pyrometry on AHSS strip temperature for continuous galvanizing. This study starts with the derivation of a pyrometry noise model, followed by a discussion of the Bayesian pyrometry framework that connects the surface temperature to the measured signal. The Bayesian framework includes appropriate prior distributions for the pyrometer calibration constants and, most importantly, the imperfectly known spectral emissivity. The spectral emissivity prior is derived from *ex situ* measurements carried out on steel coupons processed in the McMaster galvanizing simulator (MGS, Iwatani-Surtec). The Bayesian pyrometry model is then applied to *in situ* pyrometry measurement from DP980 coupons processed within the Waterloo Annealing Simulator (WAS). The availability of simultaneous *in situ* thermocouple measurements from the WAS provides a basis for demonstrating the viability of the Bayesian framework to quantify the uncertainty in pyrometrically-inferred temperature.

6.1. Pyrometry noise model

In this thesis, temperature is inferred from pyrometry measurements recorded at three wavelengths: 1.6 μm, 2.1 μm, and 2.4 μm, corresponding to the detection channels for a commercial multi-wavelength pyrometer, a Williamson PRO MWX-ST-17, which is typically used on continuous annealing and galvanizing lines. As per Section 2.2, the modelled pyrometry signal is given by

$$S_\lambda = K_\lambda\left(\lambda_d\right)\cdot\varepsilon_\lambda\left(\lambda_d, T, \theta\right)\cdot I_{\lambda b}\left(\lambda_d, T\right)\Delta\lambda \tag{6.1}$$

where λ_d is the center wavelength, K_λ is the calibration constant that describes the photoelectric efficiency of the detector and detector optics, and $I_{\lambda b}$ is given by Wien's approximation to the Planck distribution in Eq. (2.6).

Although pyrometer measurement noise is not the main source of uncertainty when it comes to the accuracy of the inferred temperature, it is important to consider how stochastic variations in the pyrometer measurements may affect the inferred surface temperature. Given the nonlinearity of the pyrometry measurement model, neglecting the measurement noise would both introduce bias and underestimate the uncertainty in the inferred temperature. Measurement noise from a photoelectric detector comes from two main sources: photon shot noise due to the discrete and random nature of generating free electrons in the detector, which obeys a Poisson distribution; and the electrical and thermal noise produced by the electronics, which is normally distributed. The signal-dependent combination of the photon shot noise and thermal and electric noise is typically described using a Poisson-Gaussian noise model [136-138]:

$$S_\lambda = \overline{S}_\lambda + \delta S_\lambda^{\text{noise}} \approx \overline{S}_\lambda + \delta S_\lambda^{\text{P}} + \delta S_\lambda^{\text{G}} \tag{6.2}$$

where $\overline{S}_\lambda$ is the expected noise-free signal modelled by Eq.(6.1), $\delta S_\lambda{}^{\text{noise}}$ is the total measurement noise, $\delta S_\lambda{}^{\text{P}}$ is the signal-dependent Poisson component, and $\delta S_\lambda{}^{\text{G}}$ describes the signal-independent Gaussian component.

For applications involving a large number of photons and electrons, which is the case here, the Poisson distribution can be modeled as a heteroskedastic Gaussian distribution having a variance equal to expected signal, $\overline{S}_\lambda$ (in counts) [136, 137]:

$$\delta S_\lambda^{\text{P}} \sim \mathcal{N}\left(0, \overline{S}_\lambda\right) \tag{6.3}$$

while the Gaussian noise component is signal-independent and therefore modelled as white noise,

$$\delta S_\lambda^{\text{G}} \sim \mathcal{N}\left(0, \sigma_{\text{G}}^2\right) \tag{6.4}$$

Since both noise components are normally distributed, the total noise affecting pyrometry measurements can also be expressed as a Gaussian distribution. If the pyrometric measurements at any instant are stored in a vector **S**, and assuming that the Gaussian noise affects each channel independently,

$$\mathbf{S}_\lambda \sim \mathcal{N}\left(\overline{\mathbf{S}}_\lambda, \mathbf{\Gamma}_S\right), \quad \mathbf{\Gamma}_S = diag\left(\overline{\mathbf{S}}_\lambda\right) + \sigma_G^2 \mathbf{I} \tag{6.5}$$

For independent measurement channels, the measurement covariance, $\mathbf{\Gamma}_S$, is simply a diagonal matrix of the signal variance, i.e., $\mathbf{\Gamma}_S = \text{diag}([\sigma_{S1}^2, \sigma_{S2}^2, \sigma_{S3}^2])$. Therefore, at each detection wavelength of the pyrometer, the signal variance, σ_{Si}^2, is given by

$$\sigma_{si}^2 = \overline{S}_{\lambda i} + \sigma_G^2 1 \tag{6.6}$$

This linear relationship between the signal variance and the average measured signal corresponds to a pure Poisson-Gaussian noise model [136, 137]. However, the actual measurement noise might differ from a strictly linear model in the presence of shot-to-shot variations [136] or clipping (over- and under-exposure) of the detector [137].

To accurately characterize the measurement noise for the pyrometer device in this thesis, the intensity from a blackbody cavity (Infrared Systems IR-563/301) is measured at temperatures between 350°C and 850°C, in increments of 50°C. A set of 1160 sequential shots is recorded at each temperature. Figure 6.1 shows a plot of the signal variance against the signal mean for all temperatures at the three detection wavelengths. The linear fit approximating the Poisson-Gaussian model in Figure 6.1 does not capture the measurement noise, indicating a highly nonlinear noise pattern. Instead, the noise profile is better described by a sigmoid function,

$$\sigma_{si}^2 = \frac{a}{1 + e^{-b\left(\overline{S}_{\lambda i} - c\right)}} \tag{6.7}$$

in order to better capture the nonlinearities that dominate at the lower and higher signal intensities. The coefficients of the sigmoid noise function at the three detection wavelengths are provided in Table 6.1. Figure 6.1 shows that Eq. (6.7) provides a more accurate model for the measurement noise.

Table 6.1. Coefficient of the sigmoid noise function modelled on the emission from a black body source at 350°C to 850°C.

Coefficient	Wavelength		
	1.6 μm	2.1 μm	2.4 μm
a	3.09×10^{6}	7.75×10^{6}	5.92×10^{6}
b	1.66×10^{-6}	8.55×10^{-7}	9.99×10^{-7}
c	2.63×10^{6}	5.21×10^{6}	4.73×10^{6}

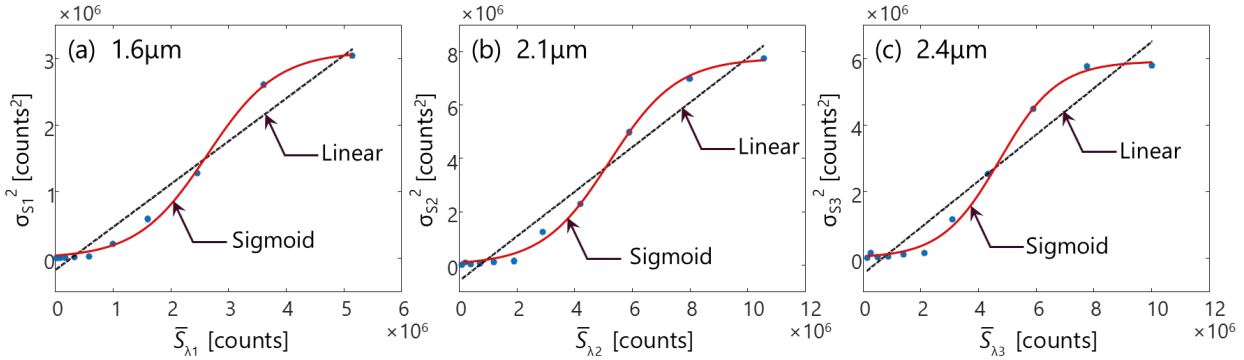


Figure 6.1. Signal variance, σ_{Si}^2, plotted against the mean signal, $\overline{S}_\lambda$ at the three detection wavelengths: (a) 1.6 μm, (a) 2.1 μm, and (c) 2.4 μm. The solid red line corresponds to the sigmoid function while the dashed black line represents the linear fit.

6.2. Bayesian framework

In current industrial practice, temperature is usually inferred from multispectral pyrometric measurements through naïve least-squares regression in which the spectral emissivities and other model parameters are interpreted as deterministic, i.e., having a single "perfectly known" value. The Bayesian framework, on the other hand, treats the quantities-of-interest (QoIs), ancillary model parameters (called nuisance parameters), and measurement data as random variables described by pdfs. In the case of three-wavelength pyrometry, the quantity-of-interest is temperature, T, the data is contained in the measured signal vector, $\mathbf{S} = [S_{\lambda 1}, S_{\lambda 2}, S_{\lambda 3}]^T$, and the nuisance parameters are the spectral emissivities, $\boldsymbol{\varepsilon} = [\varepsilon_{\lambda d1}, \varepsilon_{\lambda d2}, \varepsilon_{\lambda d3}]^T$, and the calibration constants, $\mathbf{K} = [K_{\lambda 1}, K_{\lambda 2}, K_{\lambda 3}]^T$ at the detection wavelengths. For ease of notation, the nuisance parameters are combined into a vector, $\boldsymbol{\varphi} = [\boldsymbol{\varepsilon}; \mathbf{K}]$. The pdfs that govern these variables are related by Bayes' equation

$$p\left(T,\boldsymbol{\varphi}\middle|\mathbf{S}\right)=\frac{p\left(\mathbf{S}\middle|T,\boldsymbol{\varphi}\right)p_{\mathrm{pr}}\left(T,\boldsymbol{\varphi}\right)}{p\left(\mathbf{S}\right)}\propto p\left(\mathbf{S}\middle|T,\boldsymbol{\varphi}\right)p_{\mathrm{pr}}\left(T\right)p_{\mathrm{pr}}\left(\boldsymbol{\varphi}\right) \tag{6.8}$$

where $p(T, \boldsymbol{\varphi}|\mathbf{S})$ is the posterior probability of temperature and the nuisance parameters conditional on the observed pyrometry measurements, $p(\mathbf{S}|T,\boldsymbol{\varphi})$ is the likelihood of observing the measurements given a hypothetical temperature and set of nuisance parameters in the context of the noise model, $p_{\mathrm{pr}}(T)$ and $p_{\mathrm{pr}}(\boldsymbol{\varphi})$ encodes prior knowledge about T and $\boldsymbol{\varphi}$, respectively, and $p(\mathbf{S})$ is the evidence, which scales the numerator of Eq. (6.8) so that the posterior density satisfies the Law of Total Probability. In this case, it is assumed that the priors for the target surface temperature and nuisance parameters are independent, $p_{\mathrm{pr}}(T, \boldsymbol{\varphi}) = p_{\mathrm{pr}}(T)\cdot p_{\mathrm{pr}}(\boldsymbol{\varphi})$. This is tantamount to assuming that the spectral emissivity is independent of temperature, which is not likely to be the case since the spectral emissivity depends on the temperature-dependent bulk electromagnetic properties of the steel. However, since the exact nature of the relationship between temperature and spectral emissivity is unknown, these variables are modeled as independent.

Since the measurement noise is normally-distributed, the likelihood is given by

$$p\left(\mathbf{S}\middle|T,\boldsymbol{\varphi}\right)=\frac{1}{\left[\left(2\pi\right)^{m}\cdot det\left(\boldsymbol{\Gamma}_{S}\right)\right]^{\frac{1}{2}}}\exp\left[-\frac{\left[\mathbf{S}^{\mathrm{meas}}-\mathbf{S}^{\mathrm{mod}}\left(T,\boldsymbol{\varphi}\right)\right]^{T}\mathbf{L}_{S}^{T}\mathbf{L}_{S}\left[\mathbf{S}^{\mathrm{meas}}-\mathbf{S}^{\mathrm{mod}}\left(T,\boldsymbol{\varphi}\right)\right]}{2}\right] \tag{6.9}$$

where $\mathbf{S}^{\mathrm{meas}}$ is a vector of the measured data and $\mathbf{S}^{\mathrm{mod}}(T,\boldsymbol{\varphi})$ is the modeled pyrometer signal expressed by Eq. (6.1), $\mathbf{L}_S = \mathrm{chol}(\boldsymbol{\Gamma}_S^{-1})$, and $m = 3$ represents the number of measurements.

If no information about the temperature or radiative properties is available prior to the measurements, an "uninformative" prior is used [139], and $p(T, \boldsymbol{\varphi}|\mathbf{S}) = p(\mathbf{S}|T,\boldsymbol{\varphi})$ In this case, however, the number of unknowns exceeds the number of measurements, and an infinite set of [T; $\boldsymbol{\varphi}$] exists that can explain the observations equally well. Accordingly, some prior knowledge is required to estimate surface temperature from the pyrometry measurements. Prior distributions are often defined according to the Principle of Maximum Entropy [140], which states that the distributions should maximize information entropy (i.e., minimize information content) subject to constraints of testable information. Accordingly, an uninformed prior is used for T, i.e., $p_{\mathrm{pr}}(T) = 1$, while multivariate normal (MVN) distributions are specified for $\mathbf{K}$ and $\boldsymbol{\varepsilon}$, which are maximum entropy distributions when estimates of the mean and covariance are available.

6.2.1. Sample-based spectral emissivity prior

A sample-based prior for the spectral emissivity is constructed by fitting an MVN distribution to 27 *ex situ* spectrometer measurements carried out on cold-rolled DP980 coupons

$$p_{pr}(\boldsymbol{\varepsilon}) \sim \mathcal{N}(\boldsymbol{\mu}_{\varepsilon}, \boldsymbol{\Gamma}_{\varepsilon}) \tag{6.10}$$

where $\boldsymbol{\mu}_{\varepsilon}$ and $\boldsymbol{\Gamma}_{\varepsilon}$ are the sample mean and sample covariance, respectively. The directional spectral emissivity is inferred from directional-hemispherical spectral reflectance measurements based on Kirchhoff's law. These *ex situ* spectral reflectance measurements were obtained using a Cary 5000 UV-Vis-NIR spectrophotometer (0.25 µm – 2.5 µm) and a Bruker Invenio-R FTIR infrared spectrometer (1.2 µm – 25 µm), both equipped with integrating spheres. Some of the DP980 samples were measured in their as-received state (4 samples), while 15 samples were first annealed up to 800°C using a galvanizing simulator within a 95%/5% N_2/H_2 atmosphere at two dew points, −30°C and 10°C [74, 115]. The remaining samples were quenched at various points (463°C, 704°C and 802°C) in the heating schedule to capture how the surface state may vary with processing temperature [76, 99, 116]. While previous studies (e.g., [77, 141]) have shown that the spectral emissivity varies with annealing atmosphere and processing time, in this work all measurements are grouped into one bucket irrespective of their annealing processing parameters in order to reduce variance and reflect the fact that, in lieu of a specific model that connects the evolving spectral emissivity to the as-received state and process history, combining the measurements amounts to a maximum entropy treatment. More details on the coupon preparation, annealing and emissivity measurement technique can be found in Ref. [74, 76, 99, 115, 116].

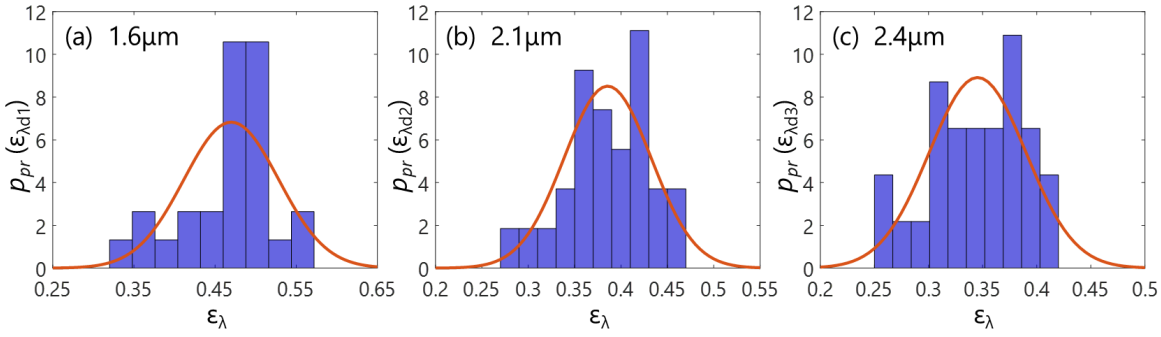


Figure 6.2. Histograms and corresponding normal distribution for the sample-based spectral emissivity priors obtained from *ex situ* measurements for the three detection wavelengths: (a) 1.6 µm; (b) 2.1 µm; and (c) 2.4 µm.

Figure 6.2 shows histograms of emissivity measurements made at the three detection wavelengths, which suggests that the emissivities are normally-distributed; this is confirmed through normal probability plots (NPP) [106] and several other normality tests at 95% confidence interval (5% significance level) [142]. Table 6.2 shows the p-values for ten different normality tests performed on the sample for each of the detection wavelengths. The distribution for 2.1 μm and 2.4 μm passed all the tests with each of the p-values greater than 0.05, while the 1.6 μm distribution failed just two out of the 10 tests. Based on this, the sample mean and covariance for the normally distributed spectral emissivity are

$$\boldsymbol{\mu}_{\varepsilon} = \begin{bmatrix} 0.4700 \\ 0.3856 \\ 0.3453 \end{bmatrix}, \quad \boldsymbol{\Gamma}_{\varepsilon} = \begin{bmatrix} 0.0034 & 0.0026 & 0.0023 \\ 0.0026 & 0.0022 & 0.0021 \\ 0.0023 & 0.0021 & 0.0020 \end{bmatrix} \tag{6.11}$$

The large magnitude of the off-diagonal elements of the covariance matrix, $\boldsymbol{\Gamma}_{\varepsilon}$, relative to the variance, indicates that ε_{λ} is monotonically decreasing with increasing λ, which is supported by electromagnetic theory [54].

Table 6.2. Normality test results for the sample-based spectral emissivity priors at 95% confidence interval.

Normality Test Name	1.6 μm		2.1 μm		2.4 μm	
	p-value	Normality	p-value	Normality	p-value	Normality
KS Test: Limiting form	0.498	✓	0.949	✓	0.909	✓
KS Test: Stephens Method	0.078	✓	0.150	✓	0.150	✓
KS Test: Marsaglia Method	0.452	✓	0.924	✓	0.875	✓
Lilliefors (KS) Test	0.076	✓	0.200	✓	0.200	✓
Anderson-Darling Test	0.026		0.699	✓	0.558	✓
Cramer-Von Mises Test	0.018		0.722	✓	0.583	✓
Shapiro-Wilk Test	0.094	✓	0.677	✓	0.463	✓
Shapiro-Francia Test	0.077	✓	0.636	✓	0.608	✓
Jarque-Bera Test	0.304	✓	0.548	✓	0.519	✓
D'Agostino and Pearson Test	0.167	✓	0.469	✓	0.457	✓

6.2.2. Calibration coefficient prior

Priors for the calibration coefficients are obtained through a calibration procedure using blackbody cavity measurements at temperatures between 350°C and 850°C, in increments of approximately 0.55°C. The pyrometer response is linear to the incident spectral irradiation [52]. In the Bayesian context,

$$p\left(\mathbf{K}\middle|\mathbf{S}_{\mathrm{C}},\mathbf{T}_{\mathrm{C}}\right)\propto p\left(\mathbf{S}_{\mathrm{C}}\middle|\mathbf{K},\mathbf{T}_{\mathrm{C}}\right)\times p_{\mathrm{pr,CAL}}\left(\mathbf{K}\right) \tag{6.12}$$

where $\mathbf{T}_{\mathrm{C}}$ is the vector of the blackbody calibration temperatures, $T_{\mathrm{C},j}$, and $\mathbf{S}_{\mathrm{C}}$ is the vector of pyrometry signals, $S_{\lambda\mathrm{C},j}$, measured at each calibration temperature. The index j labels the blackbody calibration temperature points. The blackbody source has a calibration accuracy of ±0.2°C and a short (long) term stability value of ±0.1°C (±0.2°C). In this work, the blackbody calibration temperatures in $\mathbf{T}_{\mathrm{C}}$ are assumed to be normally distributed about their nominal values with a standard deviation of ±1°C, to account for calibration accuracy, stability, and any additional variations that might be introduced due to imperfect experimental conditions. The covariance matrix for the measurement noise at the three detection wavelengths is $\mathbf{\Gamma}_{\mathrm{SC}} = \mathrm{diag}([\sigma_{\mathrm{SC1}}^2, \sigma_{\mathrm{SC2}}^2, \sigma_{\mathrm{SC3}}^2])$, where the signal variance, $\sigma_{\mathrm{SC}i}^2$, is given by the sigmoid function, Eq. (6.7) and the coefficients in Table 6.1. In the absence of prior knowledge of the calibration coefficients, $p_{\mathrm{pr,CAL}}(\mathbf{K}) = 1$, so $p(\mathbf{K}|\mathbf{S}_{\mathrm{C}},\mathbf{T}_{\mathrm{C}}) = p(\mathbf{S}_{\mathrm{C}},\mathbf{T}_{\mathrm{C}}|\mathbf{K})$. Moreover, due to the linearity of the measurement model $S_{\lambda\mathrm{C}}(T_C) = K_{\lambda} I_{\lambda\mathrm{b}}(T_C)$ it can be shown that both the likelihood and posterior are normally distributed, therefore

$$\mathbf{K}^{\mathrm{MAP}} = \mathbf{K}^{\mathrm{MLE}} = \arg\min_{\mathbf{K}} \left\| \mathbf{L}_{SC}\left[\mathbf{S}_C^{\mathrm{meas}} - \mathbf{S}_C^{\mathrm{mod}}\left(\mathbf{T}_C\right)\right]\right\|^2 = \arg\min_{\mathbf{K}} \left\| \mathbf{L}_{SC}\left[\mathbf{S}_C^{\mathrm{meas}} - \mathbf{K}\cdot\mathbf{B}\right]\right\|^2 \tag{6.13}$$

where $\mathbf{B}$ is a vector of blackbody intensities at the calibration temperature, $B_j = I_{\lambda\mathrm{b}}(T_{\mathrm{C},j})$, and $\mathbf{L}_{\mathrm{SC}} = \mathrm{chol}(\mathbf{\Gamma}_{\mathrm{SC}}^{-1})$ is a weighting matrix derived from the measurement noise covariance.

The uncertainty introduced by the measurement and model parameters is propagated through to the calibration coefficients, $\mathbf{K}$, using a Monte Carlo simulation [139]. Random values for the calibration temperature, $\mathbf{T}_{\mathrm{C}}$, and the calibration measured signal, $\mathbf{S}_{\mathrm{C}}$, are sampled from their prescribed distributions and substituted into the linear measurement model. The corresponding calibration coefficients, $\mathbf{K}$, are then evaluated for each set of random samples. After 50,000

iterations, the resulting calibration coefficient prior is normally distributed as shown in Figure 6.3 and given by $p_{\text{pr}}(\mathbf{K}) \sim \mathcal{N}(\boldsymbol{\mu}_{\text{K}}, \boldsymbol{\Gamma}_{\text{K}})$ where

$$\boldsymbol{\mu}_{\text{K}} = \begin{bmatrix} 2240.97 \\ 2585.24 \\ 2189.59 \end{bmatrix}, \quad \boldsymbol{\Gamma}_{\text{K}} = \begin{bmatrix} 1.3837 & 0 & 0 \\ 0 & 0.8645 & 0 \\ 0 & 0 & 0.4376 \end{bmatrix} \tag{6.14}$$

Comparing $\boldsymbol{\Gamma}_{\varepsilon}$ and $\boldsymbol{\Gamma}_{\text{K}}$ in Eqs. (6.11) and (6.14) respectively, relative to the mean values of their distributions, show that the uncertainty introduced by the calibration constant is small compared to the uncertainty introduced by the spectral emissivity. Additionally, based on the diagonal elements in both $\boldsymbol{\Gamma}_{\varepsilon}$ and $\boldsymbol{\Gamma}_{\text{K}}$, the uncertainty is generally largest at 1.6 μm and appears to decrease with increasing detection wavelength.

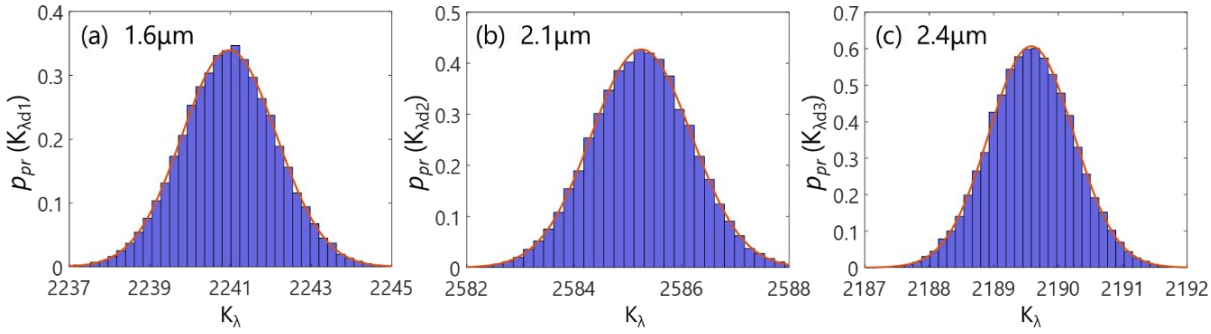


Figure 6.3. Histograms and corresponding normal distribution for the pyrometer calibration coefficient prior at the three detection wavelengths: (a) 1.6 μm; (b) 2.1 μm; and (c) 2.4 μm.

6.2.3. Inferring the temperature

The priors for spectral emissivity and the calibration coefficients can be combined into a single prior for the nuisance parameter vector $\boldsymbol{\varphi}$, $p_{\text{pr}}(\boldsymbol{\varphi}) \sim \mathcal{N}(\boldsymbol{\mu}_{\varphi}, \boldsymbol{\Gamma}_{\varphi})$, where $\boldsymbol{\mu}_{\varphi} = [\boldsymbol{\mu}_{\varepsilon}; \boldsymbol{\mu}_{\text{K}}]$ and $\boldsymbol{\Gamma}_{\varphi}$ is a block-diagonal combination of $\boldsymbol{\Gamma}_{\varepsilon}$ and $\boldsymbol{\Gamma}_{\text{K}}$

$$\boldsymbol{\Gamma}_{\varphi} = \begin{bmatrix} \boldsymbol{\Gamma}_{\varepsilon} & \mathbf{0} \\ \mathbf{0} & \boldsymbol{\Gamma}_{\text{K}} \end{bmatrix} \tag{6.15}$$

The maximum *a posteriori* (MAP) estimate for T and $\boldsymbol{\varphi}$ is found by maximizing Eq. (6.8), which is equivalent to

$$(T, \boldsymbol{\varphi})_{\text{MAP}} = \arg\max_{T,\boldsymbol{\varphi}} p(T, \boldsymbol{\varphi} | \mathbf{S}) = \arg\min_{T,\boldsymbol{\varphi}} \left\{ \left\| \mathbf{L}_{\text{S}} \left[\mathbf{S}^{\text{meas}} - \mathbf{S}^{\text{mod}}(T, \boldsymbol{\varphi}) \right] \right\|^2 + \left\| \mathbf{L}_{\varphi} \left[\boldsymbol{\varphi} - \boldsymbol{\mu}_{\varphi} \right] \right\|^2 \right\} \tag{6.16}$$

where the matrices $\mathbf{L}_S = \text{chol}(\mathbf{\Gamma}_S^{-1})$ and $\mathbf{L}_\varphi = \text{chol}(\mathbf{\Gamma}_\varphi^{-1})$ weigh the influences of the data in $\mathbf{S}$ and the prior estimate $\boldsymbol{\mu}_\varphi$ by their respective covariances/uncertainties. Equation (6.16) provides a point-estimate of T and $\boldsymbol{\varphi}$, but a key advantage of the Bayesian approach is that the uncertainties of these variables are reflected directly by the posterior pdf. Often the posterior can be modeled as normally distributed about the MAP estimate, in which case

$$\mathbf{\Gamma}_{POST} = \left\{ \begin{bmatrix} \mathbf{L}_S\mathbf{J}_T & \mathbf{L}_S\mathbf{J}_\varepsilon & \mathbf{L}_S\mathbf{J}_K \\ 0 & \mathbf{L}_\varepsilon & 0 \\ 0 & 0 & \mathbf{L}_K \end{bmatrix}^T \begin{bmatrix} \mathbf{L}_S\mathbf{J}_T & \mathbf{L}_S\mathbf{J}_\varepsilon & \mathbf{L}_S\mathbf{J}_K \\ 0 & \mathbf{L}_\varepsilon & 0 \\ 0 & 0 & \mathbf{L}_K \end{bmatrix} \right\}^{-1} \tag{6.17}$$

where $\mathbf{J}_T = (\partial S_{\lambda 1}/\partial T,\ \partial S_{\lambda 2}/\partial T,\ \partial S_{\lambda 3}/\partial T]^T$, $\mathbf{J}_\varepsilon = \text{diag}((\partial S_{\lambda 1}/\partial \varepsilon_{\lambda 1},\ \partial S_{\lambda 2}/\partial \varepsilon_{\lambda 2},\ \partial S_{\lambda 3}/\partial \varepsilon_{\lambda 3}])$ and $\mathbf{J}_K = \text{diag}((\partial S_{\lambda 1}/\partial K_{\lambda 1},\ \partial S_{\lambda 2}/\partial K_{\lambda 2},\ \partial S_{\lambda 3}/\partial K_{\lambda 3}])$, all evaluated at the MAP estimate. Finally, the univariate posterior probability density for temperature is found by marginalizing out the nuisance parameters

$$p\left(T|\mathbf{S}\right) = \int_{-\infty}^{\infty} p\left(T, \boldsymbol{\varphi}|\mathbf{S}\right) d\boldsymbol{\varphi} \tag{6.18}$$

Following the MVN approximation, $p(T|\mathbf{S})$ is simply a normal distribution centered at T_{MAP} with a variance equal to the corresponding diagonal term in $\mathbf{\Gamma}_{POST}$.

6.3. Pyrometer and *in situ* measurements

The Bayesian analysis is carried out on the same *in situ* pyrometry measurements presented in Section 5.2.1. The raw measured pyrometer signals, $\boldsymbol{S}_\lambda$, are shown in Figure 6.4 (a) alongside the thermocouple-measured temperature. The noise on the thermocouple measurement is assigned a normal distribution with a standard deviation equal to ± 0.75% of the nominal temperature values. The *in situ* normal spectral emissivities, shown in Figure 6.4 (b), is calculated from the intensity measured by the NIR spectrometer, according to $\varepsilon_\lambda = I_\lambda(T_T)/I_{\lambda b}(T_T)$, where $I_{\lambda b}$ is the blackbody intensity at the thermocouple temperature, T_T, for each time step. The spectrometer measurements and the resulting emissivity are subject to a similar uncertainty estimation procedure as described above for the pyrometer. A more detailed description of the uncertainty estimates for the *in situ* measurements are provided in the Appendix of Ref. [143]. The emissivity values calculated from the spectrometer are considered to be a more accurate representation of the spectral emissivity since they are obtained with a thermocouple reading and a perfect emitter (ε_λ for the blackbody

source is greater than 0.99), as opposed to being inferred simultaneously with the temperature in the case of a pyrometrically-inferred emissivity.

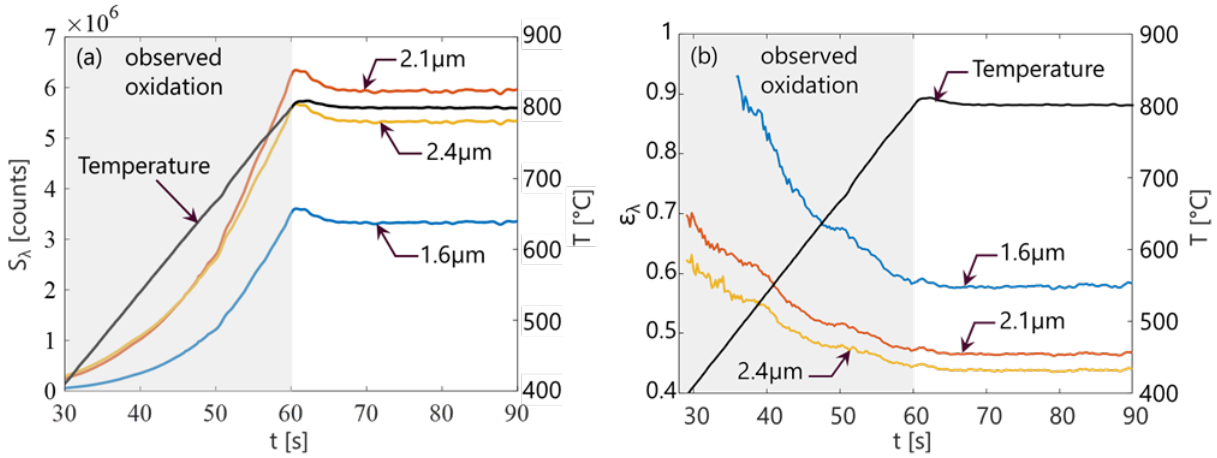


Figure 6.4. *In situ* measurements with the associated thermocouple reading. (a) Pyrometer count measurement for the three detection wavelengths, and (b) *In situ* spectral emissivities obtained using the NIR spectrometer.

Figure 6.4 (b) shows that the spectral emissivity decreases with increasing wavelength. This is expected for metals over the infrared spectrum. As discussed in Chapter 5, the higher emissivity values recorded between 400°C and 600°C is attributed to the visible oxide layer on the steel surface, as shown in Figure 5.3. The changes in oxide species and surface topography caused by the evolving oxide layer produce wavelength-dependent variation in the spectral emissivity. The shorter wavelengths (< 2μm) are more impacted by the presence of an oxide layer compared to the longer wavelengths, due to constructive and destructive interferences of thermal radiation between the oxide film and the metal substrate [100]. Once the surface oxide dissolves, the spectral emissivity remains stable as the steel reaches 800°C, and the values of ε_λ at the beginning and end of the soak period are indistinguishable.

6.4. Quantifying uncertainty in pyrometrically-inferred parameters

The main objective of this chapter is to recover the steady-state hold temperature at approximately 800°C, at which point the oxide layer that formed during the heat-up phase has been reduced entirely. The pyrometer count recorded at each time step, shown in Figure 6.4, is assumed to be the average signal, and the corresponding variance is estimated using the approximate noise model in Eq. (6.7) and the coefficients in Table 6.1.

The maximum *a posteriori* estimate, $(T, \boldsymbol{\varphi})_{MAP}$, and covariance matrix, Γ_{POST}, are determined from Eqs. (6.16) and (6.17), respectively. The marginalized posterior distribution for the temperature and spectral emissivities at 800°C during the hold period are shown in Figure 6.5 and Table 6.3. Marginalized posterior densities are also summarized by 95% credibility intervals as shown in Figure 6.5. The 95% credibility interval can be interpreted as the range of values containing the "correct" answer with 95% probability. Also shown is the temperature measured by the thermocouple and the spectral emissivities inferred from the NIR spectrometer measurement, with their corresponding 95% credibility interval (two standard deviations of the mean).

The MAP estimate and the associated credibility interval highlights the advantage of the Bayesian framework: the ability to provide a measure of the expected error in the pyrometrically-derived temperature based on the uncertainties introduced by the imperfectly known spectral emissivity, measurement noise, and other nuisance parameters.

Table 6.3. MAP estimate, *in situ* estimate and their 95% credibility intervals for the temperature and spectral emissivities at 800°C (specifically the results corresponding to the measurements at the 90s).

	In situ estimate ± 2σ	MAP estimate	Uncertainty (2σ)	Credibility interval
T [°C]	799.6 ± 11.99	820.8	27.9	(792.9, 848.7)
$\varepsilon_{\lambda d1}$ (1.6 μm)	0.59 ± 0.062	0.52	0.109	(0.409, 0.626)
$\varepsilon_{\lambda d2}$ (2.1 μm)	0.49 ± 0.041	0.44	0.070	(0.368, 0.508)
$\varepsilon_{\lambda d3}$ (2.4 μm)	0.45 ± 0.035	0.41	0.058	(0.356, 0.471)

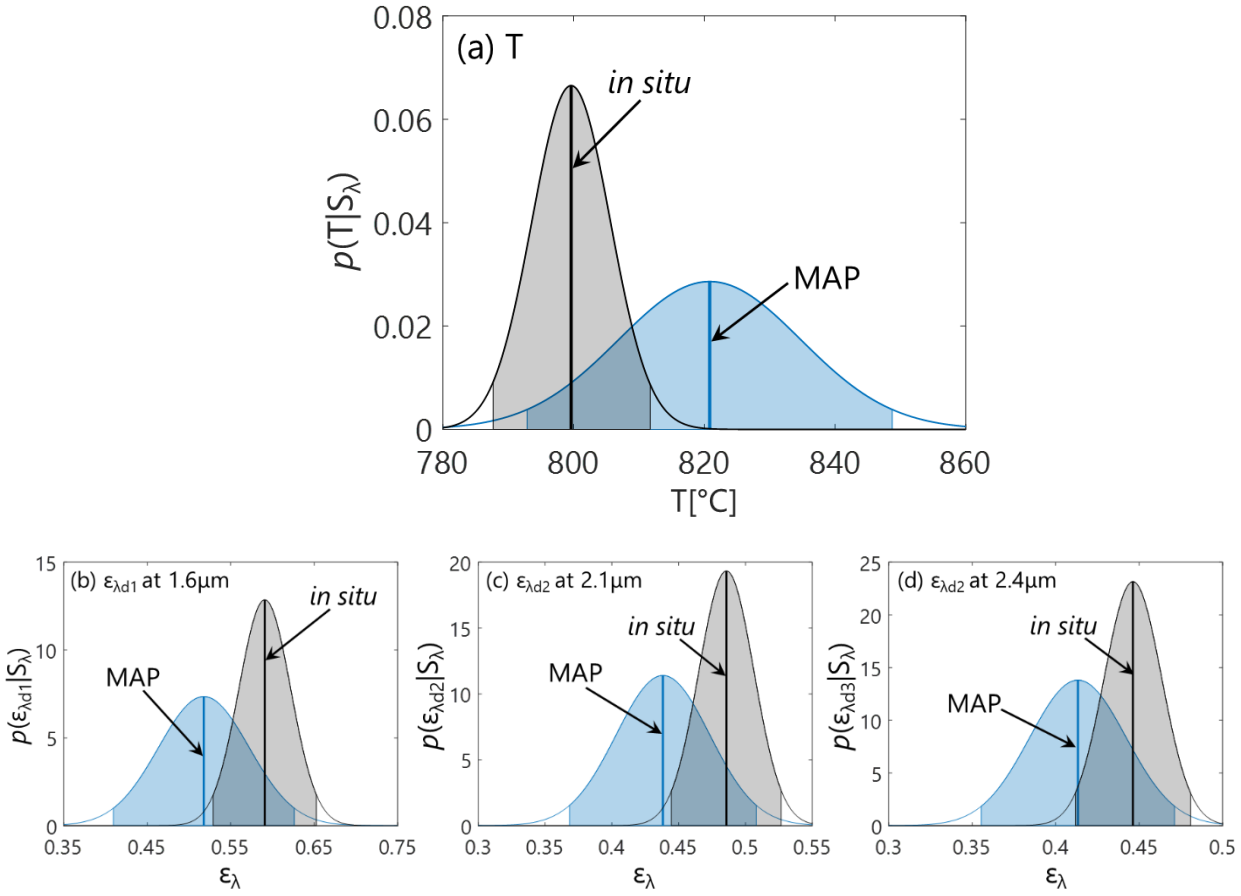


Figure 6.5. Marginalized posterior probability distributions for the hold period (800°C): (a) temperature; (b) $\varepsilon_{\lambda d1}$ at 1.6 μm; (c) $\varepsilon_{\lambda d2}$ at 2.1 μm; and (d) $\varepsilon_{\lambda d3}$ at 2.4 μm. The blue curves are the maximum *a posteriori* (MAP) distributions. The black curves indicate the *in situ* thermocouple (temperature) and NIR spectrometer (emissivity) measurement distributions. The solid lines are the mean values, and the shaded regions are 95% credibility intervals corresponding to two standard deviations of the mean.

While the posterior distribution for the pyrometrically-inferred temperature in Figure 6.5 (a) contains a significant amount of *in situ* thermocouple estimate distribution, the MAP estimate lies at the tail end of the *in situ* distribution and is not within the 95% credibility interval. Similarly, Figure 6.5 (b) – (d) shows that the *in situ* spectrometer measurements are also found towards the edge of the *in situ* spectral emissivity distributions at the three detection wavelengths. Except for the emissivity predictions at 2.4 μm, none of the nominal MAP estimates are within the 95% credibility bounds of the *in situ* measurements. This overall trend of MAP estimates being far from the *in situ* mean values is most likely due to the imperfect information content of the emissivity

prior distributions, and the limited relevance of these room-temperature measurements to the spectral emissivity of the steel at high temperature.

Further insights are found by comparing the *in situ* spectrometer measurements with the spectral emissivity priors derived from *ex situ* measurements. Figure 6.6 shows that the *in situ* spectral emissivity measurement lies at the tail of the prior distribution, outside the credibility bounds for all three detection wavelengths; consequently, the resulting posterior densities underestimates the uncertainty in the recovered parameters. The discrepancy between the prior derived from *ex situ* emissivity measurements and the *in situ* measurement could be due to a number of factors. First, the sample size used to construct the prior pdf was small (27 samples) and may not be sufficient to represent the true population. Second, *ex situ* measurements are taken at room temperature, which do not capture temperature-dependent variations in the spectral emissivity [99, 116].

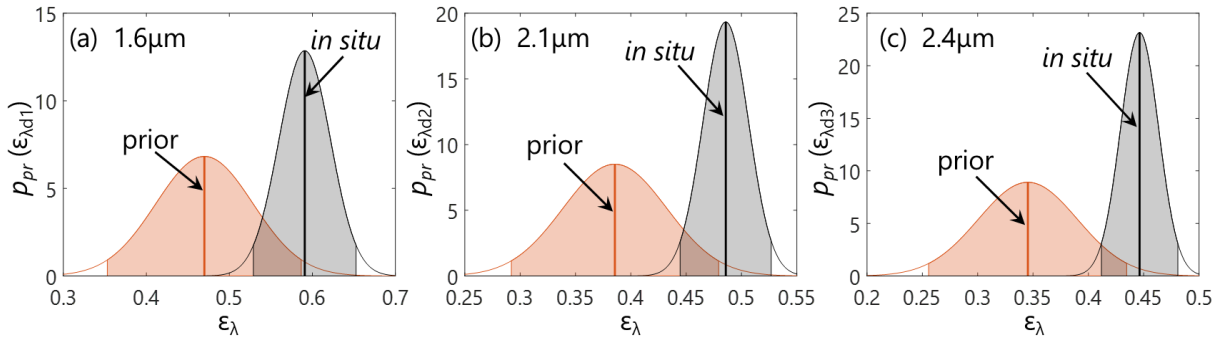


Figure 6.6. Plot of the prior and *in situ* densities for the spectral emissivities at the detection wavelengths (a) $\varepsilon_{\lambda d1}$ at 1.6 µm; (b) $\varepsilon_{\lambda d2}$ at 2.1 µm; and (c) $\varepsilon_{\lambda d3}$ at 2.4 µm. The red curves are the maximum *a posteriori* (MAP) distributions. The black curves represent the NIR spectrometer (emissivity) measurement distributions. The solid lines indicate the distribution mean and the 95% credibility intervals (shaded area) are equivalent to two standard deviations of the mean.

6.5. Comparing the Bayesian approach with a multi-wavelength model

As introduced in Sections 2.2.1.3, the typical emissivity models used for multi-wavelength (MW) pyrometry predictions are mathematical functions derived by empirical or theoretical analysis to model how the spectral emissivity varies with one or more underlying parameters (e.g., wavelength, temperature, surface roughness) [10, 144]. To evaluate the efficacy of the Bayesian approach, this section compares the predictions from a typical emissivity model against the estimated posterior distribution.

The MW emissivity model used for this comparison is a multivariate bilinear function derived from *ex situ* emissivity measurements on annealed DP980 alloys using the factorial design-of-experiments as detailed in Chapter 3, i.e.,

$$\begin{aligned}\hat{\varepsilon}_\lambda = {} & \beta_0 + \beta_1 A + \beta_2 B + \beta_3 C + \beta_4 D + \beta_{12} AB + \beta_{13} AC + \beta_{14} AD \\ & + \beta_{23} BC + \beta_{24} BD + \beta_{34} CD + \beta_{123} ABC + \beta_{124} ABD \\ & + \beta_{134} ACD + \beta_{234} BCD + \beta_{1234} ABCD\end{aligned} \tag{6.19}$$

The measurements used to derive this empirical model are included in the dataset used to calculate the Gaussian prior probabilities, Eq. (6.11). The empirical MW model in Eq. (6.19) expresses the spectral emissivity as a parametric function of four variables: dew point (A), Si/Mn ratio (B), pre-annealed surface RMS roughness (C), and wavelength (D). The model coefficients, β_0, β_i, β_{ij}, and β_{ijk}, are provided in Table 3.8. This MW model is designed to predict the spectral emissivity of DP980 alloys for dew points between −30°C and 10°C, Si/Mn ratios between 0.04 and 0.23, surface roughness, R_q between 0.15 μm and 0.65 μm, and wavelengths between 1.6 μm and 2.4 μm. The detailed description of this multivariate linear model is provided in Chapter 3. The material properties and annealing process parameters for the experimental setup described in Section 4 meet the MW model requirements with exception of the inlet dew point. Therefore, for this analysis, the dew point factor, A, is set to −30°C, to accommodate the model requirements while accounting for the effect of oxygen infiltration on the final annealing atmosphere conditions within the chamber.

Figure 6.7 illustrates how the pyrometrically-inferred temperature and spectral emissivities vary with respect to annealing time for both the Bayesian approach and the MW emissivity model. The 95% credibility intervals corresponding to two standard deviations for both the MAP estimate and *in situ* estimates are shown on each plot. Both the MAP estimate and the MW model over-predict the steel temperature in Figure 6.7 (a), as a result of the under-predicted spectral emissivity shown in Figure 6.7 (b) – (d). However, the MAP estimates are slightly closer to the nominal *in situ* thermocouple and spectrometer measurements, especially for the soak period where the steel surface is free of the visible oxide layer. It is important to also note that the MW estimate is not contained within the credibility bounds of the *in situ* thermocouple estimate. This comparison shows that given a set of *ex situ* measurements from which an empirical emissivity model is desired, describing the emissivity stochastically using a prior pdf, instead of a deterministic

function, can improve the quality of the pyrometry estimates. Overall, the superiority of the Bayesian approach lies in the ability to simultaneously estimate the expected uncertainty alongside the QoI at each time step.

In Figure 6.7 (a), during the first 60 seconds when the surface oxide evolves as the sample is being heated, the width of the credibility interval on the inferred-temperature increases with annealing time, even though the surface properties become more stable as the oxide layer dissolves. Although this trend might be seemingly categorized as temperature-dependent since the intensity measured by the pyrometer increases with temperature, this effect could also be a result of the amplification of statistical uncertainties and model errors involved with any mathematical model where the true underlying physics is unknown.

Additionally, the temporal response of the spectral emissivity posterior estimates in Figure 6.7 (b)-(d) shows that the density estimates for the spectral emissivity at 1.6 μm has the greatest uncertainty in terms of the wider credibility interval. This is most likely because the prior distribution for 1.6 μm is wider than the other wavelengths (Figure 6.2 and Figure 6.6), which means that the information contained in the 1.6 μm prior has the least influence on the posterior densities. A wider prior distribution indicates that there is less information available about that parameter, which increases the width of the posterior pdf and the associated uncertainty in quantities-of-interest.

Figure 6.7 also shows that the credibility interval on the pyrometrically-inferred temperature and spectral emissivities do not capture the nominal *in situ* thermocouple and spectrometer measurements for the heating ramp period (first 60 seconds), indicating that the specified prior distribution does not contain sufficient information about the expected emissivity variation in the presence of the oxide layer induced by oxygen infiltration in the annealing simulator. This is because none of the measurements that make up the prior distribution were collected under similar processing conditions. This emphasizes the importance of developing a statistically robust and relevant spectral emissivity prior that includes measurements made on the similar samples as the intended application, which in this case would be to include measurements on oxidized steel samples.

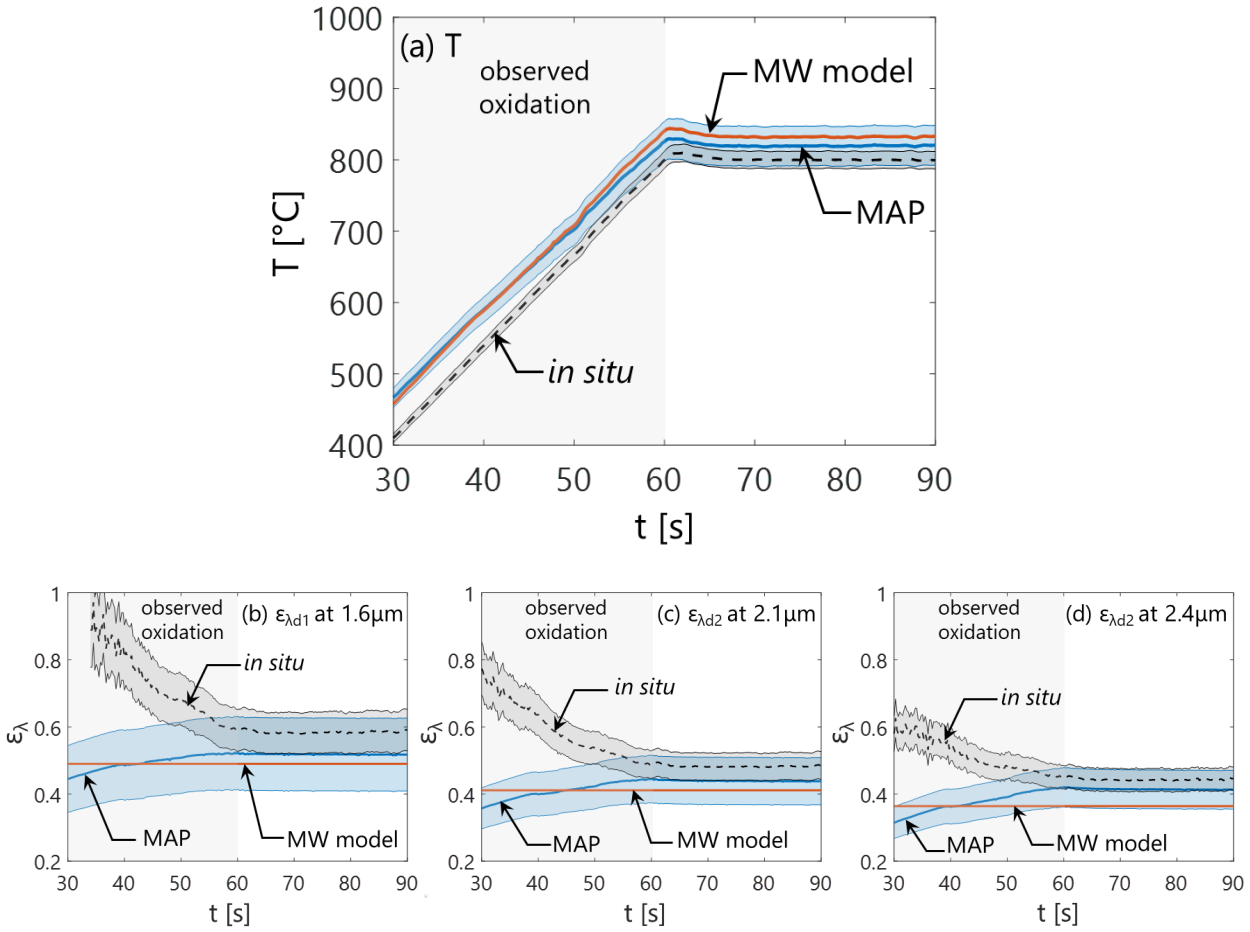


Figure 6.7. MW estimates (solid red lines), MAP estimates (solid blue lines), i*n situ* estimates (dashed lines) and 95% credibility intervals for the parameters: (a) *T*, (b) $\varepsilon_{\lambda d1}$ at 1.6 μm, (c) $\varepsilon_{\lambda d2}$ at 2.1 μm, and (d) $\varepsilon_{\lambda d3}$ at 2.4 μm. The shaded areas represent 95% credibility bounds corresponding to two standard deviations of the mean or nominal values.

6.6. Conclusions

This chapter presents a Bayesian framework for quantifying the uncertainties associated with the pyrometrically-inferred temperature estimates made using a three-channel pyrometer. The analysis accounts for measurement noise, uncertainties introduced by the calibration process, as well as uncertain spectral emissivity, which varies with alloy content and processing conditions in an uncertain way. A sample-based spectral emissivity prior was constructed using *ex situ* emissivity measurements from as-received and annealed DP980 coupons processed under a range of conditions. The prior distribution for the calibration constant described the uncertainty associated with the measurement noise present during the calibration process. The uncertainty introduced by the calibration constant prior was small, especially compared with the uncertainty in the spectral emissivity prior.

The Bayesian methodology was then applied to pyrometry signals obtained from heating DP980 coupons in an annealing simulator with a reducing atmosphere. The maximum *a posteriori* (MAP) estimate and the 95% credibility intervals are obtained for the temperature and spectral emissivities. The width of the credibility bounds on the temperature estimate increases with increasing signal intensities possibly due to the amplification of statistical uncertainties.

Finally, the Bayesian posterior pdfs for temperature are compared against point estimates obtained using a multi-wavelength emissivity function created from the same dataset as the Gaussian emissivity prior. The results clearly highlight the benefits of estimating a posterior distribution instead of a point estimate, since the former provides a measure of uncertainty that can be compared directly with predefined temperature tolerances for the mechanical properties of AHSS during intercritical annealing.

Chapter 7
Effect of dew point on the evolving radiative properties[5]

Compared to other non-ferrous metals and alloys, little is known about the *in situ* radiative properties of AHSS and how it changes with temperature and other process parameters, such as dew point and annealing schedule, especially over the near-infrared wavelengths used for pyrometry. This is especially important because AHSS include less noble alloying elements (e.g., Mn, Si, Cr, and Al) that form stable oxides on the steel surface depending on the atmospheric dew point (DP) [78], which also influence emissivity in a wavelength-dependent manner. The interdependent effect of these factors combined with non-uniform radiative properties across the length and width of the incoming pre-annealed cold-rolled coil [4, 5] limit the accuracy of pyrometric temperature estimates.

Recent experimental and theoretical studies on dual-phase DP780 and DP980 alloys [74, 75, 79, 89], including Chapter 3 of this thesis, have established that the spectral emissivity of these alloys varies with the combined effects of wavelength, dew point, alloy-composition (especially the silicon-to-manganese ratio), and surface roughness. The spectral emissivity at the shorter pyrometry wavelengths (≤ 2.5 μm) is influenced strongly by an oxide layer on the surface, which in turn depends on how the alloying elements interact with the annealing atmosphere. Most of these comparative studies focused on *ex situ* characterization rather than *in situ* time-resolved measurements, which does not fully explain how the radiative properties evolve with temperature during intercritical annealing.

---

[5] The content of this chapter has been published as:

F.K. Suleiman, N.S. Narayanan, and K. J. Daun, 2024, "Effect of dewpoint on the evolving radiative properties of advanced high-strength steel during intercritical annealing," AIST Transactions, Iron & Steel Technology, 21 (10) pp. 218-229. doi:10.33313/TR/0924.

In response to this knowledge gap, this chapter investigates *in situ* spectral emissivity measurements of cold-rolled dual-phase (DP980) AHSS alloy over near-infrared pyrometry wavelengths (1.2 μm – 2.5 μm) as it is processed in a 95%/5% vol. N_2/H_2 atmosphere with dew points (DPs) of −30°C, −10°C, and +10°C. Crucially, this chapter examines how the variation in spectral emissivity impacts the pyrometrically-inferred temperature and how a stochastic emissivity prior constructed from *ex situ* temperature-dependent spectral emissivity measurements can be used to provide robust pyrometry estimates on AHSS.

7.1. Experimental and measurement procedure

In this chapter, the 152.4 mm × 25.4 mm ×1.5 mm cold-rolled DP980 alloy (Si/Mn = 0.04) samples were annealed in a vacuum-grade thermal processing chamber described in Section 4.3 and shown in Figure 4.7. The sample preparation process and the heating schedule described in Chapter 5 and Chapter 6 were maintained for this analysis. However, due to the vacuum-based nature of this apparatus, the chamber is first pumped down and back-filled with nitrogen (≤ 5 ppm O_2) followed by a continuous purge with 95% N_2-5% H_2 (≤2 ppm O_2, certified ultra-high purity) at the desired dew point for at least 20 minutes before heating begins.

While the radiation emitted from the heated sample can be measured simultaneously with a Williamson multi-wavelength pyrometer and an OceanOptics NIRQuest512 spectrometer, this chapter uses data solely from the spectrometer, and the pyrometrically-inferred temperature will be derived from the spectrometer irradiance measurements.

7.2. Results and discussion

Three samples were annealed at the following target dew points: −30°C (243 K), −10°C (263 K), and +10°C (283 K). Comparing the spectroscopic measurements from these samples elucidates how atmospheric moisture content/oxidizing potential impacts spectral emissivity. Table 7.1 lists the actual DP and O_2 concentration values measured at the start of the experiment. The annealing atmosphere contained less than 10^{-20} ppm O_2 for all experiments, which indicates the absence of oxygen infiltration or leaks. Therefore, the overall oxidation potential of the annealing atmosphere is defined by the measured dew point of the 95%N_2-5%H_2 gas in the chamber.

Prior to annealing in the simulator, the as-received spectral emissivity of each coupon was characterized at room temperature with a Bruker Invenio X FTIR spectrometer and a 562-G integrating sphere attachment. The nearly identical emittance spectra of the as-received steel in

Figure 7.1(a) indicates that the coupons all share a similar pre-annealed surface state. Figure 7.1(b) shows the thermocouple measurements for the samples confirming that all samples were annealed with the same heating schedule. Due to the sample length (152.4 mm) and the size restriction of the FTIR sample compartment, the pre-annealed radiative properties were characterized with the rolling direction perpendicular to the incoming light within the integrating sphere. Having the rolling direction perpendicular to the incident radiation increases the measurement uncertainty due to port losses [145]. For this DP980 AHSS steel, the perpendicular orientation was found to overestimate the emissivity of the steel by 5%. However, since the measurement orientation is consistent across all the samples and the pre-annealed values are only used for comparative analysis, this additional uncertainty does not influence the results and discussion in this thesis.

Table 7.1. Dew point (DP) and oxygen concentration (O_2) of the annealing atmospheres.

Target DP (°C)	Actual DP (°C)	O_2 Concentration (ppm)
−30	−30.68	$< 5 \times 10^{-21}$
−10	−9.59	$< 5 \times 10^{-21}$
+10	+10.16	3.17×10^{-20}

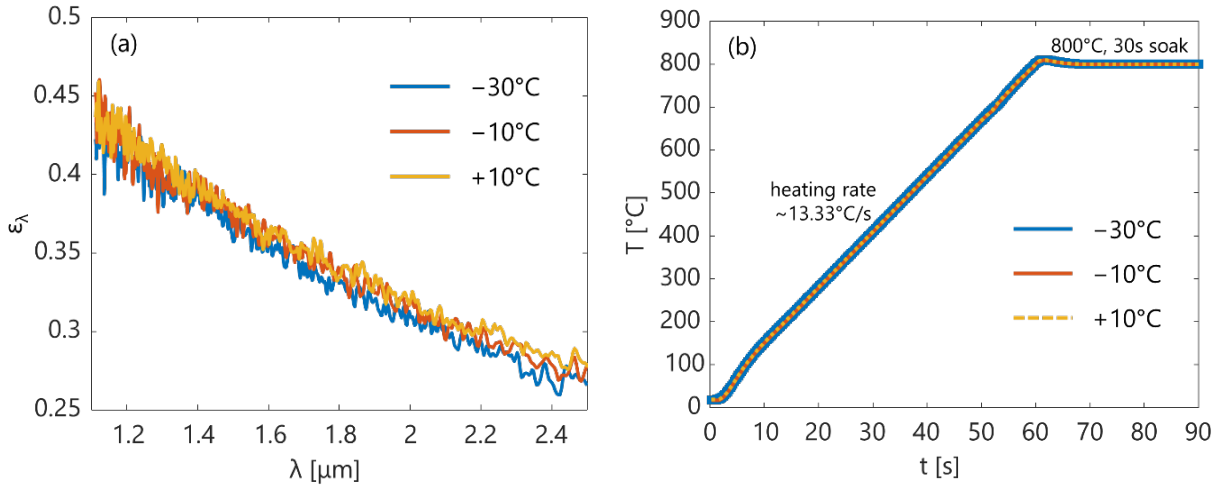


Figure 7.1. (a) Pre-annealed spectral emissivity, ε_λ, for the DP980 coupons. (b) Temperature measurements from the thermocouple attached to the samples during annealing.

7.2.1. *In situ* time-resolved spectral emissivity measurement

The *in situ* normal spectral emissivity, ε_λ, is inferred from the NIR spectrometer measurements such that, $\varepsilon_\lambda(\lambda, T) = I_\lambda(\lambda, T)/ I_{\lambda b}(\lambda, T)$, where λ is the measurement wavelength; T is the sample temperature given by the thermocouple; I_λ is the spectral intensity recorded with the spectrometer; and $I_{\lambda b}$ is the blackbody spectral intensity at the sample temperature. Figure 7.2 and Figure 7.3 show the spectral emissivity of the DP980 coupons for wavelengths between 1.2 μm – 2.5 μm and temperatures ranging from 400°C – 800°C. The contour plots in Figure 7.2 provide an overview of the relationships between emissivity, dew point, wavelength, temperature, and heating time. As expected for metallic surfaces in the infrared region, emissivity decreases monotonically with increasing wavelength [54], irrespective of the annealing dew point or temperature. This trend is expected based on the electromagnetic theory of bulk metals. Also, as the wavelength increases, the surface becomes optically smoother based on the ratio of surface RMS roughness to wavelength ($\sigma/\lambda \ll 1$) and thus the surface topographical effects on the spectral emissivity decrease with increasing wavelength.

Generally, the spectral emissivity increases with increasing dew point, especially at wavelengths below 2 μm. Figure 7.2 (d) – (f) show that the emissivity at the longest pyrometer wavelength (2.4 μm) varied the least despite the 40°C increase in dew point between −30°C and +10°C. Comparatively, the emissivity at the shorter wavelengths (< 2 μm) is more sensitive to the varying DP, with the most pronounced increase observed at 1.2 μm. This variation is a consequence of the dielectric properties of the oxide layer that forms on the surface of the steel due to the increased oxidizing potential of the process atmosphere. The presence of a metallic oxide, be it as a continuous film or as nodules, modifies the surface state in a way that impacts the spectral emissivity [72, 74, 75]. At shorter wavelengths, the oxide layer thickness is comparable to the detection wavelength, leading to thin-film interference effects. However, as the wavelength increases, the emissivity is more influenced by the overall surface roughness, which does not change significantly with the change in dew point [74, 75].

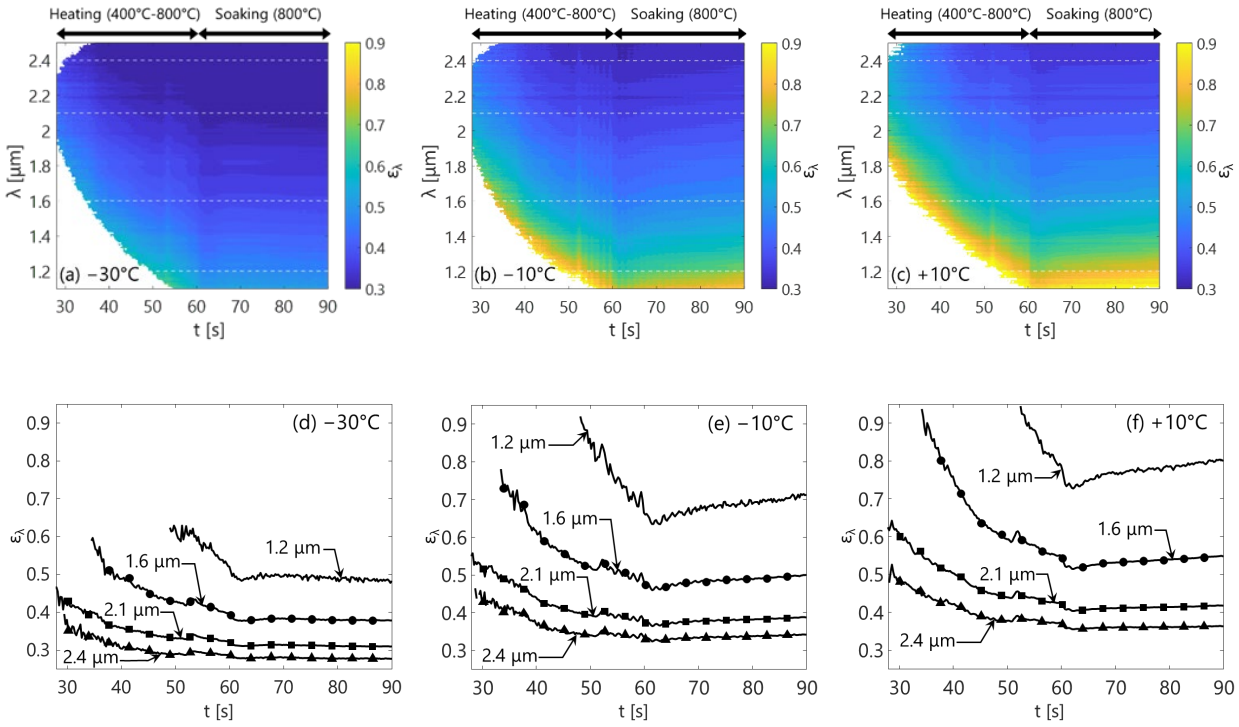


Figure 7.2. Measured time-resolved spectral emissivity, ε_λ, for the target DPs: −30°C (a, d), −10°C (b, e), and +10°C (c, f). The white horizontal lines shown in (a) – (c) correspond to the wavelengths (1.2 μm, 1.6 μm, 2.1 μm, and 2.4 μm) plotted in (d) – (f).

Figure 7.3 shows how the time-resolved spectral emissivity evolves with annealing temperature and time compared to the pre-annealed surface state. The pre-annealed spectral emissivity in Figure 7.3 (a) – (f) represents the average of the three spectra shown in Figure 7.1 (a). Changes in spectral emissivity are linked to the interdependent effects of dew point and temperature on metal oxidation. Figure 7.3 (a) shows that the resulting oxide topography, irrespective of DP, influences the rate at which the spectral emissivity changes with wavelength, as evident from the drastic change in the slope compared to the pre-annealed state.

Based on the oxygen potential diagram in Figure 2.6 and Ref. [74], all three dew points (−30°C, −10°C and +10°C) favor the segregation and selective oxidation of Si, Mn, and Cr from the bulk metal. However, the degree of internal/external selective oxidation as well as the properties of the resulting oxide layer depend on the thermodynamics and kinetics of the oxidation reaction [78, 146]. Therefore, as the samples heat up from their pre-annealed state to 400°C, the sample processed at higher oxygen partial pressure (i.e., +10°C dew point) undergo significant

internal and external oxidation, which would increase the spectral emissivity. Consequently, the change in emissivity is reduced with the reducing oxygen partial pressure at the lower dew points (−10°C and −30°C) due to the formation of a thinner external oxide film.

Figure 7.3 (b) – (g) show that, beyond 400°C, spectral emissivity decreases with increasing temperature at all three dew points. As discussed in previous chapter, one reason for the inverse relationship between emissivity and temperature is the "crossover wavelength" or "X-point" phenomenon exhibited by metals at shorter wavelengths [54, 71]. In addition, the spectral emissivity of some metallic oxides and dielectric materials has been shown to decrease with increasing temperature [101, 112, 147]. Given that spectral emissivity is a surface property, the properties of the selective oxides forming on the steel surface during annealing will influence the spectral emissivity of these DP980 coupons.

The sample annealed at the lowest DP (−30°C) undergoes the largest drop in spectral emissivity with increasing temperature. At the 800°C peak annealing temperature (PAT) shown in Figure 7.3 (e) – (g), the spectral emissivity of the −30°C sample approaches its pre-annealed values for wavelengths longer than 2 μm. This suggests that the external oxide layer may undergo reduction at these higher surface temperatures.

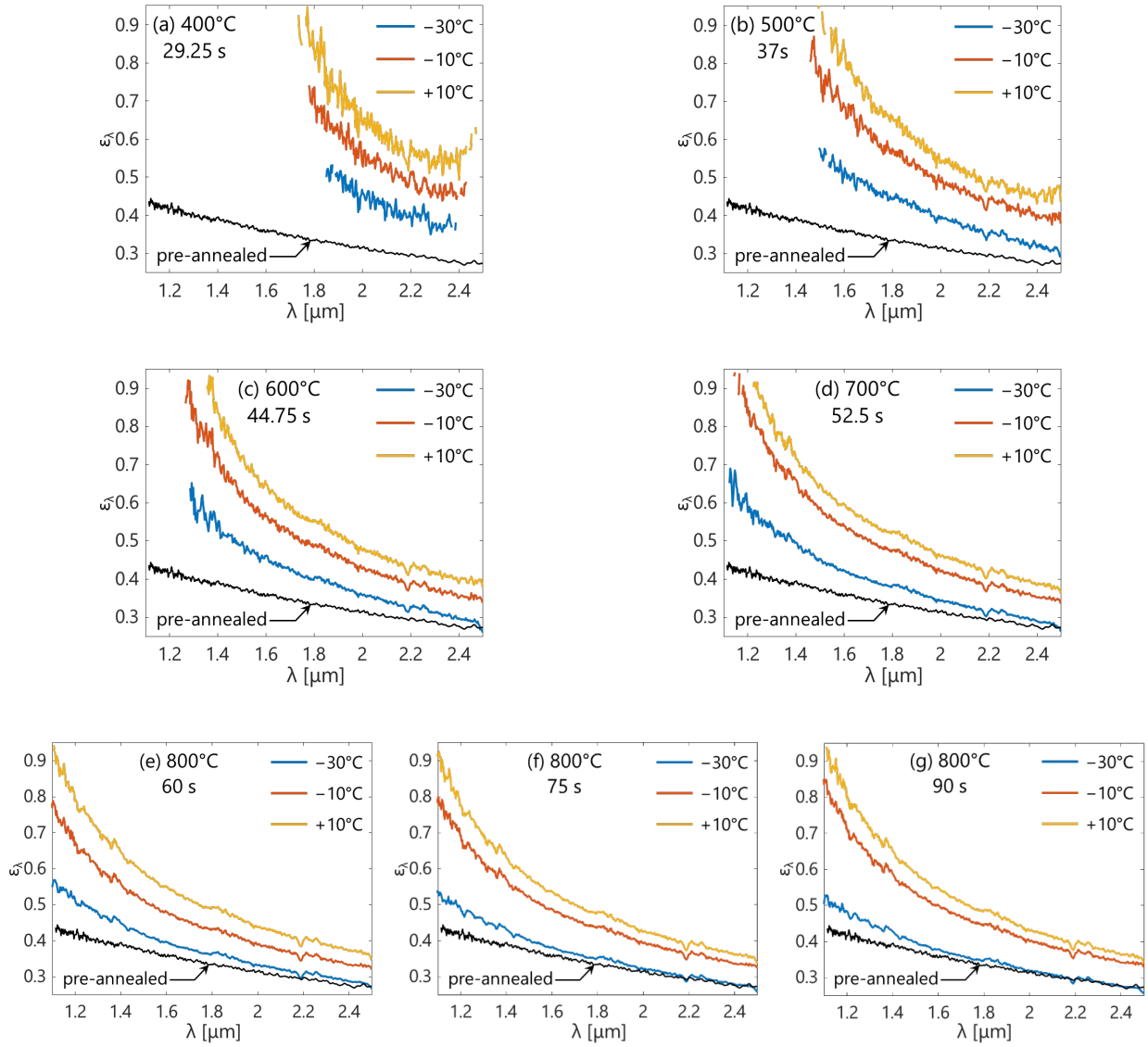


Figure 7.3. Measured spectral emissivity for the three dew points as a function of the annealing temperature and time. (a) 400°C - 29.25 s, (b) 500°C - 37 s, (e) 600°C - 44.75 s, (d) 700°C – 52.5 s, (e) 800°C - 60 s (soak starts), (f) 800°C - 75 s (mid soak), and (g) 800°C - 90 s (soak ends)

7.2.2. Multi-wavelength pyrometry estimates

When using multi-wavelength (MW) pyrometry to estimate AHSS temperature during intercritical annealing, the spectral emissivity is typically modelled in terms of underlying explanatory variables (temperature, wavelength, DP, roughness, etc.). Deterministic MW compensation algorithms predict a single value for emissivity and consequently generate a single pyrometrically-inferred temperature. A drawback of deterministic models is that the point temperature estimate does not convey the inherent uncertainty associated with the imperfectly known spectral emissivity. In contrast, the temperature posterior obtained with the Bayesian pyrometry model discussed in Chapter 6 provides a credibility interval that indicates the level of uncertainty introduced by the imperfectly known emissivity.

Table 7.2 summarizes the emissivity models selected to compare the accuracy of these approaches. Although Models #1, #2 and #3 have been previously introduced in Chapter 5, several multi-wavelength emissivity compensation algorithms from literature were first evaluated for this specific study, and only the best algorithms (Models #1 − #4) are included in Table 7.2. Typically, most pyrometry studies perform a "search" to identify a suitable emissivity compensation model because the performance of these algorithms varies significantly with material and process parameters [9, 95, 148]. This specificity seems to apply to AHSS as a similar search was conducted to identify the best performing deterministic models listed in Table 7.2. More importantly, the relative performance of the compensation algorithms varied with the annealing dew point, highlighting a major drawback of the deterministic approach.

Model #5 is the *ex situ*-based Gaussian emissivity prior from Chapter 6, which was constructed from 27 *ex situ* spectrometer measurements carried out on cold-rolled DP980 coupons. A few of the samples were left in their as-received state while the remainder were annealed within a 95%N_2-5%H_2 atmosphere at two dew points, −30°C and 10°C, and then quenched at intercritical annealing temperatures ranging from 463-802°C in a galvanizing simulator [143].

Table 7.2. Summary of deterministic emissivity compensation algorithms (Models #1 − #4) and stochastic prior (Model #5).

Model No.	Expression	Reference
#1	$\varepsilon_{\lambda d} = \exp\left(a_0 \frac{\lambda_d}{T_{\lambda d}} \right)$	[149]
#2	$\varepsilon_{\lambda d} = \exp\left(a_0 \lambda_d \right)$	[149]
#3	$\varepsilon_{\lambda d} = \exp\left(a_0 \frac{\sqrt{\lambda_d}}{T_{\lambda d}} \right)$	[148, 149]
#4	$\varepsilon_{\lambda d} = \exp\left(a_0 \sqrt{\lambda_d} \right)$	[148, 149]
#5	$p_{\mathrm{pr}}(\varepsilon_{\lambda d}) \sim \mathcal{N}(\mu_\varepsilon, \Gamma_\varepsilon)$	[143]

λ_d is the pyrometer detection wavelength; T is the inferred temperature; a_0 is the algorithm constant; $T_{\lambda d}$ is the equivalent blackbody temperature for the measured spectral irradiance; μ_ε and Γ_ε is the mean and covariance of the spectral emissivity distribution, respectively.

Figure 7.4 and Figure 7.5 show the pyrometrically-inferred temperature with respect to DP, temperature, and annealing time. Using the spectrometer intensities recorded at the three detection wavelengths of the industrial pyrometer (1.6 μm, 2.1 μm and 2.4 μm), the temperature estimates for the deterministic and stochastic models were obtained according to the procedures outlined in Chapter 5 and Chapter 6, respectively. In addition to the nominal temperature predictions, i.e., the maximum a posteriori (MAP) estimates, the Bayesian estimate for Model #5 provides a credibility interval, specifying a range of values expected to contain the "correct" temperature of the steel with a certain probability. The 95% credibility interval corresponding to two standard deviations of the nominal (MAP) values is included in Figure 7.5. Although there are uncertainties associated with the thermocouple measurements as discussed in Chapter 6, for the sake of clarity of the plots and ease of comparison, this uncertainty is omitted from the analysis in this section.

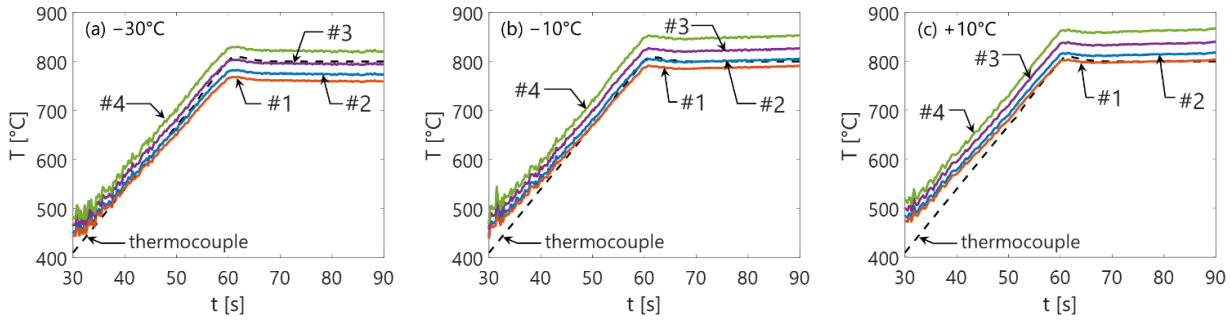


Figure 7.4. Pyrometry temperature predictions for Model #1 (red lines), Model #2 (blue lines), Model #3 (purple lines) and Model #4 (green lines) at the following target DPs: (a) −30°C, (b) −10°C and (c) +10°C. The dashed lines represent the thermocouple temperature measurements.

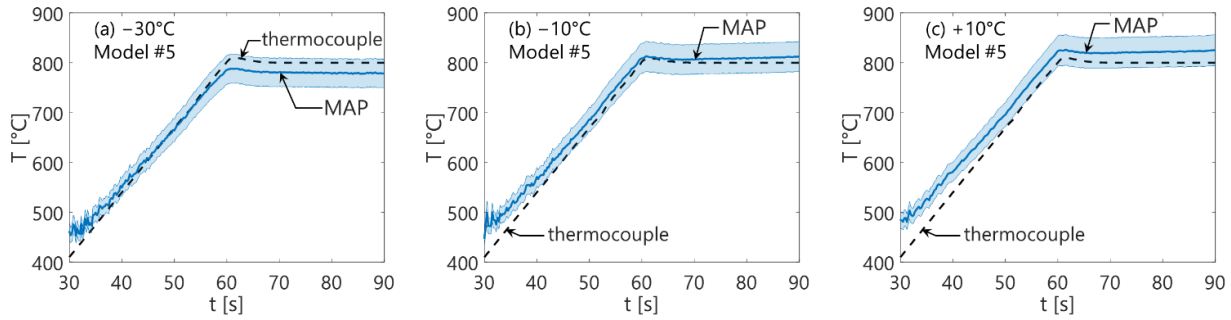


Figure 7.5. Pyrometry temperature predictions for the *ex situ* Gaussian prior (Model #5) showing the MAP estimates (solid blue lines), thermocouple temperature measurements (dashed lines) and 95% credibility intervals (shaded region) for the following target DPs: (a) −30°C, (b) −10°C, and (c) +10°C.

Generally, the pyrometrically inferred temperatures increase with increasing dew point across all the models because the enhanced emissivity caused by changes in the oxide layer with increasing DP is incorrectly interpreted as an increase in sample temperature. All models generally over-predict the temperature as the sample heats over the ramp period. This is because the models do not capture the actual inverse relationship between emissivity and temperature shown in Figure 7.3. The highest spectral emissivity for the three dew points was observed at the lowest temperatures, but the pyrometry inferences process typically attributes high emissivity values to high temperatures, which results in temperature over-prediction, especially at 400°C.

Figure 7.6 summarizes the measurement error for all five models, alongside the temperature uncertainty (credibility interval) provided by Model #5. Although the accuracy of each model varies with temperature and dew point, the temperature uncertainty provided by Model #5

is comparable to the error of its MAP estimate for most temperatures. While the thermocouple temperature of the steel is nearly constant at 60 s, 75 s, and 90 s, slight variations in the evolving spectral emissivity (Figure 7.2) cause variations in the predicted temperature as observed in the resulting error and uncertainty values.

Although both Models #2 and #4 exclude the blackbody temperature as an explanatory variable, Model #4 severely overestimates the temperature, especially at −10°C and +10°C dew points. This poor performance of Model #4 can be traced to the design criteria surrounding its original application. Modelling the spectral emissivity as a linear function of $\lambda^{1/2}$ gave an effective temperature estimate for aluminium alloys that exhibit a similar negative correlation between emissivity and temperature [148, 149]. However, the observed variations in emissivity for the aluminium alloys occur over a much smaller range compared to the variations induced by the interdependent effect of DP and temperature for the DP980 alloy in this study. Additionally, Model #4 was originally applied for $\lambda \geq 2$ μm, and therefore may not be suitable for the 1.6 μm detection wavelength.

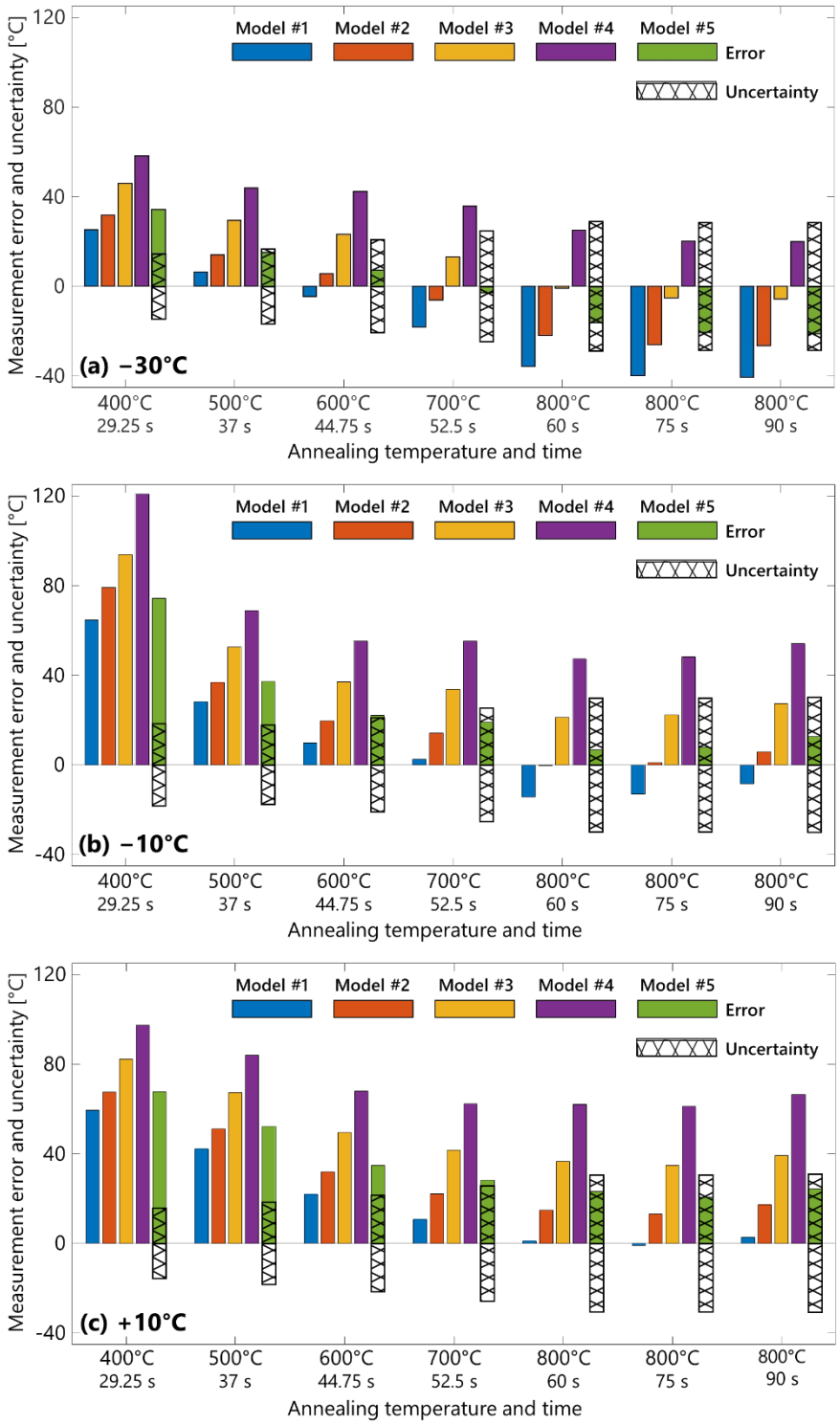


Figure 7.6. The measurement error for the emissivity models (Model #1 − #5) compared against the uncertainty (±2σ) obtained for stochastic emissivity prior (Model #5) at key temperatures for the following target DPs: (a) −30°C, (b) −10°C, and (c) +10°C.

For Model #5, the information content of a Gaussian (normal) distribution illustrated in Figure 7.7 explains why the MAP estimate either over-predicts or under-predicts the thermocouple temperature and why the 95% credibility intervals do not encompass the thermocouple estimates at some temperatures. The *ex situ*-based prior models the spectral emissivity as a normal distribution with a point estimate (mean, μ_ε) and a measure of spread (standard deviation, σ_ε). For normal distributions, 99.7% of the observation lies within three standard deviations of the mean (i.e., $\mu_\varepsilon \pm 3\sigma_\varepsilon$), with the observations becoming less probable (i.e., having lower probability density) as we move away from the mean on both sides. Therefore, when the evolving spectral emissivity of the steel lies in areas of low probability density, the temperature estimates will be inaccurate because the Bayesian framework will assign a very low probability to those emissivity values.

Figure 7.7 (a) shows that the *ex situ* probability density for the spectral emissivity at 400°C for the −10°C and +10°C DPs have near zero density, meaning that the model will assign these values to have an extremely small probability. Given that the mean value of the distribution is less than the actual spectral emissivity of the steel at these DPs, the estimated temperature overpredicts the true temperature. Similarly, comparing the *ex situ*-based prior against the emissivity at 800°C, Figure 7.7 (b) shows that the spectral emissivity of the steel at the −30°C DP has a much lower density compared to the other dew points, which affects the accuracy of the estimated temperature because the model will consider this value to be less probable. In this case, the mean of the *ex situ*-based prior model is greater than the actual emissivity of the coupon at −30°C and 800°C; therefore, the estimated pyrometric temperature will under-predict the thermocouple temperature. The plots in Figure 7.7 for the 2.1 μm detection wavelength are representative of all detection wavelengths.

The fact that the width of *ex situ*-based prior (Model #5) underestimates the variance in the spectral emissivity at lower temperatures (especially for the higher dew points) suggests that the sample size (27 samples) might be too small for this range of temperatures or that samples characterized *ex situ* do not fully capture the emissivity variations observed *in situ*. This emphasizes the importance of designing relevant and statistically robust priors that fully represent the expected variation in spectral emissivity.

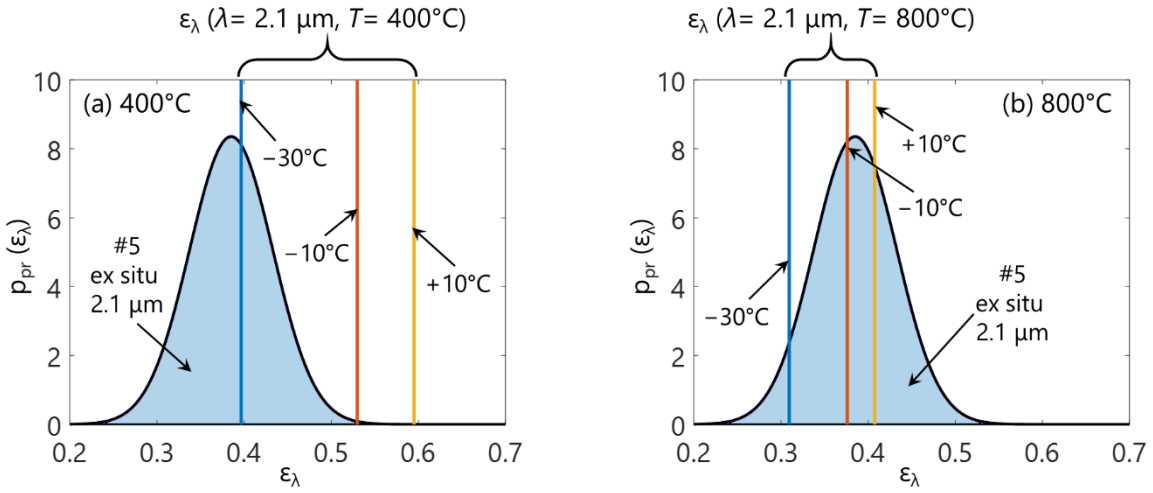


Figure 7.7. Stochastic prior distributions at 2.1 μm with vertical lines representing the spectrometer emissivity measurements at the three dew points (−30°C, −10°C and +10°C). (a) Model #5 (*ex situ*-based prior) overlapped with spectral emissivity measurements at 400°C and (b) Model #5 (*ex situ*-based prior) overlapped with spectral emissivity measurements at 800°C. The shaded region represents 99.7% of the observations, which falls within 3 standard deviations of the mean (i.e., $\mu_\varepsilon \pm 3\sigma_\varepsilon$).

In summary, while the deterministic models provide the most accurate nominal estimate of the peak annealing temperature (PAT) at 800°C (Model #3 for −30°C, Model #2 for −10°C and Model #1 for +10°C), the fact that the accuracy of these deterministic models is not consistent across the temperatures and dew points of interest is a significant challenge. On the other hand, the *ex situ*-based prior (Model #5) gives a more reliable and robust estimate across all the dew points. The credibility interval (ranging from ±15°C to ±31°C) obtained with the *ex situ*-based prior is advantageous as it compensates for the variations in emissivity induced by the changing dew point and temperature. Additionally, despite under-predicting the soak temperature estimate for the −30°C dew point, the *ex situ* prior (Model #5) gives the best estimate for both the ramp and soak period at all three dew points. Overall, the Bayesian approach provides an understanding of how reliable the temperature estimate is, which is not possible from the deterministic algorithms.

7.3. Conclusions

This chapter explores the effect of dew point, temperature, and time on the spectral emissivity of a DP980 AHSS alloy following a simple annealing schedule with a peak annealing temperature of 800°C. The spectral emissivity increases with dew point, especially at wavelengths below 2 μm. The spectral emissivity of the steel decreases with increasing temperature beyond 400°C. This is most likely due to the crossover phenomenon observed for metals at shorter wavelengths. Moreover, this inverse relationship between emissivity and temperature is more pronounced at the −30°C dew point, suggesting that the selective oxidation of the alloying elements and subsequent reduction of the oxide layer contribute to the observed changes in emissivity.

The impact of the evolving spectral emissivity on the pyrometrically-inferred temperature is also examined. Most models underpredict the soak temperature at a DP of −30°C but overpredict the soak temperature at the other dew points. Several deterministic models were identified to give reasonable temperature estimates; however, their accuracy is inconsistent across the annealing temperatures and dew points, which impairs their reliability. This chapter also examined a stochastic emissivity model that provided robust estimates for the temperature irrespective of the dew point. The results obtained with the stochastic approach highlight the benefit of estimating a measure of uncertainty alongside the nominal temperature estimate. With knowledge of the inherent uncertainty introduced by the imperfectly known emissivity, steelmakers can compare the posterior estimates against predefined temperature tolerances for AHSS during intercritical annealing.

Chapter 8
In situ and *ex situ* investigation of the radiative properties[6]

Most studies on the radiative properties of AHSS (including Chapter 3) are based on *ex situ* measurements on samples processed within simulators that replicate conditions on industrial CGLs, and then rapidly quenched. There are two key drawbacks to this approach, however: (1) it does not capture the temperature dependence of the radiative properties, e.g., as one would expect through Hagen-Rubens and Drude theories [54]; (2) the oxide state of the surface may be altered by the quenching process, leading to further differences between *in situ* and *ex situ* radiative properties. To address these deficiencies, Somveille et al. [3] attempted *in situ* spectral emissivity measurements on dual-phase AHSS alloys processed within a Gleeble® 3500 simulator following the procedure developed by Shi et al. [118] for Al-Si coated steels. Unfortunately, inadequate atmospheric control resulted in significant oxidation of the samples. More recently, Ham et al. [77] and Suleiman et al. [143, 150, 151] (i.e., Chapter 5, Chapter 6 and Chapter 7) reported *in situ* spectral emissivity measurements on annealed TRIP and DP alloys, respectively, providing much needed insight into the temporal effect of temperature on the radiative properties of AHSS.

A comparison of *ex situ* and *in situ* spectral emissivity measurements highlights the importance of *in situ* measurements. Somveille et al. [99] reported minimal variations of *ex situ* emissivity measurements on DP980 samples processed at different temperatures within a galvanizing simulator, while the *in situ* spectral emissivity measurements reported by Suleiman et

[6] The content of this chapter is an extended version of the following conference paper:

F.K. Suleiman, M. Kagaya, A. Hosseini, and K. J. Daun, 2024, "*In situ* and *ex situ* investigation of the radiative properties of AHSS," Proceedings of the 114th Galvanizers Association Meeting, Covington, Kentucky, USA.

al. [150, 151] showed significant variations in spectral emissivity with temperature. Moreover, Suleiman et al. [143] demonstrated that *ex situ*-based spectral emissivity priors constructed from samples quenched at various temperatures do not effectively compensate for *in situ* variations in emissivity experienced by the same alloy, thus impacting the accuracy of the pyrometry estimates.

To the best of the author's knowledge, there is no definitive comparative study evaluating the differences between *in situ* and *ex situ* temperature-dependent radiative properties of AHSS, especially at the near-infrared wavelengths critical to pyrometry. Therefore, this chapter characterizes and compares the *in situ* and *ex situ* radiative properties of a dual-phase AHSS alloy (DP980) annealed using two lab-scale simulators with different heating systems: (1) resistive heating with a DC power supply (Waterloo Annealing Simulator) and (2) radiative heating in a quartz lamp infrared furnace (McMaster Galvanizing Simulator, Iwatani-Surtec). In both systems, the steel is heated with the same thermal cycle in a reducing atmosphere consisting of 95%N_2 - 5% H_2 at a dew point of −30°C. The samples for *ex situ* characterization are quenched at intermitted temperatures along the same annealing cycle: 200°C, 300°C, 400°C, 650°C, 750°C, and 800°C (after 30 s soak). The *ex situ* radiative properties are analyzed with a Bruker Invenio X FTIR spectrometer and then compared to the *in situ* measurement at the same temperatures to understand the effect of annealing temperature on the radiative properties, and how it differs across *in situ* and *ex situ* measurement conditions. Crucially, comparing the *ex situ* radiative properties of the samples annealed in the Waterloo simulator against samples annealed in the Iwatani-Surtec galvanizing simulator serves as a validation step for the Waterloo simulator design.

8.1. Impact of low-temperature oxidation thermodynamics

Figure 8.1 shows the oxygen partial pressure as a function of process temperature for Cr, Fe, Mn, and Si oxides and the −30°C dew point, 5% H_2 atmosphere derived using the steps outlines in Section 2.1.3. In this case, the activity of the alloying elements is evaluated based on their mole fraction in the actual DP980 alloy analyzed in this thesis. Figure 8.1 shows that the selective oxides (MnO, SiO_2 and Cr_2O_3) are thermodynamically likely to form during annealing since their equilibrium oxygen potential curves fall below the oxygen partial pressure curve for the annealing atmosphere. The equilibrium oxygen potential curve for the iron oxides, i.e., FeO and the Fe_3O_4, coincides with the oxygen partial pressure of the annealing atmosphere at temperatures below

~400°C, so iron oxide formation is thermodynamically favorable under these conditions. This means that metallic oxides influencing pyrometry estimates for these DP980 samples are not limited to selective oxides, especially at lower temperatures.

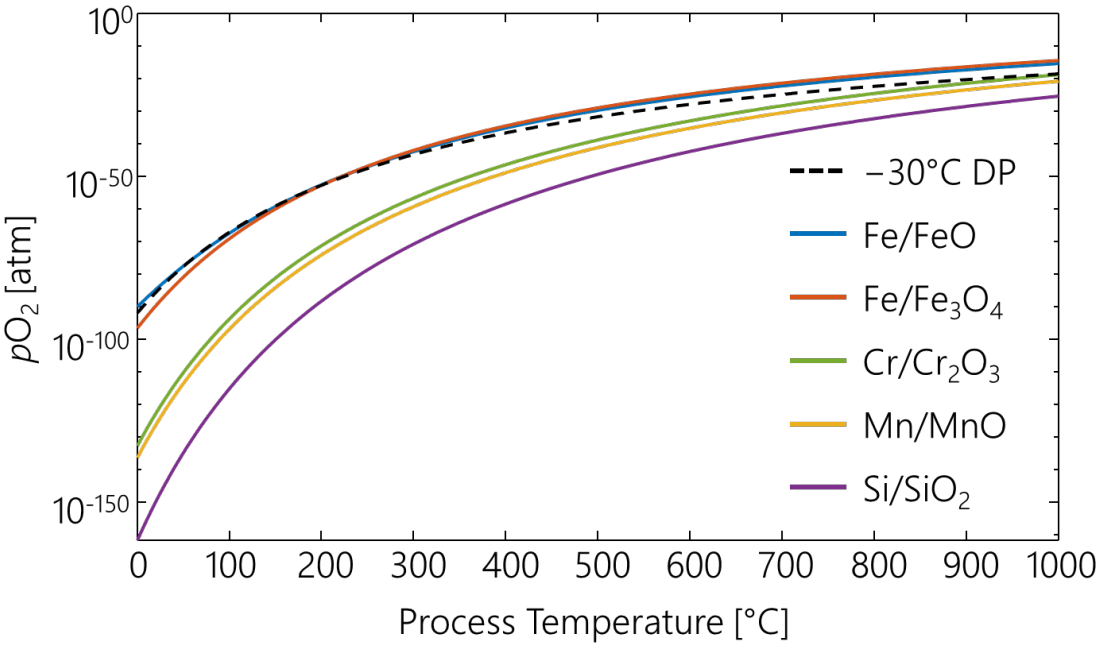


Figure 8.1. Logarithmic plot of the oxygen partial pressure (pO_2) as a function of process temperature. This shows the thermodynamic stability of the metallic oxides relative to oxygen potential of the annealing atmosphere at −30°C dew point.

Most studies on the thermodynamic stability of AHSS oxides focus on high temperature oxidation (400°C and above) due to its impact on reactive wetting and galvanizing. However, Figure 8.1 shows that low temperature oxidation is also important in CGLs since any oxidation that impacts the surface of the steel would also impact the pyrometrically-inferred temperature. Low temperature oxidation is also important when considering the differences between simulators and the industrial CGL. When predicting the thermodynamic stability of the oxides using curves such as Figure 8.1, the process temperature at the steel–atmosphere interface is often assumed to be equivalent to the steel strip temperature. This assumption may be reasonable in a CGL given that the furnace atmosphere and the steel strip are in near thermal equilibrium. However, in most simulators, the steel specimen is rapidly heated, typically by electrical resistance [77, 143] or radiant lamps [152], with the surrounding atmosphere indirectly heated by the specimen. As a result, the temperature of the atmosphere may thermally lag that of the rapidly heated steel surface,

resulting in a potential thermal gradient between the steel sample and the atmosphere. Consequently, if thermodynamic calculations are based solely on the steel surface temperature, without accounting for any potential thermal temperature gradient, the stability of selective oxides and native iron oxide formed during annealing may be overestimated.

8.2. Experimental procedure

Cold-rolled DP980 AHSS alloy with a silicon-to-manganese ratio of 0.04 were processed in the vacuum-based Waterloo Annealing Simulator (WAS) (Section 4.3) and the McMaster Galvanizing Simulator (MGS) [104, 152]. The 1.5 mm thick DP980 steel sheet was initially cut into the WAS sample size of 152.4 mm × 25.4 mm, with the rolling direction parallel to the length of the samples. Some of the WAS samples were cut in half (76.2 mm × 25.4 mm) for processing in the MGS.

In both simulators, samples were annealed according to the heating schedule in Figure 8.2 within a 95%/5% N_2/H_2 atmosphere at a dew point of −30°C. Similarly, both simulators control the heating rate using input from a K-type thermocouple welded onto the sample. Unlike the MGS, the WAS offers optical access to the specimens during heating, allowing for *in situ* spectral irradiance measurements. More details on the MGS apparatus are provided in Ref. [104].

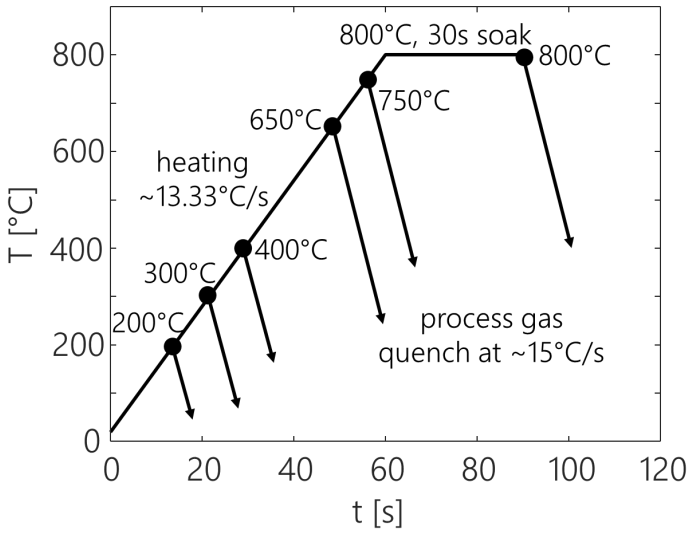


Figure 8.2. Schematic of the annealing schedule showing the heating rate, peak annealing temperature (PAT), and quench rate. This schedule was used in both simulators.

Specimens were cleaned with acetone and ethanol and the pre-annealed radiative properties were then characterized and compared with a Bruker Invenio X FTIR spectrometer in the near-

infrared (1.2 – 2.5 μm) prior to annealing. After annealing, specimens from both simulators were individually sealed in zipper sample bags for transport to the FTIR spectrometer where they were cleaned with ethanol before measuring the *ex situ* post-annealed radiative properties.

In addition to the fully annealed samples, (i.e., samples heated to 800°C with 30 s soak), five other samples were obtained from each simulator by interrupting the heating schedule in Figure 8.2 at 200°C, 300°C, 400°C, 650°C, and 750°C. All samples were rapidly quenched (~15°C/s) to freeze their surface state. The effect of annealing temperature on the spectral emissivity of the samples due to the evolving surface oxidation was then studied *ex situ* by characterizing the quenched samples with the FTIR spectrometer.

8.3. Effect of rolling direction on FTIR measurement

The near-normal directional-hemispherical spectral reflectance, ρ_λ, of the pre-and post-annealed samples, are measured using an A 562-G integrating sphere attachment with the Bruker Invenio X FTIR spectrometer. The near-normal spectral emissivity, ε_λ, required for accurate pyrometry is then obtained from ρ_λ via Kirchhoff's law:

$$\varepsilon_\lambda = 1 - \rho_\lambda \tag{8.1}$$

The A 562-G is a near-spherical cavity that is coated with Infragold®, $\rho_\lambda \approx 0.94$. While the integrating sphere is conceptualized as a perfectly spherical enclosure with perfectly reflecting surfaces, the actual integrating sphere deviates from this idealization due to the presence of the sample, i.e., single-beam substitution error [153], and the light and detection ports. These measurement imperfections are corrected using the procedure outlined by Blake et al. [154]. Generally, the FTIR has a calibration uncertainty of ±2% and a repeatability accuracy of less than ±1% for reflectance measurements over the entire spectrum.

A larger source of uncertainty comes from the interaction between the integrating sphere geometry and the anisotropy of the specimen caused by rolling. In an ideal scenario, the sphere provides the normal-hemispherical reflectance, which is independent of reflection direction, but in reality, the measured spectral reflectance on anisotropic surfaces depends on sample orientation relative to the entrance port [145, 155]. To determine the correct orientation for the FTIR measurements on the cold-rolled AHSS in this thesis, orientation-dependent variations in the reflectance were first investigated using several 25 mm × 25 mm as-received samples. Figure 8.3

plots the average spectral reflectance of these samples against the sample orientation. Maximum and minimum reflectance was obtained when the rolling direction was parallel (i.e., 0°, 180°) and perpendicular (i.e., 90° and 270°) to the incident light, respectively. The reflectance values measured with the diagonal orientation (i.e., ±45° from the rolling direction) were very close to the rolling direction values, which indicates that the baffles within the integrating sphere minimize the screening error that occurs when the rolling direction is parallel to the incident light [145, 156]. Accordingly, orienting the sample with the rolling direction parallel or perpendicular to the incident light introduces a measurement uncertainty of ±5%, with the maximum uncertainty in the perpendicular direction. The orientation test was also repeated with annealed samples and the trend remained the same. Since the orientation-dependent features of the cold-rolled DP980 alloy align with findings reported by Lindseth et al. [145] for aluminium, this thesis follows their suggestion to discard measurements perpendicular to the rolling direction.

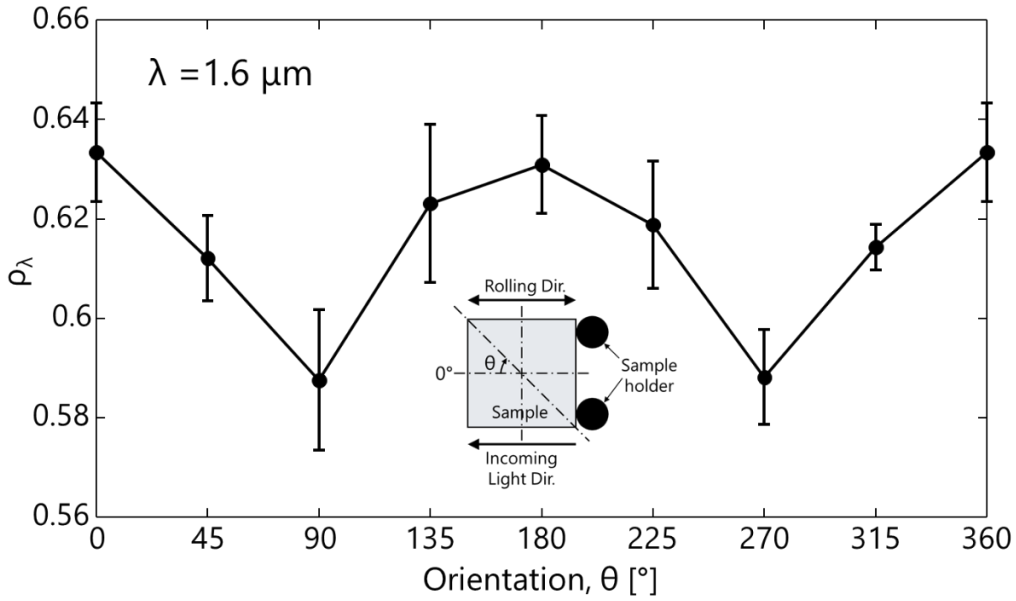


Figure 8.3. Orientation-dependent variation in the near-normal directional-hemispherical spectral reflectance (ρ_λ) of cold-rolled DP980 measured with the integrating sphere. Error bars correspond to one standard deviation of the mean of the five samples.

Therefore, all the *ex situ* spectral emissivity values were obtained by applying Kirchoff's law to reflectance values measured with the incident light diagonal to the rolling direction (i.e., within ± 45° of the rolling direction). However, the initial comparison of the pre-annealed radiative properties was done with the rolling direction perpendicular to the incident light because the

sample length (152.4 mm) was too long to be mounted in any other orientation within the FTIR sample compartment. Considering that this comparison is to confirm that the samples going into both simulators begin with similar surface features, using the perpendicular orientation does not influence this comparison since the orientation is consistent for all pre-annealed measurements.

8.4. *In situ* spectral emissivity variation in the WAS simulator

The time- and temperature-dependent spectral emissivity for the sample heated to 800°C and soaked for 30 s is shown in Figure 8.4 and Figure 8.5. At each time step, the *in situ* normal spectral emissivity, ε_λ, is obtained using the spectral intensity, I_λ, recorded simultaneously by the spectrometer and pyrometer, combined with the blackbody intensity, $I_{\lambda b}$, at the thermocouple temperature, T_T, such that $\varepsilon_\lambda = I_\lambda(T_T)/I_{\lambda b}(T_T)$. The spectrometer can only measure spectral emissivity at temperatures above 400°C due to signal-to-noise constraints, while the pyrometer measurements are viable from 250°C upwards.

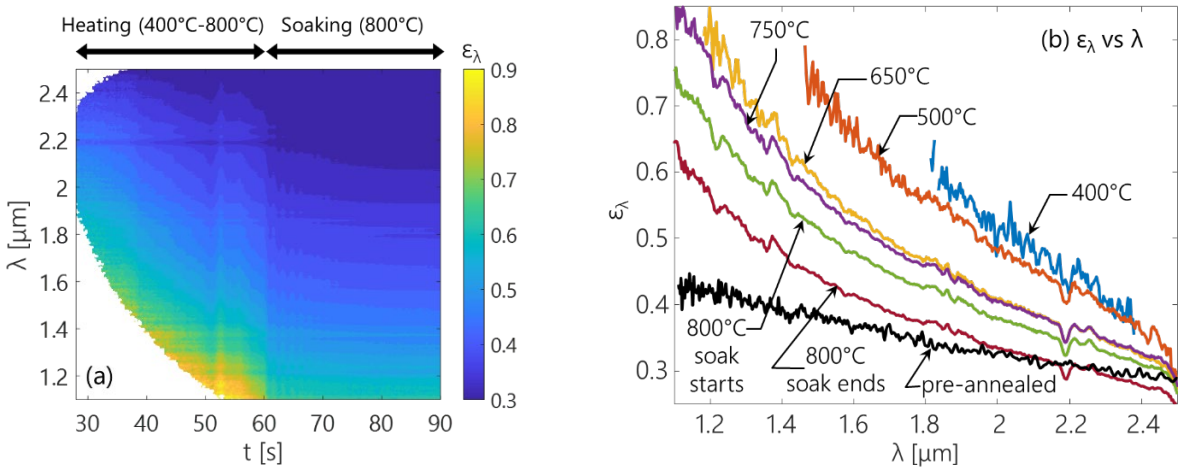


Figure 8.4. (a) Contour of the evolving spectral emissivity, highlighting the *in situ* spectral and temporal variation of the DP980 alloy during annealing. (b) The spectral emissivity from (a) plotted at key annealing temperatures: 400°C (29.25 s), 500°C (37 s), 650°C (48.5 s), 750°C (56 s), 800°C (60 s - soak starts) and 800°C (90 s - soak ends).

Figure 8.4 shows the *in situ* spectral emissivity as it evolves with wavelength, time, and temperature. Figure 8.4 (a) shows a region of higher emissivity ($\varepsilon_\lambda \geq 0.7$) at the shorter wavelengths (≤ 2 μm) during heating, which indicates the presence of an oxide layer on the steel surface. Figure 8.5 compares the spectral emissivities inferred with the spectrometer and the pyrometer as a function of time (Figure 8.5 (a)) and temperature (Figure 8.5 (b)). The two instruments generally

show good agreement, especially for the 2.1 μm detection wavelength. However, the spectrometer measurement is slightly greater than the pyrometer values at 1.6 μm but lower at 2.4 μm. This variation primarily results from differences between the defined nominal wavelength and the width of the actual spectral band being measured by the detectors.

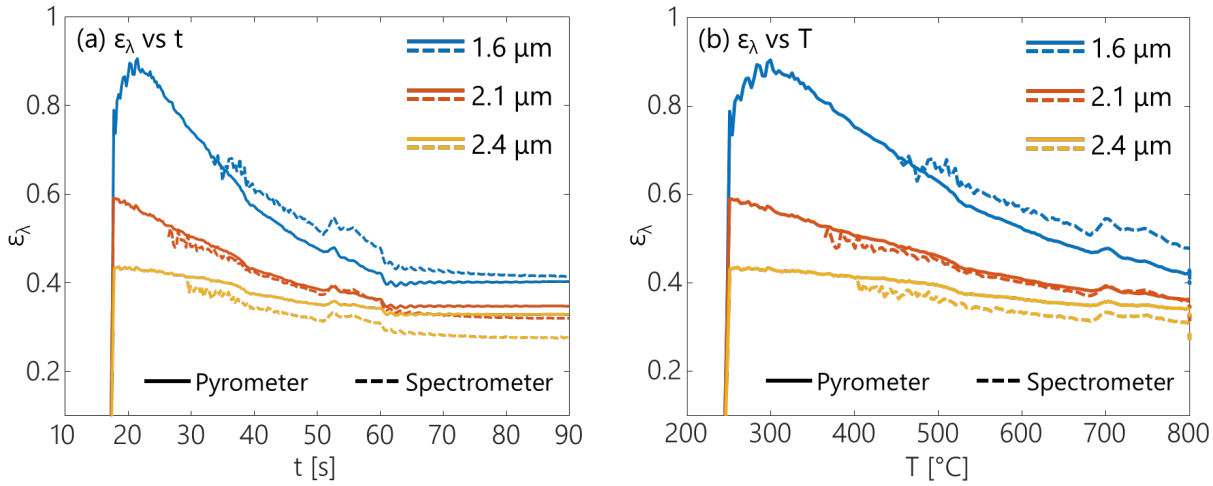


Figure 8.5. Evolving spectral emissivity, ελ, measured *in situ* with the pyrometer and spectrometer at the three-detection wavelength versus (a) annealing time, *t*; and (b) annealing temperature, *T*.

Generally, the spectral emissivity of the DP980 AHSS alloy decreases with increasing wavelength, which is expected for metals in the near-infrared region since the absorptive index of metals decreases with increasing wavelength [54]. However, contrary to the theoretical expectation for pure metals, the spectral emissivity was found to decrease with increasing temperature from 400°C upwards. A comparison with the pre-annealed emissivity in Figure 8.4 (b) implies that at some temperature below 400°C, the spectral emissivity of the steel must have increased from its pre-annealed value. Figure 8.5 identifies the specific temperature at which spectral emissivity begins to decrease with increasing temperature, based on the spectral emissivity inferred from the pyrometer. The *in situ* spectral emissivity at 1.6 μm peaked at 300°C while the spectral emissivity at the longer wavelength appears to have peaked at 250°C or lower. After this point, the emissivity decreases with increasing temperature and remains constant during the 30 s soak period where the temperature of the steel is held constant at 800°C.

This observation is connected to the thermodynamic stability of iron oxides at lower temperatures (Figure 8.1), in conjunction with selective oxidation of the alloying elements.

Although selective oxides are expected to form and evolve during annealing, the observed effects of surface oxidation in this experiment are more pronounced at lower temperatures. The 300°C to 400°C temperature range at which the oxide effect starts to diminish corresponds to the temperature at which the annealing atmosphere is predicted to reduce the iron oxides. It is important to note that there were no visible oxides on the surface of the steel during annealing which is the exact opposite of the infiltration-induced oxidation reported in previous studies [143, 151], i.e., Chapter 5 and Chapter 6. However, this low-temperature oxidation effect might be more pronounced in lab-scale simulators relative to a CGL, given that the reducing nitrogen-hydrogen gas within the simulator is not heated.

8.5. *Ex situ* spectral emissivity of quenched WAS and MGS samples

To further investigate the temperature-dependent variation in emissivity observed *in situ* for DP980 alloy processed in the WAS, several samples with similar pre-annealed radiative properties were processed in the WAS and MGS simulators and quenched at intermittent annealing temperatures. These samples are part of a larger study focused on understanding the radiative, microstructural, and physiochemical properties of annealed AHSS surfaces that contribute to uncertainties in the pyrometrically-inferred temperature. However, this thesis will focus solely on analyzing the radiative properties.

Figure 8.6 compares the *ex situ* spectral emissivity at 200°C, 300°C, 400°C, 650°C, 750°C and 800°C (after soak) against the pre-annealed *ex situ* spectral emissivity of the same DP980 alloy. The pre-annealed emissivity is the average value from five as-received samples with the measurement uncertainty omitted for clarity. Generally, the spectral emissivity of all the annealed and quenched samples is comparable to the pre-annealed values for both simulators. However, the WAS samples show more temperature-dependent variations compared to the samples processed in the MGS. The most significant difference was observed for the WAS samples quenched at 650°C and 750°C, in which the spectral emissivity was much lower with decreased variability with wavelength (i.e., lower slope). The spectral emissivity for the MGS sample at 750°C was also lower than the other samples processed in the same simulator. Since the 650°C and 750°C temperatures bound the spectral emissivity peak observed *in situ* at 700°C (Figure 8.5); this variation in radiative properties could be a consequence of the evolving ternary oxides.

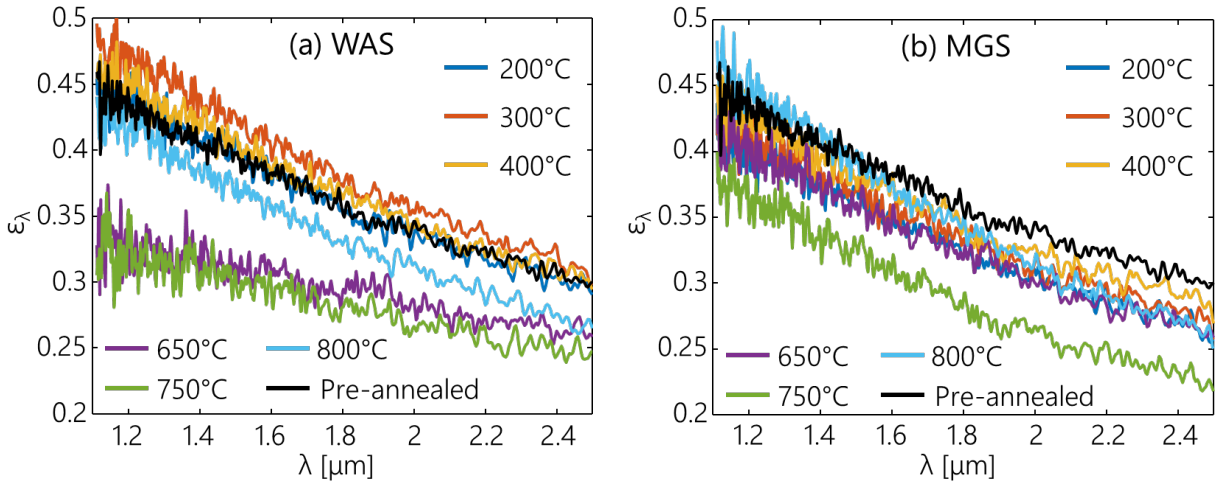


Figure 8.6. *Ex situ* spectral emissivity at different annealing temperatures for samples processed in (a) Waterloo Annealing Simulator (WAS) and (b) McMaster Galvanizing Simulator (MGS). The pre-annealed emissivity represents the average of the 5 samples analyzed in Figure 8.3 (diagonal orientation only) with the measurement uncertainty excluded for clarity.

Figure 8.7 focuses on the temperature-dependent variations in the emissivity for the *ex situ* samples at the three pyrometry detection wavelengths. Broadly speaking, the spectral emissivities of the samples processed in both simulators were highest at the lower temperatures, before decreasing with increasing temperature. The peak *ex situ* emissivity for the WAS sample was observed at 300°C which matched the *in situ* findings in Figure 8.5. However, the maximum *ex situ* spectral emissivity for the MGS samples was observed later at 400°C. The difference in the temperature at which the peak emissivity is observed for the WAS and MGS samples is probably due to varying oxidation kinetics. Nevertheless, the similar emissivity trend for both simulators indicates that the formation of an external oxide layer at lower temperatures is not merely an artefact of the WAS apparatus.

In terms of the actual spectral emissivity values, the WAS and MGS samples show good agreement at the higher temperatures (≥ 650°C). Figure 8.7 shows a dip in emissivity at 750°C for both the WAS and MGS samples, potentially due to ternary oxides. This dip in emissivity at high temperatures is consistent with the findings reported by Ham et al. [77] for TRIP steel due to the transformation of Mn as it formed complex oxides with other alloying elements. At lower temperatures, on the other hand, the spectral emissivity for the WAS samples was found to be higher than the MGS samples, specifically at 200°C and 300°C. While replicates are required to

statistically account for random errors introduced by the process in both simulators, it is currently assumed that the increased emissivity for the WAS samples compared to the MGS samples at lower temperatures is a consequence of variations in the kinetics and composition of the low-temperature oxide.

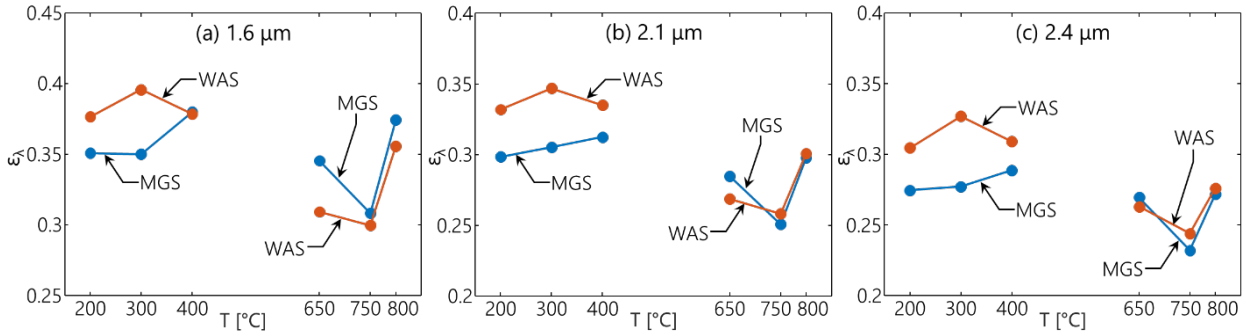


Figure 8.7. *Ex situ* spectral emissivity as a function of annealing temperature for the three detection wavelengths of the pyrometer: (a) 1.6 µm, (b) 2.1 µm, and (c) 2.4 µm. The red scatter represents the samples processed in the Waterloo Annealing Simulator (WAS), while the blue scatter is the samples processed in the McMaster Galvanizing Simulator (MGS).

8.6. Comparing *in situ* and *ex situ* temperature-dependent radiative properties

Section 4.2 focused on the differences in radiative properties between the samples processed in the WAS and MGS. Given that this comparative investigation relied exclusively on quenched samples characterized *ex situ*, it is imperative to determine if the radiative properties observed *ex situ* capture the temperature-dependent effects observed *in situ*. Since the MGS does not offer *in situ* access, this is done by comparing the *in situ* measurement from the WAS simulator with the *ex situ* measurements for samples annealed in both simulators.

Figure 8.8 compares the *in situ* spectral emissivity against the corresponding *ex situ* spectral emissivity at the same annealing temperature. The *ex situ* spectral emissivity was found to underestimate the *in situ* spectral emissivity especially at lower temperatures and at shorter wavelengths. Moreover, the *in situ* spectral emissivity varied logarithmically/exponentially with wavelength, which is quite different from the linear trend exhibited by the *ex situ* spectral emissivity measurements. Furthermore, the linear slope of the *ex situ* measurements remains relatively constant with wavelength for all the temperatures while the curvature in the *in situ* spectral emissivity flattens out with increasing temperature. The differences in the *ex situ* and *in situ* radiative properties indicate differences in the optical properties of the AHSS surfaces even though they were annealed at the same temperature. Beyhaghi et al. [157] also reported differences

in the *in situ* and *ex situ* oxide properties of Inconel at 650°C, as measured by Raman spectroscopy, highlighting variations between *in situ* and *ex situ* conditions.

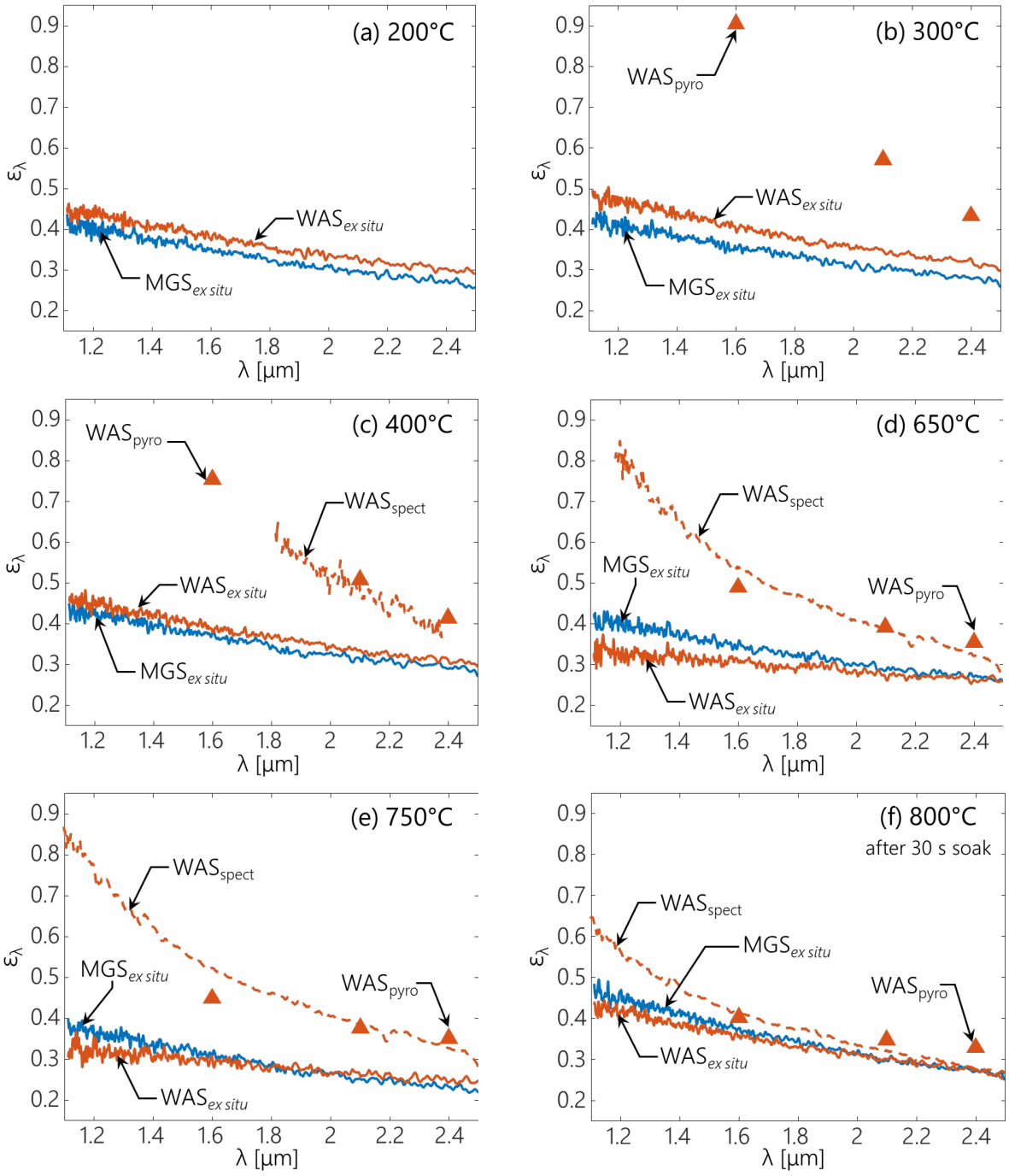


Figure 8.8. Comparing the *in situ* and *ex situ* spectral emissivity for annealed DP980 at the following temperatures: (a) 200°C, (b) 300°C, (c) 400°C, (d) 650°C, (e) 750°C, and (f) 800°C (after 30s soak). The WAS$_{spect}$ and WAS$_{pyro}$ are the *in situ* spectrometer and pyrometer readings, respectively, from Figure 8.4 and Figure 8.5. The WAS$_{ex\ situ}$ and MGS$_{ex\ situ}$ are the *ex situ* FTIR spectrometer measurements on rapidly quenched samples, shown in Figure 8.6.

The spectral emissivity of a metallic surface depends on wavelength and temperature through two main features: (1) the interaction of the EM wave with the constituent oscillators in the metal surface (mainly electrons), and (2) surface topography, which may be affected by the formation of oxides and other contaminants. In the case of polished metallic surfaces, Hagen-Rubens theory predicts that spectral emissivity should decrease with wavelength over the infrared spectrum. The emissivity should also increase with temperature at wavelengths longer than the crossover or "X" point and decrease at wavelengths shorter than this point. For most metals, the crossover point is in the visible or near-infrared spectrum. The picture is further complicated by surface roughness due to upstream processing (cold-rolling and pickling) and, especially, the emergence of oxides of varying composition and morphology in a way that depends on alloy composition, atmosphere, and heating schedule.

An evolving oxide film is most likely responsible for the pronounced difference between *ex situ* and *in situ* measured ε_λ observed in Figure 8.8. At shorter wavelengths, the oxide layer thickness is smaller or comparable to the detection wavelength, which produces a stronger constructive and destructive thin-film interference pattern that increases the emittance of the metal-oxide composite [54]. Therefore, as the surface oxides become reduced with increasing temperature, the oxide layer becomes thinner, causing the spectral emissivity of the composite metal-oxide to approach the emissivity of the steel substrate. This also explains why the *in situ* spectral emissivity at 800°C approaches the *ex situ* spectral emissivity values (which are close to the pre-annealed radiative properties of the steel as seen in Figure 8.6).

These results strongly suggest that *ex situ* characterization does not fully capture the impact of temperature on the varying radiative properties during annealing. *Ex situ* characterization in this study does seem to capture some of the temperature-induced variations such as changes in surface oxides and roughness since some of these remain at room temperature after the steel is rapidly cooled. However, it would be difficult for *ex situ* techniques at room temperature to capture temperature-dependent changes in the optical properties of the oxide layer and steel substrate that exist only at elevated intercritical annealing temperatures.

8.6.1. Pyrometry estimates with *in situ* versus *ex situ* spectral emissivity

To highlight the importance of *in situ* spectral emissivity for accurate pyrometry of AHSS, Table 8.1 summarizes the measurement error that would result if the *ex situ* emissivities from the WAS and MGS simulators were used to infer the pyrometry temperature during annealing, instead of the *in situ* ones. Using Wein's approximation to Planck's law, the pyrometry temperature, T_p, was estimated from the *in situ* pyrometer intensity, $I_{\lambda d}$, and the estimated spectral emissivities, $\varepsilon_{\lambda d,estimate}$, such that

$$I_{\lambda d} = \frac{\varepsilon_{\lambda d,estimate} C_1}{\lambda_d^5 \exp\left(\frac{C_2}{\lambda_d T_p}\right)} \tag{8.2}$$

where λ_d is the detection wavelength of the pyrometer, $C_1 = 1.191\times10^8$ W·μm^4/m^{2}sr, and $C_2 = 1.439$ μm·K. The resulting overdetermined system of equations for the three detection wavelengths was solved by least-squares minimization.

Table 8.1. Pyrometry estimates (T_p) and the corresponding absolute error (AE) and relative error (RE) obtained with the *ex situ* spectral emissivity from both simulators (WAS_{exsitu} and MGS_{exsitu}) compared against the thermocouple temperatures (T) and the estimates inferred with the *in situ* spectrometer emissivity (WAS_{spect}).

T (°C)	WAS_{spect}			WAS_{exsitu}			MGS_{exsitu}		
	T_p (°C)	AE (°C)	RE (%)	T_p (°C)	AE (°C)	RE (%)	T_p (°C)	AE (°C)	RE (%)
299.3	—	—	—	321.5	22.1	7.4	329.2	29.9	10.0
400.2	—	—	—	427.7	27.5	6.9	431.9	31.7	7.9
650.1	655.1	5.0	0.8	696.4	46.3	7.1	689.7	39.6	6.1
749.4	750.1	0.7	0.1	810.8	61.4	8.2	816.4	67	8.9
800	818.8	18.8	2.4	827.4	27.4	3.4	828.1	28.1	3.5

The *in situ* spectrometer emissivity (WAS_{spect}) and the *ex situ* spectral emissivities (WAS_{exsitu} and MGS_{exsitu}) at the three detection wavelengths (1.6 μm, 2.1 μm and 2.4 μm) were substituted for $\varepsilon_{\lambda,estimate}$ in Eq. (8.2) to obtain the pyrometry estimates in Table 8.1. Because the pyrometer detection threshold is 250°C, there are no pyrometry estimates for the 200°C sample.

Likewise, there are no WAS_{spect} estimates for 300°C and 400°C because the spectrometer detection threshold is 400°C.

Although the WAS_{spect} temperature estimates were obtained using *in situ* spectral emissivity values, some variations exist between the spectrometer and pyrometer measurements as shown in Figure 8.5 and Figure 8.8. The pyrometry error resulting from this variation is small at 650°C and 750°C but increases at 800°C (after soak) due to the increased divergence in the 2.4 μm emissivity estimates as seen in Figure 8.8 (f).

The temperature estimates derived using the *ex situ* WAS and MGS emissivity measurements overpredict the thermocouple temperature because these *ex situ* values underpredict the *in situ* WAS_{pyro} spectral emissivity as seen in Figure 8.8. As expected, the measurement error is more pronounced at lower temperatures where there is a significant difference between the *in situ* and *ex situ* radiative properties. The fact that relative measurement error can be as high as 10% emphasizes the importance of capturing temperature-dependent variations when building robust emissivity models for accurate AHSS pyrometry.

8.7. Conclusions

This chapter presents *in situ* and *ex situ* measurements of spectral emissivity of dual-phase AHSS alloy (DP980) annealed within two different annealing simulators with identical annealing process conditions. *In situ* spectrometer and pyrometer measurements were compared against *ex situ* FTIR spectrometer measurements in the near-infrared wavelengths important to pyrometry. The consistent effect of temperature across the samples processed in both simulators proves the observed trends are not artefacts of a specific annealing simulator.

The results elucidate the impact of low-temperature oxidation on the radiative properties of AHSS. Both the *in situ* and *ex situ* radiative properties of the DP980 alloy show that the spectral emissivity increases from its pre-annealed value to a peak emissivity value around 300°C − 400°C, before decreasing with increasing temperature. Thermodynamic analysis of the oxidation potential of the DP980 alloy suggests that this peak in emissivity is primarily due to stable iron and selective oxides that form at lower temperatures. However, this low-temperature oxidation effect is presumably more pronounced here due to the temperature difference between the heated steel and the annealing atmosphere. Furthermore, both the *in situ* and *ex situ* spectral emissivity evolved

significantly between 650°C and 750°C, likely indicating a phase transformation of manganese into complex ternary oxides.

Most importantly, the comparative analysis of the *ex situ* and *in situ* radiative properties of annealed DP980 samples provides crucial insight into the effect of temperature on the radiative properties of the steel substrate and the selective oxide layer. The pyrometry error resulting from the difference between the *ex situ* and *in situ* measurements highlights the fact that the evolving radiative properties of AHSS during annealing are driven by the combined effect of temperature-induced changes in the surface of the steel combined with the temperature-dependent variations in the optical properties of the composite metal-oxide AHSS surface.

Chapter 9
Conditional emissivity prior for improved temperature estimates[7]

The Bayesian pyrometry model introduced in Chapter 6 provides steelmakers with a measure of uncertainty (credibility interval) alongside the pyrometrically-inferred temperature (MAP estimate). Quantifying the uncertainty in the pyrometry estimate gives insights into the potential error in the inferred temperature, enabling better control decisions about the annealing process to ensure the desired material properties at the end of the annealing cycle. However, excessively wide uncertainties in the pyrometry estimates compromises the reliability of the measurement, thereby limiting its effectiveness in controlling the intercritical annealing process. Unfortunately, the uncertainty values for the pyrometry estimates obtained thus far in this thesis well exceed the temperature tolerance bounds for AHSS processing, primarily due to the information content of the spectral emissivity prior. The results in Chapter 7 have showed that, depending on the annealing dew point, the estimated uncertainty can range from ±14 K to ±31 K, with the credibility interval sometimes failing to capture the thermocouple temperature at lower temperatures. This is unacceptable for the industrial galvanizing line as Mosser et al. [18] have showed that temperature excursions of ±25 K or more in the annealing control pyrometry estimates for DP980 alloys will produce mechanical properties that deviate from the ASTM specification. Moreover, steel manufacturers within the GAP program desire a temperature control window of ±2°C to ±4°C of the annealing temperature, especially for second and third generation AHSS grades.

[7] Some sections of this chapter have been disseminated in the following conference paper:

F.K. Suleiman, N.S. Narayanan, and K. J. Daun, 2023, "Investigating the *in situ* effects of selective oxidation on the radiative properties of advanced high strength steel," Proceedings of the 13th International Conference on Zinc & Zinc Alloy Coated Steel Sheet, Seoul, South Korea.

While the Bayesian pyrometry model incorporates uncertainty introduced by several variables (i.e., spectral emissivity, calibration coefficients and measurement noise), the imperfectly known emissivity has been identified as the major source of uncertainty, influencing the width of the temperature posterior distribution. The *ex situ*-based emissivity prior used for DP980 alloy in previous studies [143, 158] (i.e., Chapters 6 and 7) has a wide density width (i.e., less information content) which is flexible enough to handle a wide range of emissivity variations across different dew points, but produces temperature uncertainties ranging from ±15°C to ±31°C (at 95% credibility interval), which is far greater than the desired temperature control window of ±2°C to ±4°C. Furthermore, although the width of the inferred-temperature posterior typically captures the thermocouple temperature, the absolute error on the MAP point estimates can range from ±3°C to ±74°C, with the higher errors occurring at the lower annealing temperatures (≤ 600°C). The precision and accuracy of the posterior obtained with the current emissivity prior are far from the temperature control requirements, therefore it is critical to optimize the information content of the emissivity prior distributions to improve the accuracy of the MAP temperature estimate while minimizing the uncertainty (width) of the posterior temperature distribution.

To address this challenge, this chapter introduces the conditional emissivity prior approach to represent the state of knowledge about the imperfectly known radiative properties of the AHSS alloy. A prior specification parameter increases the information content of the specified prior distribution (i.e., narrower width) without sacrificing the flexibility to adapt with the evolving emissivity. The prior specification parameters explored in this chapter are the annealing dew point and the equivalent blackbody temperature of the AHSS surface during annealing. Since the equivalent blackbody temperature is derived from time-resolved emittance data, the emissivity prior adapts to the changing surface state during the annealing process, thereby improving the accuracy and precision of the temperature posterior.

In addition to improving the accuracy of the temperature posterior, this chapter investigates the correlation between variations in spectral emissivity and the evolving surface selective oxides for a high manganese dual-phase alloys (DP980 and DP780) annealed at dew points of −30°C and −45°C. Spectral emissivity variations were observed across samples annealed at the same dew point, highlighting the impact of oxidation on the development of selective oxides. Comparing the emissivity of the dual-phase alloys against a standard EDDS grade IF steel showed peaks in the

evolving spectral emissivity around 700°C, which suggests the transformation of manganese oxide to mixed oxides.

9.1. Bayesian pyrometry model

The Bayesian pyrometry model introduced in Chapter 6 provides a statistically robust approach for accounting for the uncertainties associated with the varying and imperfectly known spectral emissivity. The Bayes' equation relating all pertinent pyrometry variables is re-stated as:

$$p\left(T,\boldsymbol{\varepsilon},\mathbf{K}\middle|\mathbf{S}\right)=\frac{p\left(\mathbf{S}\middle|T,\boldsymbol{\varepsilon},\mathbf{K}\right)p_{\text{pr}}\left(T,\boldsymbol{\varepsilon},\mathbf{K}\right)}{p\left(\mathbf{S}\right)}\propto p\left(\mathbf{S}\middle|T,\boldsymbol{\varepsilon},\mathbf{K}\right)p_{\text{pr}}\left(T\right)p_{\text{pr}}\left(\boldsymbol{\varepsilon}\right)p_{\text{pr}}\left(\mathbf{K}\right) \tag{9.1}$$

For a three channel multi-wavelength (MW) pyrometer, $\mathbf{S} = [S_{\lambda 1}, S_{\lambda 2}, S_{\lambda 3}]^{\text{T}}$, $\boldsymbol{\varepsilon} = [\varepsilon_{\lambda d1}, \varepsilon_{\lambda d2}, \varepsilon_{\lambda d3}]^{\text{T}}$, and $\mathbf{K} = [K_{\lambda 1}, K_{\lambda 2}, K_{\lambda 3}]^{\text{T}}$ contain the counts, spectral emissivity, and calibration factors at the detection wavelengths, respectively, and T is the temperature of the AHSS steel. The posterior PDF, $p(T, \boldsymbol{\varepsilon}, \mathbf{K}|\mathbf{S})$, defines the probability of these parameters (T, $\boldsymbol{\varepsilon}$, $\mathbf{K}$) being correct given the observed pyrometry counts, $\mathbf{S}$, while the likelihood $p(\mathbf{S}|T, \boldsymbol{\varepsilon}, \mathbf{K})$ defines the probability of observing the pyrometry count data, $\mathbf{S}$, conditional on measurement noise, calibration error, and uncertain radiative properties. The evidence, $p(\mathbf{S})$, is a normalizing constant that ensures that the posterior satisfies the Law of Total Probability.

The likelihood depends on a measurement model derived from Wien's approximation to Planck's distribution [19]

$$S_{\lambda\text{d}}\propto\varepsilon_{\lambda\text{d}}I_{\lambda\text{b,d}}\left(\lambda_{\text{d}},T\right)=K_{\lambda\text{d}}\cdot\varepsilon_{\lambda\text{d}}\cdot\frac{C_1}{\lambda_{\text{d}}^5\left[\exp\left(\frac{C_2}{\lambda_{\text{d}}T}\right)-1\right]}\approx\frac{K_{\lambda\text{d}}\cdot\varepsilon_{\lambda\text{d}}C_1}{\lambda_{\text{d}}^5\exp\left(\frac{C_2}{\lambda_{\text{d}}T}\right)} \tag{9.2}$$

where $I_{\lambda\text{b,d}}$ is the blackbody intensity at T, $C_1 = 1.191\times10^8$ W·μm^4/m^{2}sr, and $C_2 = 1.439$ μm·K.

The prior PDF, $p_{\text{pr}}(T, \boldsymbol{\varepsilon}, \mathbf{K})$, defines what is known about the strip temperature, radiative properties, and calibration constants before the measurements (e.g., through *ex situ* or *in situ* radiometric measurements and an offline calibration procedure). As discussed in Chapter 6, the priors for T, $\boldsymbol{\varepsilon}$, and $\mathbf{K}$ are assumed to be independent. Similarly, the prior distributions, $p_{\text{pr}}(T)$, $p_{\text{pr}}(\boldsymbol{\varepsilon})$, and $p_{\text{pr}}(\mathbf{K})$, and the likelihood distribution, $p(\mathbf{S}|T, \boldsymbol{\varepsilon}, \mathbf{K})$, are defined as normally distributed, which allows the posterior distribution, $p(T, \boldsymbol{\varepsilon}, \mathbf{K}|\mathbf{S})$, to be approximated as a Gaussian distribution.

Compared to the point temperature estimates obtained with typical MW algorithms, estimating a posterior temperature distribution provides a measure of the expected error in the inferred temperature based on the uncertainties introduced by measurement noise, calibration noise and, most importantly, the imperfectly known spectral emissivity. Ultimately, the Bayesian pyrometry model aims to provide steelmakers with a measure of uncertainty in the strip temperature that can easily be compared against predefined temperature tolerance for the mechanical properties of the AHSS grades. However, this objective can only be achieved if the prior distributions defined for each parameter accurately maximizes the information entropy to prevent under- or over-estimation of the temperature posterior density.

9.1.1. Conditional emissivity prior

The spectral emissivity of AHSS alloys is described as imperfectly known because it is difficult to understand and model the radiative properties of the alloy with respect to the many material properties and process parameters that govern the annealing process (e.g., wavelength, temperature, dew point, alloy composition, pre-annealed surface state, oxide layer thickness, oxide growth kinetics, etc.). Previous works on deterministic MW compensation algorithms have provided insight into the factors influencing emissivity variation by incorporating material and process parameters as latent or explanatory variables in the emissivity model, essentially creating a multivariate emissivity algorithm. There are many ways to define probabilistic multivariate priors in the Bayesian context, primarily by incorporating hierarchical structures and conditional dependencies. Hierarchical priors involve specifying a multi-level structure wherein the emissivity prior depends on the distribution of the latent or explanatory variables. Conditional priors, on the other hand, treat the latent or explanatory variables as conditioning factors, which affect the spectral emissivity prior distribution in an explicit way.

This present work will focus on defining a multivariate emissivity prior that accounts for the interdependent effects of atmosphere dew point, T_{dp}, and the equivalent blackbody temperature, $\mathbf{T}_{be}$, on the spectral emissivity of dual-phase AHSS alloys. $\mathbf{T}_{be}$ is a vector of the equivalent blackbody temperature of the steel surface at each wavelength, i.e., $\mathbf{T}_{be} = [T_{be\lambda 1}, T_{be\lambda 2}, T_{be\lambda 3}]^T$. The spectral equivalent blackbody temperature, $T_{be\lambda}$, is the temperature at which a perfect emitter will emit the same spectral intensity as the steel surface. At each time step, $\mathbf{T}_{be}$ is calculated from the measured spectral intensity, **S,** using Eq. (9.2) with $\varepsilon_{\lambda d} = 1$, such that

$$T_{\mathrm{be}\lambda\mathrm{d}} \approx \frac{C_2}{\lambda_{\mathrm{d}} \ln\left[\dfrac{K_{\lambda\mathrm{d}} \cdot C_1}{\lambda_{\mathrm{d}}^5 S_{\lambda\mathrm{d}}}\right]} \tag{9.3}$$

The annealing dew point is best described as an explanatory variable because it is a parameter specified before the annealing process but the equivalent blackbody temperature is a latent variable because it is inferred from the measurement obtained during annealing. Incorporating $\mathbf{T}_{\mathrm{be}}$ as a latent variable in the emissivity prior provides a good approximation for how the radiative properties change with the annealing temperature.

All quantities in the Bayesian context, including T_{dp} and $\mathbf{T}_{\mathrm{be}}$, are represented as random variables that obey a probability distribution reflecting the state of knowledge of that variable. There are many ways to define a distribution for a given dew point, T_{dp}, with the simplest form being a normal distribution that represents the measurement noise and variations in the dew point values during the annealing process, i.e., $p(T_{\mathrm{dp}}) \sim \mathcal{N}(\mu_{\mathrm{dp}}, \sigma_{\mathrm{dp}}^2)$. Next, for the equivalent blackbody temperature, since $\mathbf{T}_{\mathrm{be}}$ depends on $\mathbf{S}$, the measurement noise on the spectral intensity at each time step will be numerically propagated to give the distribution for $p(\mathbf{T}_{\mathrm{be}})$ such that, $p(\mathbf{T}_{\mathrm{be}}) = p(\mathbf{T}_{\mathrm{be}}|\mathbf{S}) \sim \mathcal{N}(\boldsymbol{\mu}_{\mathrm{be}}, \boldsymbol{\Gamma}_{\mathrm{be}})$. Therefore, the spectral emissivity prior, $p_{\mathrm{pr}}(\boldsymbol{\varepsilon}) \sim \mathcal{N}(\boldsymbol{\mu}_{\varepsilon}, \boldsymbol{\Gamma}_{\varepsilon})$, becomes a hierarchical prior with $\boldsymbol{\mu}_{\varepsilon}$ and $\boldsymbol{\Gamma}_{\varepsilon}$ determined by marginalizing over the possible values of T_{dp} and $\mathbf{T}_{\mathrm{be}}$:

$$p_{\mathrm{pr}}\left(\boldsymbol{\varepsilon}\right) = \iint p\left(\boldsymbol{\varepsilon}\middle|T_{\mathrm{dp}}, \mathbf{T}_{\mathrm{be}}\right) p\left(\mathbf{T}_{\mathrm{be}}\middle|\mathbf{S}\right) p\left(T_{\mathrm{dp}}\right) d\mathbf{T}_{\mathrm{be}} dT_{\mathrm{dp}} \tag{9.4}$$

where $p(\boldsymbol{\varepsilon}|\ T_{\mathrm{dp}}, \mathbf{T}_{\mathrm{be}})$ is the probability distribution of the spectral emissivity prior given the variables T_{dp} and $\mathbf{T}_{\mathrm{be}}$. It is assumed that T_{dp} and $\mathbf{T}_{\mathrm{be}}$ are conditionally independent. The marginalized distribution, $p_{\mathrm{pr}}(\boldsymbol{\varepsilon})$, incorporates the uncertainty introduced by T_{dp} and $\mathbf{T}_{\mathrm{be}}$.

Given the wide range of values that the continuous variables T_{dp} and $\mathbf{T}_{\mathrm{be}}$ can hold, to obtain obtaining $p_{\mathrm{pr}}(\boldsymbol{\varepsilon})$ by marginalizing $p(\boldsymbol{\varepsilon}|\ T_{\mathrm{dp}}, \mathbf{T}_{\mathrm{be}})$ over all the possible values of T_{dp} and $\mathbf{T}_{\mathrm{be}}$ is a computational expensive step. Moreover, the uncertainty (width) of $p_{\mathrm{pr}}(\boldsymbol{\varepsilon})$ depends on the uncertainty introduced by $p(T_{\mathrm{dp}})$ and $p(\mathbf{T}_{\mathrm{be}})$, so integrating over the entire range of possible values for both variables will result in a wider emissivity prior. To address this, a two-step discretization system is introduced to simplify the complex relationship between T_{dp}, $\mathbf{T}_{\mathrm{be}}$, and $\boldsymbol{\varepsilon}$.

First, an index, i, is defined to represent a discrete number of possible dew points, $T_{\mathrm{dp},i}$, for the annealing process. This treatment is justified because a finite number of possible dew points

are normally used for AHSS processing (e.g., −50°C, −30°C, +5°C, etc.). This approach also significantly reduces the number of annealing experiments that need to be conducted to collect sufficient empirical data to build the distribution for $p(\boldsymbol{\varepsilon}|\, T_{\mathrm{dp}},\mathbf{T}_{\mathrm{be}})$. Next, for each i-th nominal dew point value, i.e., $T_{\mathrm{dp},i}$, the continuous equivalent blackbody temperature at each wavelength and time step, $T_{\mathrm{be}\lambda\mathrm{d}}$, is discretized into j categorical bins based on predefined bin boundaries.

$$T_{\mathrm{be}\lambda\mathrm{d}} \mapsto r_{j\lambda\mathrm{d}} \in \left\{r_{1,\lambda\mathrm{d}}, r_{2,\lambda\mathrm{d}}, \cdots, r_{j,\lambda\mathrm{d}}\right\}$$
$$r_{j,\lambda\mathrm{d}}\left(T_{\mathrm{be}\lambda\mathrm{d}}\right) = \begin{cases} r_{1,\lambda\mathrm{d}} & \text{if } T_{\mathrm{be}\lambda\mathrm{d}} \in \left[x_{\min,1}, x_{\max,1}\right) \\ r_{2,\lambda\mathrm{d}} & \text{if } T_{\mathrm{be}\lambda\mathrm{d}} \in \left[x_{\min,2}, x_{\max,2}\right) \\ \vdots & \vdots \\ r_{j,\lambda\mathrm{d}} & \text{if } T_{\mathrm{be}\lambda\mathrm{d}} \in \left[x_{\min,j}, x_{\max,j}\right] \end{cases} \tag{9.5}$$

where r_1, r_2, …, r_j are the bin labels, and $[x_{\min,j}\ ,\ x_{\max,j}]$ defines the bin boundaries, i.e., a specific range of equivalent blackbody temperature for each bin, r_j. To simplify the bin assignment process, the same bin boundaries are used for the three detection wavelengths, i.e., $[x_{\min,j}\ ,\ x_{\max,j}]$, are independent of wavelength. However, given that the equivalent blackbody temperature varies with wavelength, each $T_{\mathrm{be}\lambda\mathrm{d}}$ will fall within a different boundary and thus would have a different bin index. After assigning each $T_{\mathrm{be}\lambda\mathrm{d}}$ to a bin, this creates a vector, $\mathbf{r}$, of bin assignments for the three detection wavelengths at each time step, i.e., $\mathbf{r} = [r_{j\lambda1}, r_{j\lambda2}, r_{j\lambda3}]^{\mathrm{T}}$.

With this two-step discretization system, the spectral emissivity prior, $p_{\mathrm{pr}}(\boldsymbol{\varepsilon})$, becomes

$$p_{\mathrm{pr}}\left(\boldsymbol{\varepsilon}\right) = \sum_{i} p\left(T_{\mathrm{dp},i}\right) \sum_{\mathbf{r}} \int_{\mathbf{T}_{\mathrm{be}} \in \Re(\mathbf{r})} p\left(\boldsymbol{\varepsilon} \,|\, T_{\mathrm{dp},i}, \mathbf{r}\right) p\left(\mathbf{r} \,|\, \mathbf{T}_{\mathrm{be}}, T_{\mathrm{dp},i}\right) p\left(\mathbf{T}_{\mathrm{be}} \,|\mathbf{S}\right) d\mathbf{T}_{\mathrm{be}} \tag{9.6}$$

where $p(T_{\mathrm{dp},i})$ is the probability of annealing at a dew point level, $T_{\mathrm{dp},i}$, $p(\mathbf{r} \mid \mathbf{T}_{\mathrm{be}},\ T_{\mathrm{dp},i})$ is the probability of the bin assignments $\mathbf{r}$ given the dew point, $T_{\mathrm{dp},i}$ and the equivalent blackbody temperature, $\mathbf{T}_{\mathrm{be}}$, and $p(\mathbf{e} \mid \mathbf{r},\ T_{\mathrm{dp},i})$ is the likelihood of the emissivity given the dew point value $T_{\mathrm{dp},i}$, and the bin assignments, $\mathbf{r}$. The integral, $\int_{\mathbf{T}_{\mathrm{be}} \in \Re(\mathbf{r})} d\mathbf{T}_{\mathrm{be}}$ integrates over values of $\mathbf{T}_{\mathrm{be}}$ that fall within the bin ranges defined by $\mathbf{r}$. $\Re(\mathbf{r})$ defines the integration limits, i.e., the bin boundaries ($[x_{\min,j},\ x_{\max,j}]$) imposed on each element of $\mathbf{T}_{\mathrm{be}}$ by the bin assignment process, such that, $\Re(\mathbf{r}) = \left\{\mathbf{T}_{\mathrm{be}} \middle| T_{\mathrm{be}\lambda\mathrm{d}} \in \left[x_{\min,j}, x_{\max,j}\right] \text{ for each } \lambda_{\mathrm{d}}\right\}$. $\sum_{\mathbf{r}}$ sums over all the possible bin assignments across all detection wavelengths, λ_{d}, to account for uncertainty in the bin assignment process. This ensures that $p_{\mathrm{pr}}(\boldsymbol{\varepsilon})$ reflects the uncertainty of all the possible bin assignment for a given $\mathbf{T}_{\mathrm{be}}$.

However, if the bin boundaries are clearly defined with no overlap, ensuring no uncertainty in the bin assignment process, each $\mathbf{T}_{be}$ will be deterministically assigned to a unique $\mathbf{r}$. This eliminates the summation over $\mathbf{r}$ and sets the probability, $p(\mathbf{r} \mid \mathbf{T}_{be}, T_{dp,i}) = 1$, which gives:

$$p_{pr}(\boldsymbol{\varepsilon}) = \sum_i p\left(T_{dp,i}\right) \int_{\mathbf{T}_{be} \in \Re(\mathbf{r})} p\left(\boldsymbol{\varepsilon} \mid T_{dp,i}, \mathbf{r}\right) p\left(\mathbf{T}_{be} \mid \mathbf{S}\right) d\mathbf{T}_{be} \tag{9.7}$$

Equivalently, the summation accounts for uncertainty in the annealing dew point by summing over all the possible annealing dew points that influence the annealing process and thus $p_{pr}(\boldsymbol{\varepsilon})$. This is a useful step when there is ambiguity on the exact annealing dew point, or it falls between two or more predefined dew point levels. This summation is also useful when defining a general emissivity prior to compensate for changes in emissivity associated with varying dew points. However, when emissivity variation is aggregated over several dew point levels, the resulting general emissivity prior, $p_{pr}(\boldsymbol{\varepsilon})$, reflects a greater amount of uncertainty, especially if the radiative properties of the material varies significantly across those dew point levels.

In this work, the dew point is assumed to be perfectly known and held constant at a single value. Therefore, there is no need to sum over all the possible dew point values and the prior for the dew point reduces to $p(T_{dp,i}) = 1$. This further simplifies the emissivity prior, $p_{pr}(\boldsymbol{\varepsilon})$:

$$p_{pr}(\boldsymbol{\varepsilon}) = \int_{\mathbf{T}_{be} \in \Re(\mathbf{r})} p\left(\boldsymbol{\varepsilon} \mid T_{dp,i}, \mathbf{r}\right) p\left(\mathbf{T}_{be} \mid \mathbf{S}\right) d\mathbf{T}_{be} \tag{9.8}$$

Finally, given that $\mathbf{T}_{be}$ is only used to determine the bin indices, $\mathbf{r}$, this can be further simplified by ignoring the uncertainty introduced into our estimate of $\mathbf{T}_{be}$ with the assumption that the measurement noise in $\mathbf{S}$ is not significant enough to influence the bin assignment. Therefore, $p(\mathbf{T}_{be}|\mathbf{S})$ becomes a Dirac delta function centered on the value of $\mathbf{T}_{be}(\mathbf{S})$ obtained via Eq. (9.3), and $\int_{\mathbf{T}_{be} \in \Re(\mathbf{r})} \delta\left(\mathbf{T}_{be} - \mathbf{T}_{be}\left(\mathbf{S}\right)\right) d\mathbf{T}_{be} = 1$. The final simplified expression for $p_{pr}(\boldsymbol{\varepsilon})$ becomes:

$$p_{pr}(\boldsymbol{\varepsilon}) = p\left(\boldsymbol{\varepsilon} \mid T_{dp,i}, \mathbf{r}\left(\mathbf{T}_{be}\right)\right) \tag{9.9}$$

With the two-step discretization system and the deterministic approximations for $T_{dp,i}$, $\mathbf{T}_{be}$, and $\mathbf{r}$, the hierarchal emissivity prior in Eq. (9.4) reduces to the conditional emissivity prior in Eq. (9.9) as the emissivity distribution is explicitly specified by the nominal values of $T_{dp,i}$ and $\mathbf{r}(\mathbf{T}_{be})$.

Although defining the conditional emissivity prior seems numerically complex, empirically, the data collection and implementation of the two-step discretization system is much

simpler. First, replicates of a given AHSS grade are annealed at a nominal dew point, $T_{\mathrm{dp},i}$. Then the spectral emissivity, at each time step is assigned to a bin, **r**, based on the j-index specified by the corresponding equivalent black body temperature, $\mathbf{T}_{\mathrm{be}}$, at that time step. When all the emissivity values have been assigned, the mean and variance of each bin at each wavelength is first evaluated, followed by all possible combinations of bin pairs across wavelengths to obtain the inter-wavelength and inter-bin covariance. The conditional emissivity prior obtained empirically can be summarized as follows:

$$p_{pr}\left(\boldsymbol{\varepsilon}\right) = p_{\mathrm{pr}}\left(\boldsymbol{\varepsilon}\right) = p\left(\boldsymbol{\varepsilon} \mid T_{\mathrm{dp},i}, \mathbf{r}\left(\mathbf{T}_{\mathrm{be}}\right)\right) \sim \mathcal{N}\left(\boldsymbol{\mu}_{\varepsilon}, \boldsymbol{\Gamma}_{\varepsilon}\right)$$

$$\boldsymbol{\mu}_{\varepsilon} = \begin{bmatrix} \mu_{\varepsilon_{\lambda 1, r_{j,\lambda 1}}} \\ \mu_{\varepsilon_{\lambda 2, r_{j,\lambda 2}}} \\ \mu_{\varepsilon_{\lambda 3, r_{j,\lambda 3}}} \end{bmatrix}, \quad \boldsymbol{\Gamma}_{\varepsilon} = \begin{bmatrix} \sigma^2_{\varepsilon_{\lambda 1, r_{j,\lambda 1}}} & \mathrm{cov}\left(\varepsilon_{\lambda 1, r_{j,\lambda 1}}, \varepsilon_{\lambda 2, r_{j,\lambda 2}}\right) & \mathrm{cov}\left(\varepsilon_{\lambda 1, r_{j,\lambda 1}}, \varepsilon_{\lambda 3, r_{j,\lambda 3}}\right) \\ \mathrm{cov}\left(\varepsilon_{\lambda 1, r_{j,\lambda 1}}, \varepsilon_{\lambda 2, r_{j,\lambda 2}}\right) & \sigma^2_{\varepsilon_{\lambda 2, r_{j,\lambda 2}}} & \mathrm{cov}\left(\varepsilon_{\lambda 2, r_{j,\lambda 2}}, \varepsilon_{\lambda 3, r_{j,\lambda 3}}\right) \\ \mathrm{cov}\left(\varepsilon_{\lambda 1, r_{j,\lambda 1}}, \varepsilon_{\lambda 3, r_{j,\lambda 3}}\right) & \mathrm{cov}\left(\varepsilon_{\lambda 2, r_{j,\lambda 2}}, \varepsilon_{\lambda 3, r_{j,\lambda 3}}\right) & \sigma^2_{\varepsilon_{\lambda 3, r_{j,\lambda 3}}} \end{bmatrix} \tag{9.10}$$

To apply the conditional emissivity prior during annealing, the dew point value, $T_{\mathrm{dp},i}$, and the equivalent blackbody temperature, $\mathbf{T}_{\mathrm{be}}$, at each time step is used to determine the appropriate bin indices vector, **r**, which defines the terms of the conditional emissivity prior in Eq. . This prior is then be used in Eq. (9.1) to obtain the MAP estimate and credibility interval of the pyrometrically-inferred temperature. If multiple dew points are used in a CGL or annealing setup, these steps are repeated for each dew point to obtain its corresponding conditional emissivity prior.

9.2. Annealing experimental procedure

Cold-rolled as-received dual-phase AHSS alloys (DP780 and DP980) are processed following the steps in Sections 7.1. The specific Si/Mn ratio for the alloys are summarized in Table 9.1. The location column describes the sample extraction location along the length of AHSS coil and the rolling direction of the coil respective to the 15 cm length of the extracted samples.

Table 9.1. Silicon-to-manganese ratio (Si/Mn), coil extraction location and annealing dew point for the AHSS alloys. The Si/Mn ratio was obtained by spark atomic emission spectrometry.

Sample No.	Alloy	Si/Mn	Location	Dew point
#1	DP980	0.04	Centre, Longitudinal	−30°C
#2				−45°C
#3	DP780	0.10	Head, Transverse	−45°C
#4	IF	-	-	−30°C

In this study, the radiative properties of the dual phase AHSS alloys are compared against a standard extra deep drawing steel (EDDS) grade IF steel (Sample #4) annealed at −30°C, to highlight variations in radiative properties due to the selective oxidation of the alloying elements in the dual phase AHSS alloys. All the steel samples are annealed in a 95% N_2-5% H_2 reducing atmosphere at the dew points listed in Table 9.1.

The samples are annealed in the chamber (Section 4.3) following the same sample preparation step and heating schedule laid out in the previous chapters. Prior to annealing, the pre-annealed radiative properties are characterized with a Bruker Invenio-X FTIR spectrometer. During heating, the emitted radiation from the sample is recorded with the OceanOptics NIRQuest512 spectrometer for wavelengths ranging from 1.2 μm − 2.5 μm. The pyrometrically-inferred temperature is derived from the spectrometer data at 1.6 μm, 2.1 μm and 2.4 μm, which corresponds to the detection wavelength of the industrial multi-wavelength pyrometer (Williamson PRO MWX-ST-17).

9.3. Variations in radiative properties

9.3.1. Pre-annealed radiative properties

Evaluating the pre-annealed radiative properties of the alloys ensures that the effect of the annealing process parameters on the radiative properties are uncoupled from the effects of the upstream processes on the radiative properties of the steel.

The *ex situ* near-infrared spectral emissivity of the cold-rolled, as-received, steel samples was measured with an integrating sphere attachment on the FTIR spectrometer. As discussed in Section 8.3, the measurement uncertainty of the FTIR is approximately ±3% with an additional ±5% introduced by the sample orientation during measurement.

Figure 9.1 shows that the pre-annealed spectral emissivity of all three steel grades have nearly identical slope. While the spectral emissivity of the DP980 samples is highest followed by the IF and then the DP780 samples, in the context of the overall measurement uncertainty (i.e., ±8%), the pre-annealed radiative properties of all samples are comparable. The two DP980 samples in Figure 9.1, i.e., Sample #1 and Sample #2, which will be annealed at −30°C and −45°C, respectively, have identical pre-annealing radiative properties. This means that any variations in the spectral emissivity for Samples #1 and #2 observed *in situ* can be solely attributed to the varying oxidation thermodynamics and kinetics during annealing.

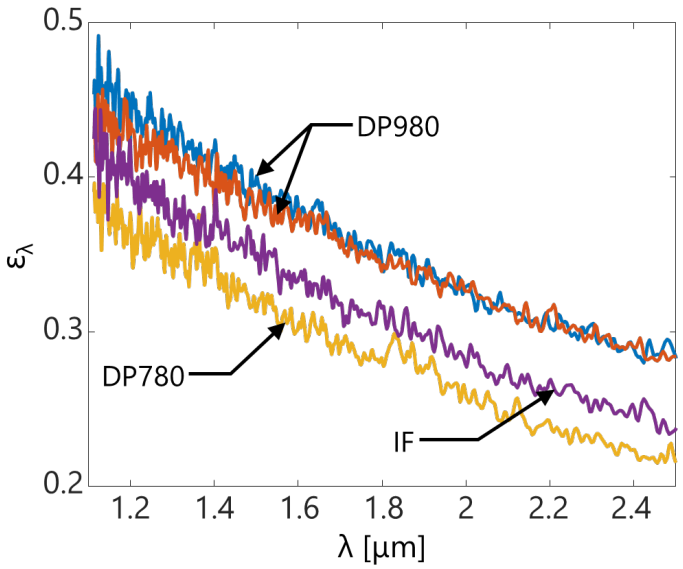


Figure 9.1. Pre-annealed spectral emissivity, ε_λ, for the AHSS and mild steel samples: DP980 (Samples #1 and #2), DP780 (Sample #3) and IF (Sample #4).

Prior to annealing, the radiative properties of these samples are predominantly influenced by variations in the surface topography of the steel. Therefore, analyzing the topographical features of the DP980, DP780 and IF samples can provide insights to the differences in their pre-annealed radiative properties. Figure 9.2 shows the optical micrographs and the roughness parameters obtained using a Keyence VHX 5000 optical microscope. The root-mean-square (RMS) roughness, S_q, and the surface slope, S_q/τ, are obtained by averaging three measurements on an individual sample. The optical images of the samples highlight that the DP780 has a 'pang' finish, a term used to describe the textured surface produced by electro-discharge texture (EDT) roll in the last stand of the cold-rolling process, while the DP980 and IF steel have bright finish typically achieved with the use ground rolls in the last stand. In terms of the roughness parameters, the surface slope unfortunately does not provide significant insight into the varying pre-annealed radiative properties, because the surface slope values for the three samples are much closer in magnitude, especially in comparison to the differences in their spectral emissivity. The lack of significant correlation between surface slope and radiative properties was also observed by Narayanan et al. [4] for DP780 samples, and was attributed to the presence of surface cavities that act as perfect emitters. Contrarily, the S_q values indicate that in the NIR wavelength range shown in Figure 9.1, the DP780 and IF samples are best described as optically-rough ($S_q/\lambda >> 1$) while the DP980 is optically-smooth ($S_q/\lambda << 1$). More specifically, the trend observed with the RMS

roughness suggests that the spectral emissivity decreases with increasing surface irregularities because the rougher surfaces produce multiple scattering events that redirect incident irradiation outwards, making the surfaces more diffuse-like [54, 79].

In previous studies by Lin et al. [74, 75], it was observed that the heterogeneity of the pre-annealed surface topography also influences the morphology of the oxide layer formed during annealing, with a uniform oxide layer more likely to form on smoother surfaces and more oxide nodules are typically found on rougher surfaces. While the scope of this chapter does not include the specific oxide morphology formed during annealing, it is important to consider how this could impact the varying *in situ* radiative properties, and thus the pyrometric estimates.

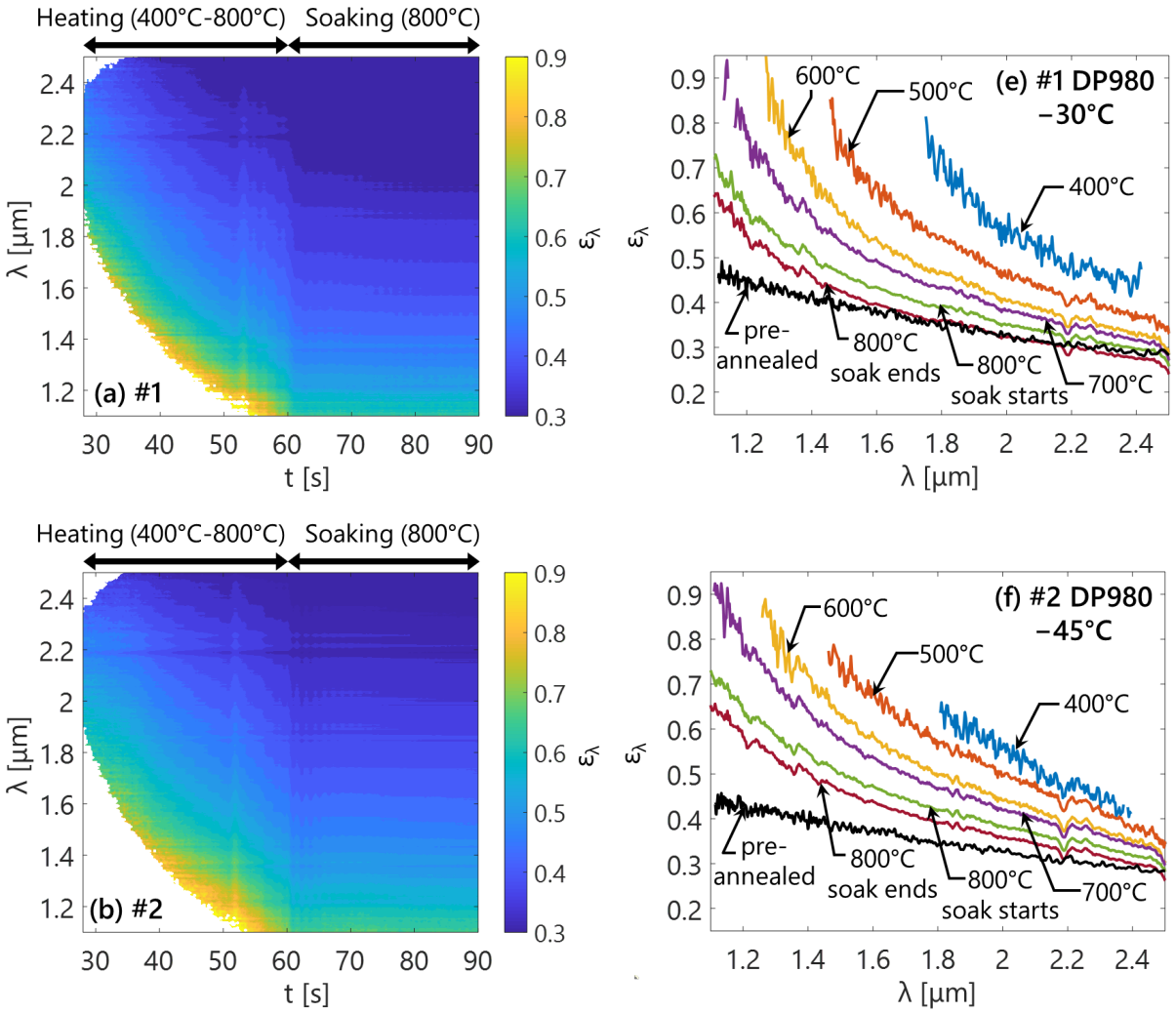


Figure 9.2. Optical micrographs and roughness parameters (S_q and S_q/τ) for the AHSS and mild steel samples: (a) DP980, DP780 and (c) IF.

9.3.2. *In situ* spectral emissivity variation

The plots in Figure 9.3 show the temporal and spectral variation in the normal spectral emissivity of the dual phase AHSS alloys calculated using Eq. (9.2), with $S_{\lambda d}$ and T obtained from the spectrometer and thermocouple measurements, respectively. The spectrometer calibration constant, $K_{\lambda d}$, is estimated using the absolute intensity calibration process. A first-order, three-frame Savitzky-Golay filter is also applied to minimize the effects of noise on the spectral signal.

Generally, the spectral emissivity of both the dual-phase and mild steels is observed to decrease with increasing temperature above 400°C and increasing wavelength, with the most significant changes occurring during the heating period. The wavelength-dependent variation in emissivity for all three steel grades is consistent with the trends observed so far in this dissertation.



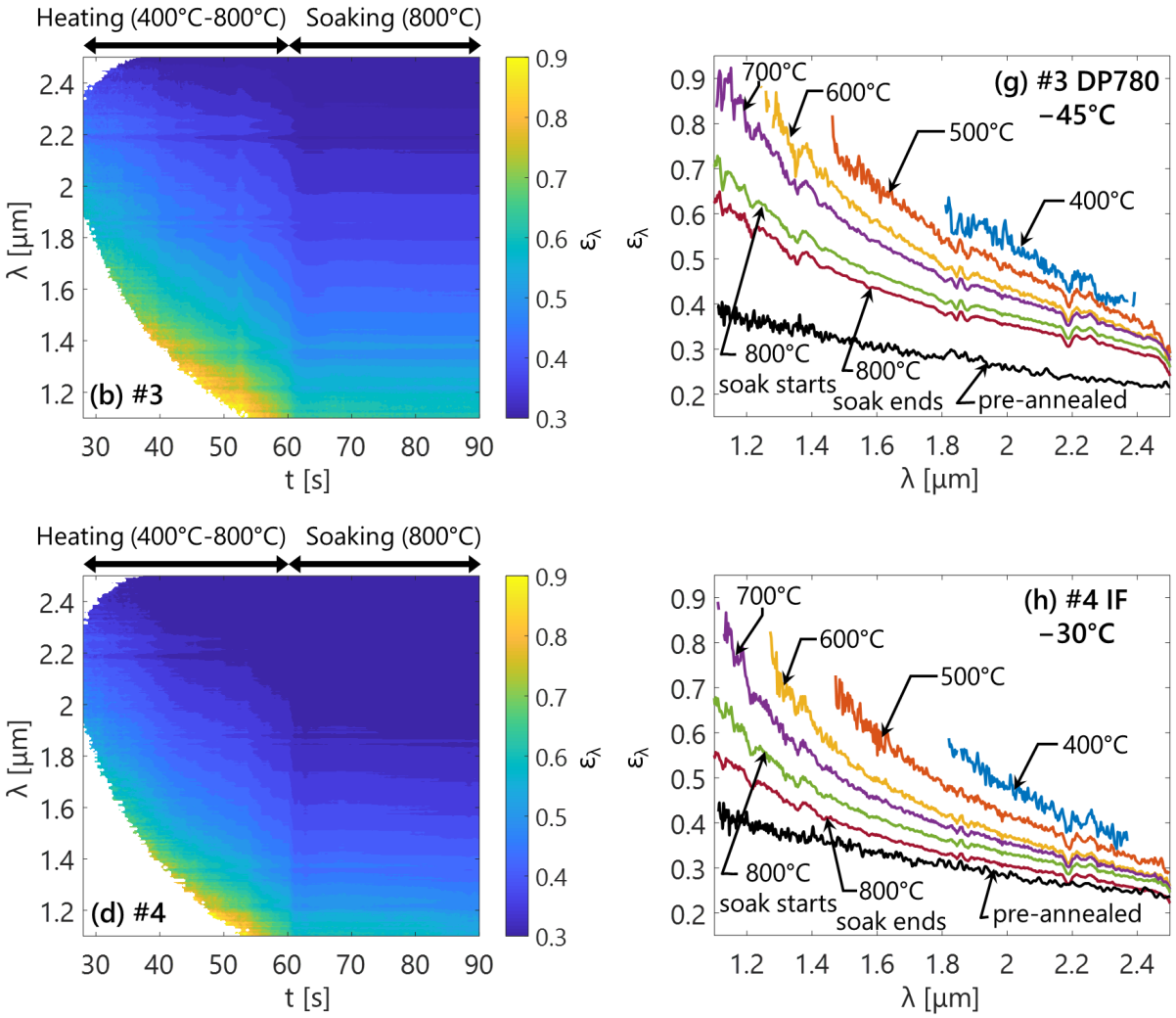


Figure 9.3. Evolving spectral emissivity, ελ, measured *in situ* as a function of time, wavelength and temperature for the annealed steel samples at their respective dew points: (a, e) Sample #1: DP980 at −30°C DP; (b, f) Sample #2: DP980 at −45°C DP; (c, g) Sample #3: DP780 at −45°C DP; and (d, h) Sample #4: IF at −30°C DP. The graphs on the right (e, f, g, and h) show the spectral emissivity at nominal temperatures relative to the pre-annealed values from Figure 9.1.

While the emissivity spectra in Figure 9.3 reveal wavelength-dependent trends at approximately 1.4 μm, 1.9 μm, and 2.2 μm; further analysis is required to exclude the influence of participating media at these wavelengths. Therefore, this chapter will focus on analyzing the spectra at the three detection wavelengths (1.6 μm, 2.1 μm, and 2.4 μm) of a commercial multi-wavelength pyrometer (Williamson PRO MWX-ST-17). The wavelengths of industrial pyrometers are typically selected to minimize the influence of participating media such as water vapour, flames, steam, and combustion products [159].

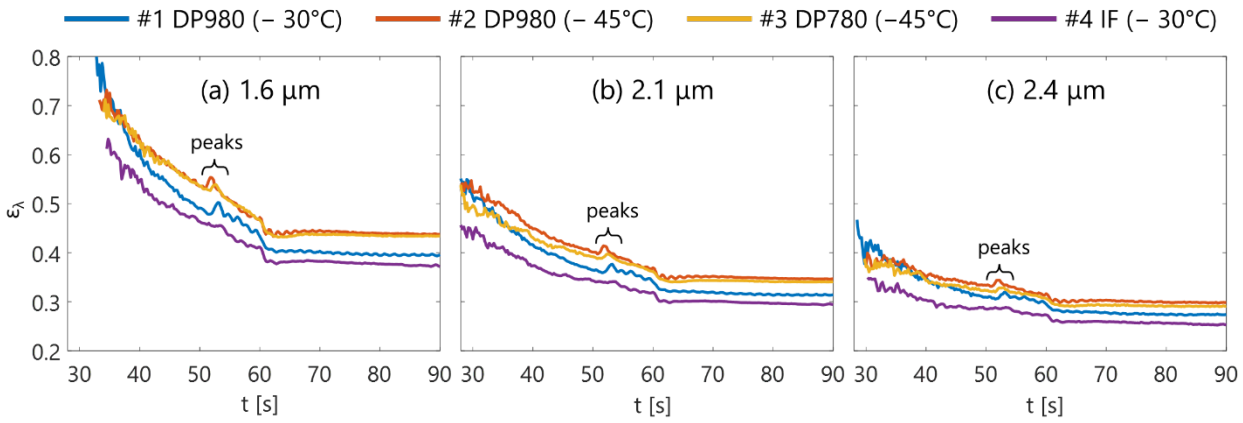


Figure 9.4. Temporal variations in the spectral emissivity at the pyrometry detection wavelengths: (a) 1.6 µm; (b) 2.1 µm; and (c) 2.4µm, highlighting the observed emissivity peaks.

Figure 9.4 and Figure 9.5 show the spectral emissivity of the dual-phase alloys, i.e., Samples #1, #2 and #3, relative to the IF mild steel (Sample #4) to highlight the impact of *in situ* selective oxidation on the varying radiative properties. The spectral emissivity curves of the dual-phase alloys are all higher than the emissivity curve of the IF steel. The oxygen potential diagram in Figure 2.6 and Ref. [74] indicates high thermodynamic stability for the formation of silicon, manganese and chromium oxides at dew points of −30°C and −45°C. However, whether the selective oxides form at the steel surface or subsurface depends on the inward flux of oxygen relative to the outward flux of alloying elements [42, 160]. Numerous studies have demonstrated that annealing AHSS alloys in low pO_2 atmospheres promote the formation of an external MnO layer compared to other oxides [44, 50, 78, 161, 162]. Lin et al. [74] also reported that the refractive indices of the DP980 alloy (Si/Mn = 0.04) annealed at 800°C and −30°C dew point are close to the published optical properties of MnO [163]. Therefore, given that spectral emissivity is a surface property, it is expected that the observed variation in spectral emissivity for the dual-phase alloys would be primarily influenced by differences in the morphology and kinetics of the Mn-rich oxide layer on the steel surface. Consequently, the difference in the radiative properties of the DP980 samples annealed at −30°C and −45°C (i.e., Samples #1 and #2, respectively) can be attributed to an increase in the outward flux of the manganese to the surface compared to the inward flux of oxygen. Sample #2, which was annealed at lower pO_2, showed higher spectral emissivity, indicating increased external oxidation.

Having the spectral emissivities at the three detection wavelengths side-by-side, as in Figure 9.4 and Figure 9.5, further highlights how the effect of an oxide layer on the radiative properties varies with wavelengths, with more pronounced effect at the shorter wavelengths. At the longest pyrometry wavelength (2.4 µm) in Figure 9.4 (c) and Figure 9.5 (c), the two dual-phase alloy grades (DP980 and DP780) exhibit very similar radiative properties irrespective of their pre-annealed surface topography, alloy composition, and annealing dew point. Knowledge of the relative sensitivity of the detection wavelengths to material and process parameters can be leveraged to design and improve the robustness of emissivity compensation algorithms.

Figure 9.4 also shows that the DP980 alloy (Sample #2) and the DP780 alloy (Sample #3), both annealed at −45°C, have very similar spectral emissivity values *in situ* at all wavelengths despite the differences in their alloy composition and pre-annealed radiative properties. This similarity suggest that the differences in the alloy composition of the two dual-phase alloys in this study are not significant enough to produce drastically different oxide layers, and furthermore, the high-temperature radiative properties of the resulting oxide layer dominate over the influence of the pre-annealed surface topography for the wavelength range considered in this study.

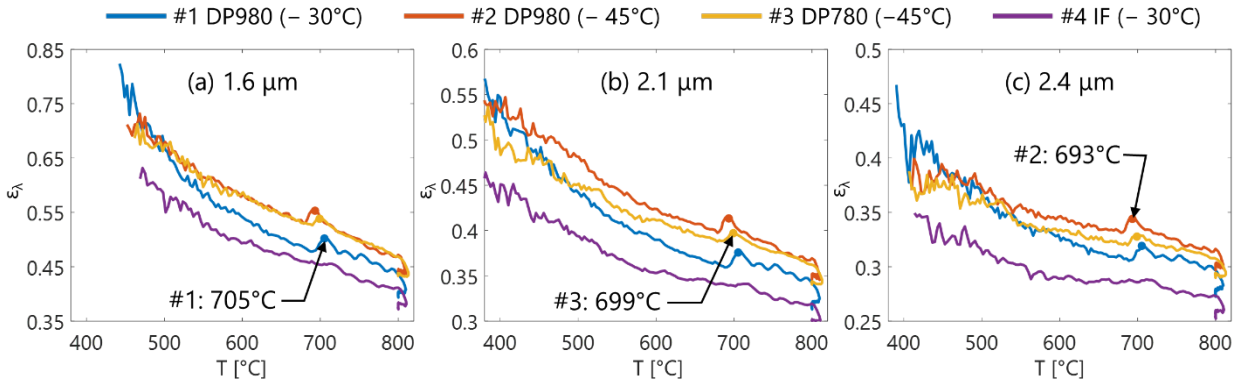


Figure 9.5. Spectral emissivity as a function of temperature at the pyrometry detection wavelengths: (a) 1.6 µm, (b) 2.1 µm, and (c) 2.4µm. The temperature of the emissivity peaks falling within a 12°C range (693°C - 705°C).

Additionally, the spectral emissivity curves of all dual-phase alloys (Samples #1 - #3) exhibit distinct peak identified around 50 - 60 seconds, which is absent for the IF steel (Sample #4). Plotting the emissivity against the temperature, Figure 9.5, reveals that this peak occurs at temperatures between 600°C and 700°C. Given the DP980 and DP780 alloy has a high Mn content (low Si/Mn ratios), this peak is most probably due to the decomposition of MnO to form Mn-Si

ternary oxides that are more thermodynamically stable [78]. Ham et al. [77] also observed changes in emissivity around 650°C due to the formation of Mn-Al mixed oxides in TRIP steel. In addition, the temperature and prominence of these peaks appear to depend slightly on the partial pressure of the annealing atmosphere and the extent of external oxidation, with the peak of the dual-phase steel sample annealed at higher dew point, i.e., Sample #1 at −30°C, occurring at a higher temperature compared to Samples #2 and #3.

9.4. Bayesian pyrometric temperature estimate

The first step towards defining more robust and precise prior distributions for the imperfectly known radiative properties of AHSS is to employ *in situ* spectral emissivity measurements since Chapter 6, Chapter 7 and Chapter 8 have clearly shown that radiative properties measured *ex situ* do not fully capture the emissivity variations observed *in situ* during annealing. Moreover, the introduction of $\mathbf{T}_{be}$ as a latent variable for the conditional emissivity prior is only possible with *in situ* measurements. This section focuses on demonstrating the impact of a conditional emissivity from *in situ* measurements on the temperature posterior uncertainty estimates. It is divided into three subsection as follows: Sec. 9.4.1 reviews the process of generating the conditional emissivity prior from *in situ* measurements on DP980 replicates annealed at −30°C; Sec, 9.4.2. discusses the accuracy and uncertainty of the pyrometrically-inferred temperature obtained with *in situ* conditional emissivity prior compared against the results from an *in situ* general emissivity prior and the *ex situ* emissivity prior from Chapter 6; and Sec. 9.4.3 presents a further validation of the conditional prior by evaluating the pyrometry estimates when applied to DP980 and other steel grades at various dew points.

9.4.1. Generating a conditional emissivity prior from *in situ* replicates

To illustrate the concept of the conditional emissivity prior, this chapter considers a single dew point level at −30°C, i.e., $T_{dp,i=1} = -30$°C, which will simply be referred to as T_{dp1} in subsequent references. Four samples of the DP980 alloy, which constitute replicates of Sample #1 discussed in Section 9.3, are annealed at T_{dp1} with the same heating schedule. Figure 9.6 shows the *in situ* spectral emissivities of the replicates alongside those of the primary sample (i.e., Sample #1) at the three detection wavelengths of the pyrometer. While the pre-annealed radiative properties, heating schedule and annealing dew point were kept constant for these specimens, the differences in the temporal variations of the radiative properties observed in Figure 9.6 indicates variations in

the oxidation kinetics and oxide morphology during annealing which in turn affects the spectral emissivity of the AHSS surface. The impact of this varying oxidation kinetics is more evident during the heating/ramp portion of the annealing cycle, especially at the shorter wavelength (1.6 µm). A clear illustration of this can be seen by comparing Replicates #1, #2, and #3, which all start out with similar radiative properties between 30 to 35 secs (around 400°C), but their radiative properties evolve differently with time and temperature especially for Replicate #1. Likewise, Sample #1 and Replicate #1 start out with different radiative properties at ~400°C (30 to 35 secs into the annealing cycle) but end up with surface states exhibiting similar radiative properties by the soak period of the annealing cycle.

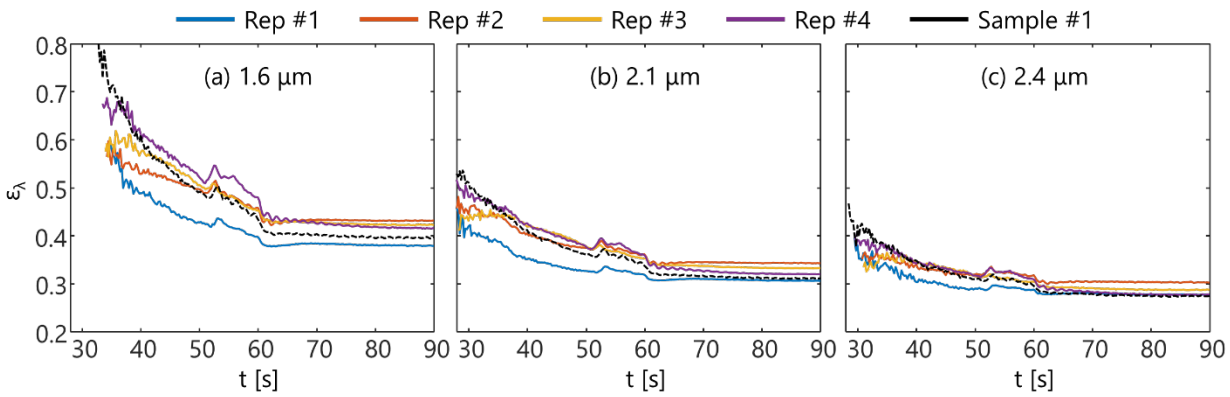


Figure 9.6. *In situ* spectral emissivity of the DP980 sample (Sample #1) and replicates (Replicate #1 - #4) annealed at $T_{dp1} = -30$°C. (a) 1.6 µm, (b) 2.1 µm, and (c) 2.4µm.

Prior to evaluating the equivalent blackbody temperature and implementing the two-step discretization system, the spectral emissivity measurements of the replicates (Rep #1- #4) in Figure 9.6 are first combined to form an *in situ* general emissivity prior distribution as shown in Figure 9.7. This *in situ* general prior represents the knowledge of the emissivity variation at the annealing dew point T_{dp1} across the temperature range of the annealing cycle (400°C - 800°C).

Compared to the *ex situ* emissivity prior introduced in Section 6.2.1, which used 27 emissivity measurements from exactly 27 samples, the *in situ* general emissivity prior in Figure 9.7 is derived from 900 measurements using four samples since the continuous nature of the *in situ* spectrometer measurements allows for more measurements over a wider temperature range without the need to quench the sample.

Although the distribution in Figure 9.7 is modeled as a Gaussian, the histogram of the spectral emissivities show that the data is skewed because we have more measurements at the soak

temperature of 800°C. Given the skewness, the mean of the fitted Gaussian distribution overestimates the spectral emissivity at 800°C, which would potentially bias the posterior. This illustrates the importance of ensuring that the data incorporated into a sample-based prior is robust and not biased to a specific annealing process parameter, such as the heating schedule in the case of Figure 9.7. While not the direct focus of this section, the bias introduced by the heating schedule can be minimized by reducing the amount of the soak period information incorporated in the sample-based prior, as long as the goal is to simply define one general prior distribution at T_{dp1}.

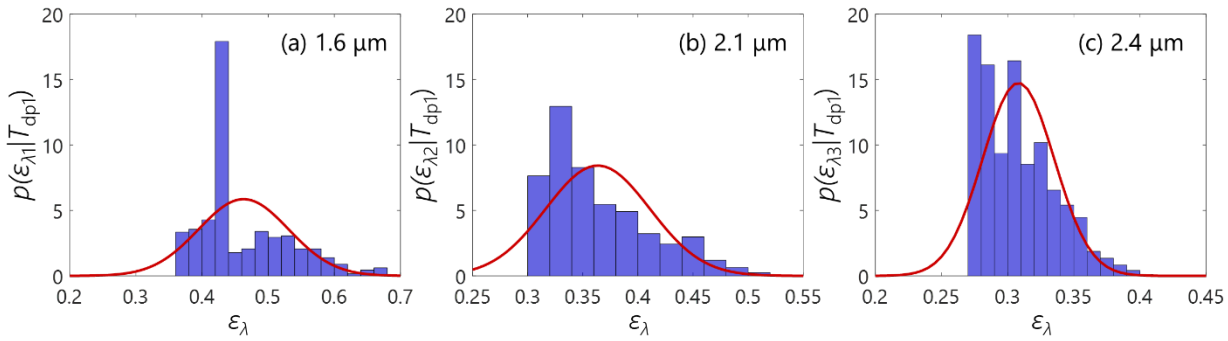


Figure 9.7. Histogram and Gaussian distribution fit for the *in situ* general emissivity distribution conditional on T_{dp1}, i.e., p(ε | T_{dp1}), at the three detection wavelengths: (a) 1.6 µm, (b) 2.1 µm, and (c) 2.4µm.

Next, the conditional *in situ* emissivity prior, $p(\boldsymbol{\varepsilon} \mid T_{dp1}, \mathbf{r}(\mathbf{T}_{be}))$, is fully defined with Eq. (9.3) applied to obtain the equivalent blackbody temperature, $\mathbf{T}_{be} = [T_{be\lambda 1}, T_{be\lambda 2}, T_{be\lambda 3}]^T$, for each of the replicates (Rep #1 - #4). Figure 9.8 plots the resulting $\mathbf{T}_{be}$ overlaid with six pre-defined bin boundaries, such that $\mathbf{r} = \{r_{j,\lambda d} \mid T_{be\lambda d} \in x_{min,j} \leq T_{be\lambda d} < x_{max,j}\}$. The bin boundaries were determined by the amount of variability in the spectral emissivity for a given temperature range $[x_{min,j}, x_{max,j})$ and not the difference between $x_{min,j}$ and $x_{max,j}$. For example, the fourth bin ($\mathbf{r}_4$: 500°C $\leq \mathbf{T}_{be} <$ 650°C) has the widest range, especially for $T_{be\lambda d}$ at 2.1 µm and 2.4 µm. However, looking at the corresponding time interval (45 secs to 90 secs) for 2.1 µm and 2.4 µm in Figure 9.6 shows that there are minimal variations in the spectral emissivity within this period. Discretizing $\mathbf{T}_{be}$ based on the corresponding emissivity variation ensures that the distribution for any given bin is not over-constrained as this would produce computational instability due to an ill-conditioned covariance matrix, $\boldsymbol{\Gamma}_\varepsilon$ [139].

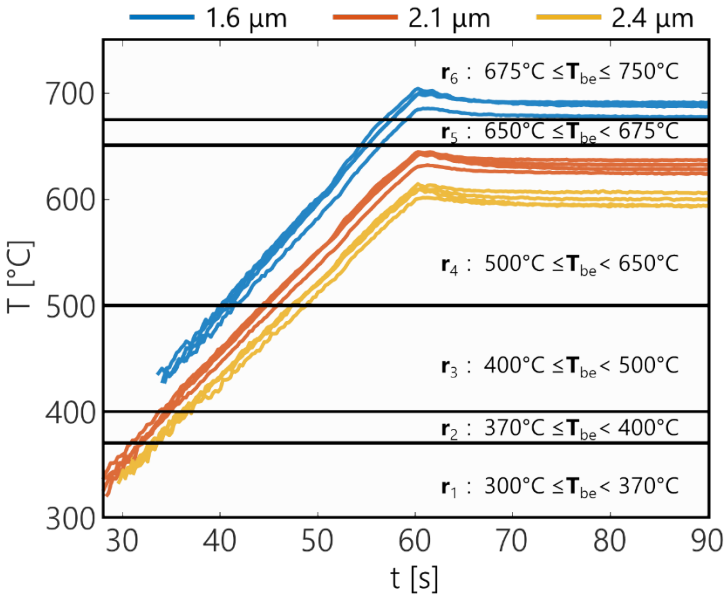


Figure 9.8. Plot of the equivalent black body temperatures, $\mathbf{T}_{be}$, for the DP980 replicates annealed at T_{pd1}, showing the bin labels, r_j, and the predefined bin boundaries.

Figure 9.9 shows the resulting conditional emissivity prior distributions, $p(\boldsymbol{\varepsilon} \mid T_{dp1}, \mathbf{r}(\mathbf{T}_{be}))$, from the *in situ* measurements on Rep #1 - #4 and based on the bin boundaries in Figure 9.8. It is observed that, contrary to Figure 9.7, the histogram for each bin, $r_{j,\lambda d}$, is symmetric, indicating that the process of discretizing the data by $\mathbf{T}_{be}$ reduced the apparent skewness in the initial general distribution. The symmetry in the data assigned to each bin makes the Gaussian distribution an appropriate representation of the prior knowledge since the uncertainty in the spectral emissivity is well-distributed around a central value. Although some of the bins (e.g., $r_{1,\lambda 1}$, $r_{5,\lambda 2}$, $r_{6,\lambda 3}$ etc.) are empty, this does not impact the posterior estimation because the emissivity values at the detection wavelengths are correlated. However, in the unlikely case that the model encounters outliers assigned to an empty bin, the prior at that wavelength will adopt the distribution of the nearest non-empty bin.

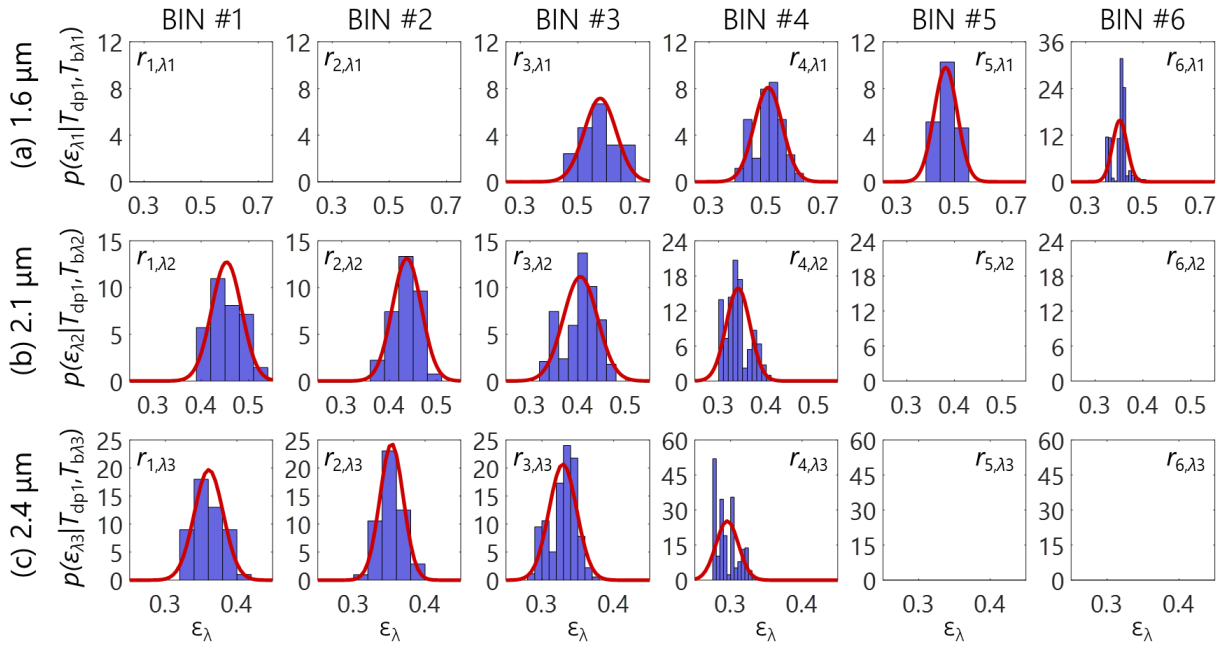


Figure 9.9. Histograms and Gaussian distributions for the conditional spectral emissivity prior, $p(\varepsilon \mid T_{dp1}, \mathbf{r}(\mathbf{T}_{be}))$, generated from *in situ* measurements on DP980 replicates annealed at the dew point, $T_{dp1} = -30°C$.

9.4.2. Temperature estimates with the conditional emissivity prior

In situ measurements from Sample #1 are used to evaluate the performance of the conditional *in situ* emissivity prior, $p(\boldsymbol{\varepsilon} \mid T_{dp1}, \mathbf{r}(\mathbf{T}_{be}))$, generated from Replicates #1 - #4. In this analysis, the relationship between the replicates (Rep #1 - #4) and Sample #1 is conceptually parallel to the train-test data split in machine learning, where the empirical prior from the replicates serves as "training" on the expected variations in emissivity and Sample #1 "tests" how well the "trained prior" compensates for unobserved variations in emissivity.

To accurately assess the improvements to the MAP and uncertainty estimates, the pyrometrically-inferred temperatures obtained with $p(\boldsymbol{\varepsilon} \mid T_{dp1}, \mathbf{r}(\mathbf{T}_{be}))$ is compared against the predictions from the *in situ* general dew point-dependent emissivity prior, $p(\boldsymbol{\varepsilon} \mid T_{dp1})$, and the *ex situ* emissivity prior from Section 6.2.1. The *in situ* spectral irradiance, $\mathbf{S}$, measured by the spectrometer has an uncorrelated centered Gaussian noise with a standard deviation of 2%, i.e., $p(\mathbf{S}^{meas}) \sim \mathcal{N}(\mathbf{S}_{meas}, \text{diag}((0.02 \cdot \mathbf{S}_{meas})^2))$. The temperature posterior distribution is obtained by incorporating $p(\mathbf{S}^{meas})$ and each of the emissivity priors as $p_{pr}(\boldsymbol{\varepsilon})$ into Eq. (9.1). Section 0 details the exact computation steps to obtain the temperature posterior. The resulting MAP pyrometric

estimates and the associated 95% credibility interval for the three candidate emissivity priors are shown in Figure 9.10. The credibility interval reflects the overall uncertainty in the temperature posterior based on the uncertainties introduced by the priors and the measurements (likelihood). Figure 9.10 (a) – (c) also show the *in situ* thermocouple measurements that serve as the ground truth estimates of the true sample temperature. The K-type thermocouple has a measurement uncertainty equivalent to 0.75% of the measured value, however, this uncertainty is omitted from the plots for easier comparison of the pyrometric estimates.

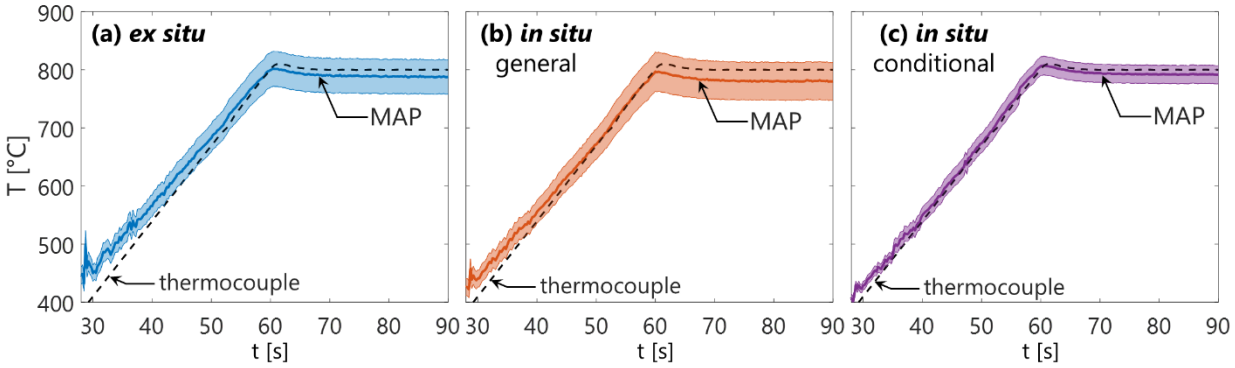


Figure 9.10. MAP estimates (solid lines) and 95% credibility interval (shaded area) for the pyrometrically-inferred temperatures computed on Sample #1 using the three emissivity priors: **(a)** *ex situ* emissivity prior, **(b)** *in situ* general emissivity prior, $p(\boldsymbol{\varepsilon} \mid T_{\mathrm{dp1}})$, and **(c)** *in situ* conditional emissivity prior, $p(\boldsymbol{\varepsilon} \mid T_{\mathrm{dp1}}, \mathbf{r}(\mathbf{T}_{\mathrm{be}}))$. The dashed lines represent *in situ* nominal thermocouple measurements.

All three emissivity priors produce credibility bounds that, for the most part, envelop the thermocouple values. However, the credibility bounds for the conditional emissivity prior are approximately half as wide as those for the other priors, indicating reduced uncertainty. Furthermore, the MAP estimates obtained with conditional emissivity prior are the closest to the thermocouple measurements, exhibiting the smallest error values as shown in Table 9.2. Although all three priors are unable to effectively compensate for the varying emissivity at the lower temperatures (≤500°C), the conditional prior produces the most accurate MAP estimate, with the resulting error being at least half of the error produced by the other priors. The better accuracy and precision obtained with the conditional prior is primarily due to the increased information content of the prior defined for each $r_{j,\lambda d}$ bin, as seen in Figure 9.9. The use of $\mathbf{T}_{\mathrm{be}}$ to specify the prior ensures the mean of the emissivity prior is more representative of the radiative properties of the

steel surface during annealing, and the narrower spread of the emissivity distribution reduces the uncertainty introduced into the temperature posterior.

Table 9.2. Signed error (Error), relative error (RE) and the uncertainty (±2σ) obtained for pyrometric estimates on Sample #1 for the three priors; *ex situ* prior, *in situ* general prior and *in situ* conditional emissivity prior, at key temperatures (*T*) during the annealing cycle.

	***Ex situ* prior**			***In situ* general prior**			***In situ* conditional prior**		
T (°C)	Error (°C)	RE (%)	±2σ (°C)	Error (°C)	RE (%)	±2σ (°C)	Error (°C)	RE (%)	±2σ (°C)
400	69.9	17.5	16.4	45.9	11.5	15.7	28.9	7.2	7.1
500	31.4	6.3	17.2	26.9	5.4	18.9	17.7	3.5	13.1
600	22.8	3.8	21.5	10.1	1.7	22.8	5.2	0.9	15.4
700	14.3	2.1	25.6	5.7	0.8	27.9	8.2	1.2	17.7
800 (60 s)	-2.1	0.3	29.9	-4.7	0.6	33.8	4.8	0.6	16.1
800 (75 s)	-10.9	1.4	29.6	-18.6	2.3	32.6	-7.1	0.9	15.7
800 (90 s)	-11.8	1.5	29.5	-19.6	2.4	32.6	-8.0	1.0	15.7

More specifically, the error obtained with the conditional prior for temperatures above 600°C ranges from ±5°C to ±8°C, which is quite close to meeting the desired temperature control window for AHSS processing (i.e., ±2°C to ±4°C). Overall, compared to the other priors, the conditional prior yields a significantly narrower credibility interval and reduced bias, meeting the objectives of improving the accuracy, precision and reliability of the pyrometrically-inferred temperature.

When evaluating the estimates obtained with the *ex situ* prior and the *in situ* general prior, it is observed that the MAP estimates for the *in situ* general prior are more accurate except at the 800°C soak temperature, which is expected because the Gaussian prior distribution does not fully represent the right-skewed nature of the emissivity data in Figure 9.7. This highlights the fact that, in addition to using appropriate *in situ* data to construct sample-based emissivity priors, the fitted distribution must also be appropriately selected to reflect the characteristics of the data and prevent bias in the posterior estimates.

9.4.3. Further validation on DP980 alloy annealed at other dew points

The definition of the conditional emissivity prior, $p(\boldsymbol{\varepsilon} \mid T_{\mathrm{dp1}}, \mathbf{r}(\mathbf{T}_{\mathrm{be}}))$ in Section 9.1.1 assumes that the nominal dew point, T_{dp1}, is known deterministically with negligible measurement uncertainty.

Although dew point measurements are inherently dynamic, this approximation is somewhat acceptable for lab-scale measurements given the short duration of the annealing cycle. However, this assumption is not entirely valid for the industrial galvanizing line since the dew point measurements are known to vary across the different sections of the furnace, even when the goal is to process the steel at a single specified dew point level.

To investigate the impact of variations in the annealing dew point on the accuracy of the MAP and uncertainty estimates, the conditional prior is applied to DP980 samples annealed at −45°C (Section 9.3.2, Sample #2) and −10°C (Section 7.2.1, Sample #2). The posterior densities for these dew points alongside the −30°C estimates, are plotted in Figure 9.11, and Table 9.3 summaries the measurement error and uncertainties at key temperatures. The MAP values overpredict the thermocouple measurements for the samples annealed at −45°C and −10°C, which indicates that the mean of the prior underpredicts the *in situ* spectral emissivity of the sample at these dew points. The 95% credibility interval estimate for the sample annealed at −45°C captures the *in situ* thermocouple measurements, and provides better estimates at temperatures below 500°C, especially compared with the estimates on the sample annealed at −30°C. The credibility interval for the sample annealed at −10°C, in contrast, narrowly fails to capture the thermocouple measurements, with pyrometric estimates during the ramp falls right at the edge of the credibility bounds. Despite this, the accuracy of the pyrometric estimates obtained with conditional prior for the ramp period of the −10°C sample is a significant improvement over the results with the *ex situ* prior shown in Figure 7.5.

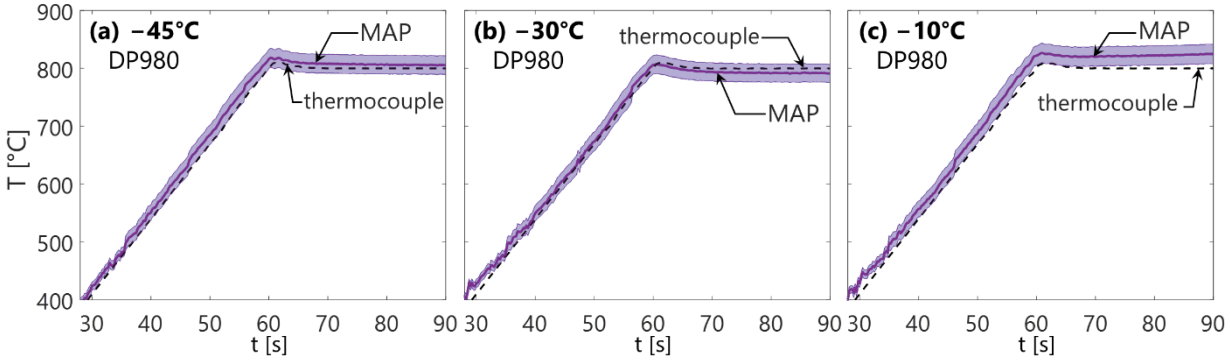


Figure 9.11. Posterior densities estimated with conditional emissivity prior for the DP980 samples annealed at **(a)** −45°C; **(b)** −30°C; and **(c)** −10°C. The solid lines indicate the posterior distribution mean and the 95% credibility intervals (shaded area) are equivalent to two standard deviations of the mean. The black dashed lines represent the *in situ* thermocouple measurements.

Table 9.3 also shows that, despite variations in the MAP estimate (and thus error) at the different annealing dew points, the estimated 95% credibility interval (±2σ) remains relatively similar, suggesting that the spectral irradiances (likelihood function) at the various dew point provide similar uncertainty information despite their impact on the MAP estimate. This indicates that the narrower variance of the prior distribution significantly dominates the posterior uncertainty, making the credibility interval mostly independent of the measurement noise included in the likelihood function.

Table 9.3. Signed error (Error), relative error (RE) and the uncertainty (±2σ) obtained with the conditional emissivity prior at key temperatures (*T*) for DP980 samples annealed at the following dew points: −45°C, −30°C and −10°C.

	DP980 annealed at various dew points								
	−45°C			**−30°C**			**−10°C**		
T (°C)	Error (°C)	RE (%)	±2*σ* (°C)	Error (°C)	RE (%)	±2*σ* (°C)	Error (°C)	RE (%)	±2*σ* (°C)
400	8.6	2.1	8.2	28.9	7.2	7.1	21.1	5.3	6.7
500	12.1	2.4	12.4	17.7	3.5	13.1	14.2	2.8	12.5
600	13.2	2.2	15.7	5.2	0.9	15.4	12.4	2.1	15.9
700	18.9	2.7	18.2	8.2	1.2	17.7	25.8	3.7	18.7
800 (60 s)	16.4	2.1	16.5	4.8	0.6	16.1	19.8	2.5	16.7
800 (75 s)	6.7	0.8	16.2	-7.1	0.9	15.7	21.5	2.7	16.6
800 (90 s)	5.7	0.7	16.1	-8.0	1.0	15.7	25.4	3.2	16.8

Broadly speaking, the robust performance of the conditional emissivity prior at other dew point in Figure 9.11 and Table 9.3 suggests that the variance captured by the replicates in the prior distribution is sufficient enough to compensate for changes in the emissivity induced by varying annealing dew point. Conservatively, this result suggests that with sufficient replicates, a conditional prior created with samples processed at a single deterministic dew point value should be resilient to at least ±10°C deviation in the annealing dew point.

9.4.4. Application to *in situ* measurements on other steel grades

To further investigate the limitations of the *in situ* conditional emissivity prior, the impact of variable alloy composition is analyzed. Examining Figure 9.4 and Figure 9.6 suggests that the variations in the replicates of the DP980 annealed at -30C, is similar to the variations in the

radiative properties of DP780 and IF steel annealed at −45°C and −30°C, respectively, despite the differences in steel grade and alloy composition. Therefore, the conditional emissivity prior created from the DP980 replicates annealed at −30°C should be able to compensate for the emissivity variations experienced by the DP780 and IF samples. Figure 9.12 shows the posterior temperature distribution obtained by applying the conditional prior to the *in situ* spectral irradiance measurements on DP780 annealed at −45°C. The estimates on the DP780 and IF steel samples are juxtaposed with the baselines results on the DP980 annealed at −30°C (Sample #1). As expected, the credibility intervals capture the thermocouple temperature for both the DP780 and IF materials. Table 9.4, which summarizes the error and uncertainties at key temperature, shows that the performance of the conditional prior on the IF mild steel annealed at −30°C is similar to the baseline performance on the DP980 sample also annealed at −30°C. Correspondingly, the MAP estimates and associated uncertainties for the DP780 annealed at −45°C, is also similar to the results obtained for the DP980 sample annealed at −45°C in Figure 9.11 and Table 9.3.

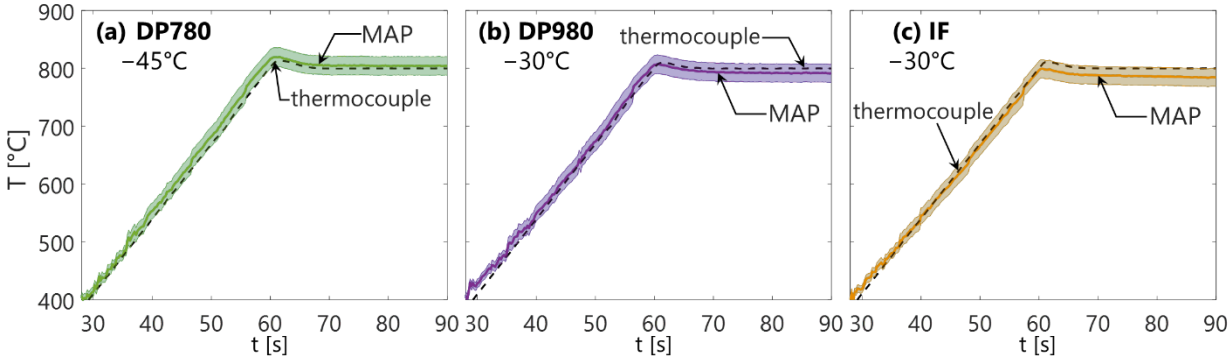


Figure 9.12. Posterior densities estimated with conditional emissivity prior for AHSS and mild steel grades annealed at various dew points: **(a)** DP780 annealed at −45°C; **(b)** DP980 annealed at −30°C; and **(c)** IF steel annealed at −30°C. The solid lines indicate the posterior distribution mean and the 95% credibility intervals (shaded area) are equivalent to two standard deviations of the mean. The black dashed lines represent the *in situ* thermocouple measurements.

In general, the accuracy of the pyrometric estimates and uncertainties for the other steel grades show that the conditional prior can provide reliable estimates on steel grades with similar composition if the expected *in situ* emissivity variations falls within the variability information content encoded within the prior distribution.

Table 9.4. Signed error (Error), relative error (RE) and the uncertainty ($\pm 2\sigma$) obtained with the conditional emissivity prior at key temperatures (T) for AHSS and mild steel grades annealed at various dew points: DP780 annealed at −45°C, DP980 annealed at −30°C, and IF mild steel annealed at −30°C.

	DP780 at −45°C			**DP980 at −30°C**			**IF at −30°C**		
T (°C)	Error (°C)	RE (%)	$\pm 2\sigma$ (°C)	Error (°C)	RE (%)	$\pm 2\sigma$ (°C)	Error (°C)	RE (%)	$\pm 2\sigma$ (°C)
400	4.7	1.2	8.1	28.9	7.2	7.1	19.1	4.8	6.5
500	17.0	3.4	13.1	17.7	3.5	13.1	6.2	1.2	12.3
600	11.3	1.9	15.7	5.2	0.9	15.4	-5.0	0.8	15.0
700	17.1	2.5	18.0	8.2	1.2	17.7	-4.7	0.7	17.2
800 (60 s)	14.1	1.8	16.5	4.8	0.6	16.1	-2.9	0.4	15.8
800 (75 s)	4.8	0.6	16.0	-7.1	0.9	15.7	-13.1	1.6	15.5
800 (90 s)	4.2	0.5	16.0	-8.0	1.0	15.7	-15.4	1.9	15.5

9.5. Conclusions

To ensure the optimal mechanical properties of the AHSS during intercritical annealing, steel manufacturers require accurate pyrometric predictions with reliable uncertainty estimates. This work presents a multivariate emissivity prior wherein the spectral emissivity prior distribution depends on two variables: annealing atmosphere dew point (T_{dp}), and the equivalent blackbody temperature ($\mathbf{T}_{be}$) during annealing. As required in the Bayesian context, T_{dp} and $\mathbf{T}_{be}$ are initially treated as stochastic variables, allowing the general hierarchical expression for the emissivity prior to account for the uncertainties in T_{dp} and $\mathbf{T}_{be}$ through marginalization. Next, the hierarchical prior is simplified into a conditional prior by assuming that the values of T_{dp} and $\mathbf{T}_{be}$ are deterministically known. This approximation eliminates the need to marginalize over these variables as their uncertainties are no longer explicitly accounted for, which results in a more straightforward conditional representation of the spectral emissivity information. While the uncertainties in T_{dp} and $\mathbf{T}_{be}$ are no longer marginalized explicitly, their covariate dependencies are still included in the conditional emissivity distribution.

The conditional emissivity prior was implemented using *in situ* spectral emissivity measurements from DP980 replicates with nearly-identical pre-annealed surface state and processed at a single dew point level, $T_{dp,i=1} = -30$°C. The *in situ* spectral emissivity measurements from these replicates was also used to create a general *in situ* prior, that represents the general

wavelength-dependent variation in emissivity without discretizing by T_{be}. Both versions of the *in situ* prior and an *ex situ*-based emissivity prior were then tested on another DP980 sample annealed at −30°C. A comparison of the pyrometrically-inferred temperature posteriors showed that the conditional *in situ* prior provided the most accurate estimate of the thermocouple measurement for both the heating and soak period of the annealing cycle. While the credibility interval from all three priors contained the thermocouple measurements, the posterior distribution obtained with conditional prior had the narrowest 95% credibility interval, significantly reducing the uncertainty associated with the pyrometrically-inferred temperature. This shows that conditioning the imperfectly known emissivity on the dew point and the equivalent black body temperature creates a robust stochastic model that effectively represents the dynamic variations in radiative properties with low levels of uncertainty.

Given that the assumption of a deterministic dew point value does not truly represent the industrial condition on the CGL, the analysis considered the impact of variability in annealing dew point on the predictions obtained with the conditional emissivity prior. The condition emissivity prior was applied to *in situ* spectral irradiance measurements on D980 samples annealed at −45°C and −10°C. The posterior temperature estimates at −45°C contained the thermocouple estimates for both the heating and soak period while the posterior estimates −10°C only contained the thermocouple estimates for just the heating section of the annealing cycle. Based on these results, it was estimated that the conditional prior defined at a single nominal dew point level, $T_{dp,i}$, would be robust to at least ±10°C deviation in the annealing dew point. Furthermore, the conditional emissivity prior was able to provide satisfactory MAP estimates and uncertainty bounds when evaluated on DP780 and IF steel annealed at −45°C and −30°C dew points, respectively. This indicates that with sufficient replicates, the information content of the conditional emissivity prior is also robust to slight variations in alloy composition and pre-annealed surface topography.

This chapter also demonstrated the use of *in situ* spectral emissivity measurements as a diagnostics technique for monitoring the evolving surface oxides during intercritical annealing of AHSS. Comparing the two DP980 samples, Sample #1 and #2, annealed at dew points of −30°C and −45°C, respectively, the sample annealed at the lowest p_{O2} (Sample #2, −45°C) had a slightly higher spectral emissivity, which suggest a more prominent external MnO oxide layer compared to the samples annealed at −30°C (Sample #1). Furthermore, the peaks in the varying emissivity

detected around 700°C for the AHSS alloys, which was absent for the IF steel, suggests the formation of mixed or ternary oxides. Similarly, despite processing the replicates for Sample #1 under identical annealing conditions at the same dew point of −30°C, their spectral emissivity varied differently with the annealing temperature and time, demonstrating the impact of oxidation kinetics on the surface oxide formation process. Finally, the DP980 and DP780 samples, both annealed at −45°C, exhibited relatively identical *in situ* spectral emissivity variations despite the distinct differences in their pre-annealed surface state, which suggests that the effect of the evolving oxide layer dominates over the pre-annealed topographical features at the pyrometry wavelengths considered in this study.

In terms of future improvements to the conditional emissivity prior, subsequent work will define unique bin boundaries for the equivalent blackbody temperature at each detection wavelengths. Furthermore, non-stationary estimation techniques, such as the Kalman filter or the particle filter, can be applied to capture the non-linear and time-varying changes in the radiative properties that impact the pyrometric temperature during annealing, thus improving the accuracy and reliability of the uncertainty estimates.

Chapter 10
Conclusions and future work

Pyrometry errors associated with imperfectly known emissivity cause temperature variations during AHSS processing, resulting in rejection rates as high as 30% [3]. The steel industry could save over a quarter billion dollars annually with more accurate temperature measurement instruments [69]. By investigating the behaviour of the spectral emissivity of AHSS during processing, specifically how it evolves with material properties and processing parameters, this thesis provides empirical algorithms that models the spectral emissivity behaviour of dual-phase AHSS alloys, and crucially, its associated uncertainties.

10.1. Key knowledge contributions

This thesis set out to develop a robust emissivity compensation algorithm to accurately infer the surface temperature of AHSSs. Through a combination of experimental and statistical analysis of the *in situ* and *ex situ* radiative properties of as-received and annealed AHSS, this thesis presents the following innovations towards improving the pyrometry of AHSS.

10.1.1. Multivariate *ex situ* spectral emissivity model

A novel multivariable emissivity model was developed to address the challenges of existing pyrometry methods by capturing the interdependent effects of critical variables on the spectral emissivity of dual-phase (DP) AHSS alloys. The four variables included in the new model are wavelength, alloy composition, annealing atmosphere, and pre-annealed surface roughness. Using factorial design of experiments, emissivity measurements were carried out on two annealed DP980 alloys having different Si/Mn ratios that were either left in their as-received rough state or mechanically polished before being processed under different dew points within a reducing atmosphere. The results showed that significant main and interaction effects vary across the wavelength range, with the ratio of alloy components and pre-annealed surface state dominating at shorter and longer wavelengths, respectively. Also, the dew point of the annealing atmosphere does not strongly affect the varying emissivity on its own, but its interaction effect with alloy composition contributes significantly to this effect, especially for wavelengths critical to

pyrometry. To account for this variation, the final model specifically includes terms that represent the interaction effects of dew point and alloy composition. The model was applied to pyrometry measurements from the annealing simulator and provided accurate temperature estimates.

10.1.2. Annealing simulator for *in situ* radiative measurements

Given the need to understand the variations in the radiative properties during intercritical annealing, an important contribution of this work is the development of an annealing simulator in order to provide *in situ* temperature, pyrometer and spectrometer measurements during intercritical annealing of AHSS. The annealing simulator resistively heats the steel coupon with a programmable DC power supply following a prescribed heating schedule. The dew point of the reducing atmosphere during annealing is controlled through a system of mass-flow controllers and hygrometers. The annealing simulator is designed to accommodate a variety of optical devices; typically, the spectrally resolved emitted radiation from the annealing samples is recorded simultaneously with OceanOptics NIRQuest512 spectrometer and Williamson PRO MWX-ST-17. Chapter 4 and Appendix B cover the design iterations and modifications made to the measurement chamber to improve experimental simulations of the intercritical annealing process. The final design of the annealing simulator is a cylindrical vacuum chamber with feedthroughs for optical, electrical and tubing access. All the atmosphere control manifolds, gas inlets/outlets, thermocouple, bus bar and optical windows were redesigned to maintain the airtight seal required when annealing AHSS. The vacuum-based design was important in addressing the oxygen infiltration problem experienced with the earlier versions of the chamber. The effectiveness of the vacuum-based chamber in simulating the intercritical annealing process was further validated in Chapter 8 by comparing the *ex situ* radiative properties of samples processed using the vacuum-based annealing simulator against samples annealed in a Iwatani-Surtec galvanizing simulator.

10.1.3. *In situ* spectral and temporal variation in radiative properties

This thesis also showed how the radiative properties of dual-phase AHSS evolve with temperature time and wavelength under varying annealing atmosphere (dew point) conditions. Chapter 5, Chapter 7 and Chapter 9 discussed several annealing experiments conducted at dew points of −45°C, −30°C, −10°C, and +10°C, with the earlier version of the experiments at −30°C (Chapter 5) providing insight into the impact of oxygen infiltration on the high-temperature emissivity. All

samples analyzed *in situ* were processed using the same annealing schedule, consisting of a 60 s ramp to the peak annealing temperature of 800°C, followed by 30 s hold.

A key trend observed is that the spectral emissivity at high temperatures varies strongly with the formation and dissolution of the oxide layer, especially at pyrometry wavelengths less than 2μm. This also ties in with the findings from applying the response surface methodology on *ex situ* radiative properties in Chapter 3 where the two effects primarily influencing the oxide layer: Si/Mn ratio (B), and dew point-Si/Mn ratio interaction (AB) were found to be dominant at shorter wavelengths. Surface oxides dominate the radiative properties at shorter wavelengths, primarily through thin-film interference for film-like oxide layer and increased scattering effects in the case of oxide nodules. The wavelength-dependent variations in emissivity reinforces the importance of carefully selecting the detection wavelength range when investigating the varying radiative properties of AHSS alloys as wavelength strongly influences the manner in which the EM wave interacts with the steel surface/substrate and oxide layer.

A comparison of the *in situ* spectral emissivity with the *ex situ* radiative properties of the pre-annealed samples showed that the spectral emissivity at all dew points increases with increasing temperature up to around 300°C to 400°C. Beyond this temperature, the emissivity decreases with increasing temperature up until the PAT, with negligible change in the spectral emissivity during the 30 second soak period. An analysis of the oxidation thermodynamics in Chapter 8 indicates that the increase in emissivity with temperature below 400°C is due to the formation of the stable iron oxides on the steel surface in addition to the formation of the selective oxides of the alloying elements (i.e., MnO, SiO_2, Al_2O_3, etc.). As the temperature increases above 400°C, however, the oxidation driving force switches, simultaneously favouring the reduction of the native iron and the continued growth of selective oxides. For samples annealed at lower dew point (≤ −30°C), it was observed that the spectral emissivity tends to approach their as-received emissivity values as the temperature approaches the peak annealing temperatures of 800°C, primarily because as the surface oxides become reduced with increasing temperature, the overall oxide layer becomes thinner, causing the spectral emissivity of the composite metal-oxide to approach the emissivity of the steel substrate.

In terms of the dew-point dependent variations in the *in situ* spectral emissivity, Chapter 7 showed that the spectral emissivity increases with increasing water vapour content above −30°C

(i.e., at −10°C and +10°C). The increase in low-temperature oxidation with increasing dew point explains the corresponding rise in spectral emissivity at the higher dew points. However, compared to −10°C and +10°C, the driving force for the reduction of the low-temperature oxides is highest at −30°C and −45°C which is why the spectral emissivity of the samples processed at −30°C or lower readily get reduced towards the pre-annealed radiative properties of the steel at higher annealing temperature.

Focusing on the DP980 samples annealed at the lower dew points (i.e., −30°C and −45°C), Chapter 9 showed that no significant difference was observed in their spectral emissivity values, especially compared to the differences observed between the samples annealed at −30°C and −10°C. However, the sample annealed at −45°C showed slightly higher spectral emissivity than the −30°C sample, which was attributed to the increasing outward flux of Mn relative to the inward flux of oxygen at the lower pO_2 of the annealing atmosphere. Moreover, from DP980 replicates with identical pre-annealed surfaces annealed at −30°C, it was observed that variations in oxidation kinetics of the surface oxides formed during annealing can produce differences in the evolving spectral emissivity observed *in situ*. Also, comparing two dual-phase alloys (DP980 and D780) alloys annealed at −45°C with similar Si/Mn ratios but very different pre-annealed surface topography showed nearly identical spectral emissivity values at high temperatures which suggests that relative to the pre-annealed roughness parameters, the radiative properties observed *in situ* are predominantly influenced by the oxide layer formed during annealing. Furthermore, Chapter 9 compared the radiative properties of these dual-phase AHSS alloys against a standard EDDS grade IF steel with minimal alloy content and the results showed that for alloy-rich metals like AHSS, variations in the evolving spectral emissivity *in situ* can potential used to identify the formation of ternary selective oxides during annealing.

Comparing the variations in radiative properties observed *ex situ* versus *in situ*, the results presented in Chapter 8 also showed that *ex situ* measurements on rapidly quenched samples do not represent the temperature-dependent changes in spectral emissivity observed *in situ*, primarily because *ex situ* measurements are unable to arrest the temperature-dependent changes in the optical properties of the oxide layer and steel substrate that are only present at high temperatures. However, *ex situ* measurements capture the temperature-induced changes in the oxide layer and topographical features that remain on the steel surface after quenching. This difference in *ex situ*

and *in situ* radiative properties has significant implications when developing empirical emissivity compensation algorithms, as using *ex situ* emissivity measurements was shown to produce absolute error in pyrometry estimates as high as ±67°C, due to the inability of *ex situ* measurements to capture temperature-dependent variations.

10.1.4. Accuracy of existing emissivity compensation algorithms for AHSS

Using *in situ* measurements from the annealing simulator, this thesis examined the suitability of existing pyrometry models for accurately predicting the surface temperature of AHSS. By comparing the performance of several dual-wavelength (ratio) and multi-wavelength (MW) pyrometry algorithms, Chapter 5 showed that both methods tend overpredict the surface temperature with maximum absolute error at the peak annealing temperature (PAT) ranging from 6°C to 42°C depending on the algorithm; however, the predictions for the multi-wavelength algorithms generally provided more accurate emissivity and temperature estimates for annealing AHSS. These algorithms were least accurate at lower temperatures since they incorrectly attributing the high emissivity values to an increase the temperature. Furthermore, the performance of the MW algorithms varies significantly with material and process parameters as demonstrated in Chapter 7 by comparing the accuracy of the pyrometrically-inferred temperature at various annealing dew point. Overall, the results show that the accuracy of a pyrometry model strongly depends on how well the underlying emissivity function captures the spectral changes produced as the surface state evolves with various material and process parameters during annealing.

10.1.5. Bayesian pyrometry model for uncertainty estimation

With the understanding that all pyrometry models approximate an imperfectly known spectral emissivity, an important focus area for this research was quantifying the uncertainties associated with the pyrometrically-inferred temperature using the Bayesian framework. To the best of the author's knowledge, the work detailed in Chapter 6 is the first attempt at applying the Bayesian framework as an uncertainty estimation technique to quantify the expected measurement error in the pyrometrically-inferred temperatures due to uncertainties introduced by the imperfectly known spectral emissivity, measurement noise, and other nuisance parameters. Typically, existing pyrometry algorithms provide a point estimate of the surface temperature, making it impossible to assess the reliability of the estimates.

In the Bayesian context, all pyrometry variables (measurements, calibration coefficients, spectral emissivity, and inferred temperature) were expressed as random variables that obey probability density functions. Developing the Bayesian pyrometry model involved defining a stochastic emissivity prior, the pyrometer calibration prior, measurement noise model, and error propagation analysis to account for uncertainties introduced by the instruments and experimental procedure. In terms of the emissivity prior, *ex situ* measurements from as-received and annealed DP980 samples were used to construct a Gaussian prior that reflected the state of knowledge of the varying spectral emissivity. The prior and measurement densities were then propagated through Bayes' equation to obtain the temperature posterior density, i.e., the pyrometrically-inferred temperature (MAP estimate) and, its associated uncertainties (credibility interval).

The Bayesian pyrometry model was first tested with *in situ* pyrometry signals from a DP980 sample annealed at a dew point of −40°C but with oxygen infiltration. Comparing the posterior estimates to deterministic predictions from a parametric MW function developed using data included in the emissivity prior showed that while both the MAP and MW overpredict the steel temperature, the MAP estimates are closer to the *in situ* thermocouple values especially for the hold/soak period where the steel surface is visibly free of the thick oxide layer caused by the oxygen infiltration. More importantly, the credibility interval provided by the temperature posterior for the hold/soak period contained the *in situ* thermocouple distribution.

To further prove the efficacy of the Bayesian pyrometry model, Chapter 7 tested the same *ex situ*-based emissivity prior on DP980 samples annealed at three dew points (−30°C, −10°C and +10°C) in the vacuum annealing chamber where the measurements are free of the impact of oxygen infiltration. The Bayesian approach was able to successfully compensate for the varying emissivity by providing a temperature posterior that captured the thermocouple temperature above 600°C across all the dew points. The temperature posteriors were then compared against deterministic estimates from existing MW emissivity models from literature. It was found that the accuracy of the deterministic models varied significantly with temperature and dewpoint, while the temperature uncertainty obtained with the stochastic emissivity prior was comparable to the absolute error of its MAP estimate for most temperatures, irrespective of dew point. This result emphasizes the advantage of stochastic emissivity models over deterministic models in providing robust temperature estimates for large variations in emissivity during intercritical annealing.

Chapter 9 focused on refining the accuracy and precision on the temperature posterior by defining a conditional spectral emissivity prior that improves the information content of the stochastic prior without sacrificing its ability to compensate for wide range of emissivity values induced by changing annealing parameters. Improving the uncertainty estimate was important because the credibility interval obtained with the *ex-situ*-based prior ranged from ±15°C to ±31°C, which does not satisfy the strict temperature control window of ±2 to ±4°C required by the steel industry for AHSS processing. The conditional prior uses *in situ* measurement to define a Gaussian prior where the mean and variance varies with the annealing dew point and the equivalent blackbody temperature at each time step. To illustrate this, DP980 replicates annealed at −30°C were used to construct a set of conditional priors where the equivalent blackbody temperature was categorized into 6 bins, with the bin number treated as a deterministic variable. These priors were then used to infer the pyrometric temperature on DP980, DP780 and IF steel annealed at −30°C and −45°C, since the emissivity does not vary significantly with varying oxygen partial pressure at the lower dew points. Compared to the *ex situ*-based prior and a general *in situ*-based prior, the conditional prior produced temperature posteriors that contained the thermocouple measurements at all temperatures (400°C − 800°C), with the credibility interval ranged reduced down to ±7°C to ±20°C. Despite the fact that the conditional prior was created with samples annealed only at −30°C, the MAP estimates obtained with the conditional prior were very close to the nominal thermocouple values with maximum absolute error being ±29°C across various dew points (−45°C, −30°C and −10°C) and alloys (DP980, DP780, and IF steel), a drastic reduction from the maximum absolute error of ±67°C obtained with the *ex situ*-based prior on DP980 (−30°C, −10°C and +10°C) in Chapter 7. More specifically, the conditional prior performed best on the DP980 sample annealed at −30°C, producing errors ranging from ±5°C to ±8°C for temperatures of 600°C and above. The performance of the conditional prior proves promising for providing accurate pyrometric temperature posterior that meet the desired temperature control window for AHSS processing, with the added advantage of reliable uncertainty estimates.

Overall, the Bayesian pyrometry approach highlights the benefits of estimating a posterior distribution instead of a point estimate since the former provides a measure of uncertainty that can be compared directly with predefined temperature tolerances for the mechanical properties of AHSS during intercritical annealing.

10.2. Ongoing and future work

While this thesis has provided insights into the evolving radiative properties of dual phase AHSS alloys during intercritical annealing, there are still many challenges involved with developing a generalized emissivity model, that is independent or at least robust to the parameters that influence the accuracy of pyrometry estimates on AHSS alloys. The following are a few key areas for further investigation.

10.2.1. Expanding the spectral range of the *in situ* radiative measurements

The trend in the temperature-dependent variations of radiative properties of the DP AHSS alloys and IF steel reported in this thesis are anomalous to the typical behaviour of metals, but can be attributed to either or both of these reasons: (1) the pyrometry wavelength range (1.2 – 2.5 μm) considered in this thesis are below the "crossover wavelength" or "X-point" of the steel where metals exhibit an inverse relationship between emissivity and temperature; and (2) low temperature oxidation of iron and selective oxides produces an oxide layer that gets reduced at higher temperature thus decreasing the emissivity. Having said that, further investigation is still required to validate these reasons given that Ham et al. [77] reported that the global emissivity for TRIP AHSS alloy and IF steel increased with increasing temperature when observed in the long-infrared wavelength range of 8 – 12 μm.

The simplest way to investigate the "X-point" phenomenon is to extend the spectral range of the *in situ* emissivity measurements to include the visible, mid-infrared and long-infrared, which can be achieved with an FTIR spectrometer. In addition to elucidating the specific crossover wavelength of the AHSS alloy, extending the detection wavelength range will provide several benefits for characterizing the material and chemical properties of the alloy during annealing. As discussed by Lin et al. [74, 75], the visible (VIS) spectrum is particularly useful for observing the thin-film interference effect of the oxide layer formed during annealing. The mid-infrared range, on the other hand, is valuable for vibrational spectroscopic characterization due to its sensitivity to the molecular vibrational signature of the oxide species. This means that *in situ* spectral emissivity measurements in the VIS and MIR range can potentially be used to identify selective oxide species and phase transformations in real-time, which would be beneficial for online control of the intercritical annealing process in a CGL.

10.2.2. Number of detection wavelengths for multiwavelength estimates

The primary motivation for multi-wavelength (MW) pyrometry over dual-wavelength (DW) pyrometry is the potential to improve the accuracy of the temperature estimates due to the increased information content of the measured emission with more detection wavelength.

In the context of the Bayesian pyrometry model, using the MW approach with three wavelengths (1.6 μm, 2.1 μm, and 2.4 μm) reduces the width of the posterior distribution relative to the DW estimate with two wavelengths (2.1 μm, and 2.4 μm). Figure 10.1 illustrates the difference between the posterior obtained with a DW approach versus a MW approach for a DP980 samples annealed at −30°C and −45°C. The spectral emissivity prior used in this case is a weakly informative prior constructed from *ex situ* measurements on as-received DP780 samples extracted from various locations along a coil [4].

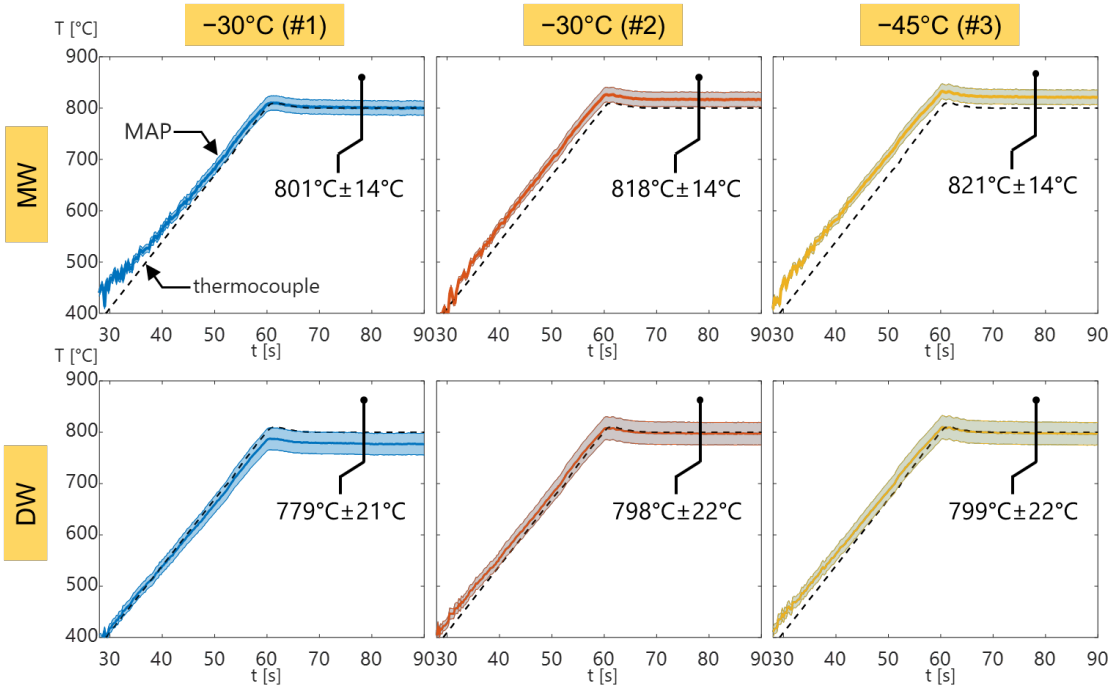


Figure 10.1. Multi-wavelength (MW) and dual-wavelength (DW) temperature posterior for a DP980 alloy (Si/Mn = 0.04) annealed at −30°C and −45°C showing the MAP estimates (solid lines); thermocouple temperature measurements (dashed lines) and error bounds corresponding to 95% credibility intervals (shaded region). Samples #1 and #2 are both −30°C replicates with varying oxidation kinetics impacting their spectral emissivity values [164].

Since increasing the detection wavelength from two to three improves the measurement uncertainty, it is expected that using even more detection wavelengths would further improve the temperature estimates. Using the spectrometer measurements, preliminary investigation of this idea was carried out by combining Principal Component Analysis (PCA) approach with the Bayesian pyrometry model to handle the highly correlated emissivity covariance problem encountered with MW pyrometry estimate with more than 5 wavelengths. However, there was not a significant decrease in the width of the posterior temperature distribution when the number of detection wavelengths was increased from 3 to 15 within a spectral range of 1.2 µm to 2.5µm. Figure 10.2 shows the effect of increasing the detection wavelength on posterior estimates at the peak annealing temperature (PAT = 800°C) for the annealed DP980 sample presented in Chapter 5 and Chapter 6, using the *ex situ* emissivity prior introduced in Chapter 6.

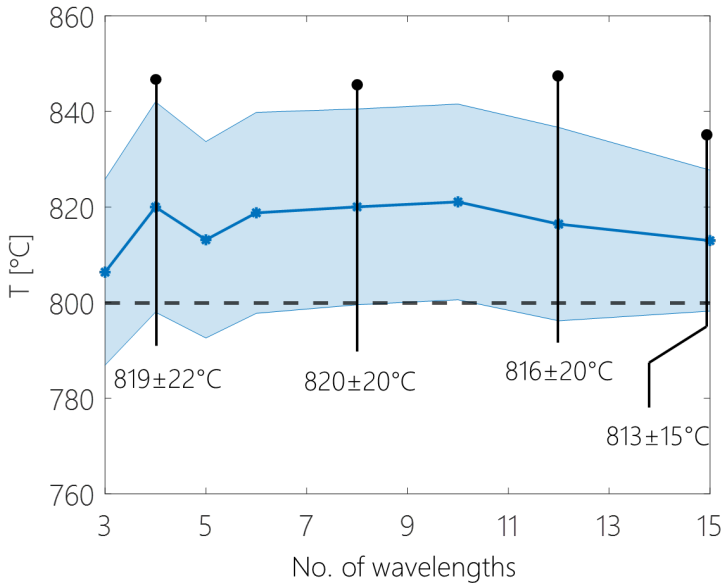


Figure 10.2. Effect of increasing the number of detection wavelengths (between 1.2 − 2.5 µm) on the MAP and credibility intervals at the peak annealing temperature (PAT = 800°C) for a DP980 sample annealed at −30°C.

As expected, the choice of the specific wavelengths combined with increasing the overall number of detection wavelengths impacts the accuracy and uncertainty of the posterior. Therefore, the next step should be to conduct a sensitivity analysis to identify the optimal wavelengths and combinations that will improve the pyrometric temperature estimates across a variety of material properties and annealing processing parameters.

10.2.3. Response surface modelling of the *in situ* radiative properties

Chapter 3 attempted to address the inadequacies of existing MW algorithms by using factorial design of experiments to account for the interdependent effects of wavelength, alloy composition, annealing atmosphere, and pre-annealed surface state on spectral emissivity. However, residual analysis from the resulting linear spectral emissivity model suggests that certain second-order effects influencing spectral emissivity variations were overlooked. Moreover, the model developed in Chapter 3 was based on *ex situ* spectral emissivity measurements which does not fully represent the variations in radiative properties observed *in situ*.

The next step should be to develop higher-order emissivity models based on *in situ* measurements using response surface methodologies, such as 3^k factorial design, central composite design (CCD), or the Box-Behnken design. This approach would enable a more precise characterization of complex interactions and non-linear effects influencing the varying spectral emissivity. Additionally, using *in situ* measurements would allow the model to capture dew point- and temperature-dependent variations in radiative properties due to oxidation effects and changing optical properties at high temperatures. The dew point levels used for the *in situ* measurements in Chapter 7 were purposely chosen to be uniformly spaced so as to ensure orthogonality and rotatability when developing higher order models using the response surface methodology.

10.2.4. Stochastic prior design for improved temperature posterior estimate

This thesis has demonstrated the advantages of expressing the imperfectly known spectral emissivity as a stochastic variable that obeys a prior distribution, rather than a deterministic variable with a single value. A natural extension of this work would be to refine the design of the spectral emissivity prior to reduce the posterior uncertainty to give accurate estimates that meet the strict temperature excursions standards required for the mechanical properties of AHSS. Chapter 9 introduced the concept of hyperpriors which can be fully implemented by emissivity priors with the mean and variances as hyperparameters that vary with material and process parameters. For the 2-step discretization system introduced for the conditional emissivity prior in Chapter 9, future work should consider defining unique bin boundaries at each detection wavelength, to further improve the accuracy and uncertainty estimates.

Future work should also consider defining priors on the coefficients of a multivariate emissivity model, introducing a stochastic component into the model structure. This approach

would incorporate the underlying relationship between spectral emissivity, material properties and process parameters, while accounting for the inherent uncertainty in the evolving emissivity.

In addition to defining emissivity priors that are conditionally dependent on other key process parameters, steelmakers may consider using different conditional stochastic priors for the heating and soaking sections of the CGL. Defining Gaussian priors where the mean and variance vary with the processing conditions within the various sections of the annealing furnace will offer the required balance of robust temperature estimates for optimum control during the heating period and a precise estimate of the peak annealing estimate during soaking.

Another extension of the Bayesian pyrometry model worth considering is the use of non-stationary estimation techniques (e.g., the Kalman Filter) to account for how uncertainties in the temperature estimates evolve with time over the annealing cycle. This is particularly important because the final mechanical properties of the AHSS alloy are both temperature- and time-dependent, with the temperature and material properties at one time step impacting the temperature and mechanical properties at subsequent time steps. Incorporating a non-stationary Bayesian approach will produce a more realistic estimate of the uncertainties impacting the evolution of the mechanical properties during annealing.

10.2.5. Online pyrometry experiment on a CGL

Referring to the general pyrometry equations, specifically Eq. (2.3), it is evident that the lab-scale annealing simulator simplifies a lot of the factors that influence the actual intensity incident on the pyrometer detector. Compared to the stable experimental conditions in the lab, the annealing process on the CGL is prone to other factors that influence the radiative properties of the alloy, e.g., varying pre-annealed conditions, fluctuating dew points, temperature gradients within the furnace, etc. Furthermore, the interdependent effects of these factors can produce oxidation kinetics that impact radiative properties differently compared to the laboratory observations used in developing the emissivity models. While the Bayesian pyrometry model helps address this to an extent by accounting for measurement and other sources of uncertainties, to ensure the accuracy and reliability of pyrometry estimates obtained when the models developed in this thesis are eventually deployed on the continuous galvanizing lines, real-time calibration and validation in on AHSS processed in a CGL is still required.

10.3. Final remarks

The models and findings from this thesis provide tools for improving pyrometry temperature estimates on AHSS, enabling steel manufacturers to make just-in-time changes to ensure that the final AHSS strips have the desired mechanical properties. This thesis also aims to educate steelmakers on how to effectively model the imperfectly known radiative properties of AHSS and other custom steel grades by constructing appropriate emissivity priors for improved temperature measurements.

The hope is that the knowledge from this thesis will contribute towards improving the accuracy and uncertainty of pyrometry estimates on AHSS, which will ultimately lower rejection rates, thus reducing manufacturing costs. Since the emissivity modelling principles discussed in this thesis can be applied to any steel grade, this information can also be used to enhance pyrometry models for the next generations of galvanized AHSS grades, consequently allowing automakers to build vehicles with improved fuel-efficiency and superior crash performance. Equally important, the resulting decrease in greenhouse gas emissions from improved AHSS grades will enable the automotive industry to reduce airborne pollution, thus slowing climate change significantly.

References

[1] Keeler, S., Kimchi, M., and Mconey, P. J., *Advanced High-Strength Steels Application Guidelines*, WorldAutoSteel.

[2] Thimons, M. A., and Sebastian, B. M., 2017, *Life Cycle Greenhouse Gas and Energy Study of Automotive Lightweighting*, Steel Recycling Institute.

[3] Somveille, Q., 2018, "Effect of Selective Oxidation on Temperature Measurements of AHSS with Pyrometry," MASc thesis, École Polytechnique de Montréal, Montréal, Canada.

[4] Narayanan, N. S., Lin, K., Suleiman, F. K., and Daun, K. J., 2023, "The Causes and Effects of Preannealed Radiative Property Variations across Full-Hard Advanced High-Strength Steel Coils," Steel Res. Int., **94**(3), p. 2200705.

[5] Narayanan, N. S., Lin, K., Suleiman, F. K., and Daun, K. J., 2024, "The Causes and Effects of Preannealed Radiative Property Variations Across Full-Hard Advanced High-Strength Steel Coils," Steel Res. Int., **95**(2), p. 2300299.

[6] Araújo, A., 2017, "Multi-spectral Pyrometry—A Review," Meas. Sci. Technol., **28**(8), p. 082002.

[7] Usamentiaga, R. N., García, D. F., Molleda, J., Bulnes, F. G., and Pérez, J. M., 2011, "Temperature Measurement Using the Wedge Method: Comparison and Application to Emissivity Estimation and Compensation," IEEE Trans. Instrum. Meas., **60**(5), pp. 1768-1778.

[8] Tsai, B., Shoemaker, R., DeWitt, D., Cowans, B., Dardas, Z., Delgass, W., and Dail, G., 1990, "Dual-wavelength Radiation Thermometry: Emissivity Compensation Algorithms," Int. J. Thermophys., **11**(1), pp. 269-281.

[9] Wen, C.-D., 2010, "Investigation of Steel Emissivity Behaviors: Examination of Multispectral Radiation Thermometry (MRT) Emissivity Models," Int. J. Heat Mass Transf., **53**(9), pp. 2035-2043.

[10] Tanaka, F., and Dewitt, D. P., 1989, "Experimental and Analytical Study on a New Radiation Thermometry Method on Oxidizing Steel," Proc. Natl. Heat Transf. Conf., ASME, Philadelphia, PA, pp. 69-75.

[11] Tanaka, F., and Dewitt, D. P., 1989, "Theory of a New Radiation Thermometry Method and an Experimental Study using Galvannealed Steel Specimens," Trans. Soc. Instrum. Control Eng., **25**(10), pp. 1031-1037.

[12] Duvaut, T., Georgeault, D., and Beaudoin, J. L., 1995, "Multiwavelength Infrared Pyrometry: Optimization and Computer Simulations," Infrared Phys. Technol., **36**(7), pp. 1089-1103.

[13] Khan, M. A., Allemand, C., and Eagar, T. W., 1991, "Noncontact temperature measurement. I. Interpolation based techniques," Rev. Sci. Instrum., **62**(2), pp. 392-402.

[14] Khan, M. A., Allemand, C., and Eagar, T. W., 1991, "Noncontact temperature measurement. II. Least squares based techniques," Rev. Sci. Instrum., **62**(2), pp. 403-409.

[15] Hoch, M., 1992, "The integral six-color pyrometer: Linear dependence of the radiance temperature T_r on the wavelength lambda," Rev. Sci. Instrum., **63**(4), pp. 2274-2281.

[16] Felice, R. A., "The spectropyrometer—a practical multi-wavelength pyrometer," AIP Conf. Proc., American Institute of Physics, pp. 711-716.

[17] Thiessen, R., Bocharova, E., Mattissen, D., and Sebald, R., 2010, "Temperature Measurement Deviation during Annealing of Multiphase Steels," Metall. Mater. Trans. B, **41**(4), pp. 857-863.

[18] Mosser, P., Somveille, Q., Daun, K., and Brochu, M.,2017, "Effect of Temperature Deviation During Critical Annealing of HSLA and DP980 Steels," Proc. 11th Int. Conf. Zinc Alloy Coated Steel Sheet, pp. 218-225.

[19] Demeri, M. Y., 2013, "*Advanced high-strength steels: science, technology, and applications*."

[20] Freudenberger, J., Göllner, J., Heilmaier, M., Mook, G., Saage, H., Srivastava, V., and Wendt, U., 2009, "Materials Science and Engineering," Springer Handbook of Mechanical Engineering, K.-H. Grote, and E. K. Antonsson, eds., Springer Berlin Heidelberg, eds., Springer, Berlin, Heidelberg, pp. 73-222.

[21] ASTM International, 2024, "ASTM A1008/A1008M-24 Standard Specification for Steel, Sheet, Cold-Rolled, Carbon, Structural, High-Strength Low-Alloy, High-Strength Low-Alloy with Improved Formability, Required Hardness, Solution Hardened, and Bake Hardenable," ASTM International, West Conshohocken, PA.

[22] ASTM International, 2023, "ASTM A1079-17(2023) Standard Specification for Steel Sheet, Complex Phase (CP), Dual Phase (DP) and Transformation Induced Plasticity (TRIP), Zinc-Coated (Galvanized) or Zinc-Iron Alloy-Coated (Galvannealed) by the Hot-Dip Process," ASTM International, West Conshohocken, PA.

[23] ASTM International, 2019, "ASTM A1088-13(2019) Standard Specification for Steel, Sheet, Cold-Rolled, Complex Phase (CP), Dual Phase (DP) and Transformation Induced Plasticity (TRIP)," ASTM International, West Conshohocken, PA.

[24] Taub, A. I., and Luo, A. A., 2015, "Advanced Lightweight Materials and Manufacturing Processes for Automotive Applications," MRS Bull., **40**(12), pp. 1045-1054.

[25] E. Billur, S. Karabulut, İ. Ö. Yılmaz, S. Erzincanoğlu, H. Çelik, E. Altınok, T. Başer, 2018, "Mechanical Properties of Trip Aided Bainitic Ferrite TBF Steels in Production and Service Conditions," Hittite J. Sci. Eng., **5**(3), pp. 231-237.

[26] Billur, E., 2019, "Introduction," *Hot Stamping of Ultra High-Strength Steels: From a Technological and Business Perspective*, E. Billur, ed., Springer International Publishing, Cham, pp. 1-17.

[27] Chatterjee, S., Koley, S., Sarkar, R. B., Behera, N., Manna, M., Mukherjee, S., and Kundu, S., 2019, "Design and Development of Galvannealed Dual-Phase Steel: Microstructure, Mechanical Properties and Weldability," J. Mater. Eng. Perform., **28**(1), pp. 231-241.

[28] Ennis, B., 2016, "A Review of the Effects of Chemical and Phase Segregation on the Mechanical Behaviour of Multi-Phase Steels," *arXiv preprint*, arXiv:1604.06485.

[29] Wang, Y., Tomota, Y., Ohmura, T., Gong, W., Harjo, S., and Tanaka, M., 2020, "Continuous and Discontinuous Yielding Behaviors in Ferrite-Cementite Steels," Acta Mater., **196**, pp. 565-575.

[30] Rashid, M., 1977, "GM 980X —Potential Applications and Review," SAE Technical Paper, No. 0148-7191.

[31] Belgasam, T. M., and Zbib, H. M., 2018, "Key Factors Influencing the Energy Absorption of Dual-Phase Steels: Multiscale Material Model Approach and Microstructural Optimization," Metall. Mater. Trans. A, **49**(6), pp. 2419-2440.

[32] Cornette, D., and Galtier, A., 2002, "Influence of The Forming Process on Crash and Fatigue Performance of High Strength Steels for Automotive Components," SAE Technical Paper, No. 0148-7191.

[33] Ajersch, F., and Ilinca, F., 2018, "Review of Modeling and Simulation of Galvanizing Operations," Steel Res. Int., **89**(1), p. 1700074.

[34] Marder, A., and Goodwin, F., 2023, *The Metallurgy of Zinc Coated Steels*, Elsevier.

[35] Mahieu, J., Claessens, S., and De Cooman, B., 2001, "Galvanizability of High-Strength Steels for Automotive Applications," Metall. Mater. Trans., **32**(11), p. 2905.

[36] Marder, A. R., 2000, "The Metallurgy of Zinc-Coated Steel," Prog. Mater. Sci., **45**(3), pp. 191-271.

[37] Autio, M., Cheng, F., Desai, A., Dinda, S., Fistler, M., Johnson, R., Kelley, D., Klix, T., Nielsen, D., Patria, G., Reed, D., Rozenbaum, J., Siekirk, J., Stephens, M., and Traficante, R., 2006, *Galvanneal (GA) vs. Galvanize (GI) Steels*, BIW Materials Strategy Team, Chrysler Group LLC.

[38] Davies, R., 1978, "Influence of martensite composition and content on the properties of dual phase steels," Metall. Trans. A, **9**(5), pp. 671-679.

[39] Sommers, U., C., K., Daube, T., Brühl, F., Sasse, C., Ionescu, C., Van den Berg, F., Fintelman, D., Melzer, S., Montagna, E., Krauthäuser, H., Terlau, T., Lhoest, A., Pensis, O., and Crutzen, J.-P., 2019, "Closed-loop control of the AHSS annealing process via X-ray phase fraction measurement," 111th Galvanizers Assoc. Meeting, Charleston, South Carolina.

[40] Gaskell, D. R., and Laughlin, D. E., 2017, *Introduction to the Thermodynamics of Materials*, CRC Press.

[41] Gleeson, B., 2010, "1.09-Thermodynamics and Theory of External and Internal Oxidation of Alloys," Shreir's Corrosion, pp. 182-184.

[42] Suzuki, Y., Yamashita, T., Sugimoto, Y., Fujita, S., and Yamaguchi, S., 2009, "Thermodynamic analysis of selective oxidation behavior of Si and Mn-added steel during recrystallization annealing," ISIJ Int., **49**(4), pp. 564-573.

[43] Bellhouse, E. M., Mertens, A. I. M., and McDermid, J. R., 2007, "Development of the surface structure of TRIP steels prior to hot-dip galvanizing," Mater. Sci. Eng. A., **463**(1-2), pp. 147-156.

[44] Khondker, R., Mertens, A., and McDermid, J. R., 2007, "Effect of annealing atmosphere on the galvanizing behavior of a dual-phase steel," Mater. Sci. Eng. A., **463**(1-2), pp. 157-165.

[45] Bhadhon, K. M. H., 2022, "Mechanical Property Development, Selective Oxidation, and Galvanizing of Medium-Mn Third Generation Advanced High Strength Steel," PhD dissertation, McMaster University, Hamilton, Canada.

[46] Bellhouse, E. M., 2010, "Galvanization of Al-Si Trip-Assisted Steels."

[47] Pourmajidian, M., 2018, "Selective oxidation and reactive wetting of Fe-0.1 C-6Mn-2Si-xSn advanced high strength steels during continuous hot-dip galvanizing," PhD dissertation, McMaster University, Hamilton, Canada.

[48] Alibeigi, S., 2014, "Short-term Formation Kinetics of the Continuous Galvanizing Interfacial Layer on Mn-containing Steels," PhD dissertation, McMaster University, Hamilton, Canada.

[49] Khanna, A. S., 2005, "High Temperature Oxidation," *Handbook of Environmental Degradation of Materials*, Elsevier, pp. 105-152.

[50] Swaminathan, S., and Spiegel, M., 2007, "Thermodynamic and Kinetic Aspects on the Selective Surface Oxidation of Binary, Ternary and Quarternary Model Alloys," Appl. Surf. Sci., **253**(10), pp. 4607-4619.

[51] Zentner, L. K., Dewitt, D. P., and White, D. A., 1993, "Temperature measurements during the galvanneal process," Thermochim. Acta, 218(C), pp. 317-328.

[52] DeWitt, D. P., and Nutter, G. D., 1988, *Theory and Practice of Radiation Thermometry,* Wiley.

[53] Lin, K., 2021, "Effect of Surface State on Radiative Properties of Advanced High Strength Steel Strips," PhD dissertation, University of Waterloo, Waterloo, Ontario, Canada.

[54] Howell, J. R., Mengüç, M. P., Daun, K. J., and Siegel, R., 2021, *Thermal Radiation Heat Transfer*, CRC Press, Boca Raton, FL.

[55] Wang, P., Hu, Z., Xie, Z., and Yan, M., 2018, "A New Experimental Apparatus for Emissivity Measurements of Steel and the Application of Multi-wavelength Thermometry to Continuous Casting Billets," Rev. Sci. Instrum., **89**(5), p. 054903.

[56] Iuchi, T., and Furukawa, T., "Emissivity-compensated Radiation Thermometry," Proc. 16th IMEKO World Congr. Austrian Society for Measurement and Automation, Vienna, pp. 365-369.

[57] Iuchi, T., Furukawa, T., and Wada, S., 2003, "Emissivity modeling of metals during the growth of oxide film and comparison of the model with experimental results, " Appl. Opt., **42**(13), p. 2317.

[58] Pellerin, M., 1999, "Multispectral Radiation Thermometry for Industrial Applications," PhD dissertation, Purdue University, West Lafayette, IN.

[59] Usamentiaga, R., Molleda, J., Garcia, D. F., Perez, L., and Vecino, G., 2010, "Real-time line scan extraction from infrared images using the wedge method in industrial environments," J. Electron. Imaging, **19**(4), p. 043017.

[60] Beckmann, P., and Spizzichino, A., 1987, *The Scattering of Electromagnetic Waves from Rough Surfaces*, Pergamon Press.

[61] Zentner, L., DeWitt, D., White, D., and Gaskell, D., 1994, "Computer algorithms for radiometric measurement of temperature during the galvanneal process," Metall. Mater. Trans. B, 25(3), pp. 459-462.

[62] Tanaka, F., Ohira, H., and Naganuma, Y., "Application of a New Radiation Thermometry Method to Galvannealed and Cold-Rolled Steels," Proc. 6th IEEE Conference Record, Instrumentation and Measurement Technology Conf., IEEE, pp. 24-28.

[63] Tanaka, F., Ohira, H., Maruyama, K., and Nakano, K., 1992, "New Type of Trace Thermometer for Determining Temperature and Emissivities of Oxidized Cold Rolled Steel," IFAC Proc. Vol., **25**(19), pp. 247-251.

[64] Wen, C.-D., and Mudawar, I., 2005, "Emissivity Characteristics of Polished Aluminium Alloy Surfaces and Assessment of Multispectral Radiation Thermometry (MRT) Emissivity Models," Int. J. Heat Mass Transf., **48**(7), pp. 1316-1329.

[65] Coates, P. B., 1981, "Multi-wavelength Pyrometry," Metrologia, **17**(3), pp. 103-109.

[66] Wen, C.-D., 2005, "Emissivity Characteristics of Aluminium Alloy Surfaces and Assessment of Multispectral Radiation Thermometry (MRT) Emissivity Models," PhD dissertation, Purdue University, West Lafayette, IN.

[67] Hagen, E., and Rubens, H., 1900, "Metallic Reflection," Ann. Phys, **1**(2), pp. 352-375.

[68] Wen, C.-D., and Mudawar, I., 2006, "Modeling the Effects Of Surface Roughness On The Emissivity Of Aluminium Alloys," Int. J. Heat Mass Transf., **49**(23-24), pp. 4279-4289.

[69] Tsai, B. K., Dewitt, D. P., and Dail, G. J., 1993, "Application of Dual-Wavelength Radiation Thermometry To The Aluminium Industry," Measurement, **11**(3), pp. 211-221.

[70] Reynolds, P., 1964, "A Review of Multicolour Pyrometry for Temperatures Below 1500°C," Br. J. Appl. Phys., **15**(5), p. 579.

[71] Modest, M. F., 2013, *Radiative Heat Transfe*r, Academic Press.

[72] Jo, H., King, J. L., Blomstrand, K., and Sridharan, K., 2017, "Spectral Emissivity of Oxidized and Roughened Metal Surfaces," Int. J. Heat Mass Transf., **115**(PB), pp. 1065-1071.

[73] Li, L., Yu, K., Zhang, K., and Liu, Y., 2016, "Study of Ti–6Al–4V Alloy Spectral Emissivity Characteristics During Thermal Oxidation Process," Int. J. Heat Mass Transf., **101**, pp. 699-706.

[74] Lin, K., Pourmajidian, M., Suleiman, F. K., McDermid, J. R., and Daun, K. J., 2022, "Effect of Annealing Atmosphere and Steel Alloy Composition on Oxide Formation and Radiative Properties of Advanced High-Strength Steel Strip," Metall. Mater. Trans.. B, Process Metallurgy and Materials Processing Science, **53**(1), pp. 380-393.

[75] Lin, K., Pourmajidian, M., Suleiman, F. K., McDermid, J. R., and Daun, K. J., 2022, "Interpreting the Radiative Properties of Advanced High Strength Steel Strip Using a Hybrid Thin Film/Geometric Optics Model," J. Quant. Spectrosc. Radiat. Transf., **277**, p. 107963.

[76] Lin, K., and Daun, K. J., 2020, "Interpreting the Spectral Reflectance of Advanced High Strength Steels Using the Davies' Model," J. Quant. Spectrosc. Radiat. Transf., **242**, p. 106796.

[77] Ham, S. H., Carteret, C., Angulo, J., and Fricout, G., 2018, "Relation Between Emissivity Evolution During Annealing and Selective Oxidation of TRIP Steel," Corros. Sci., **132**, pp. 185-193.

[78] Pourmajidian, M., and McDermid, J. R., 2018, "Selective Oxidation of a 0.1C-6Mn-2Si Third Generation Advanced High-Strength Steel During Dew-Point Controlled Annealing," Metall. Mater. Trans. A, Physical Metallurgy and Materials Science, **49**(5), pp. 1795-1808.

[79] Lin, K., Suleiman, F. K., and Daun, K. J., 2021, "Interpreting the Radiative Properties of Advanced High Strength Steel Using the Geometric Optics Ray-Tracing Approximation," Int. J. Heat Mass Transf., **176**, p. 121429.

[80] Bellhouse, E. M., and McDermid, J. R., 2010, "Effect of Continuous Galvanizing Heat Treatments on the Microstructure and Mechanical Properties of High Al-Low Si Transformation Induced Plasticity Steels," Metall. Mater. Trans. A, **41**(6), pp. 1460-1473.

[81] Bellhouse, E. M., and McDermid, J. R., 2010, "Selective Oxidation and Reactive Wetting of 1.0 Pct Si-0.5 Pct Al and 1.5 Pct Si TRIP-Assisted Steels," Metall. Mater. Trans. A, **41**(6), pp. 1539-1553.

[82] Deng, Y., Di, H., and Misra, R. D. K., 2018, "Influence of Dew Point on the Selective Oxidation, Microstructure and Mechanical Properties of a High-Al Low-Si Dual Phase Steel during Hot-Dip Galvanizing Process," Protect. Met. Phys. Chem. Surf., **54**(3), pp. 496-502.

[83] Pallisco, D. M., and McDermid, J. R., 2023**,** "On the Selective Oxidation of a 0.15C-6Mn-2Al-1Si Third-Generation Advanced High Strength Steel During Two-Stage Annealing Treatments," *Metall. Mater. Trans. A*, **54**(4), pp. 1296–1319.

[84] Sohn, I.-R., Kim, J.-S., and Sridhar, S., 2015, "Effect of Dew Point and Gas Flow Rate On the Surface Oxidation of Advanced High Strength Steels," ISIJ Int., **55**(9), pp. 2008-2017.

[85] Blumenau, M., Barnoush, A., Thomas, I., Hofmann, H., and Vehoff, H., 2011, "Impact of Selective Oxidation During Inline Annealing Prior to Hot-Dip Galvanizing on Zn Wetting And Hydrogen-induced Delayed Cracking of Austenitic FeMnC Steel," Surf. Coat. Technol., **206**(2-3), pp. 542-552.

[86] Gong, Y. F., Kim, H. S., and De Cooman, B. C., 2008, "Formation of Surface and Subsurface Oxides During Ferritic, Intercritical and Austenitic Annealing of CMnSi TRIP Steel," ISIJ Int., **48**(12), pp. 1745-1751.

[87] Liu, H., He, Y., Swaminathan, S., Rohwerder, M., and Li, L., 2011, "Effect of dew point on the surface selective oxidation and subsurface microstructure of TRIP-aided Steel," Surf. Coat. Technol., **206**(6), pp. 1237-1243.

[88] Ham, S., Ferté, M., Fricout, G., Depalo, L., and Carteret, C., 2016, "In-situ Spectral Emissivity Measurement of Alloy Steels During Annealing in Controlled Atmosphere," 13th Int. Quant. InfraRed Thermography Conf. (QIRT 2016), pp. 315-321.

[89] Somveille, Q., Mosser, P., Brochu, M., and Daun, K. J., 2017, "Effect of Oxidation on Emissivity for DP780 and DP980 Steels," 11th Int. Conf. on Zinc and Zinc Alloy Coated Steel Sheet, Tokyo, Japan.

[90] Cao, G., Weber, S. J., Martin, S. O., Malaney, T. L., Slattery, S. R., Anderson, M. H., Sridharan, K., and Allen, T. R., 2011, "In Situ Measurements of Spectral Emissivity of Materials for Very High Temperature Reactors," Nucl. Technol., **175**(2), pp. 460-467.

[91] Cao, G., Weber, S. J., Martin, S. O., Sridharan, K., Anderson, M. H., and Allen, T. R., 2013, "Spectral Emissivity of Candidate Alloys for Very High Temperature Reactors in High Temperature Air Environment," J. Nucl. Mater., **441**(1-3), pp. 667-673.

[92] King, J. L., Jo, H., Tirawat, R., Blomstrand, K., and Sridharan, K., 2017, "Effects of Surface Roughness, Oxidation, and Temperature on the Emissivity of Reactor Pressure Vessel Alloys," Nucl. Technol., **200**(1), pp. 1-14.

[93] del Campo, L., Pérez-Sáez, R. B., González-Fernández, L., Esquisabel, X., Fernández, I., González-Martín, P., and Tello, M. J., 2010, "Emissivity Measurements on Aeronautical Alloys," J. Alloys Compd., **489**(2), pp. 482-487.

[94] Zhao, S., Li, X., Zhou, X., Cheng, K., and Huai, X., 2016, "Investigation of The Effects of Ni-Based Alloy K465 On the Normal Spectral Emissivity During Oxidation," Infrared Phys. Technol., **78**, pp. 214-222.

[95] Weng, K.-H., and Wen, C.-D., 2011, "Effect of Oxidation on Aluminium Alloys Temperature Prediction Using Multispectral Radiation Thermometry," Int. J. Heat Mass Transf., **54**(23-24), pp. 4834-4843.

[96] Hagqvist, P., Sikström, F., and Christiansson, A.-K., 2013, "Emissivity Estimation for High Temperature Radiation Pyrometry on Ti–6Al–4V," Meas., **46**(2), pp. 871-880.

[97] Agababov, S., 1970, "Effect of Secondary Roughness on the Emissive Properties of Solid Bodies," Teplofiz. Vysok. Temp., **8**(1), pp. 220-222.

[98] King, J. L., Jo, H., Loyalka, S. K., Tompson, R. V., and Sridharan, K., 2017, "Computation of Total Hemispherical Emissivity from Directional Spectral Models," Int. J. Heat Mass Transf., **109**(C), pp. 894-906.

[99] Somveille, Q., Mosser, P., Brochu, M., and Daun, K., 2017, "Effect of Oxidation on Emissivity for DP780 And DP980 Steels," Proc. 11th Int. Conf. on Zinc and Zinc Alloy Coated Steel Sheet, Tokyo Japan, pp. 210-217.

[100] del Campo, L., Pérez-Sáez, R. B., and Tello, M. J., 2008, "Iron Oxidation Kinetics Study by Using Infrared Spectral Emissivity Measurements Below 570°C," Corros. Sci., **50**(1), pp. 194-199.

[101] Jackson, J., and Yen, C.-C.,1994, "Measurements of Total and Spectral Emissivities of Some Ceramic Fibre Insulation Materials," Proc. Inst. Energy 2nd Int. Conf. on Ceramics in Energy Applications, London, UK, Elsevier, pp. 159-174.

[102] Davies, H., 1954, "The Reflection of Electromagnetic Waves from a Rough Surface," Proc. IEE, Part IV: Inst. Monogr., **101**(7), pp. 209-214.

[103] ASTM International, 2017, "ASTM A1079-17 Standard Specification for Steel Sheet, Complex Phase (CP), Dual Phase (DP) and Transformation Induced Plasticity (TRIP), Zinc-Coated (Galvanized) or Zinc-Iron Alloy-Coated (Galvannealed) by the Hot-Dip Process," ASTM International, West Conshohocken, PA.

[104] Chen, L., Fourmentin, R., and Mc Dermid, J., 2008, "Morphology and Kinetics of Interfacial Layer Formation During Continuous Hot-Dip Galvanizing and Galvannealing," Metall. Mater. Trans. A, **39**(9), pp. 2128-2142.

[105] Howell, J. R., Menguc, M. P., and Siegel, R., 2015, *Thermal Radiation Heat Transfer*, CRC Press.

[106] Montgomery, D. C., 2013, *Design and Analysis of Experiments*, 8th ed., John Wiley & Sons, Hoboken, NJ.

[107] Witek-Krowiak, A., Chojnacka, K., Podstawczyk, D., Dawiec, A., and Pokomeda, K., 2014, "Application of Response Surface Methodology and Artificial Neural Network Methods in Modelling and Optimization of Biosorption Process," Bioresour. Technol., **160**, pp. 150-160.

[108] Elemuren, R., Evitts, R., Oguocha, I. N. A., Kennell, G., Gerspacher, R., and Odeshi, A. G., 2020, "Full Factorial, Microscopic and Spectroscopic Study of Erosion-Corrosion of AISI 1018 Steel Elbows in Potash Brine-Sand Slurry," Tribol. Int., **142**, p. 105989.

[109] Veliaković, A. V., Stamenković, O. S., Todorović, Z. B., and Veljković, V. B., 2013, "Application of the Full Factorial Design to Optimization of Base-Catalyzed Sunflower Oil Ethanolysis," Fuel, **104**, p. 433.

[110] Srinivasan, A., and Viraraghavan, T., 2010, "Oil Removal From Water by Fungal Biomass: A Factorial Design Analysis," J. Hazard. Mater., **175**(1), pp. 695-702.

[111] Ogilvy, J. A., 1987, "Wave Scattering from Rough Surfaces," Rep. Prog. Phys., **50**, pp. 1553-1608.

[112] Brannon, R. R., and Goldstein, R. J., 1970, "Emittance of Oxide Layers on a Metal Substrate," J. Heat Transf., **92**(2), pp. 257-263.

[113] Uran, S., Veal, B., Grimsditch, M., Pearson, J., and Berger, A., 2000, "Effect of Surface Roughness on Oxidation: Changes in Scale Thickness, Composition, and Residual Stress," Oxid. Met., **54**(1), pp. 73-85.

[114] Chang, Y. A., and Oates, W. A., 2010, *Materials Thermodynamics*, Wiley.

[115] Suleiman, F. K., Lin, K., and Daun, K. J., 2021, "Development of a Multivariate Spectral Emissivity Model for an Advanced High Strength Steel Alloy Through Factorial Design-Of-Experiments," J. Quant. Spectrosc. Radiat. Transf., **271**, p. 107693.

[116] Lin, K., and Daun, K. J., 2018, "Impact of Roughness Length Scale on Spectral Emissivity During Intercritical Annealing of Advanced High Strength Steels," Proc. Mater. Sci. Technol. Symp., Columbus, Ohio.

[117] Lin, K., and Daun, K. J., 2019, "Interpreting the Radiative Properties of Advanced High Strength Steels Using the Kirchhoff-Helmholtz Model," Proc. 9th Int. Symp. Radiat. Transf. (RAD-19), Begel House.

[118] Shi, C., Daun, K. J., and Wells, M. A., 2015, "Spectral Emissivity Characteristics of the Usibor® 1500P Steel During Austenitization in Argon and Air Atmospheres," Int. J. Heat Mass Transf., **91**, pp. 818-828.

[119] Gobbi, C., 2016, "Low Cost Thermal Imaging System for Welding Applications," MASc thesis, University of Waterloo, Waterloo, Ontario, Canada.

[120] ASTM International, 2017, "ASTM E230/E230M-17 Standard Specification for Temperature-Electromotive Force (EMF) Tables for Standardized Thermocouples," ASTM International, West Conshohocken, PA.

[121] González-Fernández, L., Risueño, E., Pérez-Sáez, R. B., and Tello, M. J., 2012, "Infrared Normal Spectral Emissivity of Ti–6Al–4V Alloy in the 500–1150 K Temperature Range," J. Alloys Compd., **541**, pp. 144-149.

[122] Teodorescu, G., and Jones, P. D., 2008, "Spectral and Directional Emittance of Alumina at 823 K," J. Mater. Sci., **43**(22), pp. 7225-7229.

[123] Teodorescu, G., Jones, P. D., Overfelt, R. A., and Guo, B., 2008, "Normal Emissivity of High-Purity Nickel at Temperatures Between 1440 and 1605 K," J. Phys. Chem. Solids, **69**(1), pp. 133-138.

[124] Teodorescu, G., 2007, "Radiative Emissivity of Metals and Oxidized Metals at High Temperature," PhD dissertation, Auburn University, Auburn, Alabama.

[125] Norton, O. P., 1990, "An Analysis of Error in Two Color Pyrometry," Proc. 5th AIAA/ASME Joint Thermophys. Heat Transf. Conf., No. AIAA 90-1716.

[126] Gathers, G., 1992, "Error Analysis by Numerical Simulation for a Three-Color Pyrometer assuming a Blackbody Spectrum and a Wavelength- and Temperature-Dependent Emissivity," Int. J. Thermophys., **13**(1), pp. 187-198.

[127] Gathers, G., 1992, "Error Analysis of a Ratio Pyrometer by Numerical Simulation," Int. J. Thermophys., **13**(1), pp. 173-185.

[128] Araújo, A., and Martins, N., 2015, "Monte Carlo Simulations of Ambient Temperature Uncertainty Determined by Dual-Band Pyrometry," Meas. Sci. Technol., **26**(8), p. 085016.

[129] Peter, S., 2003, "Propagation of Uncertainty for Non-Linear Calibration Equations With an Application in Radiation Thermometry," Metrologia, **40**(2), pp. 93-101.

[130] Joint Committee for Guides in Metrology (JCGM), 2008, JCGM 100: Evaluation of Measurement Data – Guide to the Expression of Uncertainty in Measurement, JCGM.

[131] Pierre, T., Krapez, J.-C., Orlande, H. R. B., Rodiet, C., Maux, D. L., Courtois, M., Masson, P. L., and Lamien, B., 2022, "Simultaneous Estimation of Temperature and Emissivity of Metals Around Their Melting Points by Deterministic and Bayesian Techniques," Int. J. Heat Mass Transf., **183**, p. 122077.

[132] Hadwin, P. J., Sipkens, T. A., Thomson, K. A., Liu, F., and Daun, K. J., 2016, "Quantifying Uncertainty in Soot Volume Fraction Estimates Using Bayesian Inference of Auto-Correlated Laser-Induced Incandescence Measurements," Appl. Phys. B, Lasers and Optics, **122**(1), pp. 1-16.

[133] Hadwin, P. J., Sipkens, T. A., Thomson, K. A., Liu, F., and Daun, K. J., 2017, "Quantifying Uncertainty in Auto-Compensating Laser-Induced Incandescence Parameters Due to Multiple Nuisance Parameters," Appl. Phys. B, Lasers and Optics, 123(4), pp. 1-15.

[134] Morgan, J. A., 2011, "Comparison of Bayesian Land Surface Temperature Algorithm Performance with Terra MODIS Observations," Int. J. Remote Sens., **32**(23), pp. 8139-8159.

[135] Wübbeler, G., Schmähling, F., Beyer, J., Engert, J., and Elster, C., 2012, "Analysis of Magnetic Field Fluctuation Thermometry Using Bayesian Inference," Meas. Sci. Technol., **23**(12), p. 125004.

[136] Sipkens, T. A., Hadwin, P. J., Grauer, S. J., and Daun, K. J., 2017, "General Error Model for Analysis of Laser-Induced Incandescence Signals," Appl. Opt., **56**(30), p. 8436.

[137] Foi, A., Trimeche, M., Katkovnik, V., and Egiazarian, K., 2008, "Practical Poissonian-Gaussian Noise Modeling and Fitting for Single-Image Raw-Data," IEEE Trans. Image Process., **17**(10), pp. 1737-1754.

[138] Ye, M., and Qian, Y., 2012, “Mixed Poisson-Gaussian Noise Model Based Sparse Denoising for Hyperspectral Imagery,” Proc. 4th Workshop Hyperspectral Image Signal Process.: Evol. Remote Sens. (WHISPERS), IEEE, pp. 1–4.

[139] Aster, R. C., 2013, *Parameter Estimation and Inverse Problems*, Elsevier, Amsterdam.

[140] Ulrych, T. J., and Sacchi, M. D., 2005, "3.3.3 Jaynes' Principle of Maximum Entropy," *Information-Based Inversion and Processing with Applications*, Elsevier.

[141] Del Campo, L., Pérez-Sáez, R. B., Esquisabel, X., Fernández, I., and Tello, M. J., 2006, "New Experimental Device for Infrared Spectral Directional Emissivity Measurements in a Controlled Environment," Rev. Sci. Instrum., **77**(11).

[142] Öner, M., and Deveci Kocakoç, İ., 2017, "JMASM 49: A Compilation of Some Popular Goodness of Fit Tests for Normal Distribution: Their algorithms and MATLAB Codes (MATLAB)," Journal of Modern Applied Statistical Methods, **16**(2), p. 30.

[143] Suleiman, F. K., Lin, K., Tsang, R., and Daun, K. J., 2022, "Bayesian Approach to Pyrometry During Intercritical Annealing of Advanced High Strength Steel," Meas. Sci. Technol., **33**(11), p. 115012.

[144] Wen, C.-D., and Mudawar, I., 2002, "Experimental Investigation of Emissivity of Aluminium Alloys and Temperature Determination Using Multispectral Radiation Thermometry (MRT) Algorithms," J. Mater. Eng. Perform., **11**(5), pp. 551-562.

[145] Lindseth, I., Bardal, A., and Spooren, R., 1999, "Reflectance Measurements of Aluminium Surfaces Using Integrating Spheres," Opt. Lasers Eng., **32**(5), pp. 419-435.

[146] Cho, L., Jung, G. S., and De Cooman, B. C., 2014, "On the Transition of Internal to External Selective Oxidation on CMnSi TRIP Steel," Metall. Mater. Trans. A, **45**(11), pp. 5158-5172.

[147] Jones, J. M., Mason, P. E., and Williams, A., 2019, "A Compilation of Data on the Radiant Emissivity of Some Materials at High Temperatures," J. Energy Inst., **92**(3), pp. 523-534.

[148] Wen, C.-D., and Mudawar, I., 2006, "Mathematical Determination of Emissivity and Surface Temperature of Aluminium Alloys Using Multispectral Radiation Thermometry," Int. Commun. Heat Mass Transf., **33**(9), pp. 1063-1070.

[149] Wen, C.-D., and Mudawar, I., 2004, "Emissivity Characteristics of Roughened Aluminium Alloy Surfaces and Assessment of Multispectral Radiation Thermometry (MRT) Emissivity Models," Int. J. Heat Mass Transf., **47**(17), pp. 3591-3605.

[150] Suleiman, F. K., Narayanan, N. S., and Daun, K. J., 2023, "Effect of Dewpoint on the Evolving Spectral Emissivity of Advanced High-Strength Steel during Intercritical Annealing," Proc. Iron Steel Technol. Conf., pp. 1598-1607.

[151] Suleiman, F. K., Lin, K., Tsang, R., Larrick, T. F., and Daun, K. J., 2019, "Impact of Evolving Spectral Emissivity on Pyrometry During Intercritical Annealing," 111th Galvanizers Association Meeting, Charleston, South Carolina.

[152] Bellhouse, E. M., and McDermid, J. R., 2011, "Selective Oxidation and Reactive Wetting during Galvanizing of a CMnAl TRIP-Assisted Steel," Metall. Mater. Trans.. A, **42**(9), pp. 2753-2768.

[153] Vidovič, L., and Majaron, B., 2014, "Elimination of Single-Beam Substitution Error in Diffuse Reflectance Measurements Using an Integrating Sphere," J. Biomed. Opt., **19**(2), pp. 027006-027006.

[154] Blake, T. A., Johnson, T. J., Tonkyn, R. G., land, B. M., Myers, T. L., Brauer, C. S., Su, Y.-F., Bernacki, B. E., Hanssen, L., and Gonzalez, G., 2018, "Methods For Quantitative Infrared Directional-Hemispherical and Diffuse Reflectance Measurements Using an FTIR and a Commercial Integrating Sphere," Appl. Opt., **57**(3), pp. 432-446.

[155] Roos, A., Ribbing, C. G., and Bergkvist, M., 1988, "Anomalies in Integrating Sphere Measurements on Structured Samples," Appl. Opt., **27**(18), pp. 3828-3832.

[156] Clarke, F. J. J., and Compton, J. A., 1986, "Correction Methods for Integrating-Sphere Measurement of Hemispherical Reflectance," Color Res. Appl., **11**(4), pp. 253-262.

[157] Beyhaghi, M., Rouhani, M., Hobley, J., and Jeng, Y.-R., 2021, "In-Situ and Ex-Situ Comparison of Oxidation of Inconel 718 Manufactured by Selective Laser Melting and Conventional Methods up to 650 °C," Appl. Surf. Sci., **569**, p. 151037.

[158] Suleiman, F. K., Narayanan, N. S., and Daun, K. J., 2024, "Effect of Dewpoint on the Evolving Radiative Properties of Advanced High-Strength Steel During Intercritical Annealing," AIST Trans., **21**(10), pp. 218-229.

[159] Larrick, T., *Understanding Modern Infrared Pyrometers for Demanding Steel Mill Applications*, Williamson Corporation, Concord MA, USA, pp. 1-17.

[160] Abuluwefa, H., 2012, "Thermodynamics and Kinetics of Surface Oxidation of Steels During Annealing in H_2-N_2 Atmospheres," Proc. Int. MultiConference of Engineers and Computer Scientists (IMECS 2012), Vol. II, Hong Kong.

[161] Alibeigi, S., Kavitha, R., Meguerian, R. J., and McDermid, J. R., 2011, "Reactive Wetting of High Mn Steels During Continuous Hot-Dip Galvanizing," Acta Mater., **59**(9), pp. 3537-3549.

[162] Ollivier-Leduc, A., Giorgi, M. L., Balloy, D., and Guillot, J. B., 2010, "Nucleation and Growth of Selective Oxide Particles on Ferritic Steel," Corros. Sci., **52**(7), pp. 2498-2504.

[163] Hugel, J., and Carabatos, C., 1986, "Band Structure and Optical Properties of MnO," Solid State Commun., **60**(4), pp. 369-372.

[164] Suleiman, F. K., Narayanan, N. S., and Daun, K. J., 2023, "Investigating the *In situ* Effects of Selective Oxidation on the Radiative Properties of Advanced High Strength Steel," Proc. 13th Int. Conf. Zinc & Zinc Alloy Coated Steel Sheet, Seoul South Korea.

[165] Rey, M., Kramer, D., Henderson, W., and Abney, L., 1984, *Dew point/Temperature Curves for Selected Metal/Metal Oxide Systems in Hydrogen Atmospheres*, Monsanto Research Corp., Miamisburg, OH.

[166] Ragone, D. V., 1995, *Thermodynamics of materials*, Vol. I, Wiley, New York.

[167] Huin, D., Flauder, P., and Leblond, J. B., 2005, "Numerical Simulation of Internal Oxidation of Steels during Annealing Treatments," Oxid. Met., **64**(1), pp. 131-167.

[168] Bhadhon, K. M. H., and McDermid, J. R., 2022, "Selective Oxidation of a Medium-Mn Third Generation Advanced High Strength Steel during Austenitizing and Intercritical Annealing," J. Electrochem. Soc., **169**(6), p. 61504.

Appendix A
Thermodynamic analysis of the gas-metal oxidation reaction

This appendix details thermodynamic calculations for the gas-metal oxidation/reduction diagram inferring the likelihood of alloy elements forming selective oxides during intercritical annealing.

A.1. Oxygen partial pressure of the annealing atmosphere

The oxygen partial pressure (pO_2) of the annealing atmosphere indicates oxidation potential of the reducing atmosphere during intercritical annealing. It is inferred from the equilibrium of the water vapor content in the atmosphere, which is conveniently monitored via dew point measurement. Dew point provides an indirect measure of water vapour partial pressure, $p\mathrm{H_2O}$, and thus pO_2, especially when the hydrogen partial pressure ($p\mathrm{H_2}$) is fixed [165].

The dew point is the temperature at which the atmosphere is saturated with water vapor, such that cooling the gas below this point would cause the water vapor to condense into liquid water. Therefore, at a given dew point temperature, T_{dp}, water vapor in the saturated atmosphere is in equilibrium with liquid water, such that:

$$\mathrm{H_2O_{(l)}} \rightleftarrows \mathrm{H_2O_{(g)}} \tag{A.1}$$

The Gibbs free energy change, ΔG_1, for this equilibrium reaction under isobaric conditions is given by:

$$\Delta G_1 = \Delta G_1^{\mathrm{o}} + RT_{dp} \ln K_1 = 0 \tag{A.2}$$

where ΔG_1^{o} is the standard Gibbs free energy of formation, R is the universal gas constant (8.3145 J/K·mol) and K_1 is the equilibrium constant. The equilibrium constant for any reaction is a dimensionless value defined by the thermodynamic activities of the reactants and products.

$$K_1 = \frac{a_{\mathrm{H_2O_{(g)}}}}{a_{\mathrm{H_2O_{(l)}}}} = \frac{\dfrac{p\mathrm{H_2O}}{1\ \mathrm{atm}}}{1} = p\mathrm{H_2O} \tag{A.3}$$

The thermodynamic activity, a, describes the effective concentration of a chemical substance relative to a reference ideal state [166]. The phase of the chemical substance determines the corresponding reference state. The activity for an ideal gaseous substance is obtained by using a reference state of 1 atm partial pressure, while the activity of the individual element in an ideal solid solution (alloy) is described by its atomic or mole fraction. Pure condensed phases (i.e., pure solids and pure liquids) have an activity of 1. In the case of the dew point controlled annealing atmosphere, $H_2O_{(g)}$ is assumed to be an ideal gas and the condensed water vapor, $H_2O_{(l)}$ is assumed to be a pure liquid.

The standard Gibbs free energy of formation, ΔG_1° in Eq. (A.2) can also be expressed in terms of the difference in the free standard energies of the product and reactants such that

$$\Delta G_1^{\circ} = \Delta G_{1p}^{\circ} - \Delta G_{1r}^{\circ} \tag{A.4}$$

where ΔG_{1p}° and ΔG_{1r}° is the standard free energy of formation for $H_2O_{(g)}$ and $H_2O_{(l)}$ respectively, at the dew point temperature. Substituting Eqs. (A.4) and (A.3) into Eq. (A.2), and rearranging the variables to give the water vapor partial pressure in terms of the dew point temperature:

$$p\,\mathrm{H_2O} = \exp\left[-\frac{\Delta G_{1p}^{\circ} - \Delta G_{1r}^{\circ}}{RT_{dp}}\right] \tag{A.5}$$

An approximate value for the water vapor partial pressure can also be obtained using the Huin model [167]. Since the hydrogen content of the annealing atmosphere is fixed for any given process temperature, T_{pr}, the oxygen partial pressure can be inferred from the water vapor partial pressure and hydrogen partial pressure at the dissociation equilibrium of $H_2O_{(g)}$:

$$\mathrm{H_{2(g)}} + \frac{1}{2}\mathrm{O_{2(g)}} \rightleftarrows \mathrm{H_2O_{(g)}} \tag{A.6}$$

and the Gibbs free energy change, ΔG_2 at equilibrium for Eq. (A.6) is given by

$$\Delta G_2 = \Delta G_2^{\circ} + RT_{pr} \ln K_2 = 0 \tag{A.7}$$

$$K_2 = \frac{a_{\mathrm{H_2O_{(g)}}}}{a_{\mathrm{H_{2(g)}}} \times a_{\mathrm{O_{2(g)}}}^{\frac{1}{2}}} = \frac{\dfrac{p\,\mathrm{H_2O}}{1\ \mathrm{atm}}}{\dfrac{p\,\mathrm{H_2}}{1\ \mathrm{atm}} \times \left[\dfrac{p\,\mathrm{O_2}}{1\ \mathrm{atm}}\right]^{\frac{1}{2}}} = \frac{p\,\mathrm{H_2O}}{p\,\mathrm{H_2} \cdot \left[p\,\mathrm{O_2}\right]^{\frac{1}{2}}} \tag{A.8}$$

where ΔG_2° is the standard Gibbs free energy of formation for water vapour ($H_2O_{(g)}$), T_{pr} is the temperature of the reaction in Kelvin and K_2 is the equilibrium constant. The equilibrium constant is a dimensionless constant defined in terms of the thermodynamic activity of the chemical substances or species that make up the product and reactant. The gases are assumed to be ideal; therefore, their activities are defined with respect to a reference state of 1 atm partial pressure.

Combining Eqs. (A.7) and (A.8) with Eq. (A.5), and rearranging for pO_2 gives

$$p\,\mathrm{O}_2 = \left[\frac{p\,\mathrm{H_2O}}{p\,\mathrm{H}_2 \cdot \exp\left(-\dfrac{\Delta G_2^{\circ}}{RT_{pr}}\right)}\right]^2 = \left[\frac{\exp\left(-\dfrac{\Delta G_{1\mathrm{p}}^{\circ} - \Delta G_{1\mathrm{r}}^{\circ}}{RT_{dp}}\right)}{p\,\mathrm{H}_2 \cdot \exp\left(-\dfrac{\Delta G_2^{\circ}}{RT_{pr}}\right)}\right]^2 \tag{A.9}$$

Equation (A.9) shows that the pO_2 of the annealing atmosphere is directly proportional to pH_2O (and T_{dp}) but inversely proportional to pH_2. Therefore, in addition to decreasing the water vapor content, the oxidation potential of the atmosphere can also be decreased by increasing the hydrogen content. All experiments discussed in this thesis would carried out in annealing atmosphere with the hydrogen content fixed at 5%, therefore Eq. (A.9) will only be evaluated for $pH_2 = 0.05$.

A.2. Oxygen partial pressure of the metal oxides

For a given metal element, M, the thermodynamic stability of its stoichiometric oxide, M_xO_y, in terms of the equilibrium oxygen partial pressure can be obtained from the reaction equation:

$$\frac{\mathrm{x}}{\mathrm{y}}\mathrm{M}_{(\mathrm{s})} + \frac{1}{2}\mathrm{O}_{2(\mathrm{g})} \rightleftarrows \frac{1}{\mathrm{y}}\mathrm{M}_{\mathrm{x}}\mathrm{O}_{\mathrm{y}(\mathrm{s})} \tag{A.10}$$

Similar to Eqs. (A.2) and (A.7) the equilibrium Gibbs free energy change at the temperature (T_{pr}) of the reaction in Eq. (A.10) is given by

$$\Delta G_3 = \Delta G_3^{\circ} + RT_{pr} \ln K_3 = 0 \tag{A.11}$$

$$K_3 = \frac{a_{\mathrm{M_xO_y}}^{\frac{1}{\mathrm{y}}}}{a_{\mathrm{M}}^{\frac{\mathrm{x}}{\mathrm{y}}} \times a_{\mathrm{O}_{2(\mathrm{g})}}^{\frac{1}{2}}} = \frac{1^{\frac{1}{\mathrm{y}}}}{a_{\mathrm{M}}^{\frac{\mathrm{x}}{\mathrm{y}}} \times \left[\dfrac{p\,\mathrm{O}_2}{1\ \mathrm{atm}}\right]^{\frac{1}{2}}} = \frac{1}{a_{\mathrm{M}}^{\frac{\mathrm{x}}{\mathrm{y}}} \cdot \left[p\,\mathrm{O}_2\right]^{\frac{1}{2}}} \tag{A.12}$$

where ΔG_3° is standard free energy of formation for $1/yM_xO_y$, and K_3 is the equilibrium constant of the oxidation reaction. All the chemical species are assumed to be ideal; therefore, the

activity of the ideal oxygen gas is written in terms of its partial pressure. The condensed oxide is assumed to be a pure solid, hence the activity of unity. The thermodynamic activity of the individual element in an ideal solid solution is described by its atomic or mole fraction, thus, the activity, a_M, of element M is given by its atomic fraction in the alloy composition.

Combining Eqs. (A.11) and (A.12), and rearranging for the oxygen partial pressure of the oxide at the equilibrium gives

$$pO_2 = \left[\frac{1}{a_M^{\frac{x}{y}} \cdot \exp\left(-\frac{\Delta G_3^o}{RT_{pr}} \right)} \right]^2 \tag{A.13}$$

The oxidation potential diagram in Figure 2.6 and Figure 8.1 plots the oxygen partial pressure of the atmosphere from Eq. (A.9) and the equilibrium oxygen partial pressure of the oxides obtained with Eq. (A.13). Figure 2.6 assumes $a_M = 1$ for all elements, while Figure 8.1 uses the true activity of the alloying elements based on their mole fraction in the DP980 alloy. The thermodynamic data for the Gibbs free energy calculation is obtained from Refs. [74, 168]. The standard Gibbs energy (ΔG_{1p}^o, ΔG_{1r}^o, ΔG_2^o, and ΔG_3^o) in J/mol as are calculated using:

$$\Delta G = AT\ln(T) + BT + CT^2 + DT^{-1} + ET^{1/2} + F \times 10^{-7} T^3 + G \tag{A.14}$$

with the coefficients A (J/mol K), B (J/mol K), C (J/mol K^2), D (J/mol K^{-1}), E (J/mol K$^{0.5}$), F (J/mol K^3), and G (J/mol) for each compound listed in Table A.1. The values for ΔG_{1p}^o and ΔG_{1r}^o are evaluated at T_{dp}, while ΔG_2^o, and ΔG_3^o are evaluated at T_{pr}.

Table A.1. Coefficients for the standard Gibbs energy of formation for each compound [74, 168].

Compound	***A***	***B***	***C***	***D***	***E***	***F***	***G***
H_2O (l)	-2304.0466	18256.7583	1.4416257	-8161063.5	-121879.48	-3158.67	245617.101
H_2O (g)	14.5914916	-49.440744	-0.0053297	-122643.5	-76.542088	3.47762	-236434.09
FeO (s)	-312.37974	2289.59246	0.1296543	35023345.2	1042.28461	5.85664	-536965.33
Fe_3O_4 (s)	-819.5096	6020.9804	0.3753117	62252807.2	4169.1384	2.69232	-1722055.5
MnO (s)	1.3662852	36.6929348	0.00481023	352614.968	1042.28461	-3.9889179	-395773.02
Cr_2O_3 (s)	297.7993	-2306.32	-0.10063	4175977	23712.64	119.406	-1292002
Al_2O_3 (s)	-11.4987	441.7964	-0.003572678	14.34315	-677.741	2.03343	-1700491
SiO_2 (s)	8.21930022	79.2570095	-0.0009297	1322689.18	2084.56922	-1.1798608	-932891.64

Appendix B
Vacuum chamber design and implementation

Table B.1 summarizes the key functional, constraint, and non-functional requirements defined for the vacuum chamber design. The functional requirements define the main functions of the design, i.e., the distinct and non-negotiable characteristics of the chamber. The constraint requirements are the limitations that constrain the design space while the non-functional requirements are the qualities that are required for the quality operation of the chamber. Although most of the requirements, except for the leak-proof vacuum constraint, are consistent across Chambers 1 and 2, the approach to their implementation significantly differs.

Table B.1. Functional, constraint and non-functional requirement for the vacuum chamber.

Functional requirement	Constraint requirement	Non-functional requirement
• Controlled heating of samples • Controlled annealing atmosphere • Optical access for emission measurement	• Leak proof vacuum • CSA standards compliance • Affordability	• Compatible with *in situ* FTIR measurement • Reliability; can be operated repeatedly for experiments • Ease of upgrade and modification • Ergonomics; easy to use and manoeuvre • Easy to clean and maintain

B.1. Modular flange design

One issue identified with the box design of Chamber 1 is the potential for stagnation in the corners. Therefore, the entire vacuum chamber is designed as a ConFlat (CF) full nipple (14″ diameter, 10.5″ length) to minimize stagnation in corners. The flanges on the chamber are non-rotatable on both ends and several smaller CF half nipples for coupling instrumentations and gas lines are welded onto the front and back blank flanges. All the flanges and blanks are made from 304 stainless steel. The size of the chamber is sufficient to satisfy the "small object in a large isothermal enclosure" assumption, which ensures that the measured emission is coming solely from the AHSS

sample with no reflection or interaction from the walls of the chamber. The CF flange design is inherently modular for two key reasons. First, having a cylindrical chamber means that all instrumentation will connect to the front or back flanges, which makes it easier to carry out major modification without needing to redesign the entire chamber. Secondly, the need for vacuum feedthroughs for all the instrumentation means that each device can be independently replaced or upgraded. The design included mounting brackets to orient the chamber as well as a custom hinge system to support the front flange. The custom hinge system converts the front flange into a door, which: (1) eliminates the need to lift and align the >23 kg front flange each time; and (2) prevents potential damage to the knife-edge and optical lens from moving the front flange around constantly. The chamber cart was also redesigned to better accommodate the increased size and weight of the vacuum chamber. The new cart resulted in a more compact annealing simulator assembly, making it easier to maneuver the chamber despite its increased weight. The caster wheels on the cart are also height-adjustable, which would be useful for aligning the chamber viewports with optical systems like the FTIR spectrometer.

The next step was to select the gasket material; this decision is crucial, since it determines the attainable vacuum pressure and total pump down time. Stainless steel CF flanges for high and ultra-high vacuum applications are typically fitted with oxygen-free, high conductivity (OFHC) copper gasket, which is compressed between the knife-edges to create an impermeable metal-to-metal seal. Therefore, copper gaskets are used for all the CF flanges with the exception of the main front door flange because copper gaskets are single-use seals, as the knife-edge deforms the copper by cutting into it. Instead, a reusable Viton® gasket made from a fluorocarbon polymer is used to create an elastomer seal on the front flange. Copper gaskets were selected all the other flanges since these would be rarely, if ever, disassembled, while the Viton® gasket is necessary for the front flange since the chamber door will be opened and closed frequently. Equally important, due to the horizontal orientation of the chamber, some vacuum grease is used to hold the rubber gasket in the place when sealing the front door before an experiment. Lastly, having to fasten and torque down all 30 bolts on the 14″ front flange before each experiment was burdensome, so bolts are installed in six of these holes to seal the chamber. The six bolts were arranged in an equilateral hexagonal pattern across the original circular bolt pattern, which ensures uniform seal on the rubber gasket.

B.2. Vacuum feedthroughs

Selecting appropriate CF flange feedthroughs and vacuum-compatible materials was crucial for connecting all the necessary instruments and gas lines while ensuring the chamber could maintain a vacuum. Commercially available gas and thermocouple feedthroughs were compatible with the chamber requirements, but custom solutions had to be designed for optical and power connections.

In terms of the optical feedthroughs, typical viewports for vacuum chambers consist of a quartz lens brazed to the metal flange to create a hermetical seal. However, quartz is not transparent over the infrared measurement spectrum of interest. Instead, demountable viewports were developed that use Viton O-rings to create an airtight seal between a glass/lens and a metal flange. The demountable view ports had to be custom-made to accommodate lens that will give the desired view diameter of the heated spot on the AHSS coupon. The calcium fluoride (CaF_2) lens from Chamber 1 was re-used for the pyrometer view port (2″ view diameter on a 4.5″ CF flange), while a new sapphire (Al_2O_3) lens was obtained for the spectrometer view port (1.19″ view diameter on a 2.75″ CF flange). The pyrometer view port is on the outside of the chamber while the spectrometer view port is inside of the chamber. The mounting angle for the spectrometer-collimating lens assembly was also increased from 25° to 35° to better fit both optical view ports on the front of the chamber. The transmittances of the CaF_2 and Al_2O_3 lens were measured with the FTIR spectrometer before assembling them in their respective view ports. The average spectral transmittance of the CaF_2 and Al_2O_3 viewports over the near-infrared wavelengths are 0.95 and 0.86, respectively. While the demountable view ports allow for easier cleaning/replacement of the lens in the case of surface contaminations that affects the transmittance and efficacy of the lens; it is expected that the lens will remain relatively clean (with fairly constant transmittance) over time because the annealing process does not produce deposits that would coat the chamber surfaces.

The O-ring seal design from the upgraded Chamber 1 was reused for the electrical busbar feedthrough because the commercially available electrical feedthroughs were not suitable for the intended application. However, the feedthrough and inserts were modified to fit with the other components on the back flange. The number, location and sizes of the O-rings were also modified to improve the quality of the vacuum seal. After assembly, snap rings (external retaining rings) were added to both sides of the copper inserts to keep them from falling into the chamber under vacuum or pulling out at positive pressures when the chamber is back filled with the reducing gas.

B.3. Atmosphere control

Although the atmosphere control system was installed and operational in the upgraded version of Chamber 1, it was never used for experiments because the chamber-processed samples had a visible oxide layer with just the ultra-high purity, low dew point ($\leq -40°C$) reducing gas introduced directly from the cylinder. After Chamber 2 was built, it was discovered that the existing humidification system (i.e., water and mixing chambers) were not compatible with a vacuum-based design. To address this, the humidification chambers were redesigned as full nipple flanges that seal with high vacuum O-rings. Figure B.1 shows the image of the new humidification system in comparison to the version created for Chamber 1. The new flanges for the humidification system are similar in size to the old versions so the apparatus could fit on the chamber cart. Due to their size, these flanges were custom-made, and they are more similar to ISO-F flanges than CF flanges because custom machining cost for CF knife-edge grooves are expensive. A K-type thermocouple probe was added to the water chamber for potential high dew point experiments that would require heating the water with the use of a flexible wrap-around heater; however, this was not needed for any of the experiments described in this thesis.

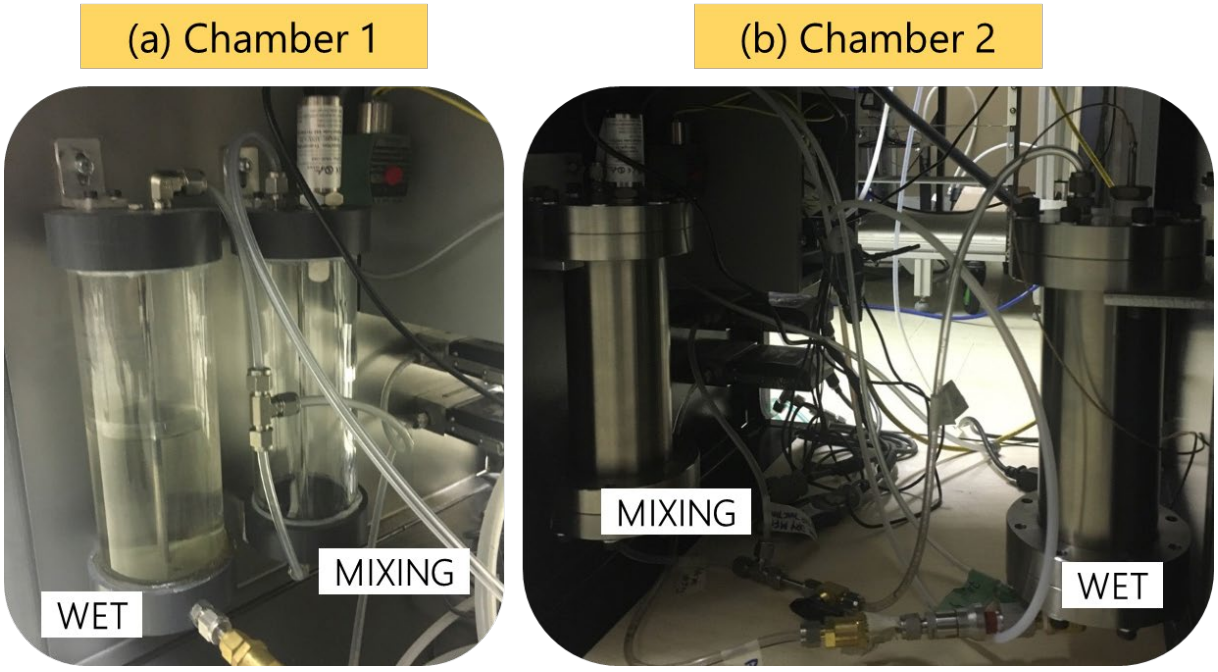


Figure B.1. Images of the wet and mixing chamber designed for the humidification system in (a) Chamber 1 and (b) Chamber 2.

Next, the gas cylinders and humidification system are connected to the main vacuum chamber according to the piping and instrumentation diagram (P&ID) in Figure B.2. First, in addition to the check valve at the inlet of the wet humidification chamber, a unidirectional Swagelok® QC4 quick connect fitting with double-end shutoff is installed for easy disconnection of the wet flow during extremely low dew point experiments. The quick connect only allows flow in one direction which further prevents backflow of water into the MFCs and gas lines. Chamber 1 used a check valve for this purpose, but it became susceptible to back flow of water over time. Further, several ball valves were installed across the new vacuum-based system to prevent water from inadvertently getting into the chamber, MFCs, and gas lines, especially when the vacuum pump is operating. Similarly, the N_2 and N_2-H_2 gas lines have ball valves installed on both the regulator and chamber ends of the line to minimize trace infiltration from the regulator and PTFE tubing, especially since the pressure regulators on the cylinders are not helium leak certified, high purity regulators. The ball valves are operated in a sequence that ensures that the chamber, regulator, and tubing always have gas flowing through them when they are not under vacuum. This pressure differential ensures that any locations with imperfect seal is leaking out N_2 or N_2-H_2, instead letting air into the chamber during experiments.

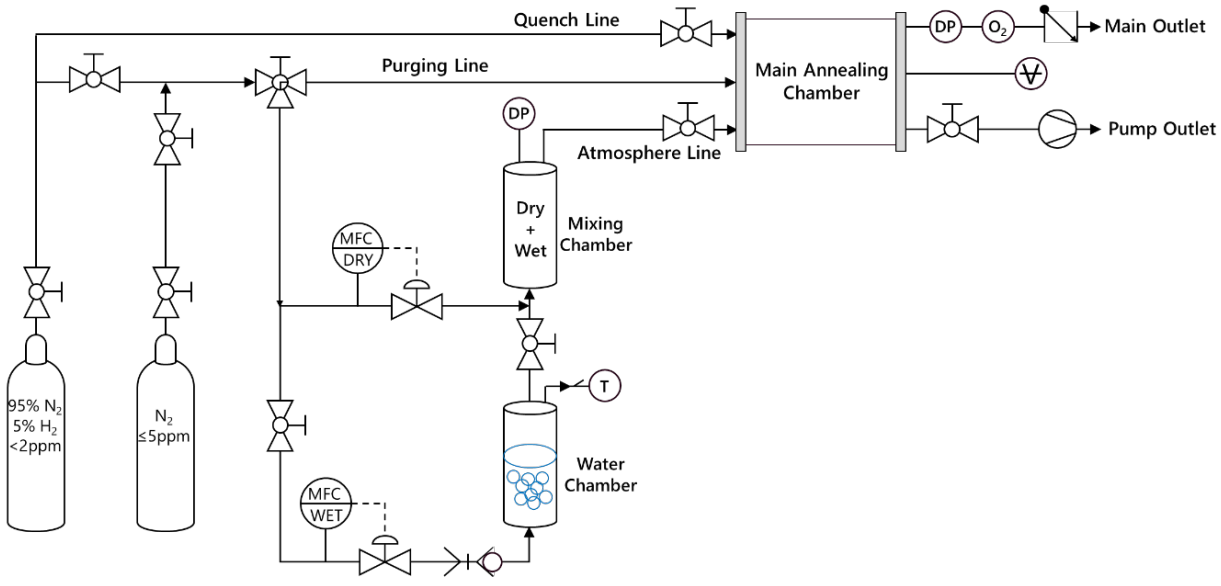


Figure B.2. Piping and instrumentation diagram (P&ID) for the vacuum-based annealing simulator (Chamber 2).

B.4. Quench system

The previous chamber was fitted with a solenoid valve to automatically quench the samples at the end of the heating schedule. However, the imperfect seal on the solenoid valve was found to be a source of oxygen infiltration in the vacuum chamber setup so this was substituted with a manual quench system consisting of a Swagelok® ball valve and stainless-steel tubing. A helium gas cylinder was initially connected to the quench line to achieve faster quench rates, but the samples quenched with helium showed visible oxidation on the backside of the sample (where the nozzle is pointed), due to O_2 impurities in the He. Accordingly, ultra-high purity N_2/H_2 gas was used to quench the specimens instead of helium; however, it is important to note that the He-quenched samples in the vacuum chamber had a visible oxide layer on their backsides, while samples quenched with ultra-high purity N_2/H_2 gas in the previous chamber had visible layers on both sides. Quenching with the ultra-high purity N_2/H_2 in the vacuum chamber does not produce visible oxidation on either sides of the sample, as seen in Figure B.3, which compares the visible oxidation on the samples quenched with helium against those quenched with the reducing gas.

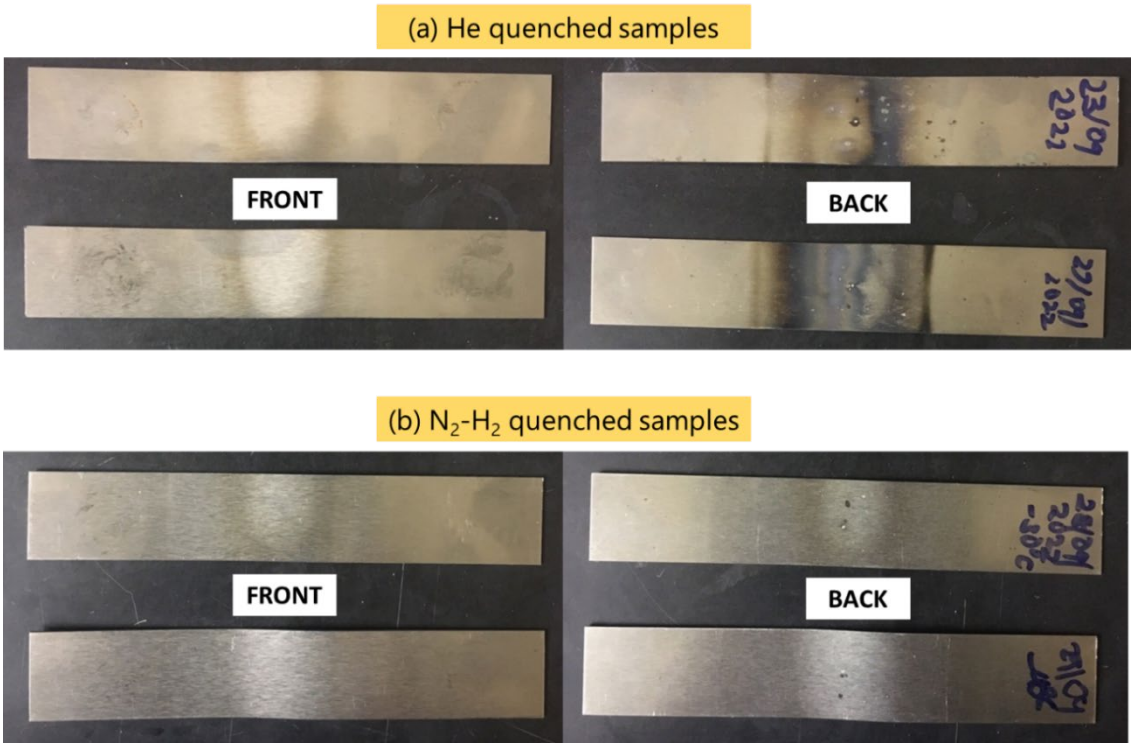
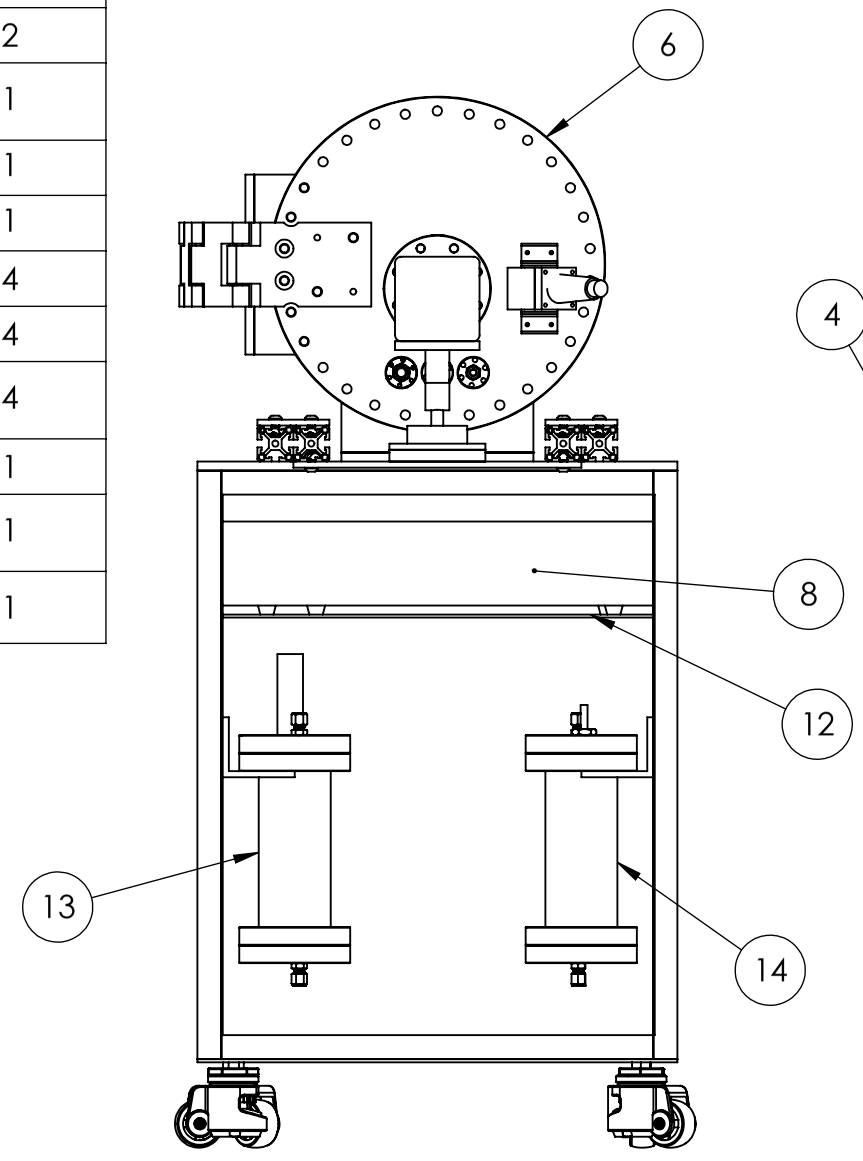
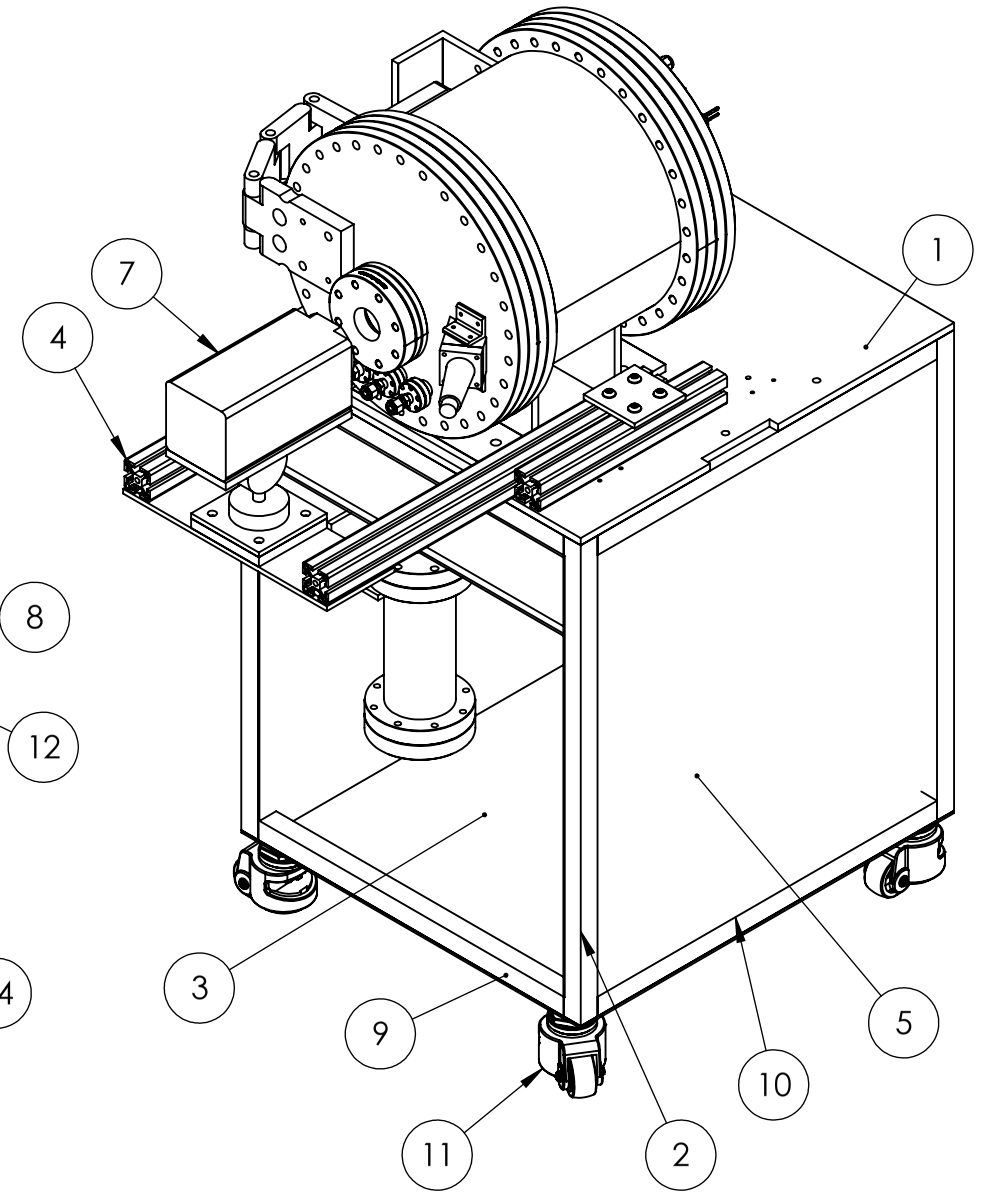


Figure B.3. Comparing the anomalous visible oxide layer on (a) samples quenched in helium against (b) samples quenched with ultra-high purity nitrogen-hydrogen mixture.

ITEM NO.	PART NUMBER	DESCRIPTION	QTY.
1	Shelf	SHELF FROM OLD CHAMBER	1
2	Steel Tube	SHEET 22 & SHEET 23	4
3	BottomShelf	BOTTOM PANEL FOR NEW CART	1
4	PyrometerMount	EXISTING PYROMETER MOUNT	1
5	SidePanel	SIDE PANEL FOR THE NEW CART	2
6	CylindricalChamber_HingesV2	SHEET 2 - SHEET 22	1
7	Pyrometer	EXISTING PYROMETER	1
8	Power Supply	EXISTING POWER SUPPLY	1
9	Side Tube 1	SHEET 22 & SHEET 23	4
10	Side Tube 2	SHEET 22 & SHEET 23	4
11	2445T12	Threaded-Stem Leveling Caster	4
12	PowerShelf	SHELF FOR POWER SUPPLY	1
13	Mixing Chamber 304SS	SHEET 24 - SHEET 32	1
14	Water Chamber 304SS	SHEET 24 - SHEET 32	1





NOTE:
ITEMS 7 AND 8 ARE THE EQUIPMENT TO BE MOUNTED ON THE CART.

ITEMS 1, 4 AND 12 ARE TO BE TRANSFERRED FROM THE EXISTING CART.

ITEMS MOUNTED ON THE LEFT PANEL OF THE EXISTING CART WILL ALSO BE TRANSFERRED TO THE LEFT PANEL OF NEW CART

PROPRIETARY AND CONFIDENTIAL

THE INFORMATION CONTAINED IN THIS DRAWING IS THE SOLE PROPERTY OF <INSERT COMPANY NAME HERE>. ANY REPRODUCTION IN PART OR AS A WHOLE WITHOUT THE WRITTEN PERMISSION OF <INSERT COMPANY NAME HERE> IS PROHIBITED.

NEXT ASSY	USED ON
APPLICATION	

UNLESS OTHERWISE SPECIFIED:

DIMENSIONS ARE IN INCHES
TOLERANCES:
FRACTIONAL ±
ANGULAR: MACH ± BEND ±
TWO PLACE DECIMAL ±
THREE PLACE DECIMAL ±

INTERPRET GEOMETRIC TOLERANCING PER:

MATERIAL

FINISH

DO NOT SCALE DRAWING

	NAME	DATE
DRAWN	F.K. SULEIMAN	
CHECKED		
ENG APPR.		
MFG APPR.		
Q.A.		

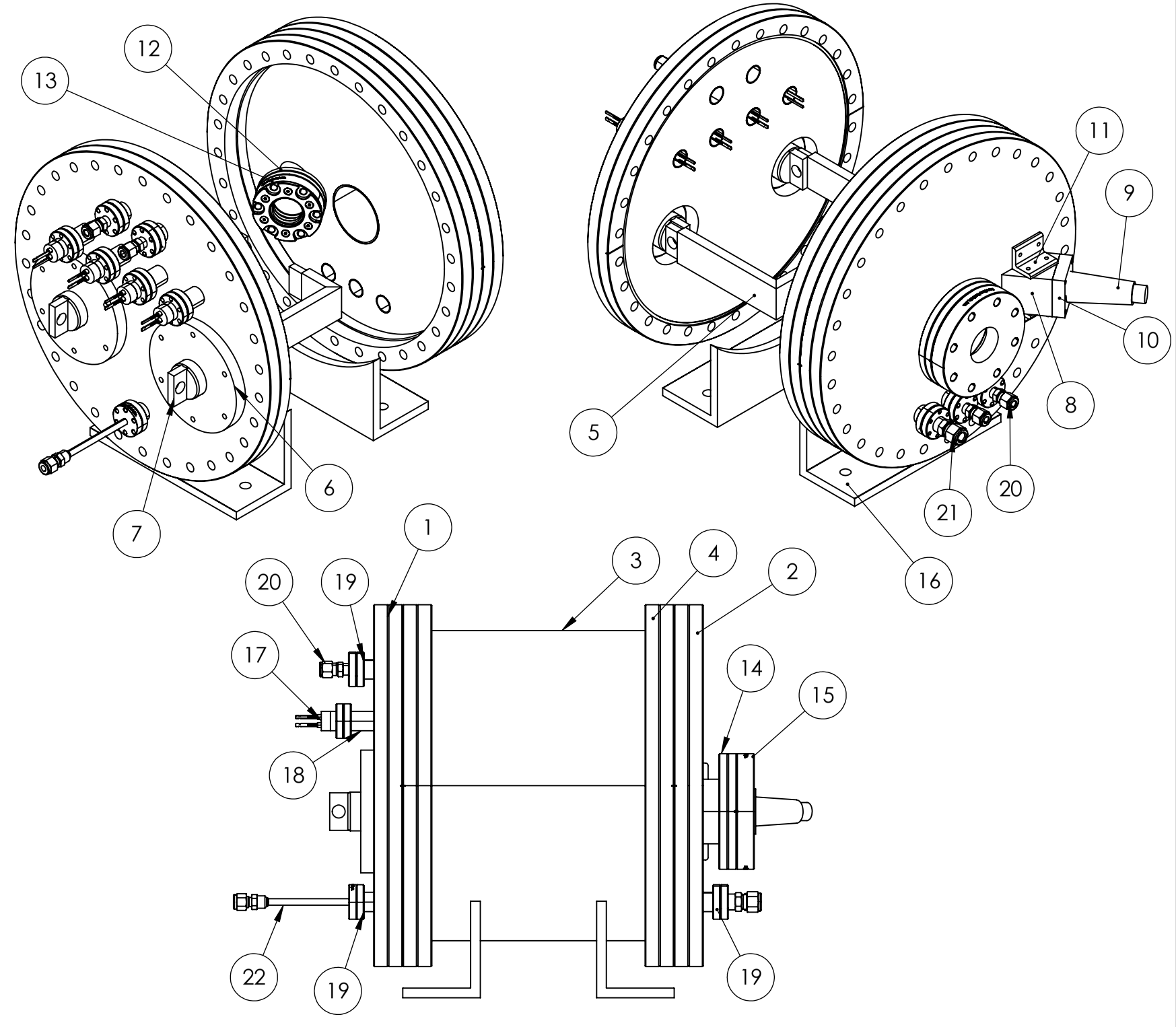
COMMENTS:

TITLE:
AHSS ANNEALING SIMULATOR SETUP

SIZE	DWG. NO.	REV
B		

SCALE: 1:20 | WEIGHT: | SHEET 1 OF 32

ITEM NO.	PART NUMBER	DESCRIPTION	QTY.
1	1400_000N_BACK	SHEET 5 & SHEET 17	1
2	1400_000N_FRONT	SHEET 6 & SHEET 16	1
3	1N_1200	SHEET 15	1
4	1400_1200N	SHEET 15	1
5	Bus Bar	SHEET 4	2
6	Bus bar flange	SHEET 11 & SHEET 17	2
7	Copper_Insert	SHEET 17	2
8	Lens Mount	SHEET 12	1
9	Spectrometer lens	ASSEMBLY ONLY	1
10	Lens collar	ASSEMBLY ONLY	1
11	8982K151	SHEET 13	2
12	2N_150_Angled	SHEET 8 & SHEET 16	1
13	112667 AGP	ASSEMBLY ONLY	1
14	1N_250_Reduced	SHEET 7 & SHEET 16	1
15	200122	ASSEMBLY ONLY	1
16	1260T581	SHEET 14 & SHEET 15	2
17	P108108_TC	ASSEMBLY ONLY	4
18	2N_075_TC	SHEET 10 & SHEET 17	4
19	2N_075_SWAG	SHEET 9 & SHEET 16 & SHEET 17	6
20	133_1_4_SWAG	ASSEMBLY ONLY	4
21	133_3_8_SWAG	ASSEMBLY ONLY	1
22	113001	ASSEMBLY ONLY	1



NOTE:
SHEET 1 to SHEET 15 IS THE DRAWINGS FOR THE ORIGINAL CHAMBER DESIGN,
WHILE **SHEET 16 to SHEET 21** COVERS THE DRAWING FOR THE HINGE DESIGN FOR THE FRONT DOOR.

PROPRIETARY AND CONFIDENTIAL
THE INFORMATION CONTAINED IN THIS DRAWING IS THE SOLE PROPERTY OF <INSERT COMPANY NAME HERE>. ANY REPRODUCTION IN PART OR AS A WHOLE WITHOUT THE WRITTEN PERMISSION OF <INSERT COMPANY NAME HERE> IS PROHIBITED.

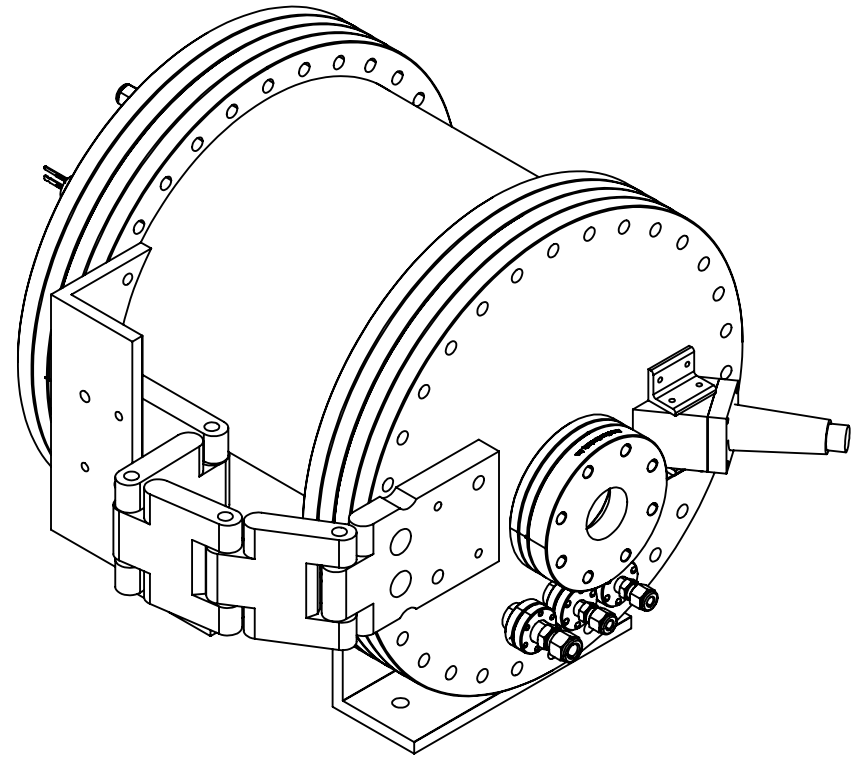
		UNLESS OTHERWISE SPECIFIED:		NAME	DATE
		DIMENSIONS ARE IN INCHES TOLERANCES: FRACTIONAL ± ANGULAR: MACH ± BEND ± TWO PLACE DECIMAL ± THREE PLACE DECIMAL ±	DRAWN	F.K. SULEIMAN	
			CHECKED		
			ENG APPR.		
			MFG APPR.		
		INTERPRET GEOMETRIC TOLERANCING PER:	Q.A.		
		MATERIAL	COMMENTS:		
NEXT ASSY	USED ON	FINISH			
APPLICATION		DO NOT SCALE DRAWING			

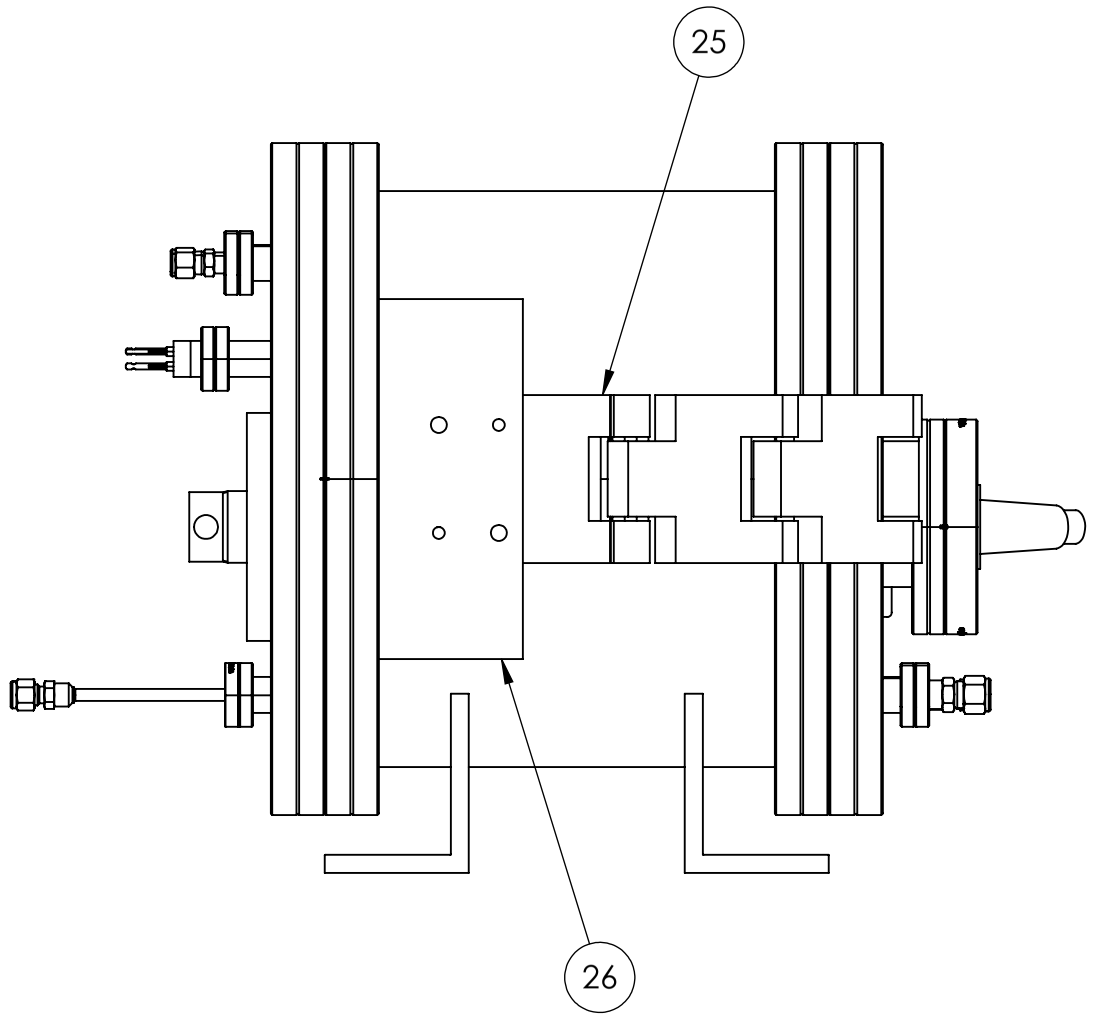
TITLE:
VACUUM ANNEALING CHAMBER
(HINGES NOT SHOWN)

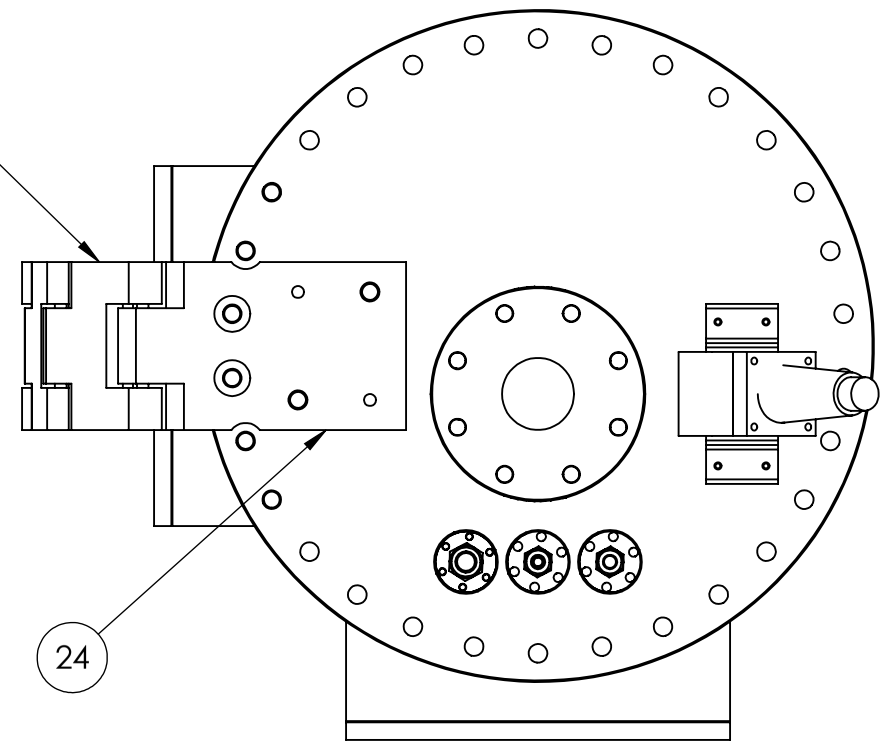
SIZE	DWG. NO.	REV
B		

SCALE: 1:10 | WEIGHT: | SHEET 2 OF 32

ITEM NO.	PART NUMBER	DESCRIPTION	QTY.
23	Hinge3and4and5_MIDDLE	SHEET 18	3
24	Hinge2_FRONT	SHEET 19	1
25	Hinge6_BACK	SHEET 20	1
26	1260T581_BRACKET	SHEET 21	1







NOTE:
THE SCREWS, SHOULDER BOLTS AND WASHERS FOR ASSEMBLING THE HINGES AND CHAMBER ARE NOT VISIBLE IN THESE DRAWINGS

PROPRIETARY AND CONFIDENTIAL
THE INFORMATION CONTAINED IN THIS DRAWING IS THE SOLE PROPERTY OF <INSERT COMPANY NAME HERE>. ANY REPRODUCTION IN PART OR AS A WHOLE WITHOUT THE WRITTEN PERMISSION OF <INSERT COMPANY NAME HERE> IS PROHIBITED.

		UNLESS OTHERWISE SPECIFIED:
		DIMENSIONS ARE IN INCHES TOLERANCES: FRACTIONAL ± ANGULAR: MACH ± BEND ± TWO PLACE DECIMAL ± THREE PLACE DECIMAL ±
		INTERPRET GEOMETRIC TOLERANCING PER:
		MATERIAL
NEXT ASSY	USED ON	FINISH
APPLICATION		DO NOT SCALE DRAWING

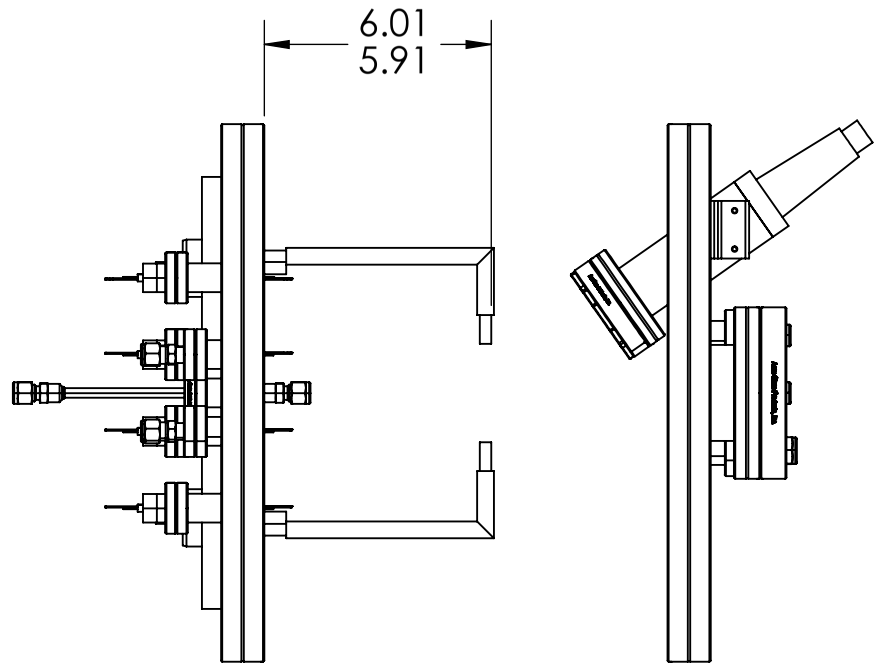
	NAME	DATE
DRAWN	F.K. SULEIMAN	
CHECKED		
ENG APPR.		
MFG APPR.		
Q.A.		

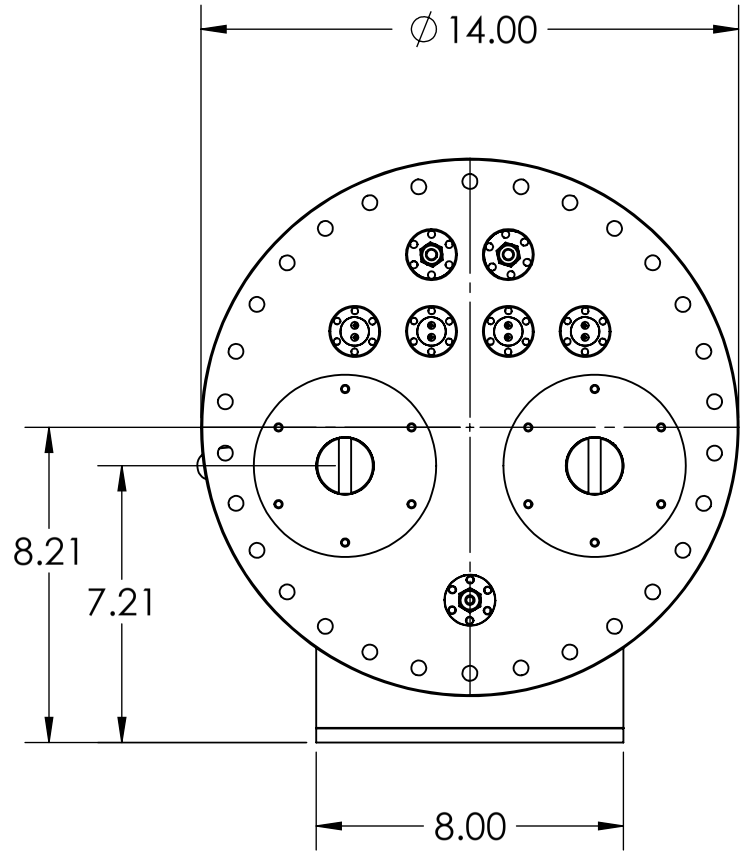
COMMENTS:

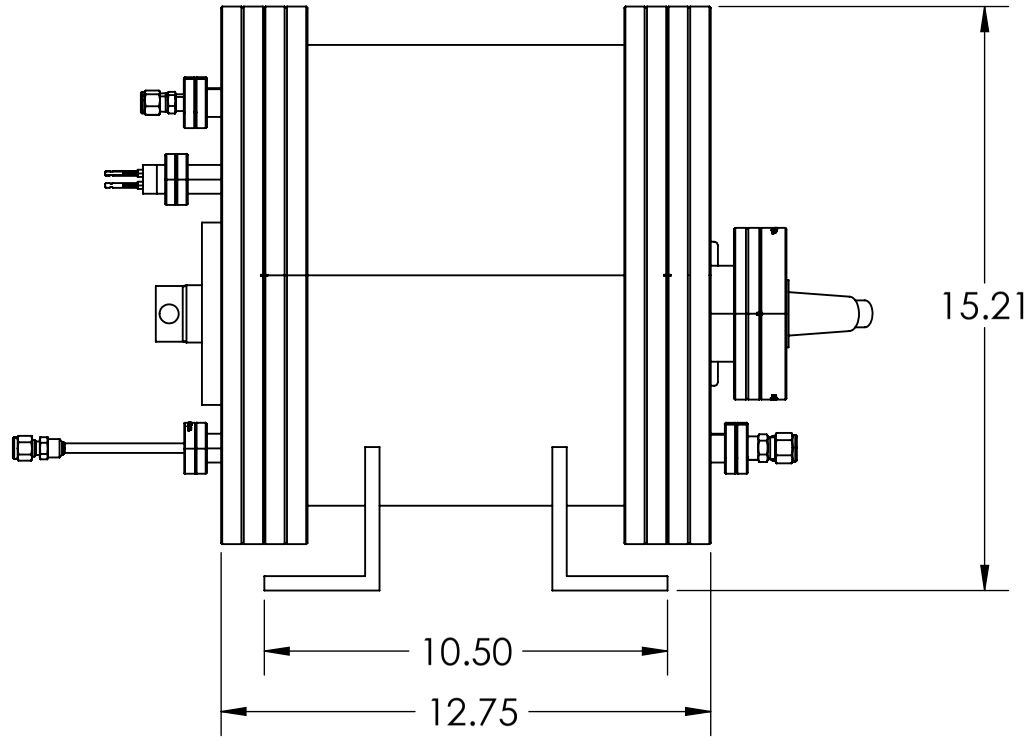
TITLE:
VACUUM ANNEALING CHAMBER
(HINGES SHOWN)

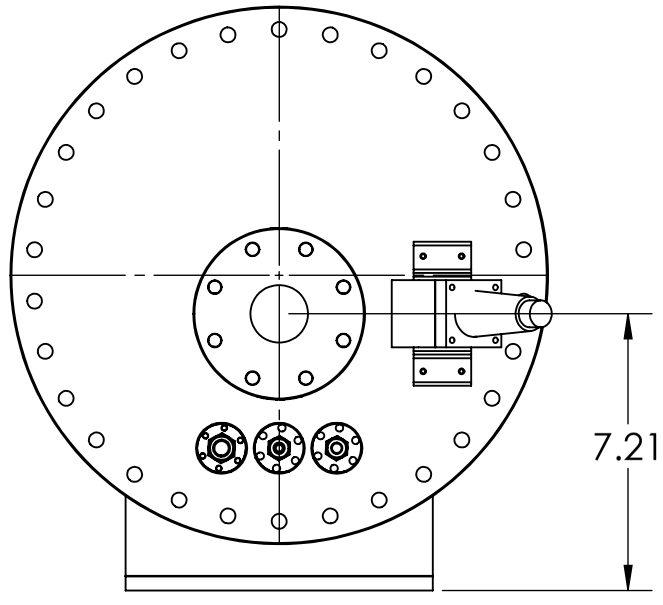
SIZE	DWG. NO.	REV
B		

SCALE: 1:8	WEIGHT:	SHEET 3 OF 32









NOTE:
THE BUS BAR MATERIAL WILL BE PROVIDED, BUT IT WILL NEED TO BE MODIFIED TO THE LENGTH SPECIFIED ABOVE. ALSO, WE WOULD LIKE TO CONSIDER THE POSSIBILITY OF STRIPPING THE BUS BAR INSULATION WITHOUT THE LAMINATED COPPER SHEET FALLING APART.

PROPRIETARY AND CONFIDENTIAL
THE INFORMATION CONTAINED IN THIS DRAWING IS THE SOLE PROPERTY OF <INSERT COMPANY NAME HERE>. ANY REPRODUCTION IN PART OR AS A WHOLE WITHOUT THE WRITTEN PERMISSION OF <INSERT COMPANY NAME HERE> IS PROHIBITED.

NEXT ASSY	USED ON
APPLICATION	

UNLESS OTHERWISE SPECIFIED:
DIMENSIONS ARE IN INCHES
TOLERANCES:
FRACTIONAL ±
ANGULAR: MACH ± BEND ±
TWO PLACE DECIMAL ±
THREE PLACE DECIMAL ±
INTERPRET GEOMETRIC TOLERANCING PER:
MATERIAL
FINISH
DO NOT SCALE DRAWING

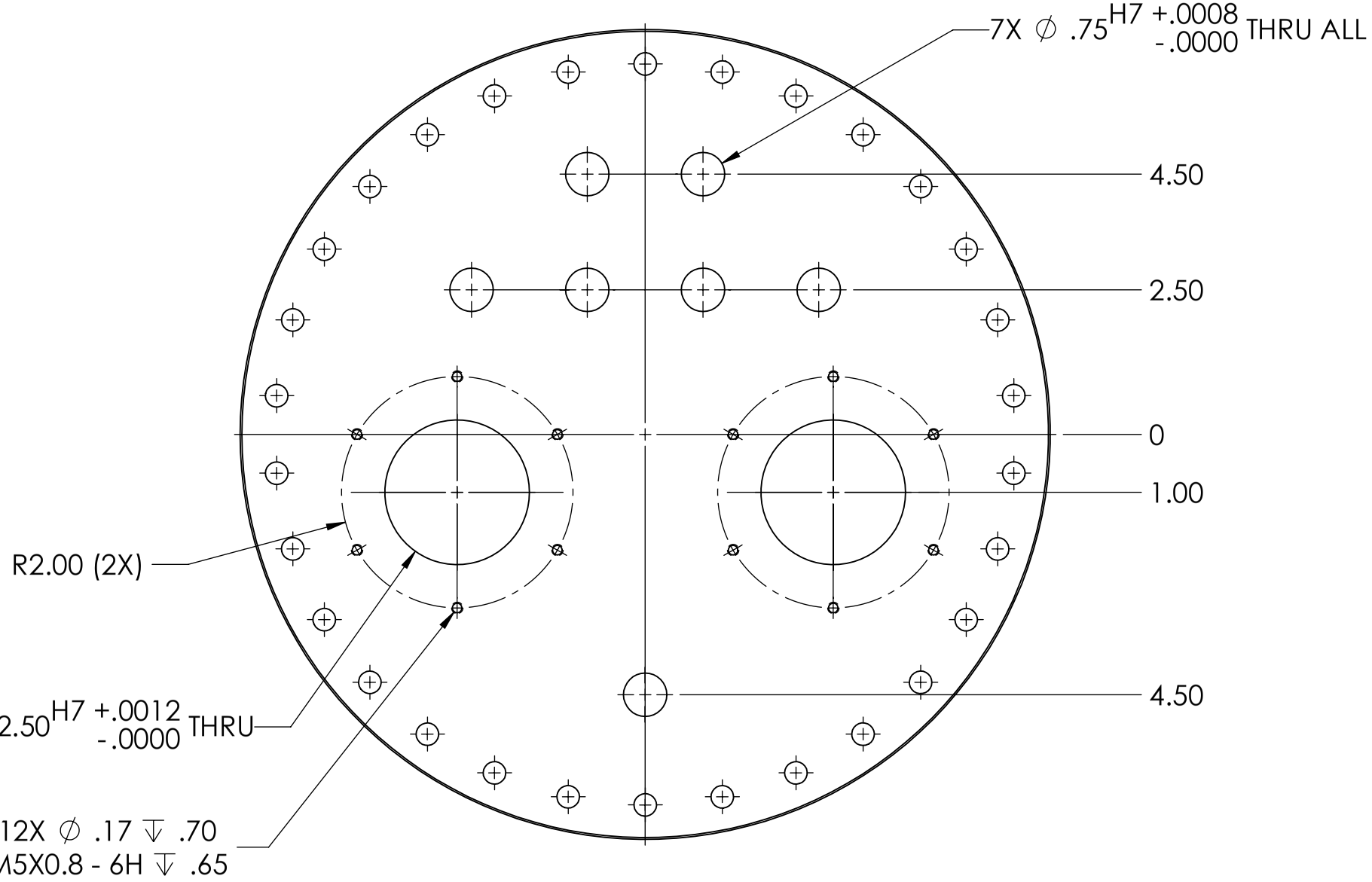
	NAME	DATE
DRAWN	F.K. SULEIMAN	
CHECKED		
ENG APPR.		
MFG APPR.		
Q.A.		

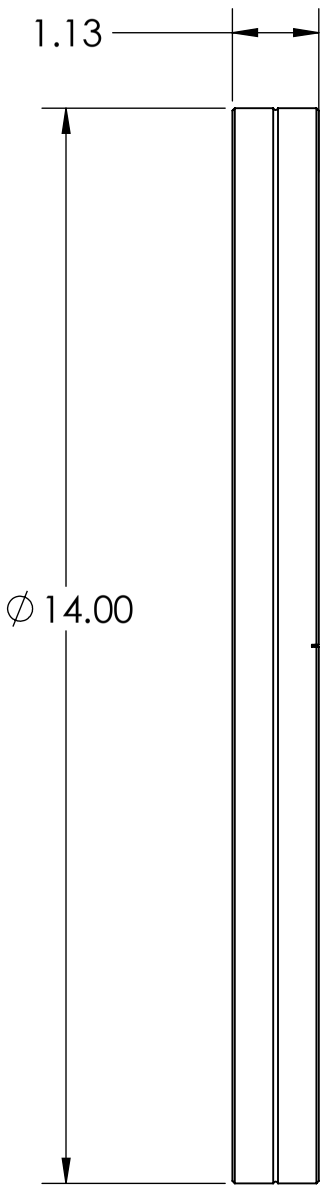
COMMENTS:

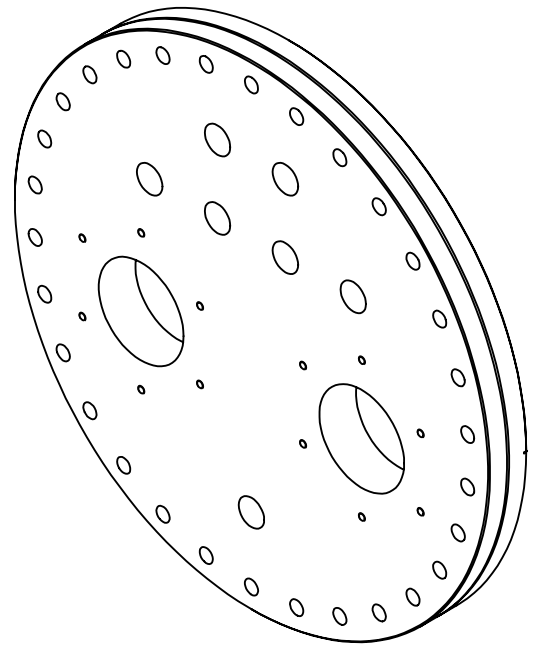
TITLE:
VACUUM ANNEALING CHAMBER
(HINGES NOT SHOWN)

SIZE	DWG. NO.	REV
B		

SCALE: 1:5 | WEIGHT: | SHEET 4 OF 32







NOTE:
MATERIAL: 14" X 12" BLANK CF FLANGE (1400-1200N)
CLEARANCE FIT: THE HOLE BASIS LIMIT (**2.5" H7**) IS TO ACCOMODATE THE POLYURETHANE FLANGE (SHEET 10), WHILE THE **0.75" H7** FIT IS TO ACCOMODATE CF HALF NIPPLE TUBES. `
THE CF NIPPLES ARE MASS PRODUCED WHICH MEANS THAT THE DIAMETER OF THE PURCHASED TUBE MIGHT DIFFER SLIGHTLY FROM THE NOMINAL VALUES STATED HERE. PLEASE KINDLY CONFIRM THE DIAMETER ON THE PURCHASED PARTS, ONCE THEY ARRIVE.

PROPRIETARY AND CONFIDENTIAL
THE INFORMATION CONTAINED IN THIS DRAWING IS THE SOLE PROPERTY OF <INSERT COMPANY NAME HERE>. ANY REPRODUCTION IN PART OR AS A WHOLE WITHOUT THE WRITTEN PERMISSION OF <INSERT COMPANY NAME HERE> IS PROHIBITED.

NEXT ASSY	USED ON
APPLICATION	

UNLESS OTHERWISE SPECIFIED:
DIMENSIONS ARE IN INCHES
TOLERANCES:
FRACTIONAL ±
ANGULAR: MACH ± BEND ±
TWO PLACE DECIMAL ±
THREE PLACE DECIMAL ±
INTERPRET GEOMETRIC TOLERANCING PER:
MATERIAL
FINISH
DO NOT SCALE DRAWING

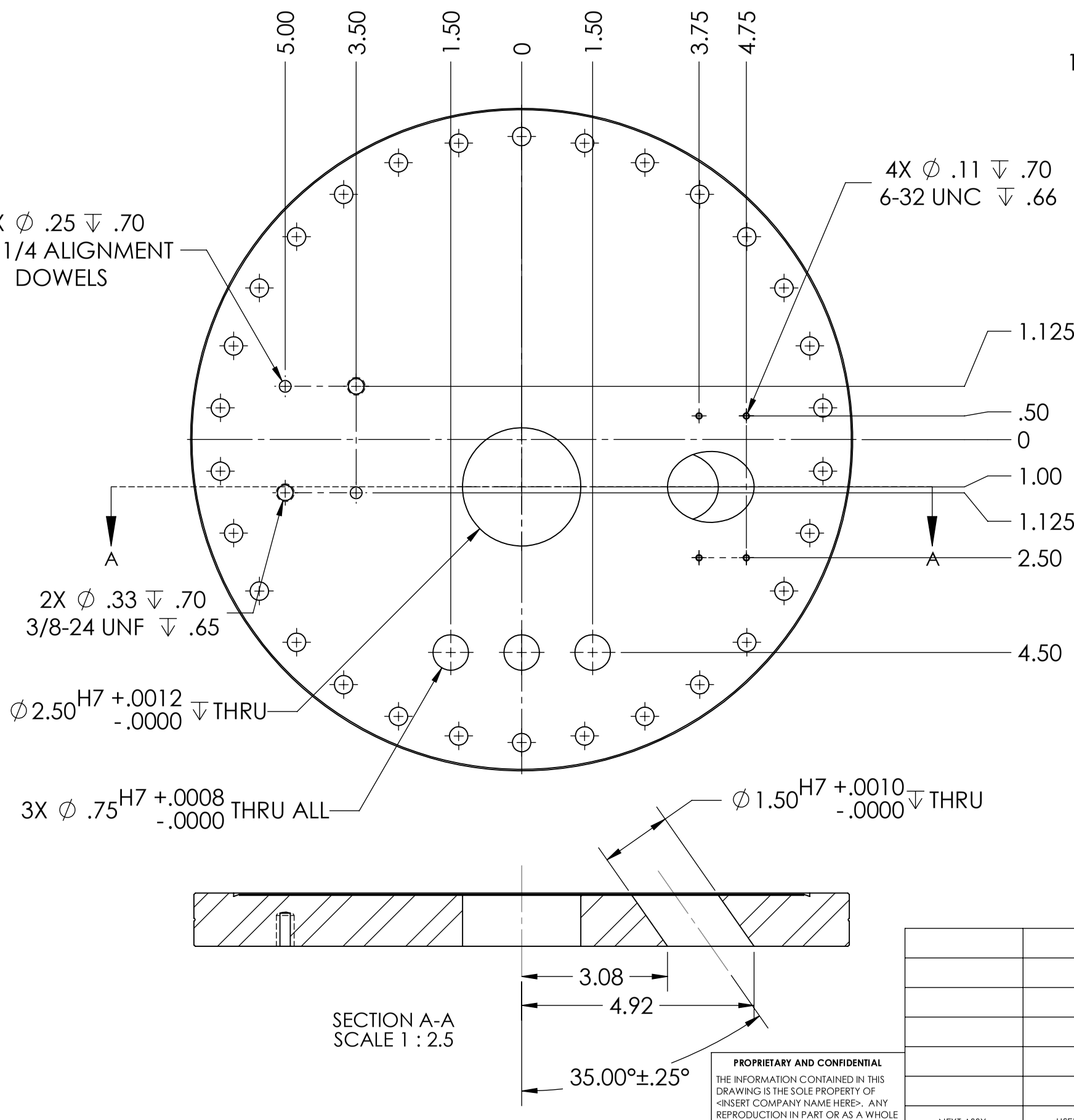
	NAME	DATE
DRAWN	F.K. SULEIMAN	
CHECKED		
ENG APPR.		
MFG APPR.		
Q.A.		

COMMENTS:

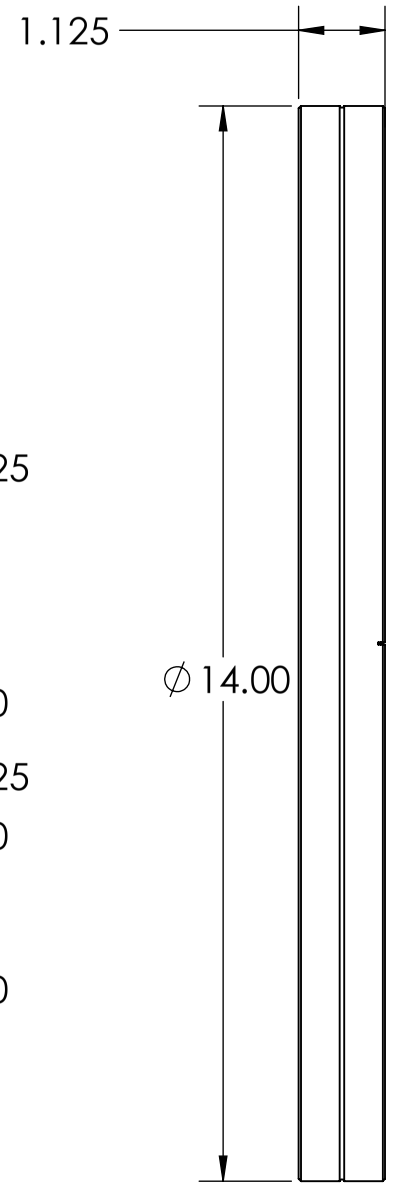
TITLE:
BACK FLANGE - CF 14" NON ROTATABLE

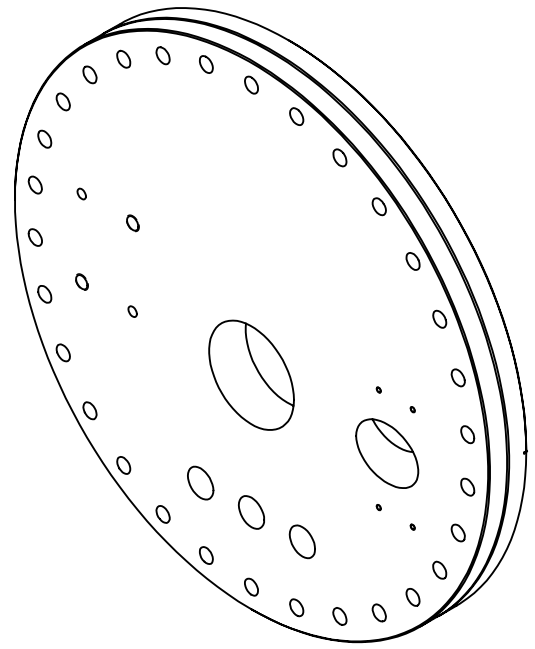
SIZE	DWG. NO.	REV
B		

SCALE: 1:4 | WEIGHT: | SHEET 5 OF 32



SECTION A-A
SCALE 1 : 2.5





NOTE:
MATERIAL: 14" X 12" BLANK CF FLANGE (1400-1200N)
CLEARANCE FIT: ALL THE **H7** FITS ARE DEFINED TO ACCOMODATE CF HALF NIPPLE TUBES.
THE CF NIPPLES ARE MASS PRODUCED WHICH MEANS THAT THE DIAMETER OF THE PURCHASED TUBE MIGHT DIFFER SLIGHTLY FROM THE NOMINAL VALUES STATED HERE.
PLEASE KINDLY CONFIRM THE DIAMETER ON THE PURCHASED PARTS, ONCE THEY ARRIVE.

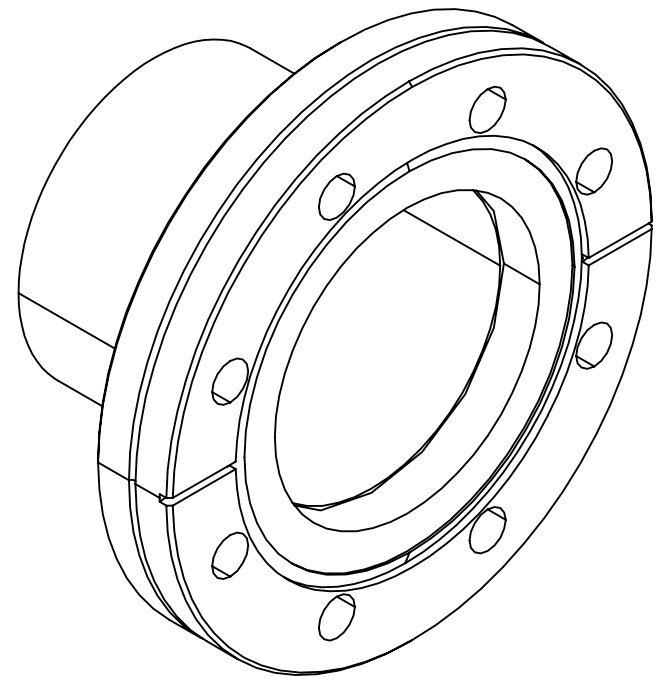
PROPRIETARY AND CONFIDENTIAL
THE INFORMATION CONTAINED IN THIS DRAWING IS THE SOLE PROPERTY OF <INSERT COMPANY NAME HERE>. ANY REPRODUCTION IN PART OR AS A WHOLE WITHOUT THE WRITTEN PERMISSION OF <INSERT COMPANY NAME HERE> IS PROHIBITED.

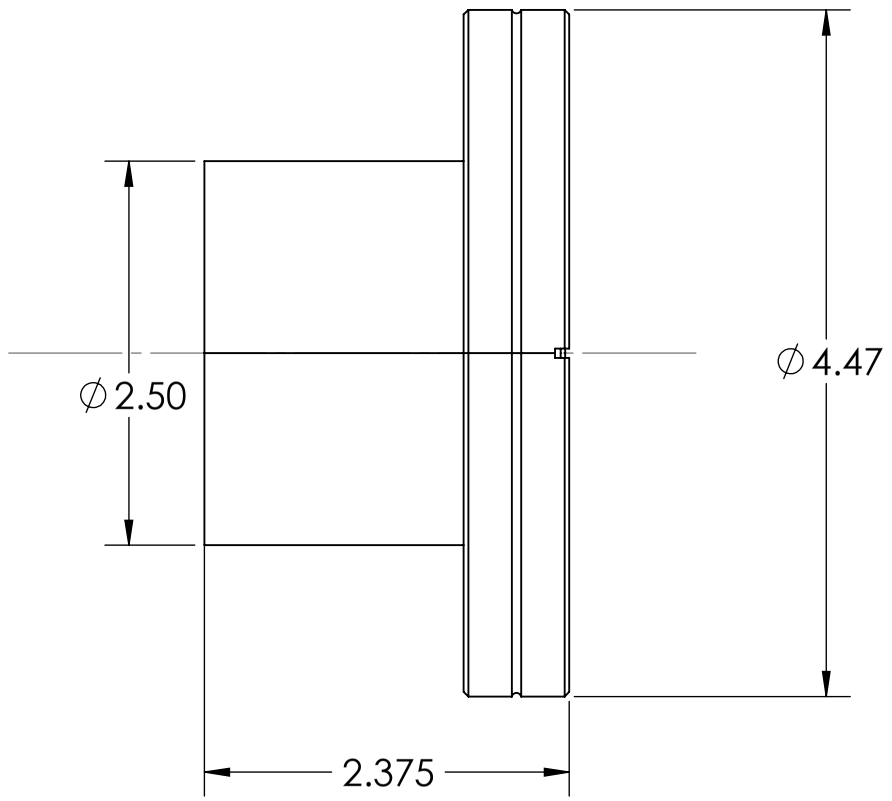
		UNLESS OTHERWISE SPECIFIED:		NAME	DATE
		DIMENSIONS ARE IN INCHES TOLERANCES: FRACTIONAL ± ANGULAR: MACH ± BEND ± TWO PLACE DECIMAL ± THREE PLACE DECIMAL ±	DRAWN	F.K. SULEIMAN	
			CHECKED		
			ENG APPR.		
			MFG APPR.		
		INTERPRET GEOMETRIC TOLERANCING PER:	Q.A.		
		MATERIAL	COMMENTS:		
NEXT ASSY	USED ON	FINISH			
APPLICATION		DO NOT SCALE DRAWING			

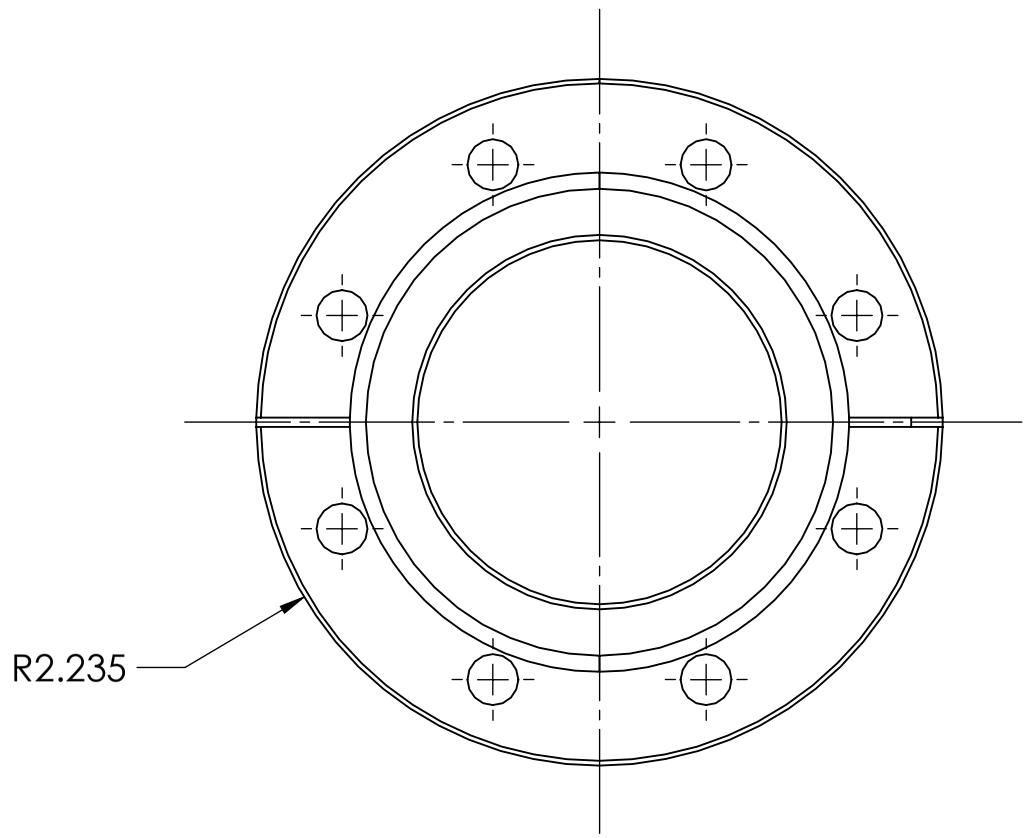
TITLE:
FRONT FLANGE - CF 14" NON ROTATABLE BLANK

SIZE	DWG. NO.	REV
B		

SCALE: 1:4 | WEIGHT: | SHEET 6 OF 32







NOTE:
THE ORIGINAL MASS-PRODUCED PART (1N-250, 4.5" HALF NIPPLE) IS 3.38" LONG, IT ONLY NEEDS TO BE CUT TO THE LENGTH SPECIFIED ABOVE.

PROPRIETARY AND CONFIDENTIAL
THE INFORMATION CONTAINED IN THIS DRAWING IS THE SOLE PROPERTY OF <INSERT COMPANY NAME HERE>. ANY REPRODUCTION IN PART OR AS A WHOLE WITHOUT THE WRITTEN PERMISSION OF <INSERT COMPANY NAME HERE> IS PROHIBITED.

NEXT ASSY	USED ON
APPLICATION	

UNLESS OTHERWISE SPECIFIED:
DIMENSIONS ARE IN INCHES
TOLERANCES:
FRACTIONAL ±
ANGULAR: MACH ± BEND ±
TWO PLACE DECIMAL ±
THREE PLACE DECIMAL ±
INTERPRET GEOMETRIC TOLERANCING PER:
MATERIAL
FINISH
DO NOT SCALE DRAWING

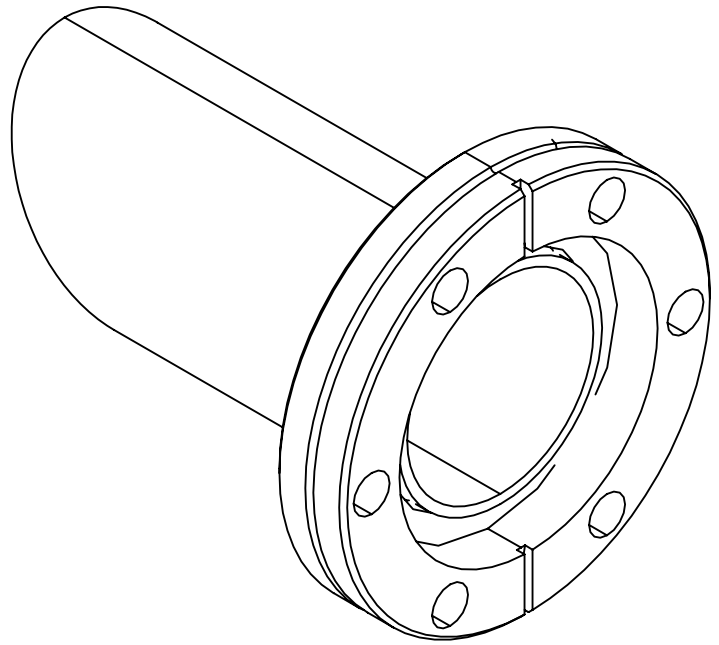
	NAME	DATE
DRAWN	F.K. SULEIMAN	
CHECKED		
ENG APPR.		
MFG APPR.		
Q.A.		

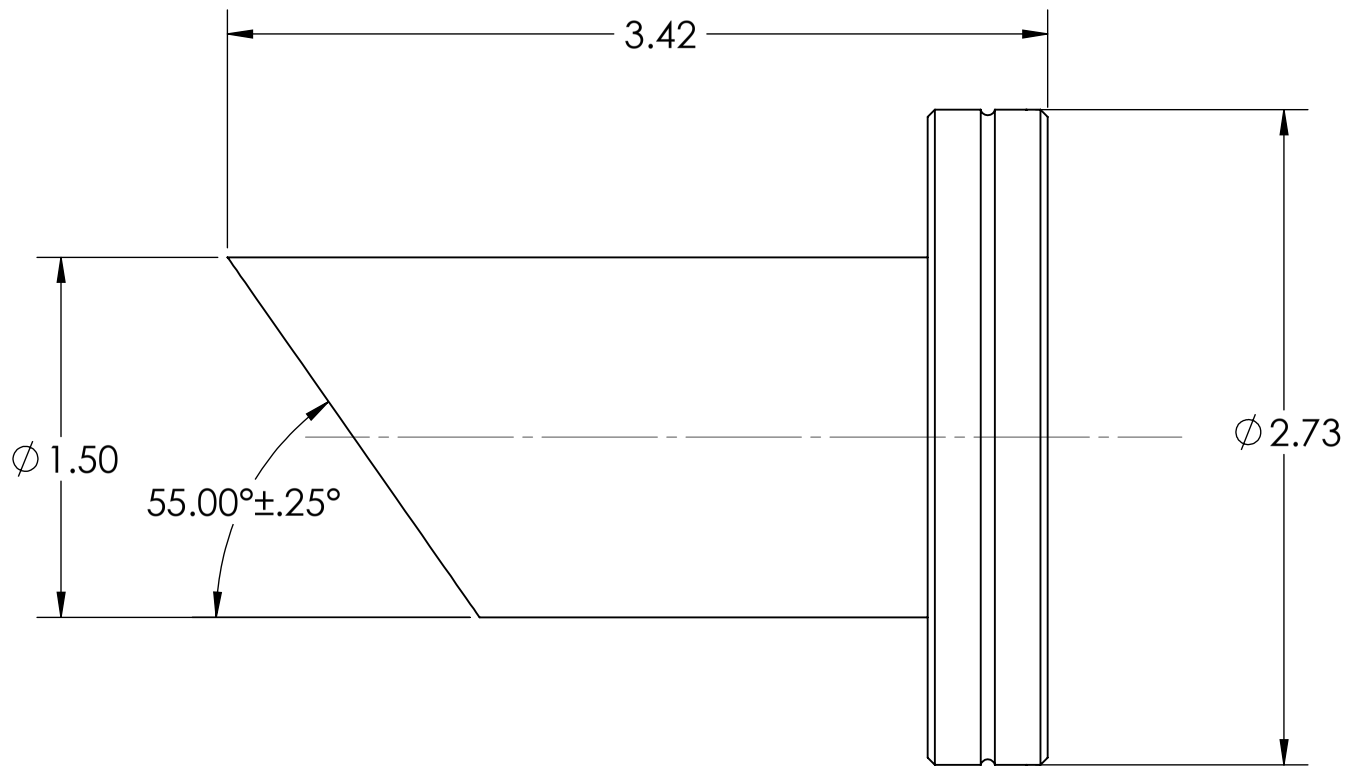
COMMENTS:

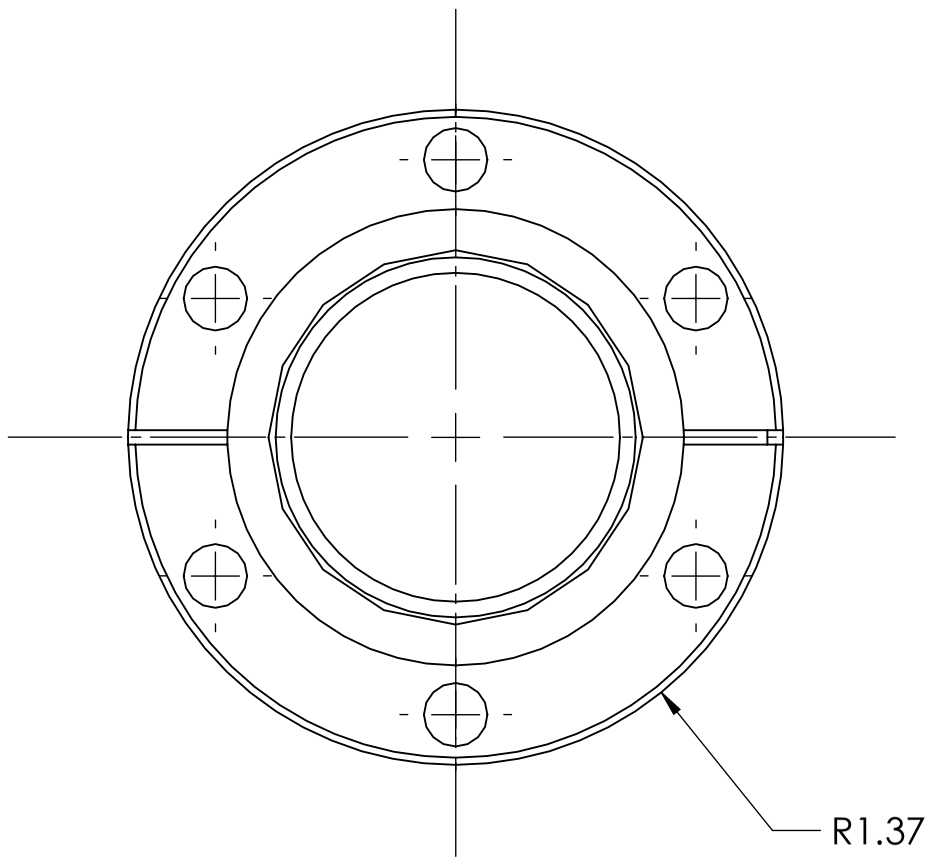
TITLE:
MAIN VIEWPORT - CF 4.5" HALF NIPPLE

SIZE	DWG. NO.	REV
B		

SCALE: 1:2	WEIGHT:	SHEET 7 OF 32







NOTE:
THE ORIGINAL MASS-PRODUCED PART (2N-150, 2.75" FULL NIPPLE) IS 4.92" LONG, IT ONLY NEEDS TO BE CUT TO THE LENGTH AND GEOMETRY SPECIFIED ABOVE.

PROPRIETARY AND CONFIDENTIAL
THE INFORMATION CONTAINED IN THIS DRAWING IS THE SOLE PROPERTY OF <INSERT COMPANY NAME HERE>. ANY REPRODUCTION IN PART OR AS A WHOLE WITHOUT THE WRITTEN PERMISSION OF <INSERT COMPANY NAME HERE> IS PROHIBITED.

NEXT ASSY	USED ON
APPLICATION	

UNLESS OTHERWISE SPECIFIED:
DIMENSIONS ARE IN INCHES
TOLERANCES:
FRACTIONAL ±
ANGULAR: MACH ± BEND ±
TWO PLACE DECIMAL ±
THREE PLACE DECIMAL ±
INTERPRET GEOMETRIC TOLERANCING PER:
MATERIAL
FINISH
DO NOT SCALE DRAWING

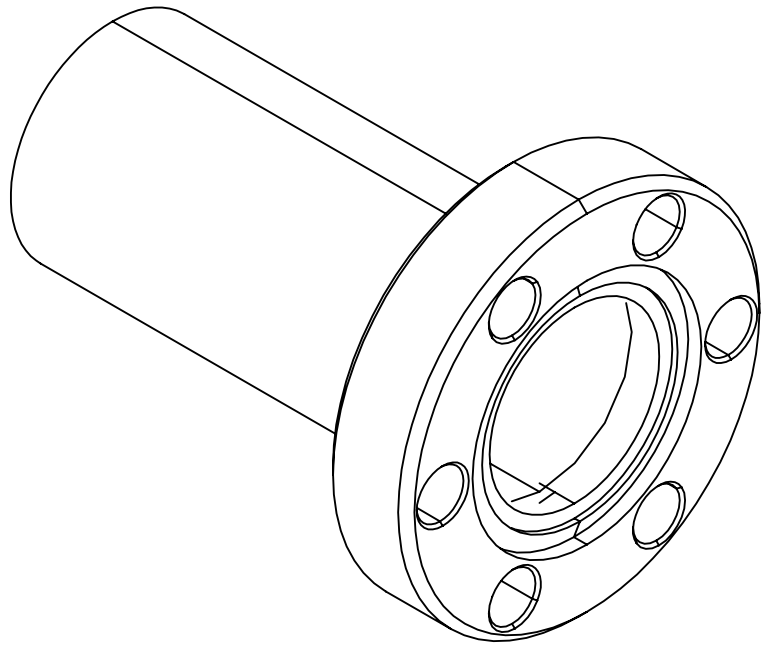
	NAME	DATE
DRAWN	F.K. SULEIMAN	
CHECKED		
ENG APPR.		
MFG APPR.		
Q.A.		

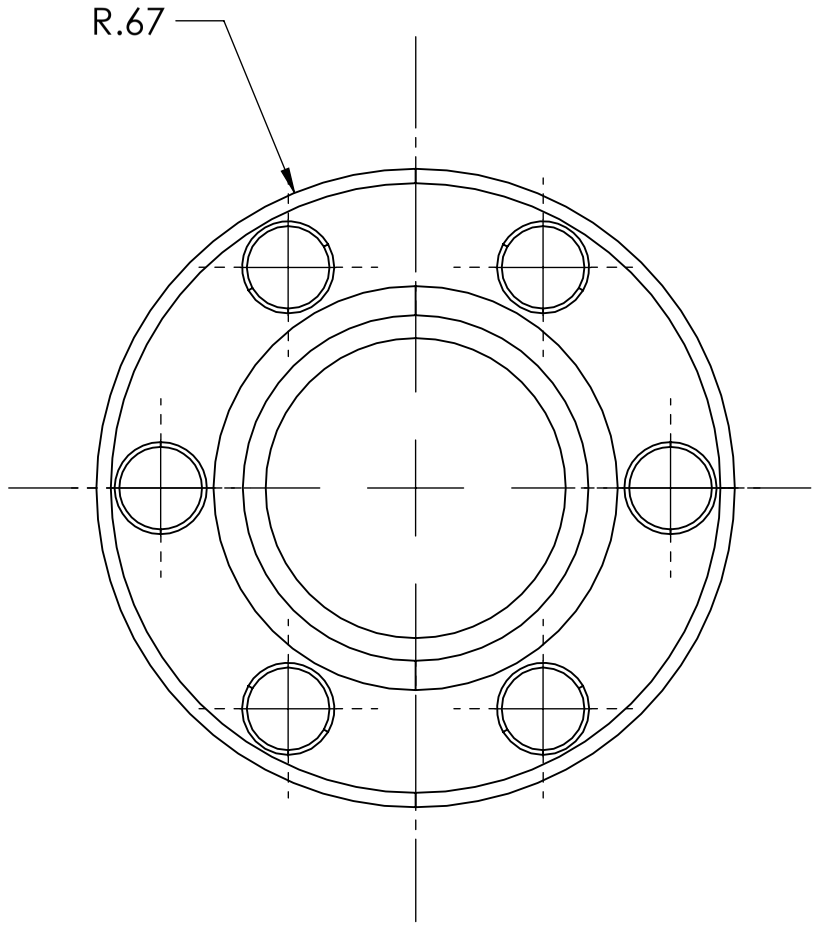
COMMENTS:

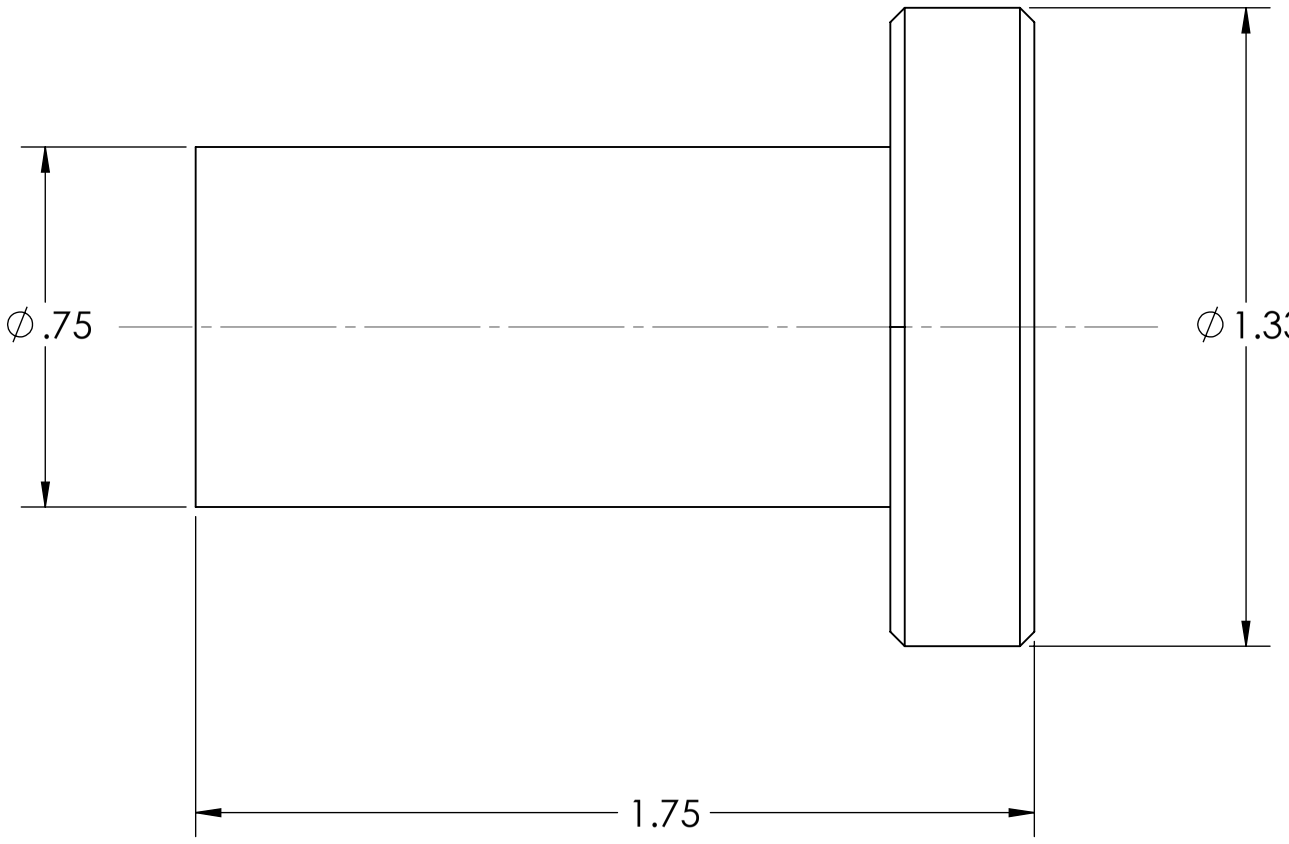
TITLE:
ANGLED VIEWPORT -CF 2.75" HALF NIPPLE

SIZE	DWG. NO.	REV
B		

SCALE: 1:2 | WEIGHT: | SHEET 8 OF 32







NOTE:
THE ORIGINAL MASS-PRODUCED PART (2N-075, 1.33" FULL NIPPLE) IS 3" LONG, IT ONLY NEEDS TO BE CUT TO THE LENGTH SPECIFIED ABOVE.

PROPRIETARY AND CONFIDENTIAL
THE INFORMATION CONTAINED IN THIS DRAWING IS THE SOLE PROPERTY OF <INSERT COMPANY NAME HERE>. ANY REPRODUCTION IN PART OR AS A WHOLE WITHOUT THE WRITTEN PERMISSION OF <INSERT COMPANY NAME HERE> IS PROHIBITED.

NEXT ASSY	USED ON
APPLICATION	

UNLESS OTHERWISE SPECIFIED:
DIMENSIONS ARE IN INCHES
TOLERANCES:
FRACTIONAL ±
ANGULAR: MACH ± BEND ±
TWO PLACE DECIMAL ±
THREE PLACE DECIMAL ±
INTERPRET GEOMETRIC TOLERANCING PER:
MATERIAL
FINISH
DO NOT SCALE DRAWING

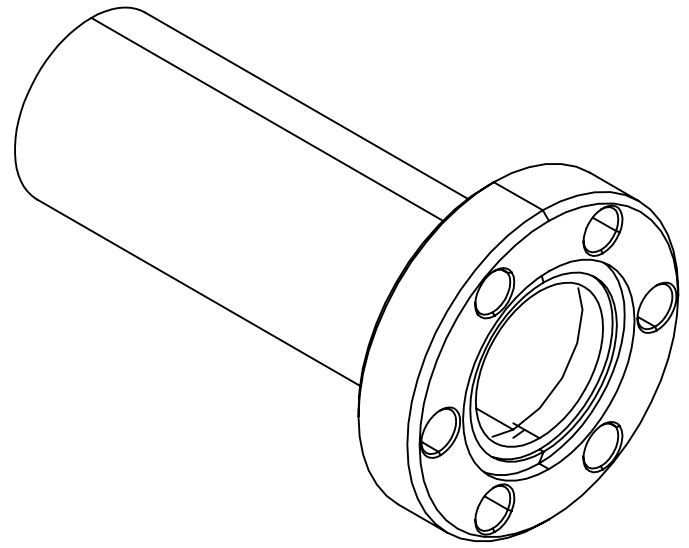
	NAME	DATE
DRAWN	F.K. SULEIMAN	
CHECKED		
ENG APPR.		
MFG APPR.		
Q.A.		

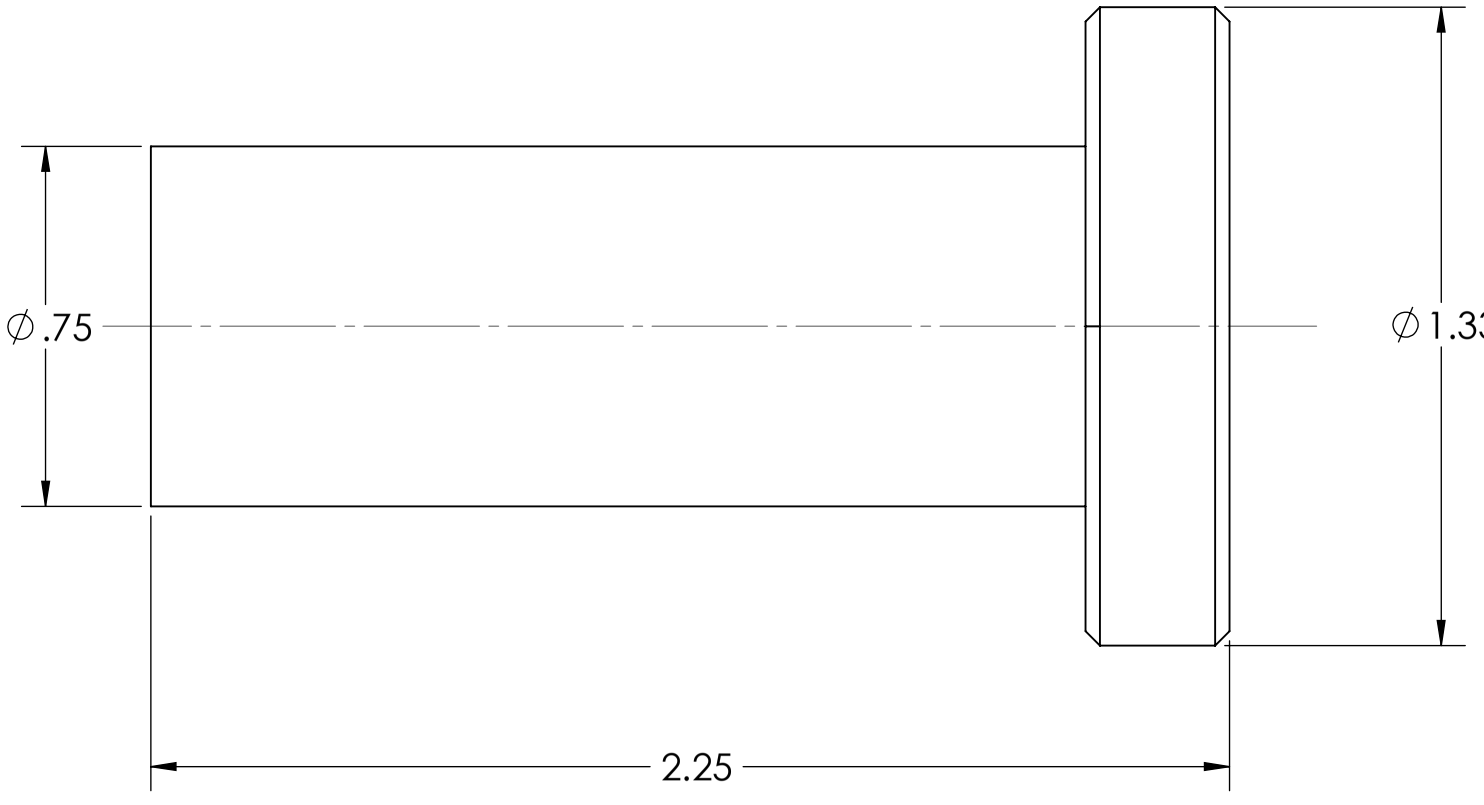
COMMENTS:

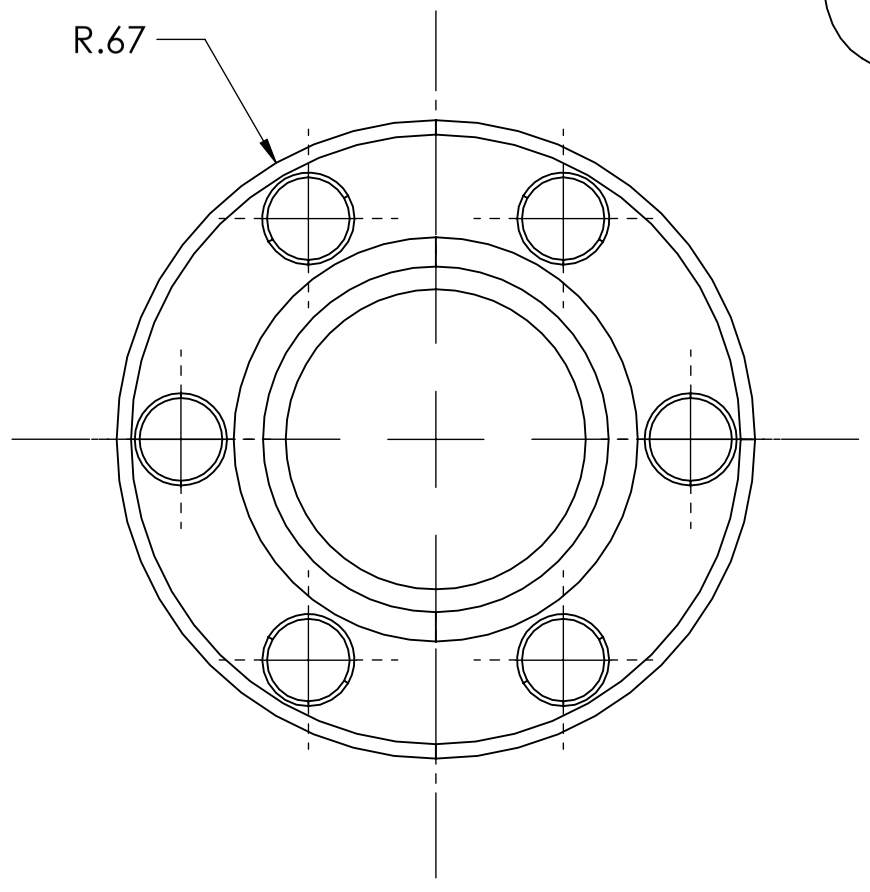
TITLE:
SWAGELOK NIPPLE - CF 1.33" HALF NIPPLE

SIZE	DWG. NO.	REV
B		

SCALE: 1:1 | WEIGHT: | SHEET 9 OF 32







NOTE:
THE ORIGINAL MASS-PRODUCED PART (2N-075, 1.33" FULL NIPPLE) IS 3" LONG, IT ONLY NEEDS TO BE CUT TO THE LENGTH SPECIFIED ABOVE.

PROPRIETARY AND CONFIDENTIAL
THE INFORMATION CONTAINED IN THIS DRAWING IS THE SOLE PROPERTY OF <INSERT COMPANY NAME HERE>. ANY REPRODUCTION IN PART OR AS A WHOLE WITHOUT THE WRITTEN PERMISSION OF <INSERT COMPANY NAME HERE> IS PROHIBITED.

NEXT ASSY	USED ON
APPLICATION	

UNLESS OTHERWISE SPECIFIED:
DIMENSIONS ARE IN INCHES
TOLERANCES:
FRACTIONAL ±
ANGULAR: MACH ± BEND ±
TWO PLACE DECIMAL ±
THREE PLACE DECIMAL ±
INTERPRET GEOMETRIC TOLERANCING PER:
MATERIAL
FINISH
DO NOT SCALE DRAWING

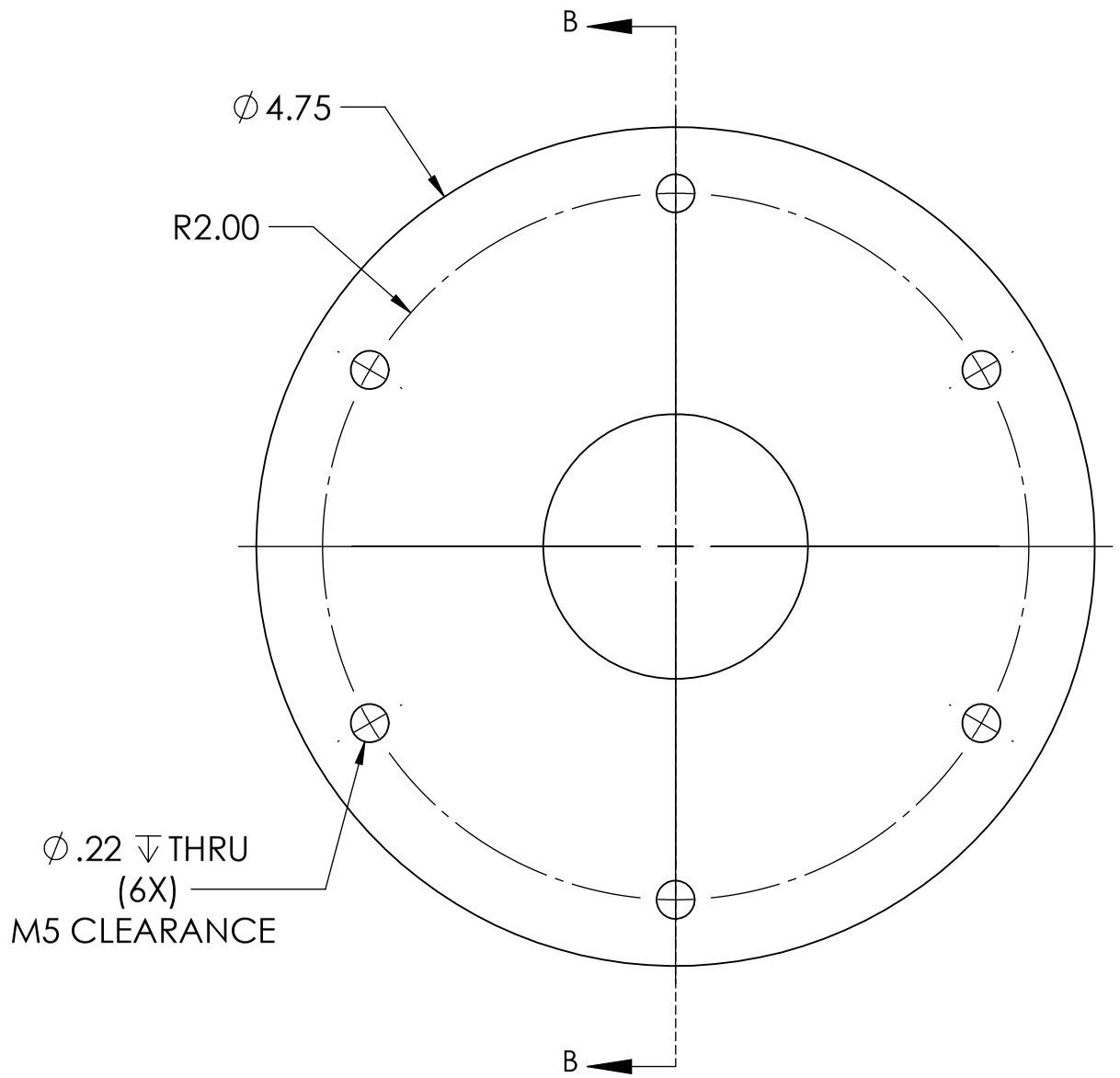
	NAME	DATE
DRAWN	F.K. SULEIMAN	
CHECKED		
ENG APPR.		
MFG APPR.		
Q.A.		

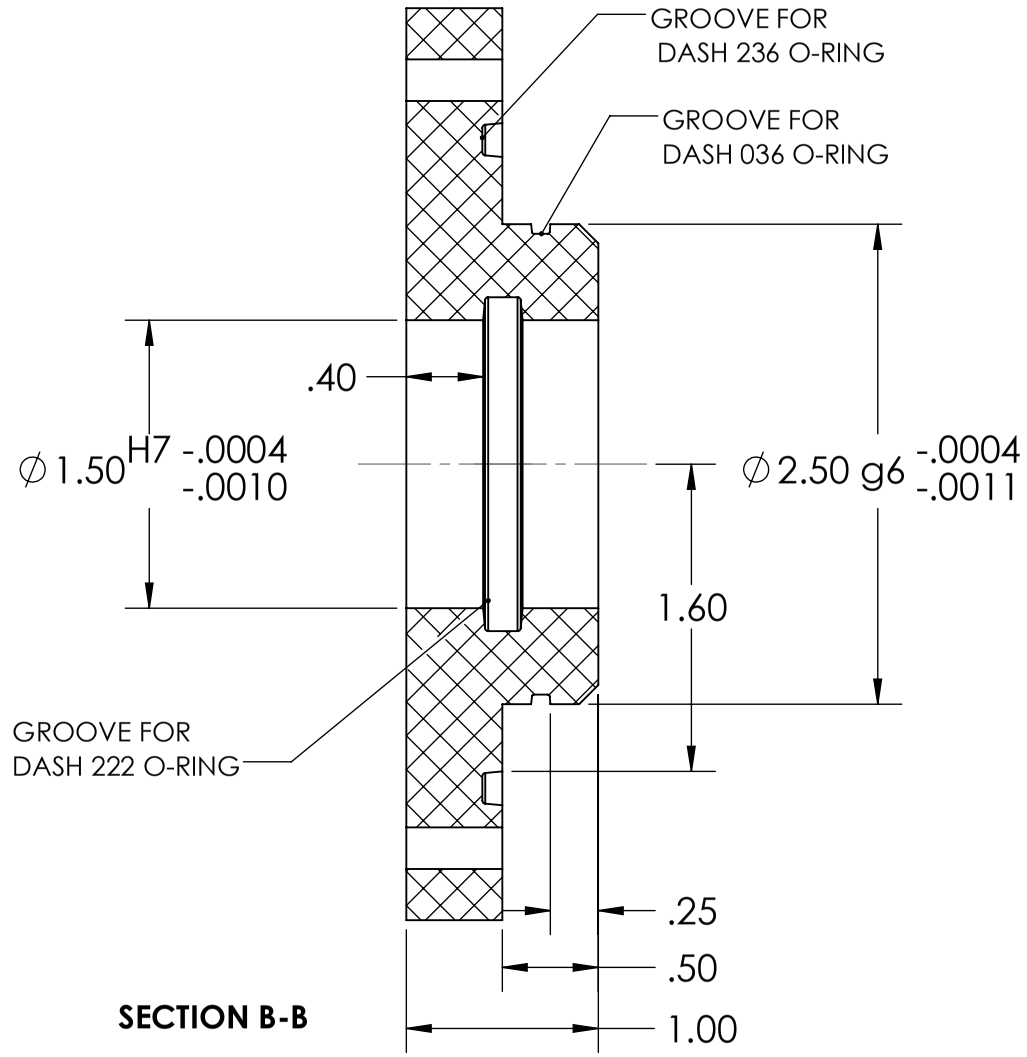
COMMENTS:

TITLE:
THERMOCOUPLE NIPPLE - CF 1.33" HALF NIPPLE

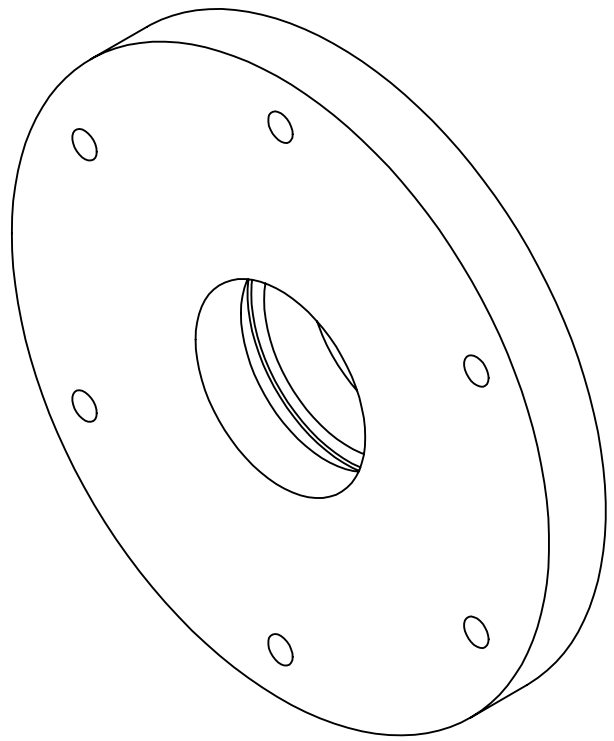
SIZE	DWG. NO.	REV
B		

SCALE: 1:1 | WEIGHT: | SHEET 10 OF 32





SECTION B-B



NOTE:
MATERIAL: POLYURETHANE (SAME AS THE OLD FLANGE)
CLEARANCE FIT: THE HOLE BASIS LIMIT (**1.5" H7**) IS TO ACCOMODATE A COPPER INSERT FROM THE OLD CHAMBER. THE ORIGINAL (DESIGN) DIAMETER OF THE COPPER INSERT IS 1.496"±0.001" BUT THERE MIGHT BE DEVIATIONS IN THE FINAL PART, PLEASE KINDLY MEASURE THE PROVIDED INSERT TO CONFIRM THE DIAMETER.
THE SHAFT BASIS LIMIT (**2.5" g6**) IS TO FIT INTO THE CORRESPONDING HOLE (2.5" H7) ON THE BACK FLANGE (SHEET 3).

PROPRIETARY AND CONFIDENTIAL
THE INFORMATION CONTAINED IN THIS DRAWING IS THE SOLE PROPERTY OF <INSERT COMPANY NAME HERE>. ANY REPRODUCTION IN PART OR AS A WHOLE WITHOUT THE WRITTEN PERMISSION OF <INSERT COMPANY NAME HERE> IS PROHIBITED.

NEXT ASSY	USED ON	
APPLICATION		DO NOT SCALE DRAWING

UNLESS OTHERWISE SPECIFIED:
DIMENSIONS ARE IN INCHES
TOLERANCES:
FRACTIONAL ±
ANGULAR: MACH ± BEND ±
TWO PLACE DECIMAL ±
THREE PLACE DECIMAL ±
INTERPRET GEOMETRIC TOLERANCING PER:
MATERIAL
FINISH

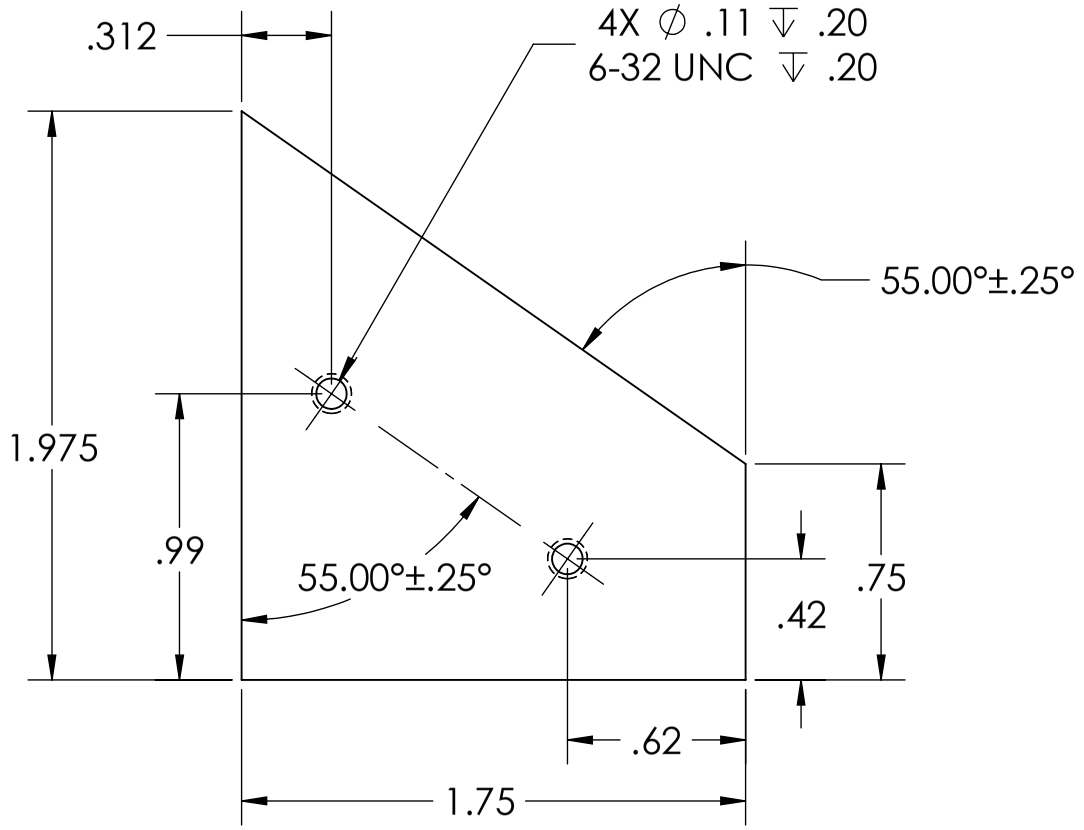
	NAME	DATE
DRAWN	F.K. SULEIMAN	
CHECKED		
ENG APPR.		
MFG APPR.		
Q.A.		

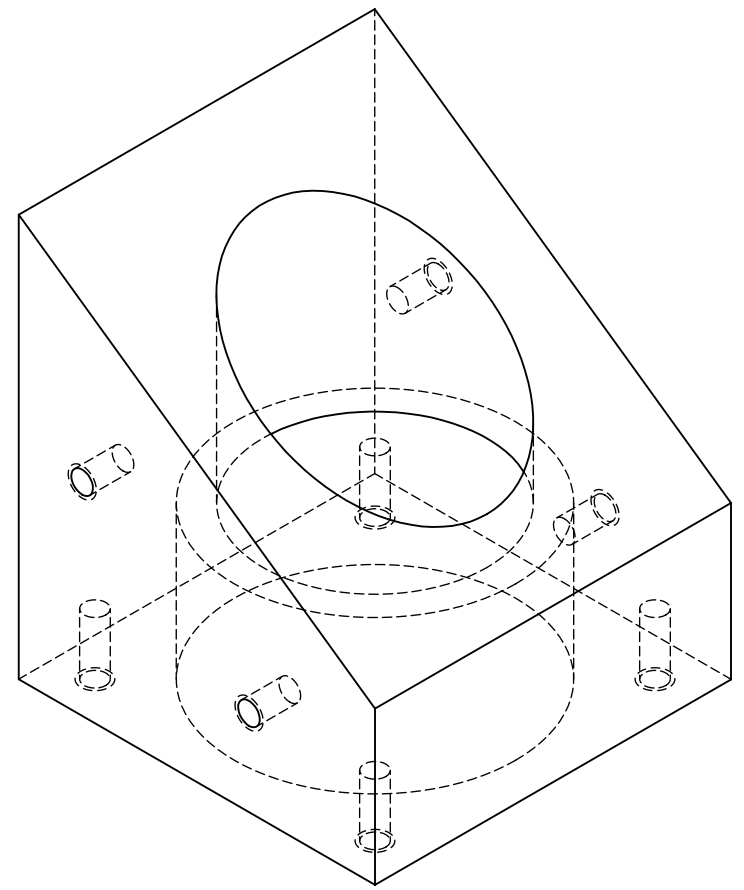
COMMENTS:

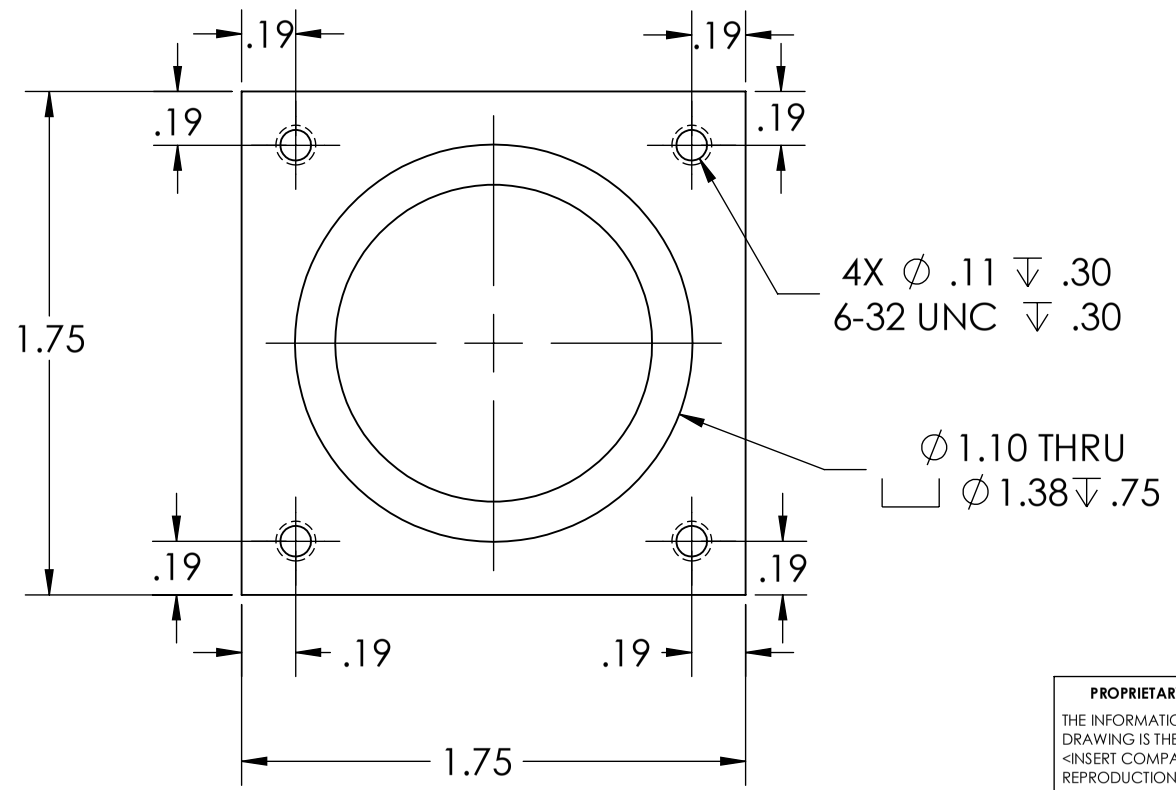
TITLE:
BUS BAR/COPPER INSERT FLANGE

SIZE	DWG. NO.	REV
B		

SCALE: 1:1 | WEIGHT: | SHEET 11 OF 32







PROPRIETARY AND CONFIDENTIAL

THE INFORMATION CONTAINED IN THIS DRAWING IS THE SOLE PROPERTY OF <INSERT COMPANY NAME HERE>. ANY REPRODUCTION IN PART OR AS A WHOLE WITHOUT THE WRITTEN PERMISSION OF <INSERT COMPANY NAME HERE> IS PROHIBITED.

NEXT ASSY	USED ON
APPLICATION	

UNLESS OTHERWISE SPECIFIED:

DIMENSIONS ARE IN INCHES
TOLERANCES:
FRACTIONAL ±
ANGULAR: MACH ± BEND ±
TWO PLACE DECIMAL ±
THREE PLACE DECIMAL ±

INTERPRET GEOMETRIC TOLERANCING PER:

MATERIAL
ALUMINIUM

FINISH

DO NOT SCALE DRAWING

	NAME	DATE
DRAWN	F.K. SULEIMAN	
CHECKED		
ENG APPR.		
MFG APPR.		
Q.A.		

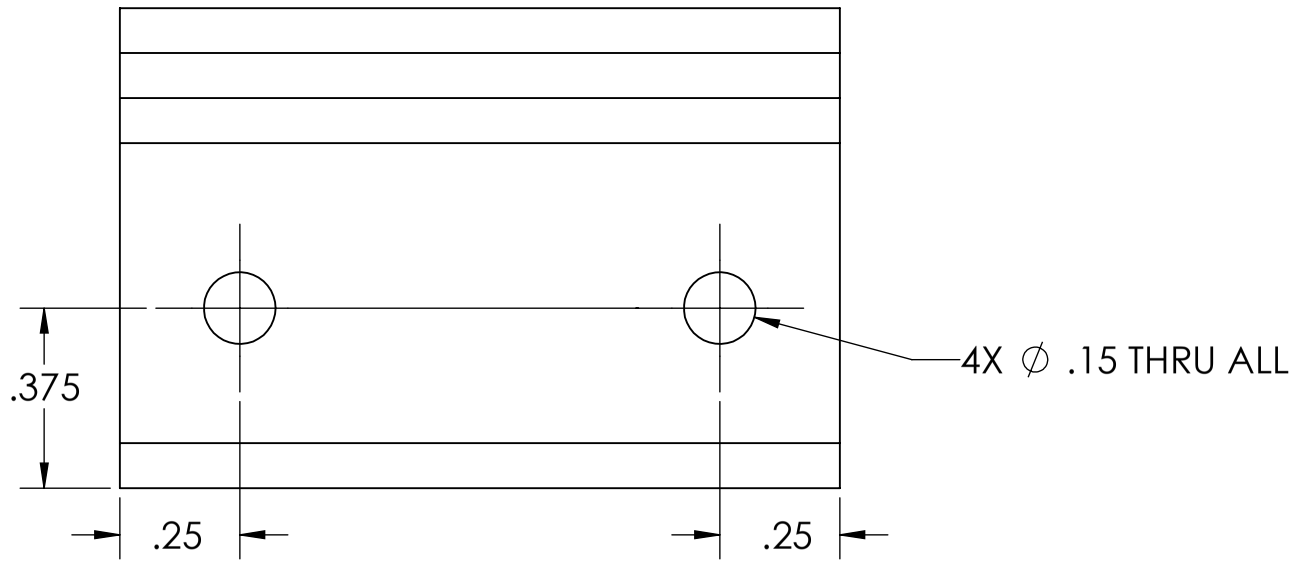
COMMENTS:

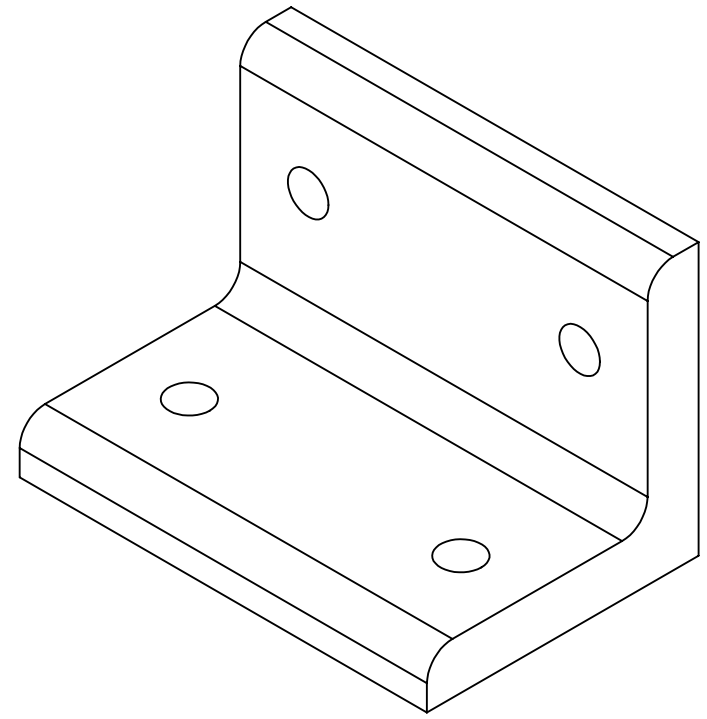
TITLE:

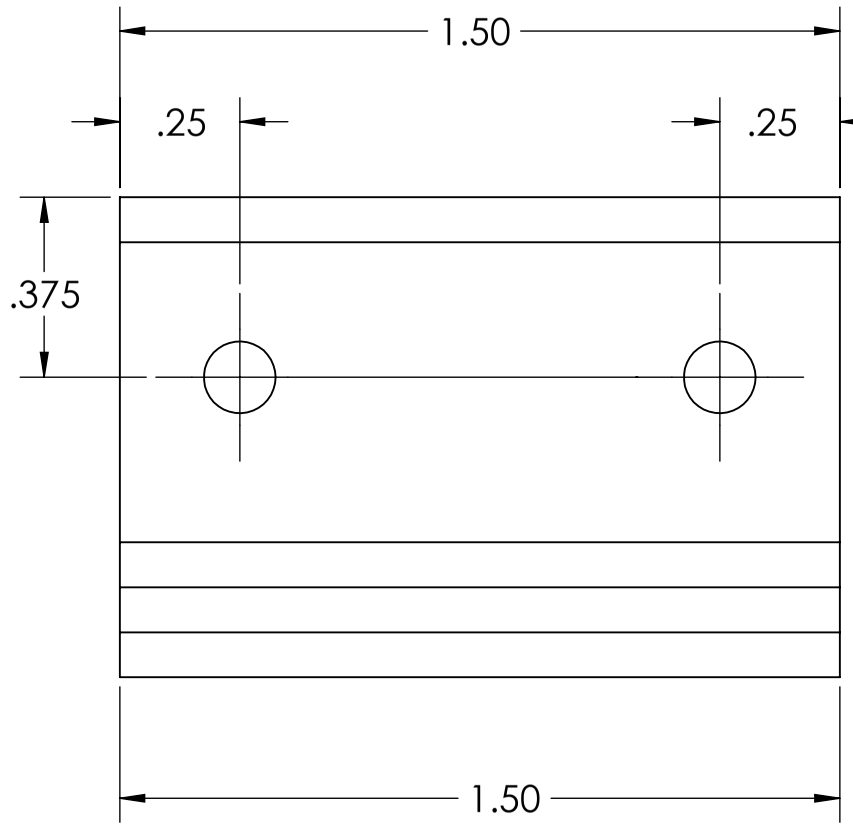
SPECTROMETER MOUNT AND HOLDER

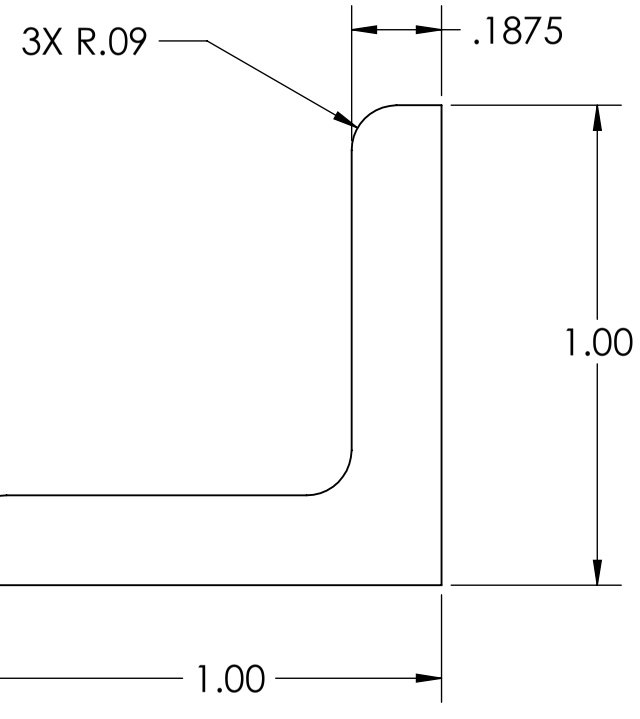
SIZE	DWG. NO.	REV
B		

SCALE: 1:1 | WEIGHT: | SHEET 12 OF 32









NOTE:
THE PART IS DESIGNED BASED ON THE PROFILE FOR MCMASTER-CARR-8982K151 BUT ANY SUITABLE/ALTERNATIVE PROFILE CAN BE USED.

PROPRIETARY AND CONFIDENTIAL
THE INFORMATION CONTAINED IN THIS DRAWING IS THE SOLE PROPERTY OF <INSERT COMPANY NAME HERE>. ANY REPRODUCTION IN PART OR AS A WHOLE WITHOUT THE WRITTEN PERMISSION OF <INSERT COMPANY NAME HERE> IS PROHIBITED.

NEXT ASSY	USED ON
APPLICATION	

UNLESS OTHERWISE SPECIFIED:
DIMENSIONS ARE IN INCHES
TOLERANCES:
FRACTIONAL ±
ANGULAR: MACH ± BEND ±
TWO PLACE DECIMAL ±
THREE PLACE DECIMAL ±
INTERPRET GEOMETRIC TOLERANCING PER:
MATERIAL ALUMINIUM
FINISH
DO NOT SCALE DRAWING

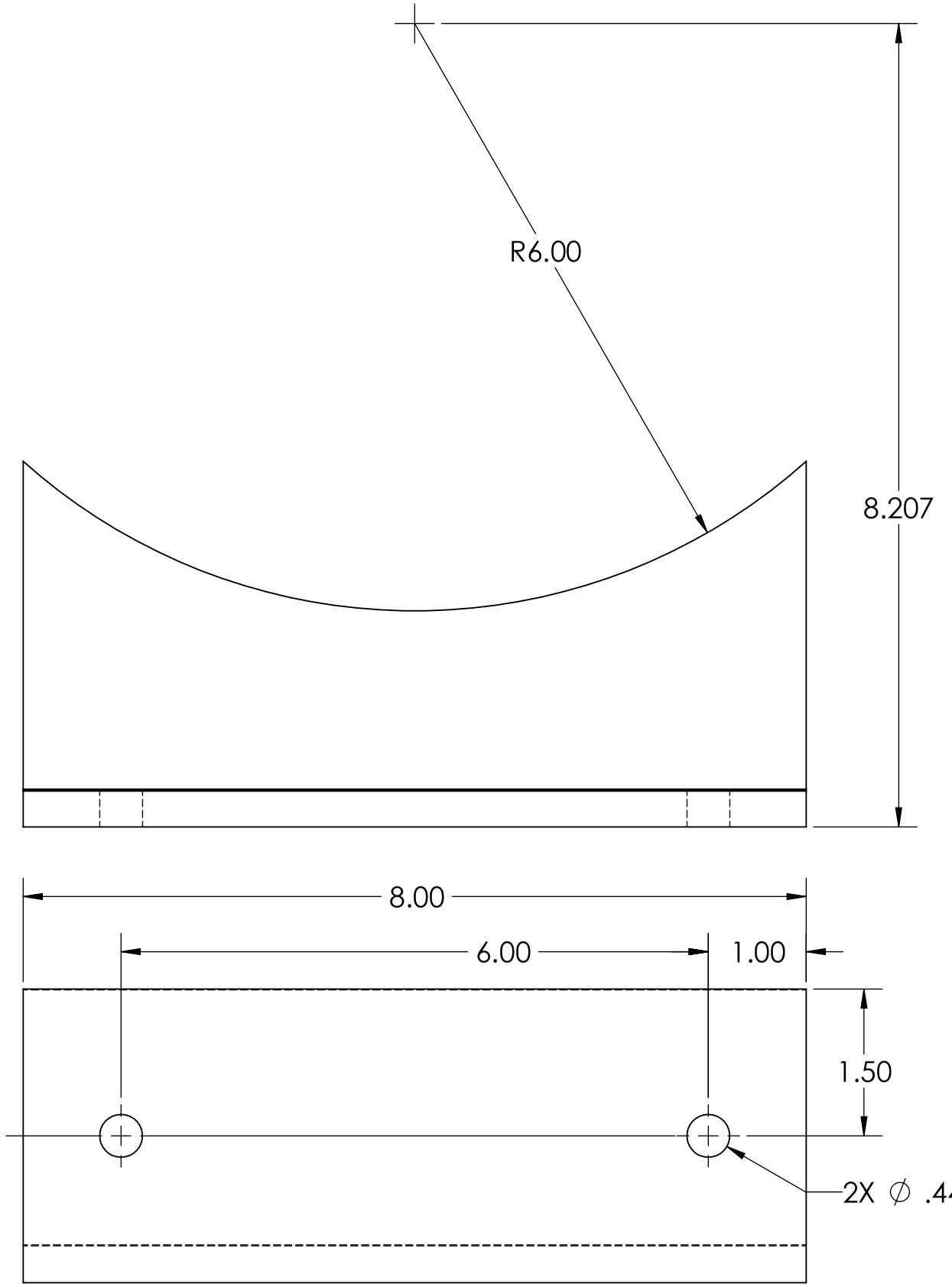
	NAME	DATE
DRAWN	F.K. SULEIMAN	
CHECKED		
ENG APPR.		
MFG APPR.		
Q.A.		

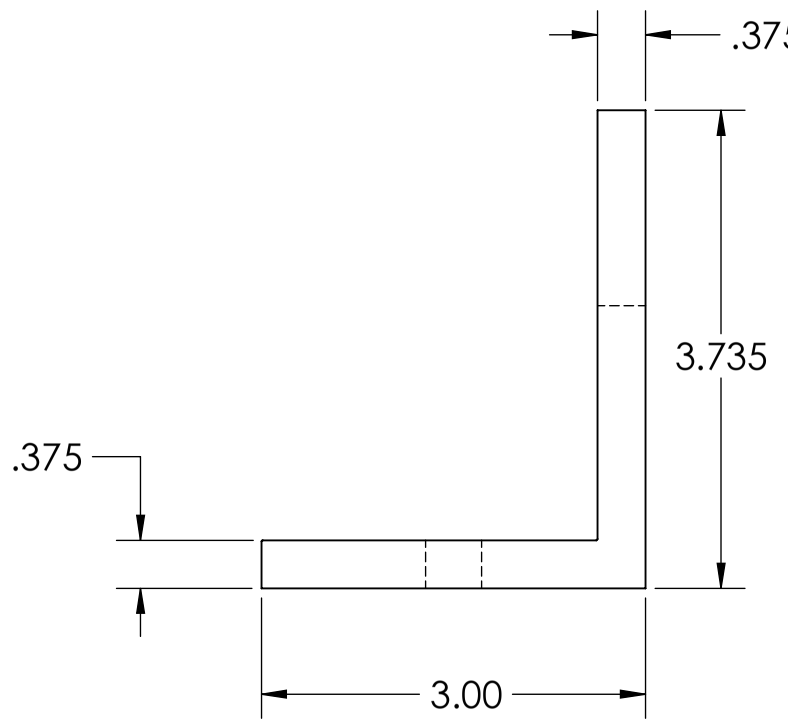
COMMENTS:

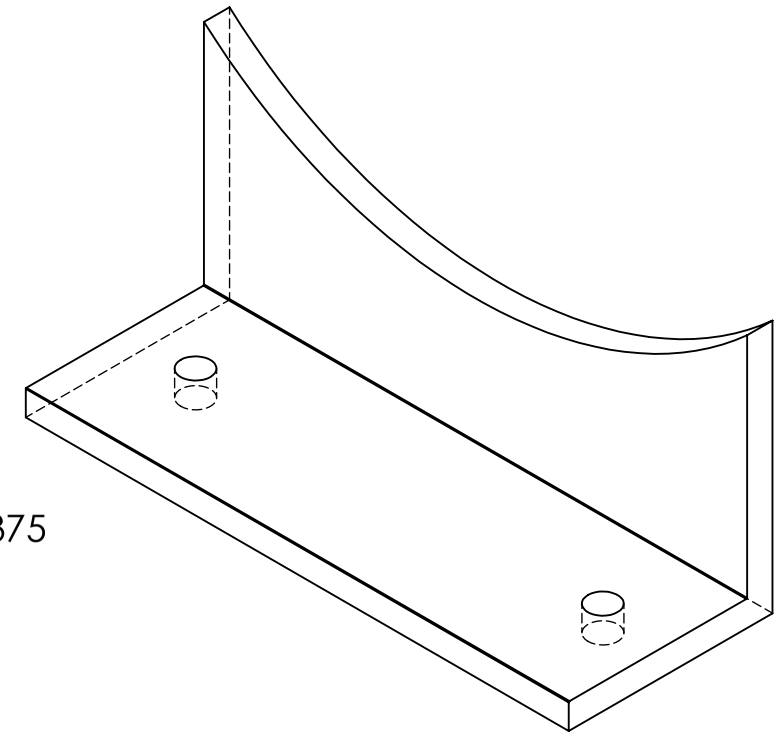
TITLE:
MOUNTING BRACKET FOR SPECTROMETER HOLDER

SIZE	DWG. NO.	REV
B		

SCALE: 2:1 | WEIGHT: | SHEET 13 OF 32







NOTE:
THE PART IS DESIGNED BASED ON THE PROFILE FOR MCMASTER-CARR-1260T58 BUT ANY SUITABLE/ALTERNATIVE PROFILE CAN BE USED.

PROPRIETARY AND CONFIDENTIAL
THE INFORMATION CONTAINED IN THIS DRAWING IS THE SOLE PROPERTY OF <INSERT COMPANY NAME HERE>. ANY REPRODUCTION IN PART OR AS A WHOLE WITHOUT THE WRITTEN PERMISSION OF <INSERT COMPANY NAME HERE> IS PROHIBITED.

NEXT ASSY	USED ON
APPLICATION	

UNLESS OTHERWISE SPECIFIED:
DIMENSIONS ARE IN INCHES
TOLERANCES:
FRACTIONAL ±
ANGULAR: MACH ± BEND ±
TWO PLACE DECIMAL ±
THREE PLACE DECIMAL ±
INTERPRET GEOMETRIC TOLERANCING PER:
MATERIAL
304 STAINLESS STEEL
FINISH
DO NOT SCALE DRAWING

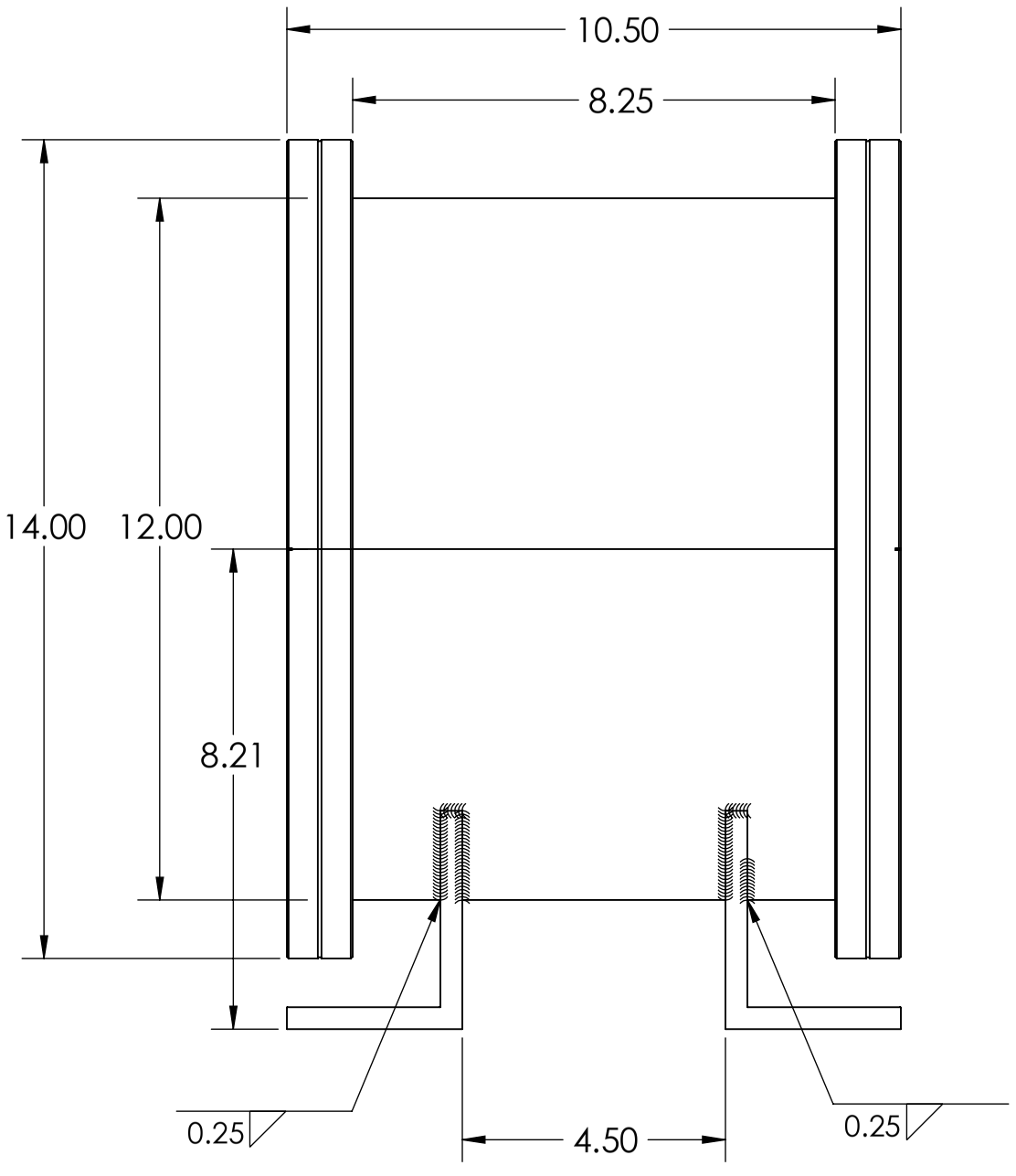
	NAME	DATE
DRAWN	F.K. SULEIMAN	
CHECKED		
ENG APPR.		
MFG APPR.		
Q.A.		

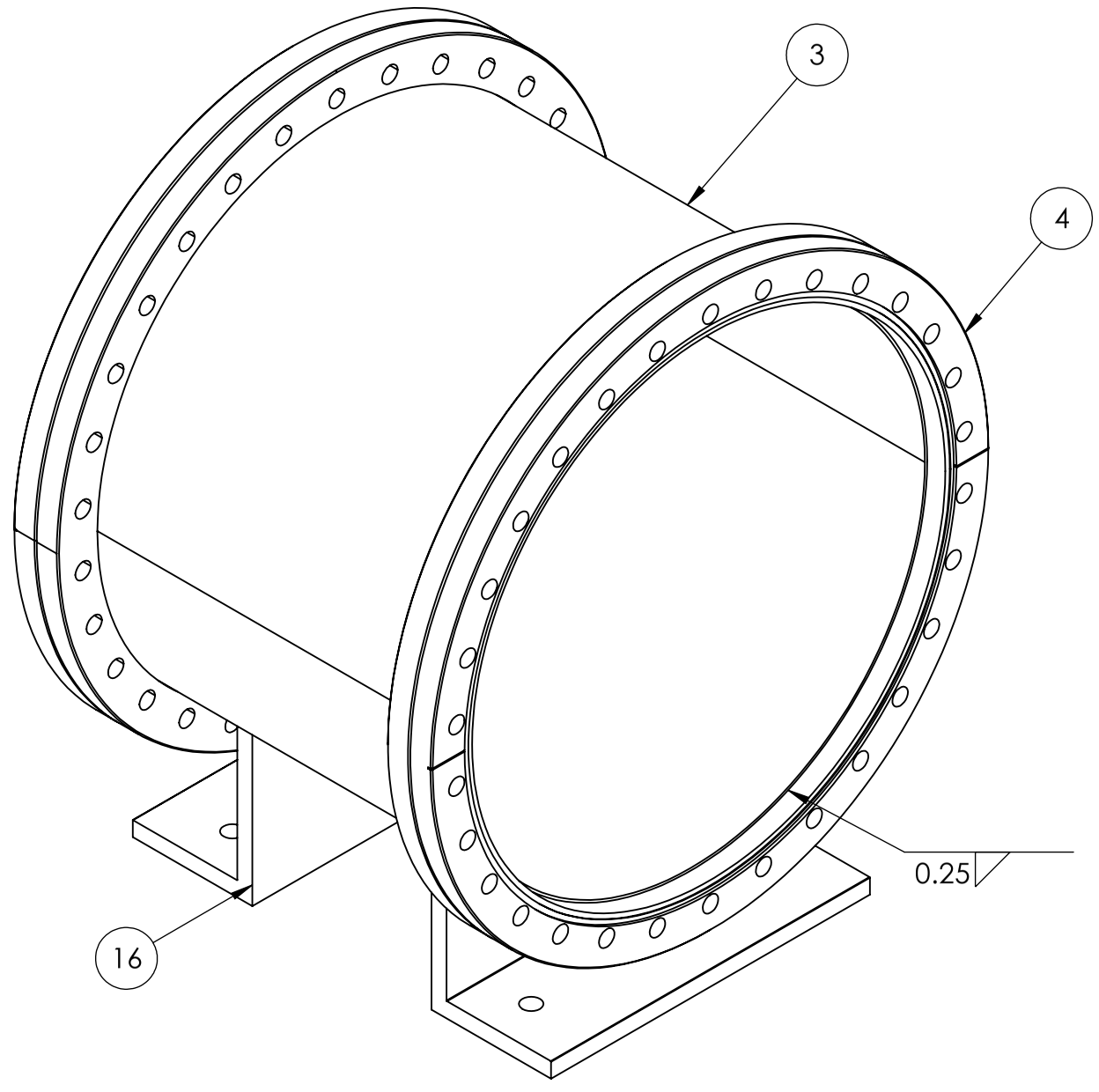
COMMENTS:

TITLE:
MAIN SUPPORT/MOUNTING BRACKET FOR CHAMBER

SIZE	DWG. NO.	REV
B		

SCALE: 1:2 | WEIGHT: | SHEET 14 OF 32





NOTE:
THE FILLET WELD BEAD SIZE SPECIFIED FOR EACH WELD IN THIS DRAWING = 2 x TUBE THICKNESS.
PLEASE FEEL FREE TO SPECIFY AN ALTERNATIVE BEAD SIZE IF THIS VALUE IS NOT THE MOST APPROPRAITE.
SYMMETRY: WHEN WELDING, PLEASE MAINTAIN THE SYMMETRY AND FIT OF THE ENTIRE ASSEMBLY IN SHEET 2.
GUIDING DOWELS: THE GUIDING DOWELS FOR THE FRONT DOOR ARE NOT SHOWN IN THIS DRAWING.

PROPRIETARY AND CONFIDENTIAL
THE INFORMATION CONTAINED IN THIS DRAWING IS THE SOLE PROPERTY OF <INSERT COMPANY NAME HERE>. ANY REPRODUCTION IN PART OR AS A WHOLE WITHOUT THE WRITTEN PERMISSION OF <INSERT COMPANY NAME HERE> IS PROHIBITED.

NEXT ASSY	USED ON	
APPLICATION		DO NOT SCALE DRAWING

UNLESS OTHERWISE SPECIFIED:
DIMENSIONS ARE IN INCHES
TOLERANCES:
FRACTIONAL ±
ANGULAR: MACH ± BEND ±
TWO PLACE DECIMAL ±
THREE PLACE DECIMAL ±
INTERPRET GEOMETRIC TOLERANCING PER:
MATERIAL
FINISH

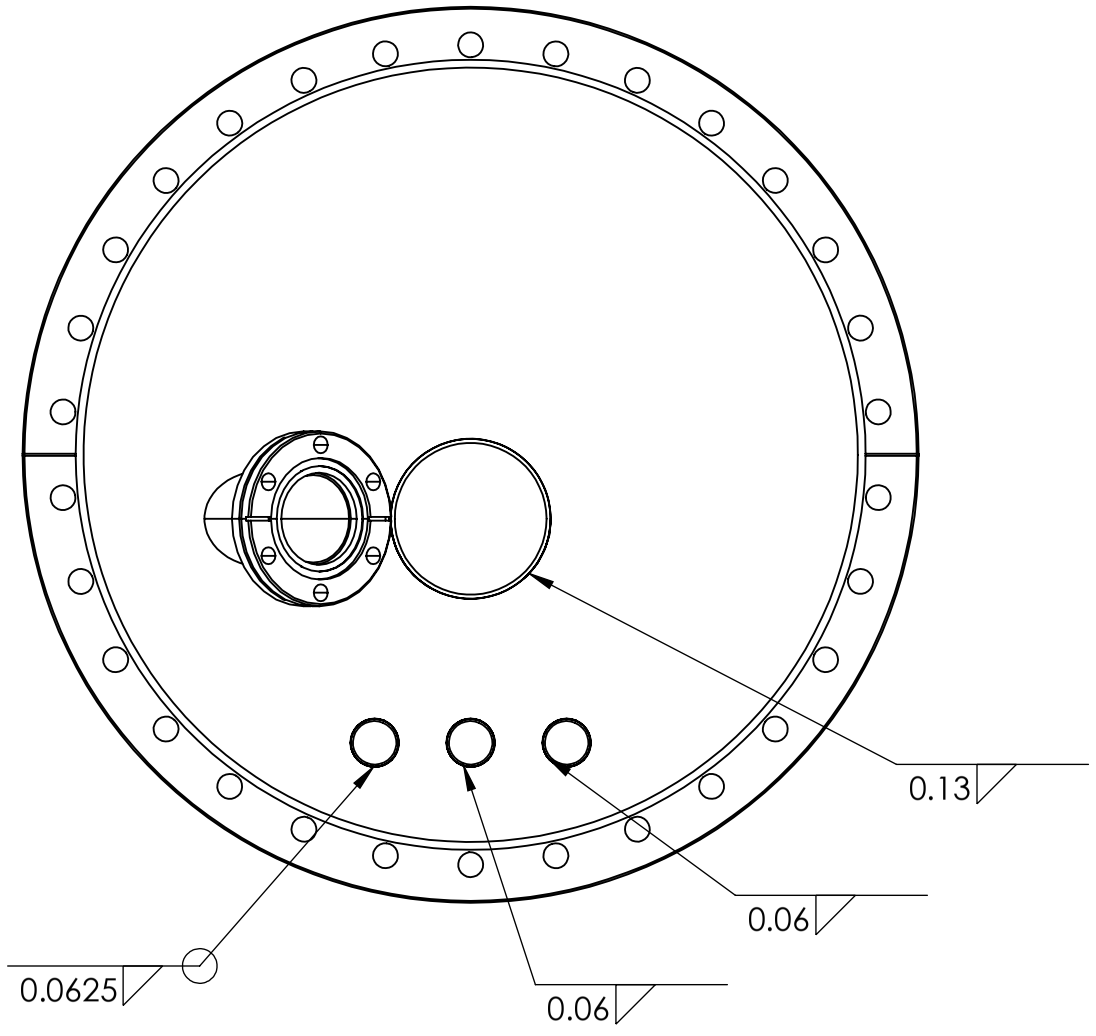
	NAME	DATE
DRAWN	F.K. SULEIMAN	
CHECKED		
ENG APPR.		
MFG APPR.		
Q.A.		

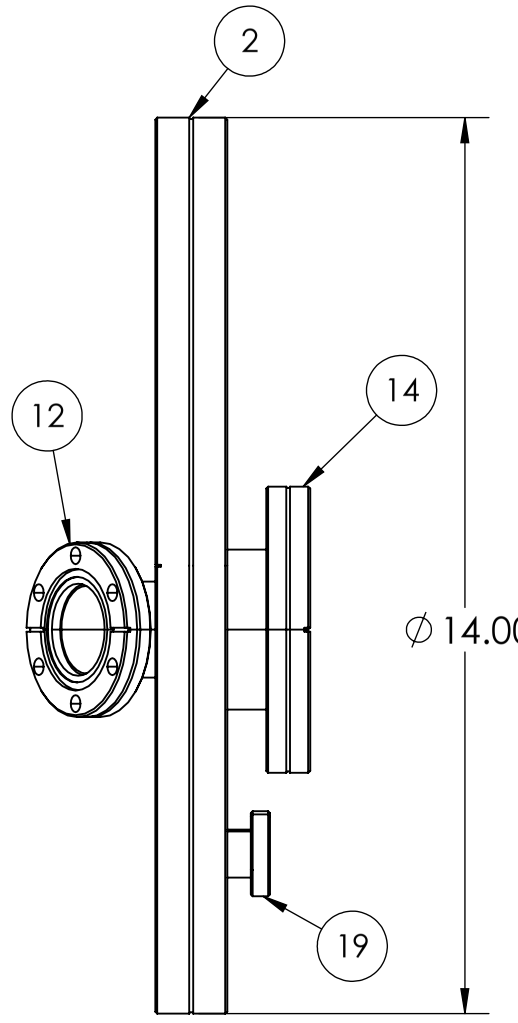
COMMENTS:

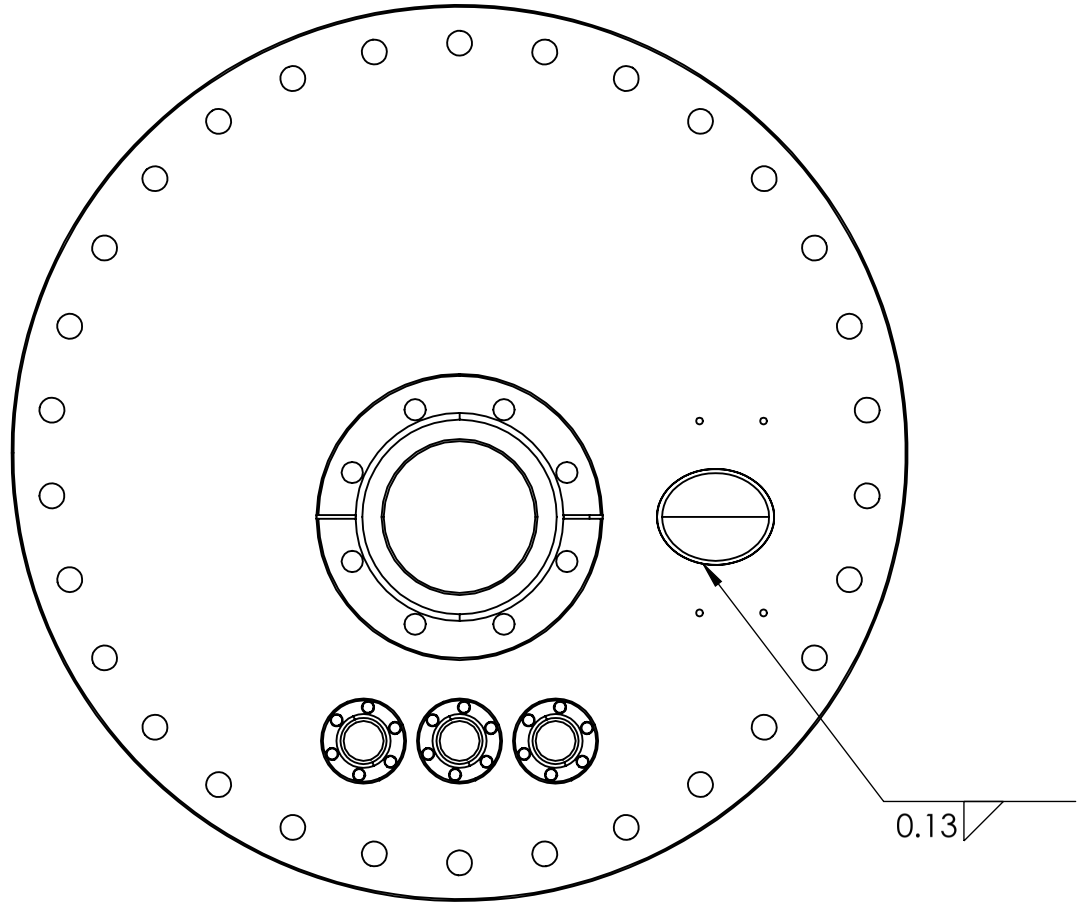
TITLE:
Main Chamber Welds

SIZE	DWG. NO.	REV
B		

SCALE: 1:8 | WEIGHT: | SHEET 15 OF 32







NOTE:
THE FILLET WELD BEAD SIZE SPECIFIED FOR EACH WELD IN THIS DRAWING = 2 x TUBE THICKNESS.
PLEASE FEEL FREE TO SPECIFY AN ALTERNATIVE BEAD SIZE IF THIS VALUE IS NOT THE MOST APPROPRAITE.

PROPRIETARY AND CONFIDENTIAL
THE INFORMATION CONTAINED IN THIS DRAWING IS THE SOLE PROPERTY OF <INSERT COMPANY NAME HERE>. ANY REPRODUCTION IN PART OR AS A WHOLE WITHOUT THE WRITTEN PERMISSION OF <INSERT COMPANY NAME HERE> IS PROHIBITED.

NEXT ASSY	USED ON	
APPLICATION		DO NOT SCALE DRAWING

UNLESS OTHERWISE SPECIFIED:
DIMENSIONS ARE IN INCHES
TOLERANCES:
FRACTIONAL ±
ANGULAR: MACH ± BEND ±
TWO PLACE DECIMAL ±
THREE PLACE DECIMAL ±
INTERPRET GEOMETRIC TOLERANCING PER:
MATERIAL
FINISH

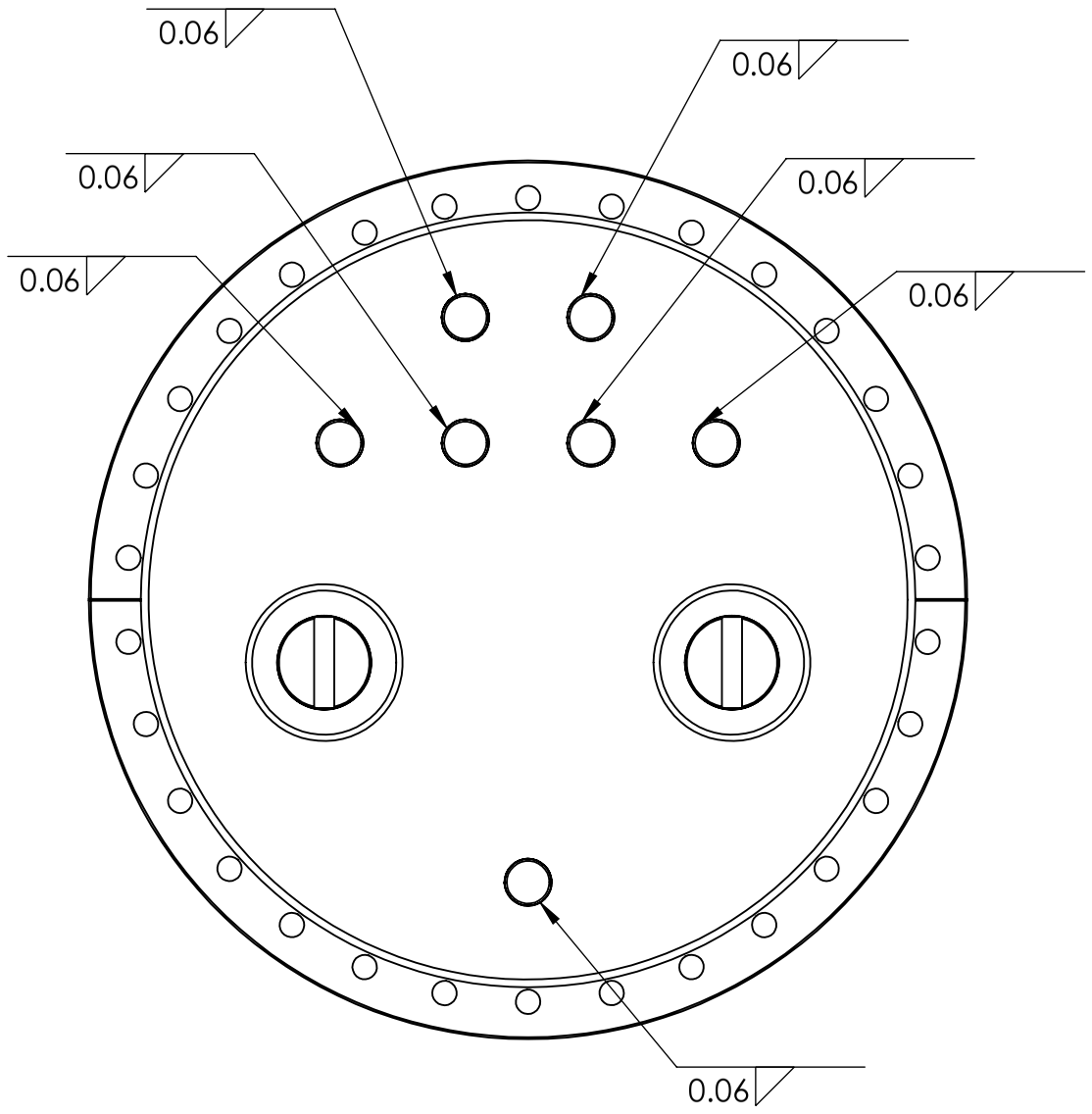
	NAME	DATE
DRAWN	F.K. SULEIMAN	
CHECKED		
ENG APPR.		
MFG APPR.		
Q.A.		

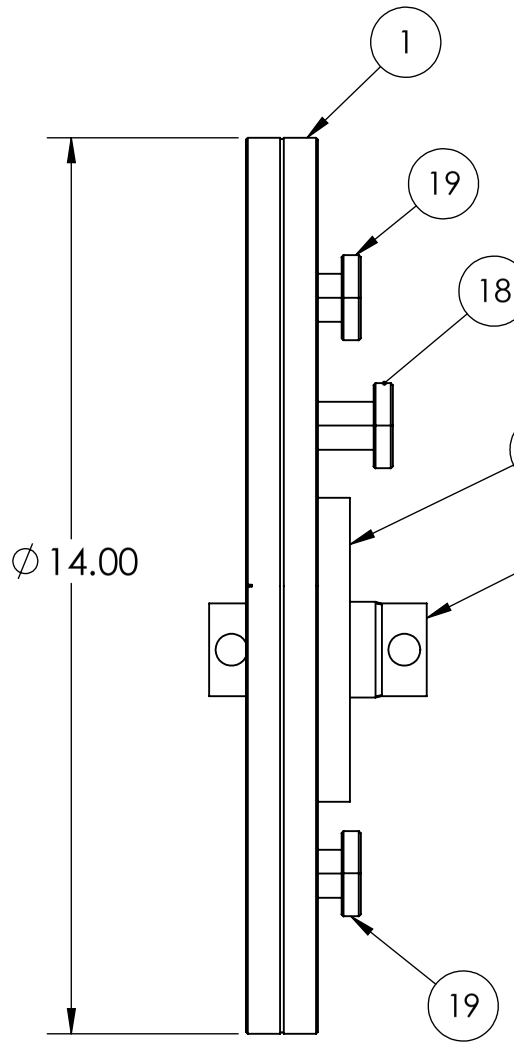
COMMENTS:

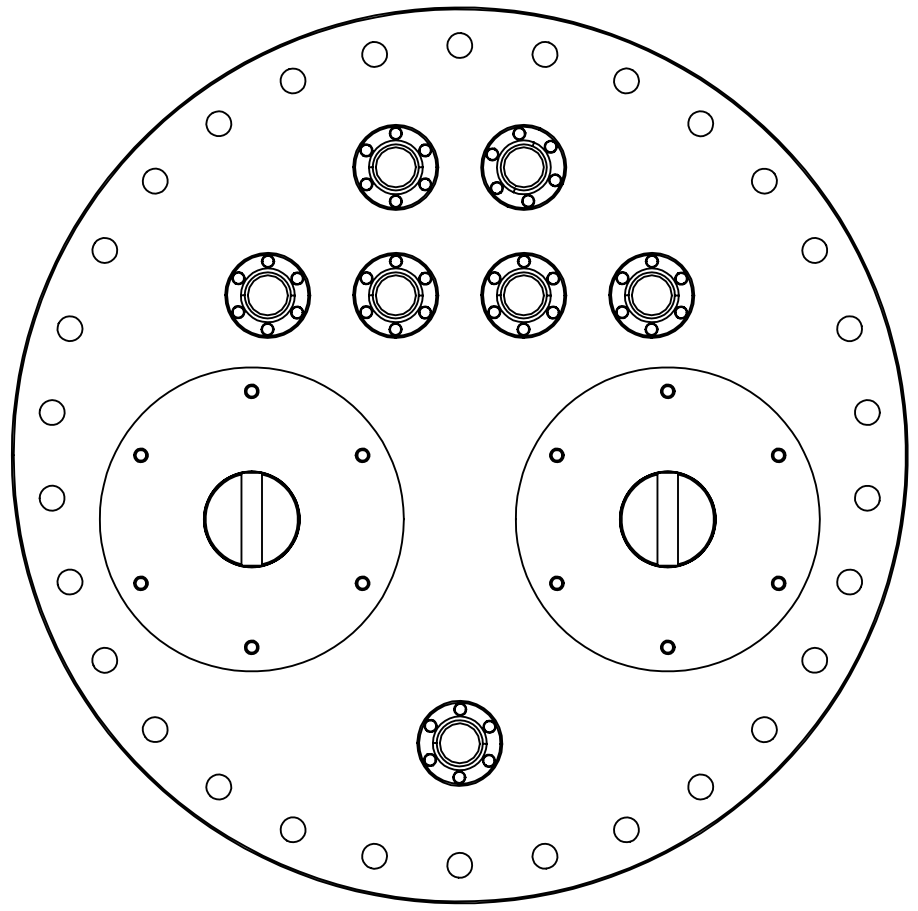
TITLE:
Front Cover (Flange) Welds

SIZE	DWG. NO.	REV
B		

SCALE: 1:8 | WEIGHT: | SHEET 16 OF 32







NOTE:
THE FILLET WELD BEAD SIZE SPECIFIED FOR EACH WELD IN THIS DRAWING = 2 x TUBE THICKNESS.
PLEASE FEEL FREE TO SPECIFY AN ALTERNATIVE BEAD SIZE IF THIS VALUE IS NOT THE MOST APPROPRAITE.

PROPRIETARY AND CONFIDENTIAL
THE INFORMATION CONTAINED IN THIS DRAWING IS THE SOLE PROPERTY OF <INSERT COMPANY NAME HERE>. ANY REPRODUCTION IN PART OR AS A WHOLE WITHOUT THE WRITTEN PERMISSION OF <INSERT COMPANY NAME HERE> IS PROHIBITED.

NEXT ASSY	USED ON
APPLICATION	

UNLESS OTHERWISE SPECIFIED:
DIMENSIONS ARE IN INCHES
TOLERANCES:
FRACTIONAL ±
ANGULAR: MACH ± BEND ±
TWO PLACE DECIMAL ±
THREE PLACE DECIMAL ±
INTERPRET GEOMETRIC TOLERANCING PER:
MATERIAL
FINISH
DO NOT SCALE DRAWING

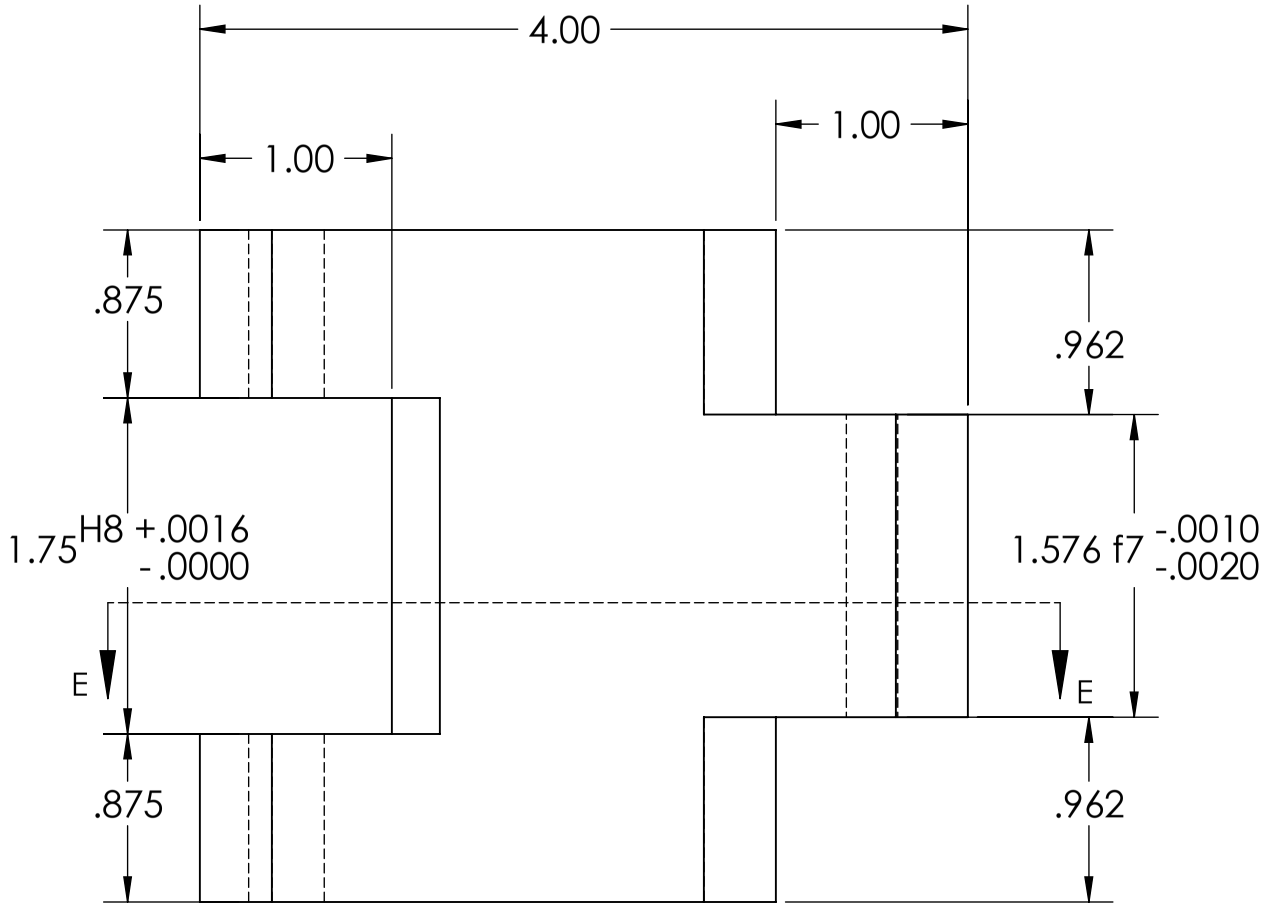
	NAME	DATE
DRAWN	F.K. SULEIMAN	
CHECKED		
ENG APPR.		
MFG APPR.		
Q.A.		

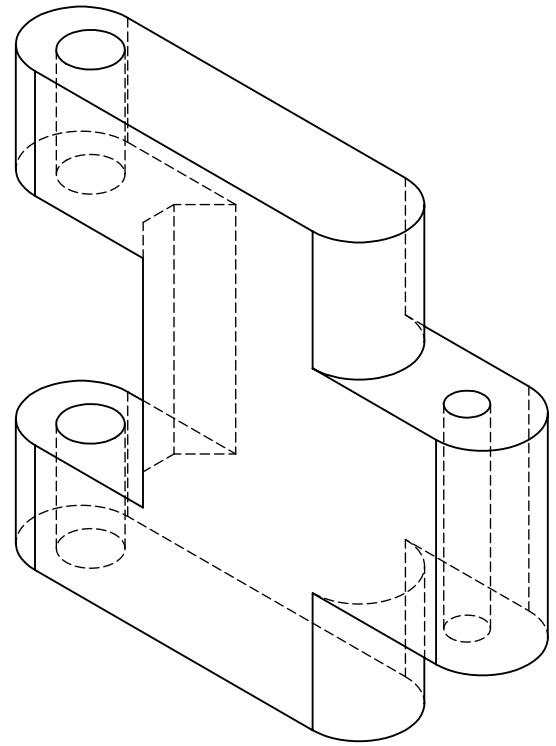
COMMENTS:

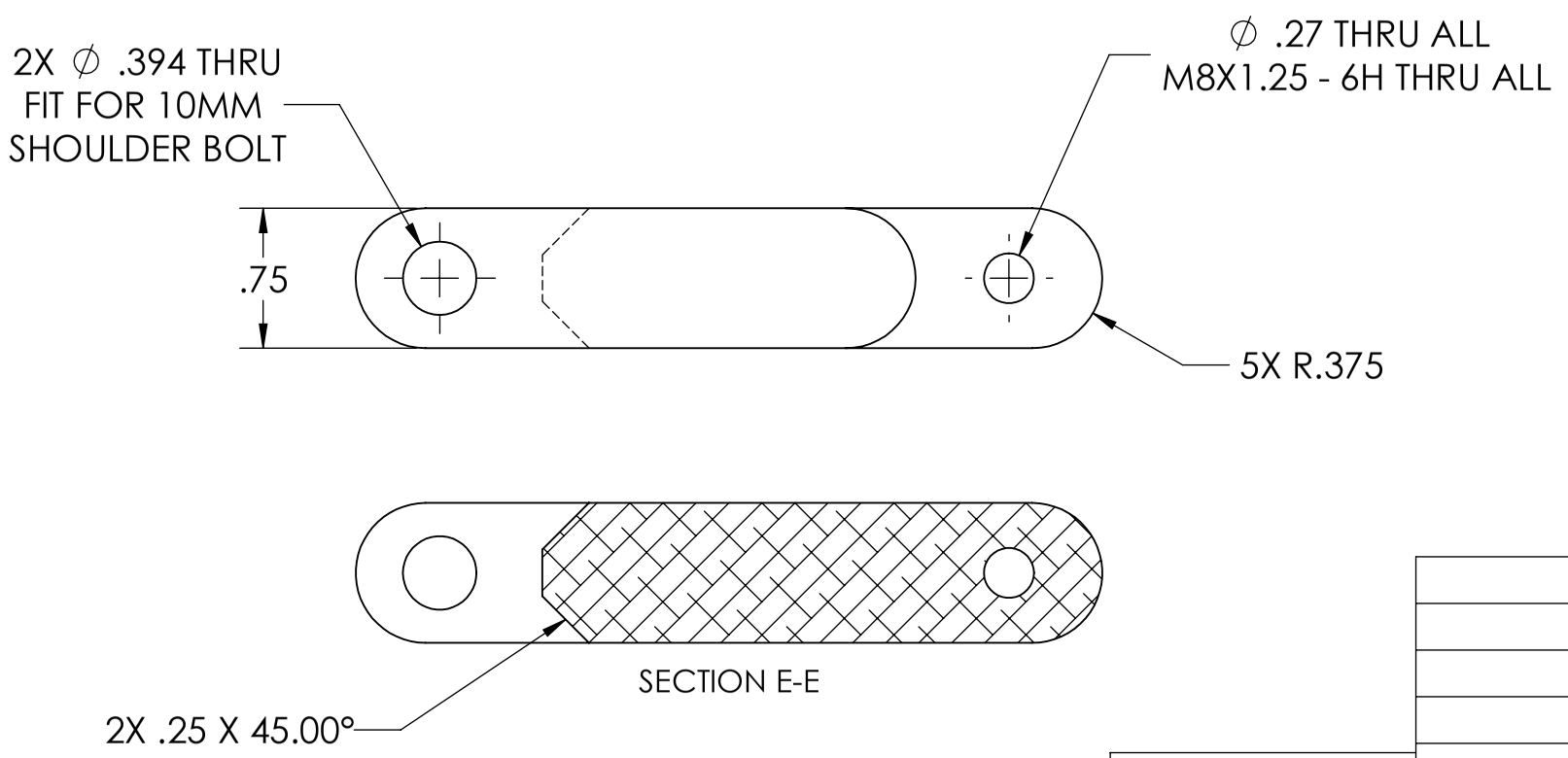
TITLE:
Back Cover (Flange) Welds

SIZE	DWG. NO.	REV
B		

SCALE: 1:8 | WEIGHT: | SHEET 17 OF 32







NOTE:
CLEARANCE FIT: THE HINGE HOLE (**1.75" H8**) IS TO ACCOMODATE A MATING HINGE SHAFT (**1.576" f7**) AND TWO WASHERS.
THE WASHERS ARE STANDARD M10 WASHERS, AND THEREFORE THEIR THICKNESS RANGE IS 1.8MM - 2.2MM. THE CURRENT DIMENSION ACCOUNTS FOR THE HIGHEST POSSIBLE THICKNESS OF 2.2MM BUT ACTUAL PURCHASED PART MAY VARY.

PROPRIETARY AND CONFIDENTIAL
THE INFORMATION CONTAINED IN THIS DRAWING IS THE SOLE PROPERTY OF <INSERT COMPANY NAME HERE>. ANY REPRODUCTION IN PART OR AS A WHOLE WITHOUT THE WRITTEN PERMISSION OF <INSERT COMPANY NAME HERE> IS PROHIBITED.

		UNLESS OTHERWISE SPECIFIED:
		DIMENSIONS ARE IN INCHES TOLERANCES: FRACTIONAL ± ANGULAR: MACH ± BEND ± TWO PLACE DECIMAL ± THREE PLACE DECIMAL ±
		INTERPRET GEOMETRIC TOLERANCING PER:
		MATERIAL ALUMINIUM
NEXT ASSY	USED ON	FINISH
APPLICATION		DO NOT SCALE DRAWING

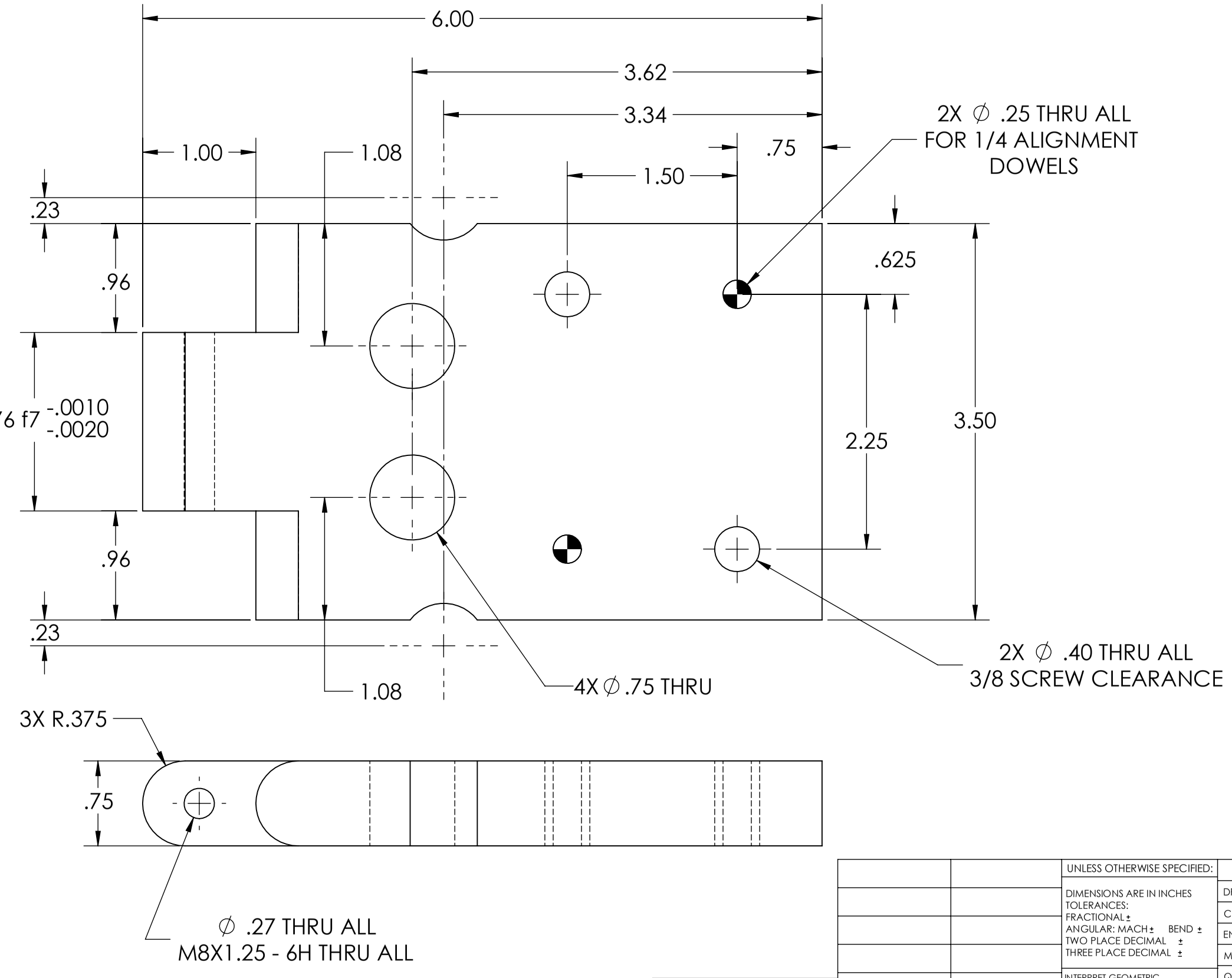
	NAME	DATE
DRAWN	F.K. SULEIMAN	
CHECKED		
ENG APPR.		
MFG APPR.		
Q.A.		

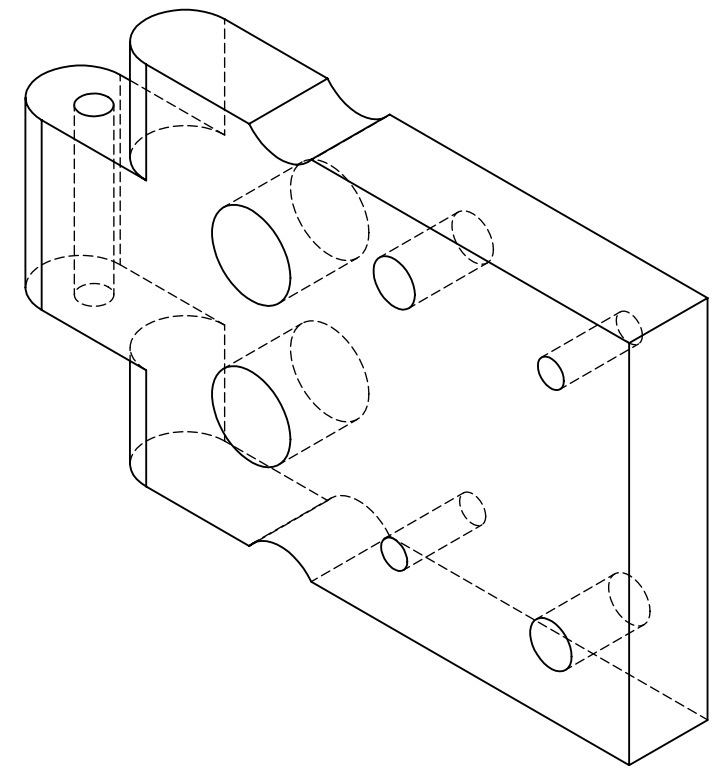
COMMENTS:

TITLE:
MIDDLE HINGES

SIZE	DWG. NO.	REV
B		

SCALE: 1:1 | WEIGHT: | SHEET 18 OF 32





NOTE:
MATERIAL: ALUMINIUM

PROPRIETARY AND CONFIDENTIAL
THE INFORMATION CONTAINED IN THIS DRAWING IS THE SOLE PROPERTY OF <INSERT COMPANY NAME HERE>. ANY REPRODUCTION IN PART OR AS A WHOLE WITHOUT THE WRITTEN PERMISSION OF <INSERT COMPANY NAME HERE> IS PROHIBITED.

NEXT ASSY	USED ON
APPLICATION	

UNLESS OTHERWISE SPECIFIED:
DIMENSIONS ARE IN INCHES
TOLERANCES:
FRACTIONAL ±
ANGULAR: MACH ± BEND ±
TWO PLACE DECIMAL ±
THREE PLACE DECIMAL ±
INTERPRET GEOMETRIC TOLERANCING PER:
MATERIAL
FINISH
DO NOT SCALE DRAWING

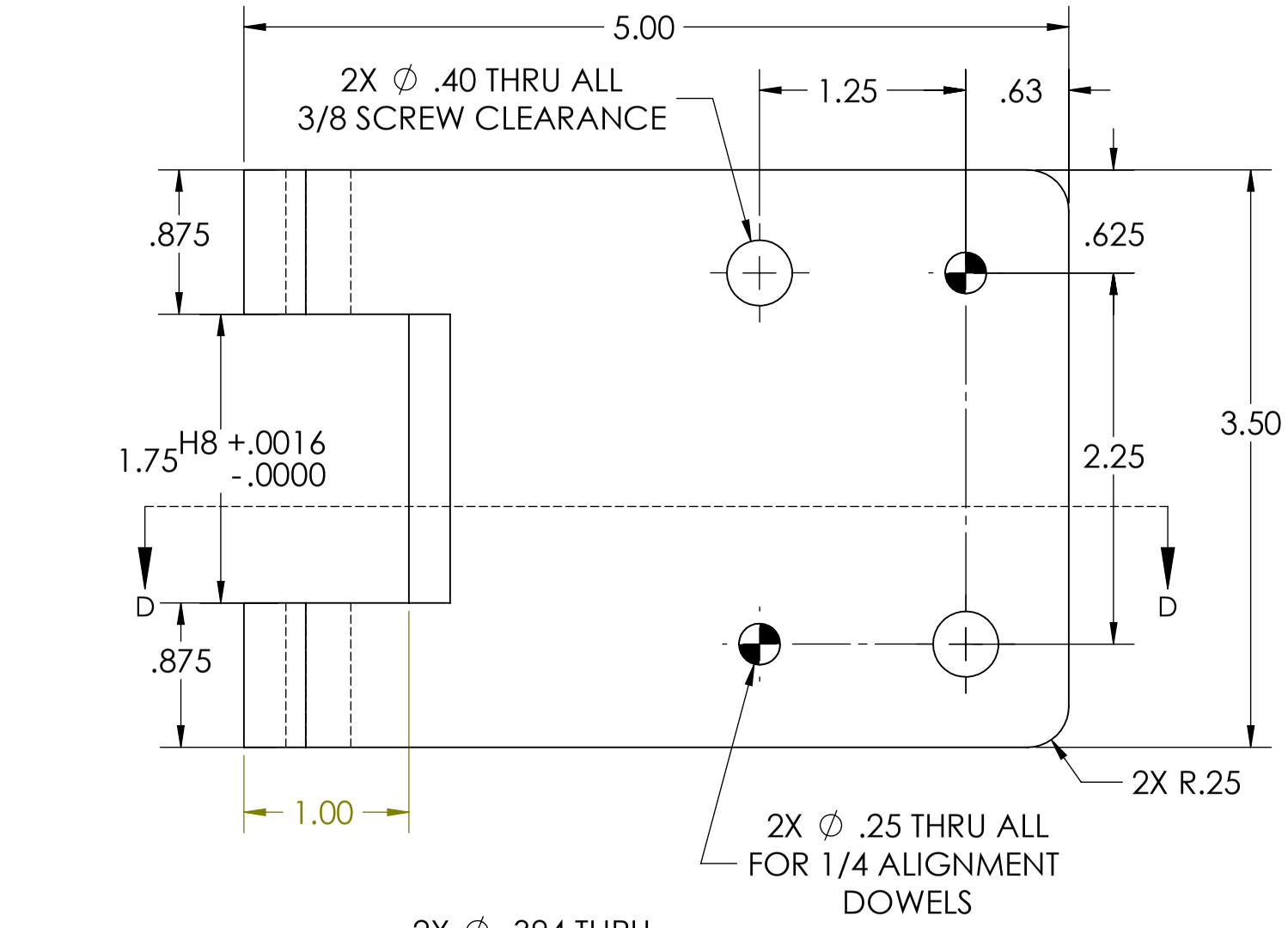
	NAME	DATE
DRAWN	F.K. SULEIMAN	
CHECKED		
ENG APPR.		
MFG APPR.		
Q.A.		

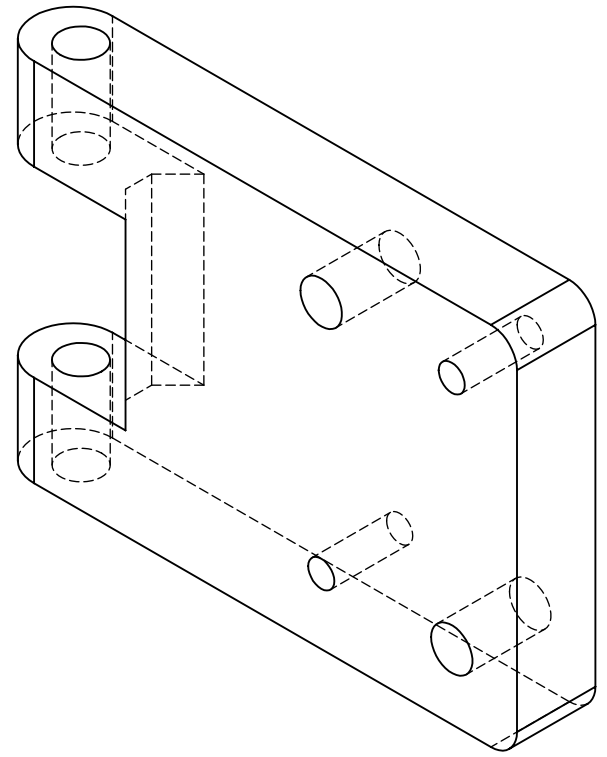
COMMENTS:

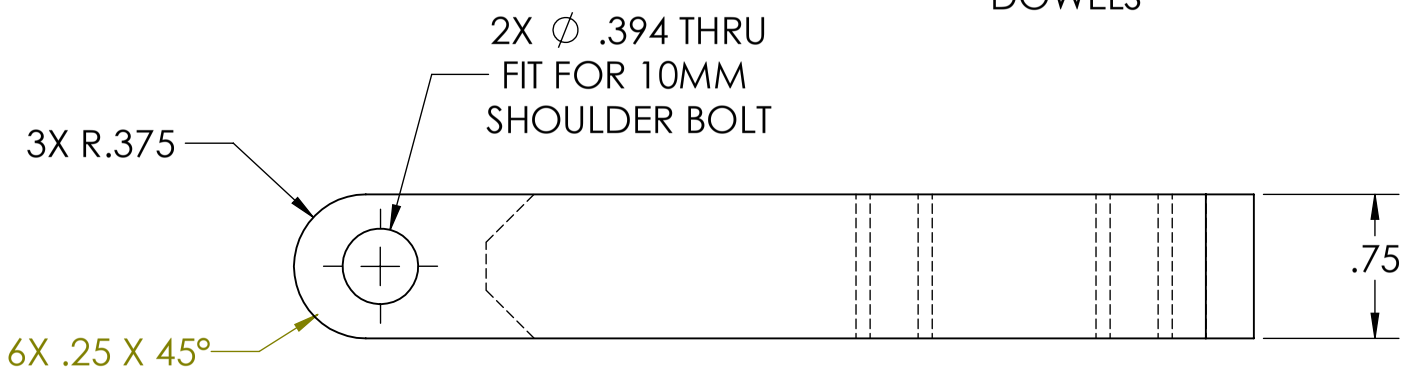
TITLE:
FRONT HINGE

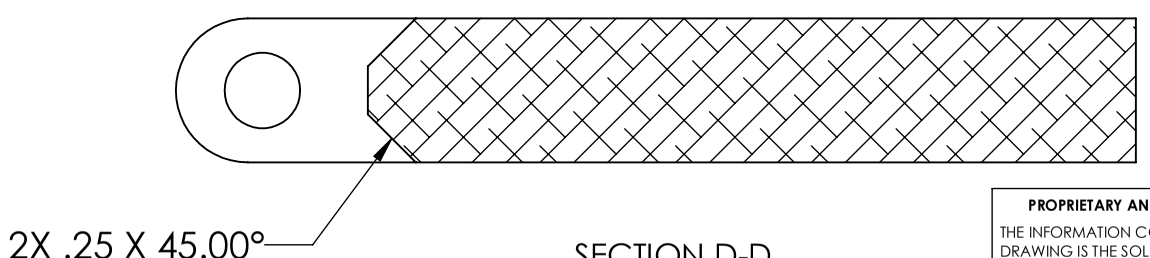
SIZE	DWG. NO.	REV
B		

SCALE: 1:1 | WEIGHT: | SHEET 19 OF 32









SECTION D-D

NOTE:
MATERIAL: ALUMINIUM
CLEARANCE FIT: THE HINGE HOLE (**1.75" H8**) IS TO ACCOMODATE A MATING HINGE SHAFT (**1.576" f7**) AND TWO WASHERS.
THE WASHERS ARE STANDARD M10 WASHERS, AND THEREFORE THEIR THICKNESS RANGE IS 1.8MM - 2.2MM. THE CURRENT DIMENSION ACCOUNTS FOR THE HIGHEST POSSIBLE THICKNESS OF 2.2MM BUT ACTUAL PURCHASED PART MAY VARY.

PROPRIETARY AND CONFIDENTIAL
THE INFORMATION CONTAINED IN THIS DRAWING IS THE SOLE PROPERTY OF <INSERT COMPANY NAME HERE>. ANY REPRODUCTION IN PART OR AS A WHOLE WITHOUT THE WRITTEN PERMISSION OF <INSERT COMPANY NAME HERE> IS PROHIBITED.

NEXT ASSY	USED ON
APPLICATION	

UNLESS OTHERWISE SPECIFIED:
DIMENSIONS ARE IN INCHES
TOLERANCES:
FRACTIONAL ±
ANGULAR: MACH ± BEND ±
TWO PLACE DECIMAL ±
THREE PLACE DECIMAL ±
INTERPRET GEOMETRIC TOLERANCING PER:
MATERIAL
FINISH
DO NOT SCALE DRAWING

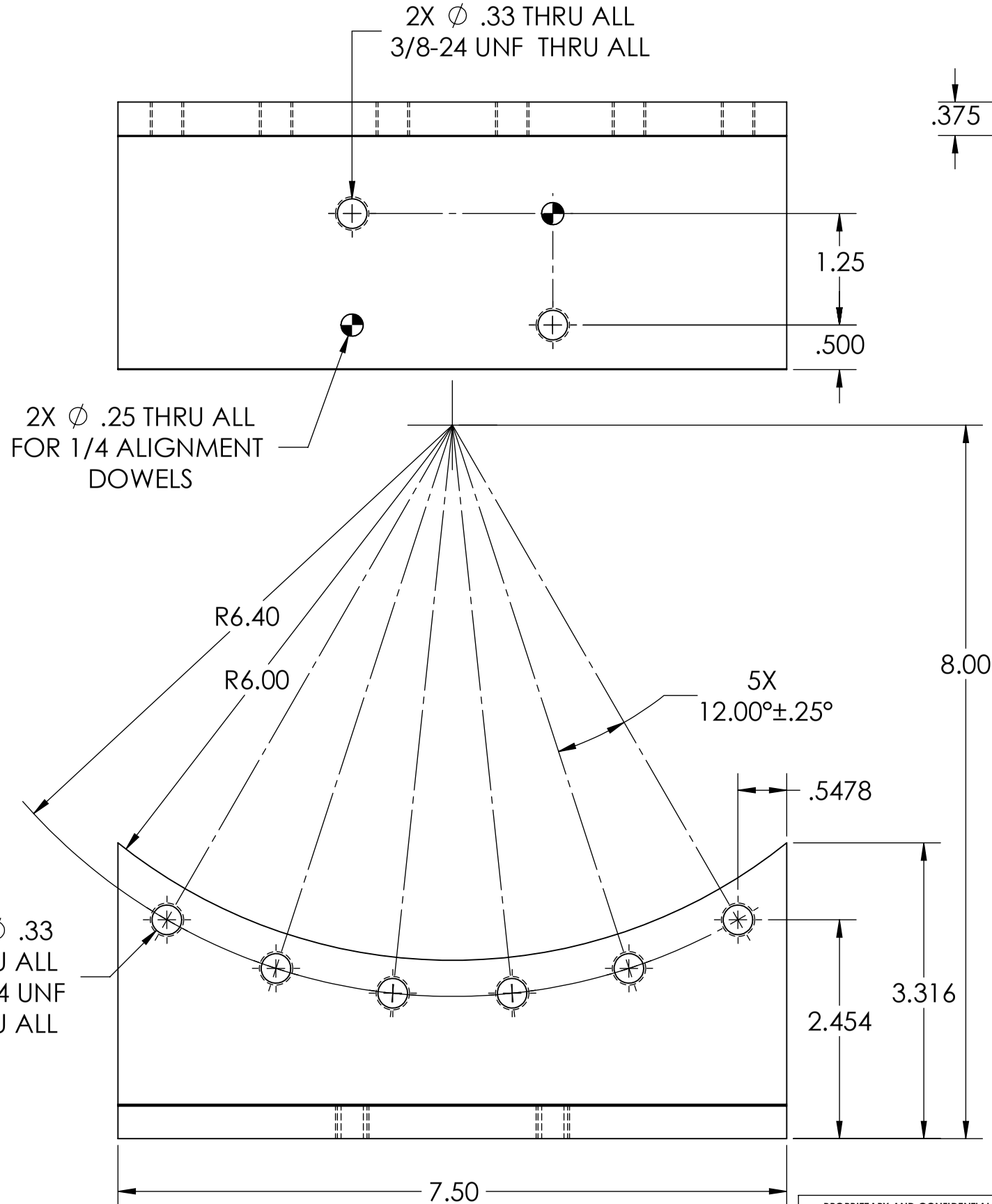
	NAME	DATE
DRAWN	F.K. SULEIMAN	
CHECKED		
ENG APPR.		
MFG APPR.		
Q.A.		

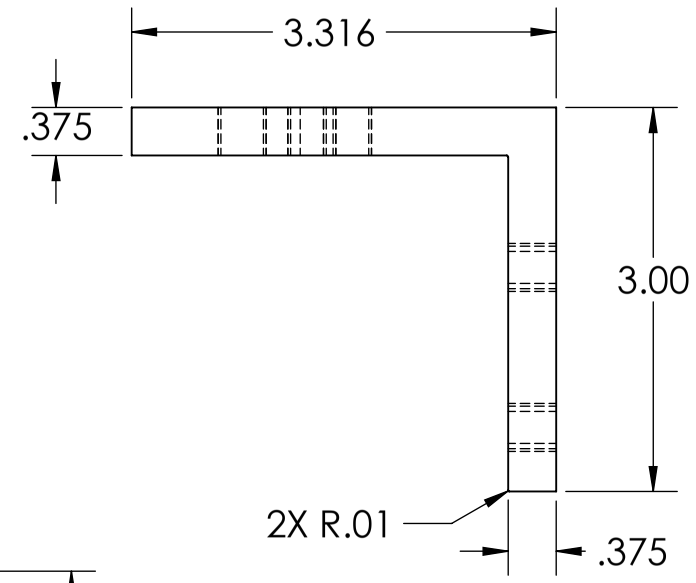
COMMENTS:

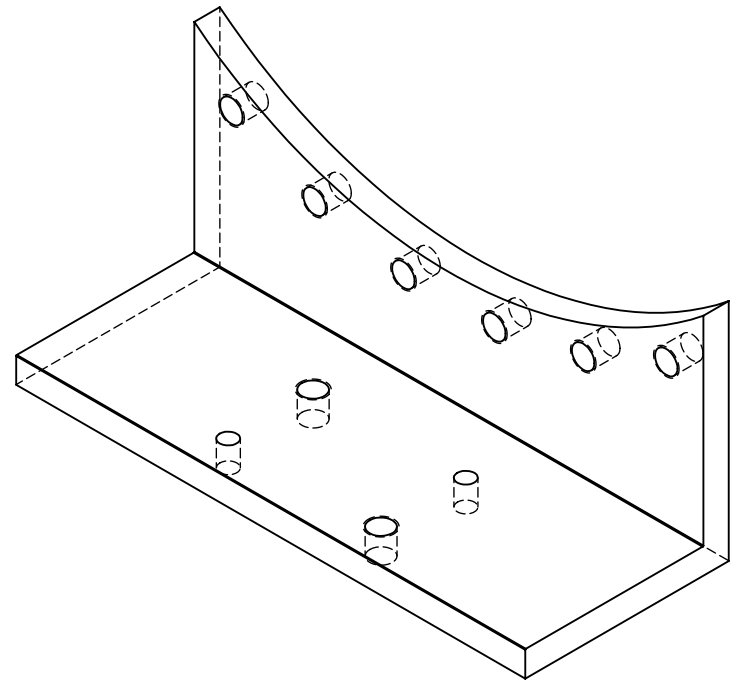
TITLE:
BACK/REAR HINGE

SIZE	DWG. NO.	REV
B		

SCALE: 1:1 | WEIGHT: | SHEET 20 OF 32







NOTE:
THE PART IS DESIGNED BASED ON THE PROFILE FOR MCMASTER-CARR-1260T58 BUT ANY SUITABLE/ALTERNATIVE PROFILE CAN BE USED.

PROPRIETARY AND CONFIDENTIAL
THE INFORMATION CONTAINED IN THIS DRAWING IS THE SOLE PROPERTY OF <INSERT COMPANY NAME HERE>. ANY REPRODUCTION IN PART OR AS A WHOLE WITHOUT THE WRITTEN PERMISSION OF <INSERT COMPANY NAME HERE> IS PROHIBITED.

NEXT ASSY	USED ON	
APPLICATION		DO NOT SCALE DRAWING

UNLESS OTHERWISE SPECIFIED:
DIMENSIONS ARE IN INCHES
TOLERANCES:
FRACTIONAL ±
ANGULAR: MACH ± BEND ±
TWO PLACE DECIMAL ±
THREE PLACE DECIMAL ±
INTERPRET GEOMETRIC TOLERANCING PER:
MATERIAL
304 STAINLESS STEEL
FINISH

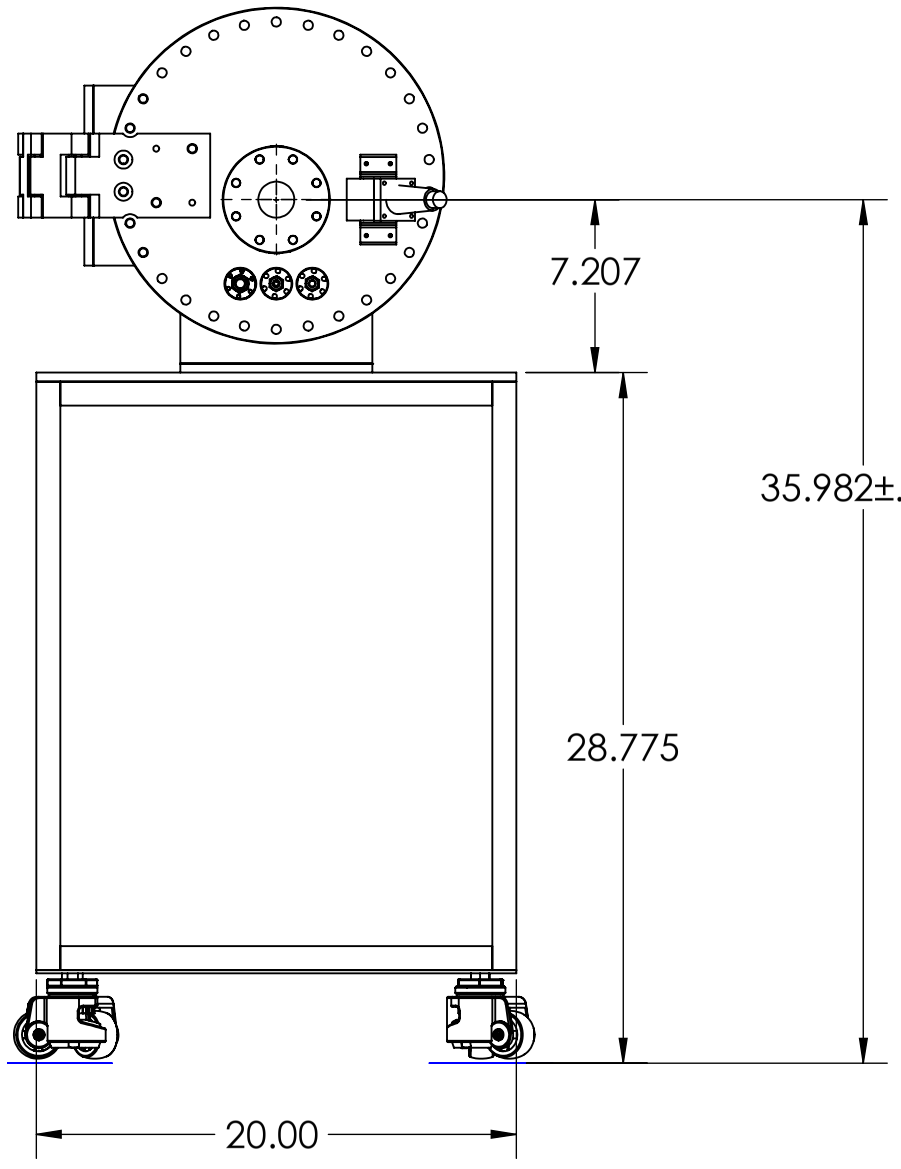
	NAME	DATE
DRAWN	F.K. SULEIMAN	
CHECKED		
ENG APPR.		
MFG APPR.		
Q.A.		

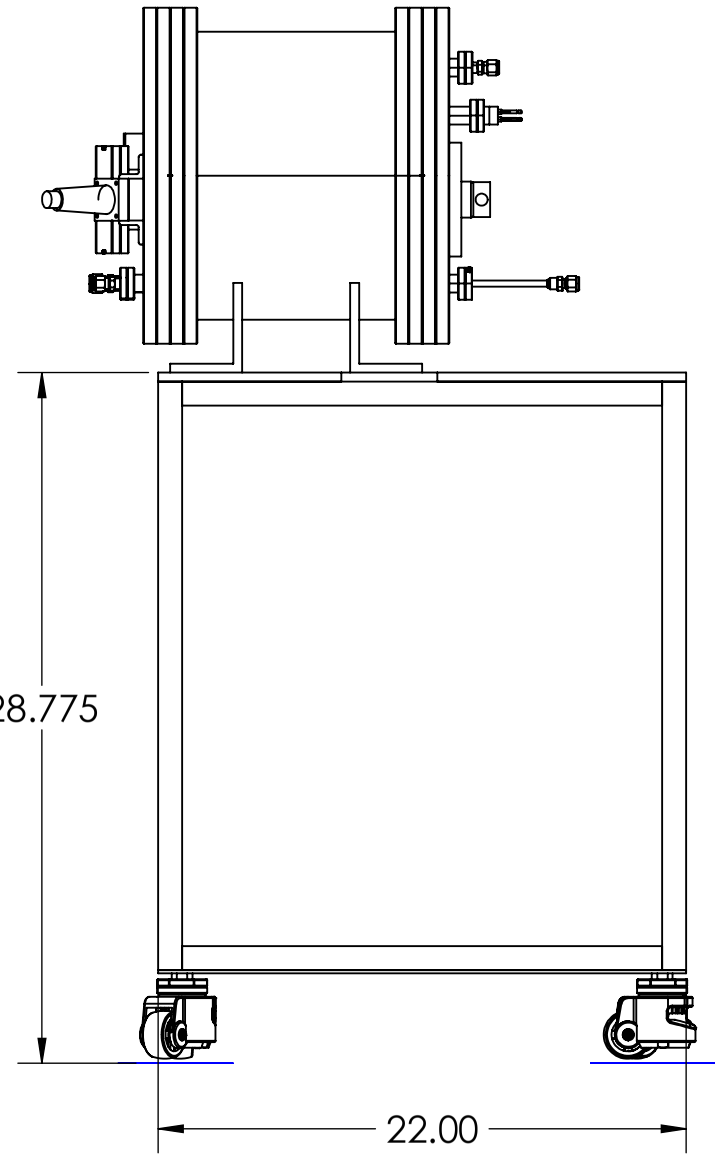
COMMENTS:

TITLE:
HINGE BRACKET

SIZE	DWG. NO.	REV
B		

SCALE: 1:2 | WEIGHT: | SHEET 21 OF 32





NOTE:

- 35.982" IS THE REQUIRED HEIGHT WITH RESPECT TO THE VIEWPORT ON THE CHAMBER.
- THE MID HEIGHT OF THE CASTER WHEN THE LEVELING PADS ARE DOWN IS 3.5" (HEIGHT RANGE OF CASTER =3.3125" - 3.6875").
- THE LENGHT OF THE VERTICAL STEEL TUBE USED IN THIS DRAWING IS THEN CALCULATED AS SUCH:
- 35.982 - (MID CASTER HEIGHT + CASTER HEX NUT THICKNESS+BOTTOM SHELF THICKNESS+ TOP SHELF THICKNESS+ VIEWPORT HEIGHT)=35.982-(3.5+0.25+ 0.125+0.375+7.207)=24.525"
- IF ANY OF THESE DEPENDENT DEIMENSIONS ARE MODIFIED E.G. CASTER OR SHELF DIMENSIONS, THE LENGTH OF THE VERTICAL TUBE MIGHT NEED TO BE ADJUSTED.
- THE LENGTH AND BREATHE OF THE SHELF FROM THE OLD CHAMBER IS 20" X 22" WHICH DETERMINES THE DIMENSION OF THE HORIZONTAL STEEL TUBES

PROPRIETARY AND CONFIDENTIAL

THE INFORMATION CONTAINED IN THIS DRAWING IS THE SOLE PROPERTY OF <INSERT COMPANY NAME HERE>. ANY REPRODUCTION IN PART OR AS A WHOLE WITHOUT THE WRITTEN PERMISSION OF <INSERT COMPANY NAME HERE> IS PROHIBITED.

		UNLESS OTHERWISE SPECIFIED:		NAME	DATE
		DIMENSIONS ARE IN INCHES TOLERANCES: FRACTIONAL ± ANGULAR: MACH ± BEND ± TWO PLACE DECIMAL ± THREE PLACE DECIMAL ±	DRAWN	F.K. SULEIMAN	
			CHECKED		
			ENG APPR.		
			MFG APPR.		
			Q.A.		
		INTERPRET GEOMETRIC TOLERANCING PER:	COMMENTS:		
		MATERIAL			
NEXT ASSY	USED ON	FINISH			
APPLICATION		DO NOT SCALE DRAWING			

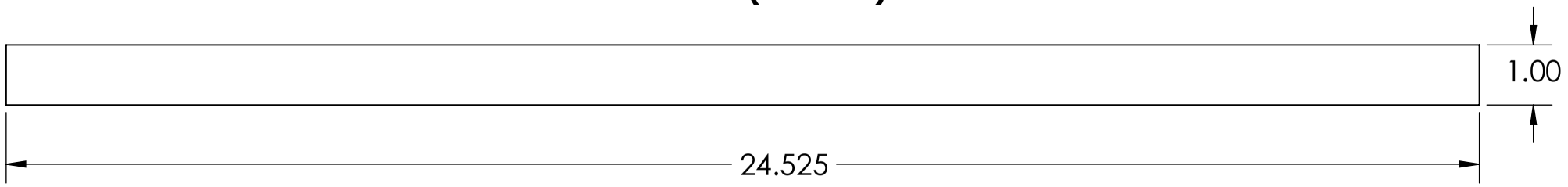
TITLE:

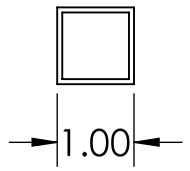
CHAMBER AND CART ASSEMBLY

SIZE	DWG. NO.	REV
B		

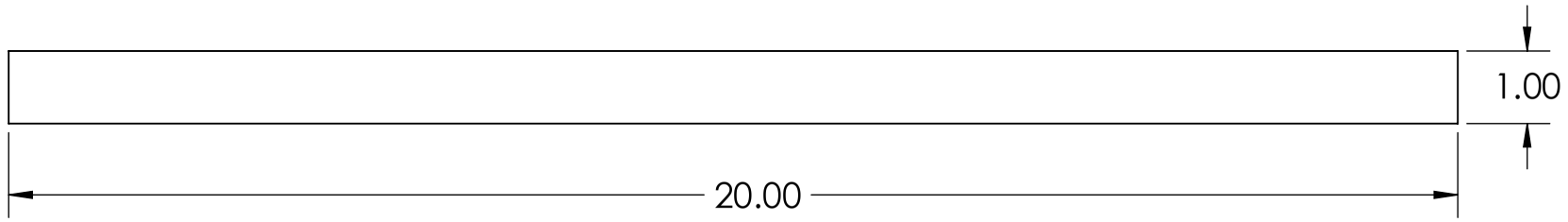
SCALE: 1:20 | WEIGHT: | SHEET 22 OF 32

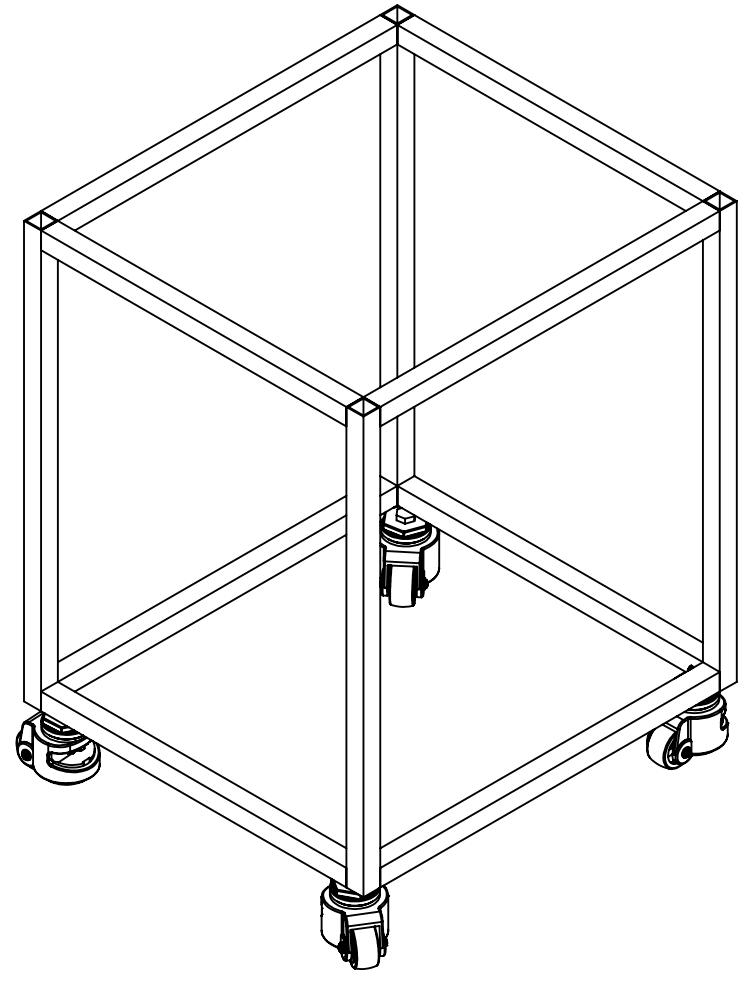
VERTICAL (HEIGHT):



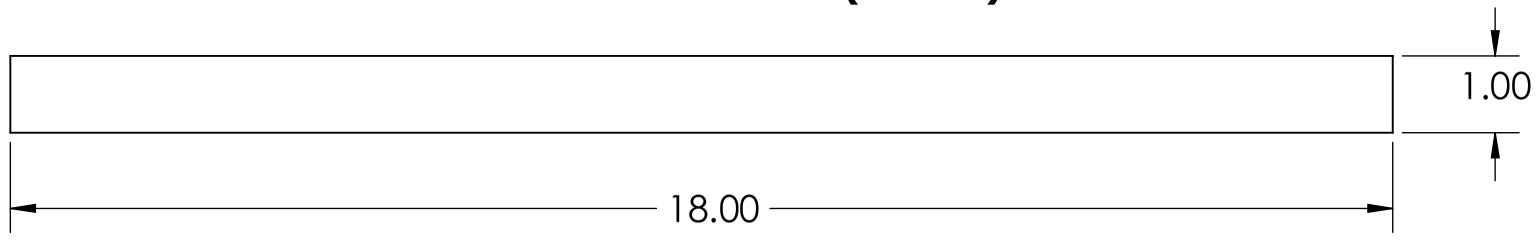


HORIZONTAL (LENGTH):





HORIZONTAL (WIDTH):



NOTE:
1" SQUARE STEEL TUBING WELDED TOGETHER TO MAKE THE CART

PROPRIETARY AND CONFIDENTIAL
THE INFORMATION CONTAINED IN THIS DRAWING IS THE SOLE PROPERTY OF <INSERT COMPANY NAME HERE>. ANY REPRODUCTION IN PART OR AS A WHOLE WITHOUT THE WRITTEN PERMISSION OF <INSERT COMPANY NAME HERE> IS PROHIBITED.

		UNLESS OTHERWISE SPECIFIED:		NAME	DATE
		DIMENSIONS ARE IN INCHES TOLERANCES: FRACTIONAL ± ANGULAR: MACH ± BEND ± TWO PLACE DECIMAL ± THREE PLACE DECIMAL ±	DRAWN	F.K. SULEIMAN	
			CHECKED		
			ENG APPR.		
			MFG APPR.		
			Q.A.		
		INTERPRET GEOMETRIC TOLERANCING PER:	COMMENTS:		
		MATERIAL			
NEXT ASSY	USED ON	FINISH			
APPLICATION		DO NOT SCALE DRAWING			

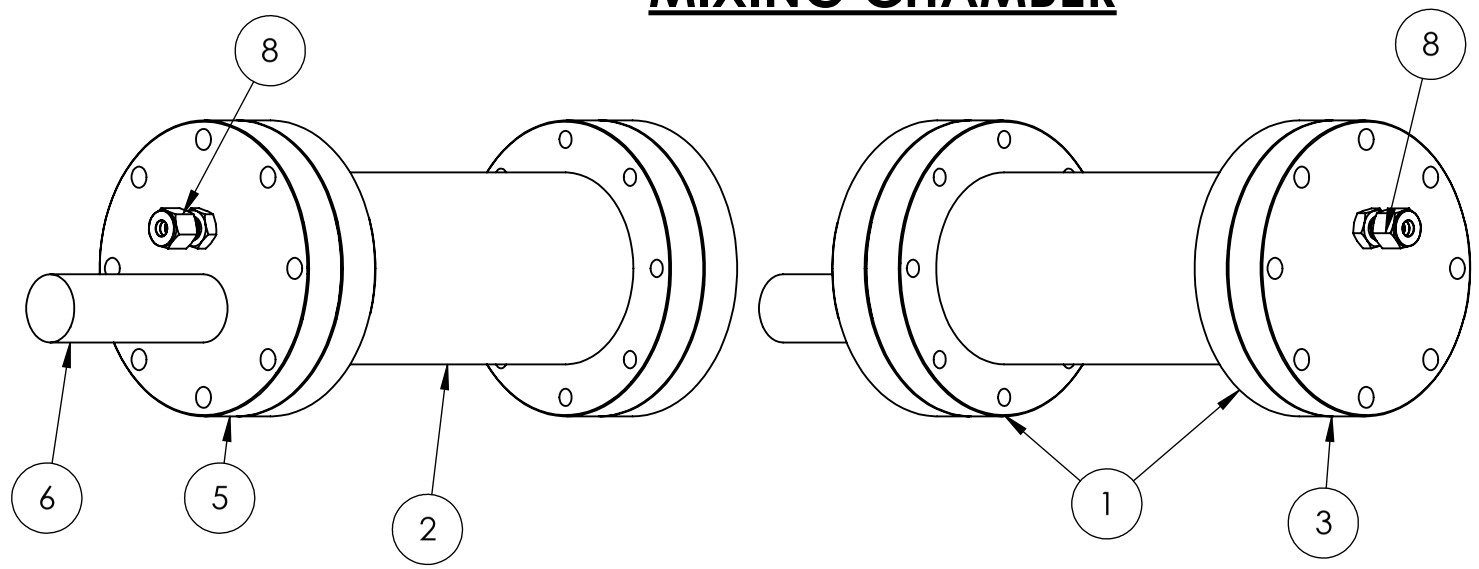
TITLE:
STEEL TUBINGS FOR CART ASSEMBLY

SIZE	DWG. NO.	REV
B		

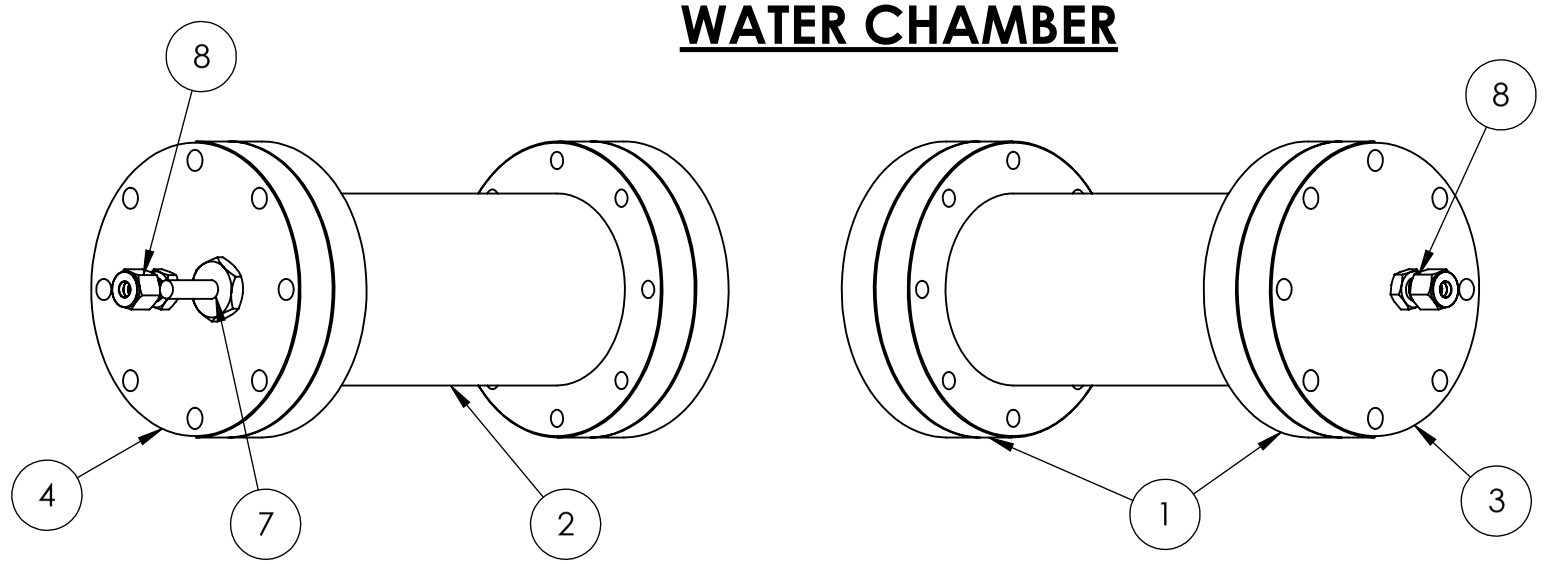
SCALE: 1:8 | WEIGHT: | SHEET 23 OF 32

ITEM NO.	PART NUMBER	DESCRIPTION	QTY.
1	BoredTappedFlange	BORED FLANGE WITH TAPPED HOLES	4
2	Tube	3" OD, 16-GAUGE (0.065") TUBING	2
3	BlankThroughFlange	BLANK FLANGE WITH THROUGH HOLES - NPT INLET	2
4	BlankThroughFlange_ WaterTop	BLANK FLANGE WITH THROUGH HOLES - NPT & THERMOCOUPLE	1
5	BlankThroughFlange_ MixingTop	BLANK FLANGE WITH THROUGH HOLES - NPT & DEW POINT	1
6	EA2-TX-100-HD	MICHELL DEW POINT TRANSMITTER	1
7	1245N31	TYPE K THERMOCOUPLE PROBE	1
8	5943K111	SWAGELOK STRAIGHT ADAPTER FOR 1/4" TUBE OD x 1/4 NPT MALE	4

MIXING CHAMBER



WATER CHAMBER



PROPRIETARY AND CONFIDENTIAL

THE INFORMATION CONTAINED IN THIS DRAWING IS THE SOLE PROPERTY OF <INSERT COMPANY NAME HERE>. ANY REPRODUCTION IN PART OR AS A WHOLE WITHOUT THE WRITTEN PERMISSION OF <INSERT COMPANY NAME HERE> IS PROHIBITED.

		UNLESS OTHERWISE SPECIFIED:
		DIMENSIONS ARE IN INCHES TOLERANCES: FRACTIONAL ± ANGULAR: MACH ± BEND ± TWO PLACE DECIMAL ± THREE PLACE DECIMAL ±
		INTERPRET GEOMETRIC TOLERANCING PER:
		MATERIAL
NEXT ASSY	USED ON	FINISH
APPLICATION		DO NOT SCALE DRAWING

	NAME	DATE
DRAWN	F.K. SULEIMAN	
CHECKED		
ENG APPR.		
MFG APPR.		
Q.A.		

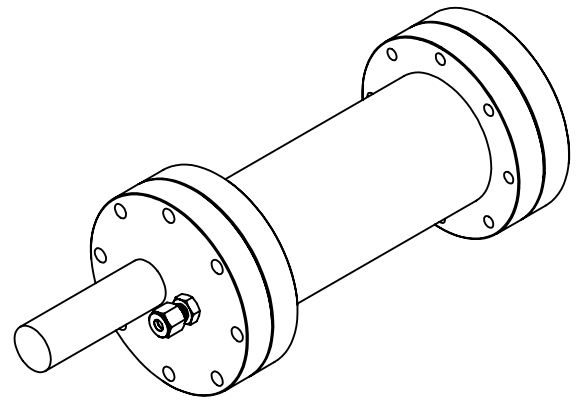
COMMENTS:

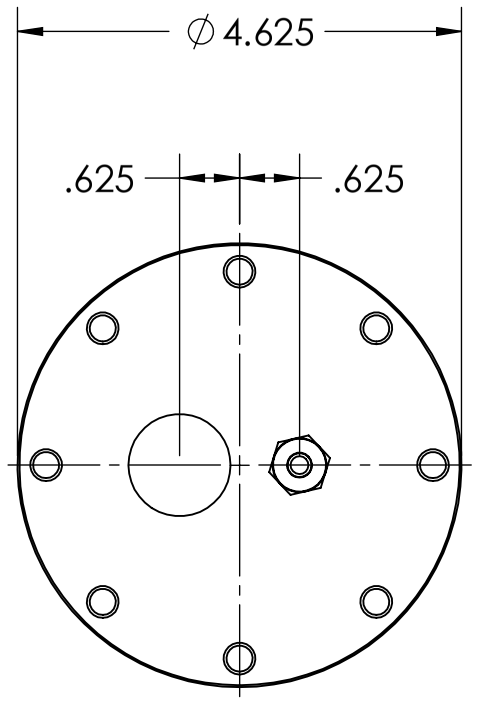
TITLE:

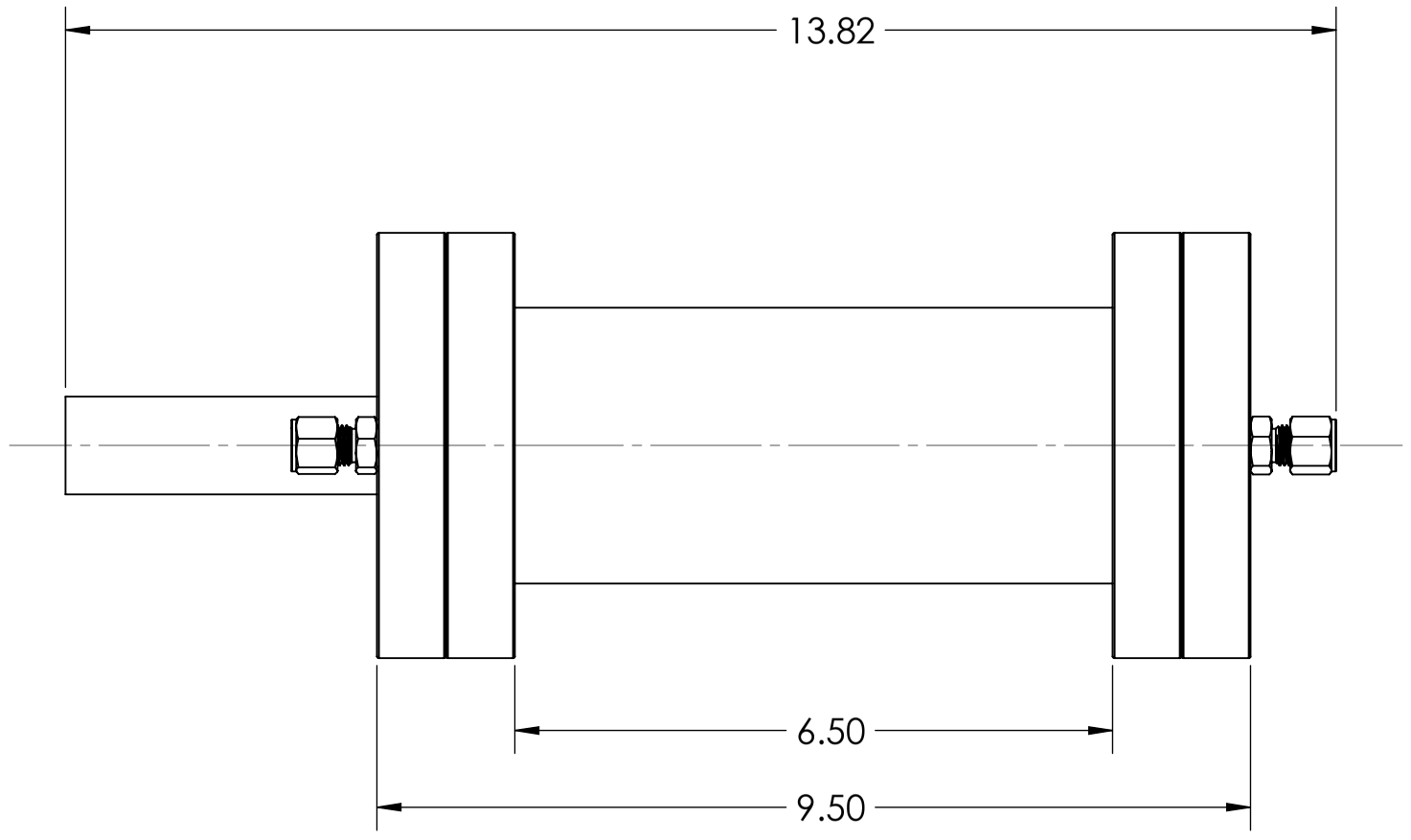
HUMIDIFICATION CELL ASSEMBLY

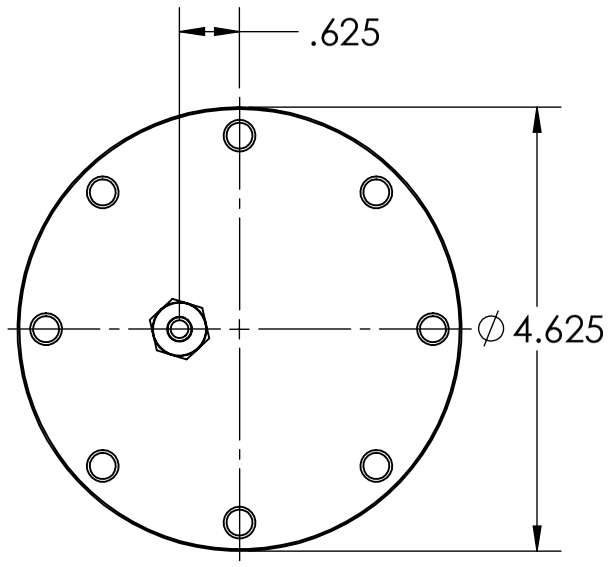
SIZE	DWG. NO.	REV
B		

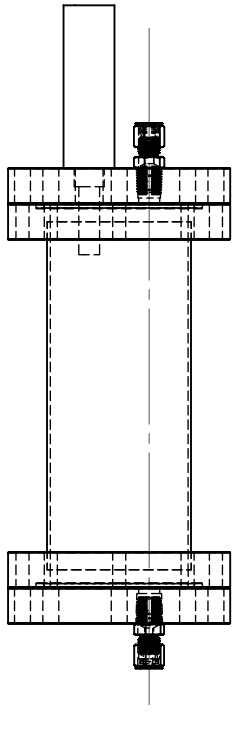
SCALE: 1:4 | WEIGHT: | SHEET 24 OF 32











PROPRIETARY AND CONFIDENTIAL

THE INFORMATION CONTAINED IN THIS DRAWING IS THE SOLE PROPERTY OF <INSERT COMPANY NAME HERE>. ANY REPRODUCTION IN PART OR AS A WHOLE WITHOUT THE WRITTEN PERMISSION OF <INSERT COMPANY NAME HERE> IS PROHIBITED.

NEXT ASSY	USED ON	
APPLICATION		

UNLESS OTHERWISE SPECIFIED:

DIMENSIONS ARE IN INCHES
TOLERANCES:
FRACTIONAL ±
ANGULAR: MACH ± BEND ±
TWO PLACE DECIMAL ±
THREE PLACE DECIMAL ±

INTERPRET GEOMETRIC TOLERANCING PER:

MATERIAL

FINISH

DO NOT SCALE DRAWING

	NAME	DATE
DRAWN	F.K. SULEIMAN	
CHECKED		
ENG APPR.		
MFG APPR.		
Q.A.		

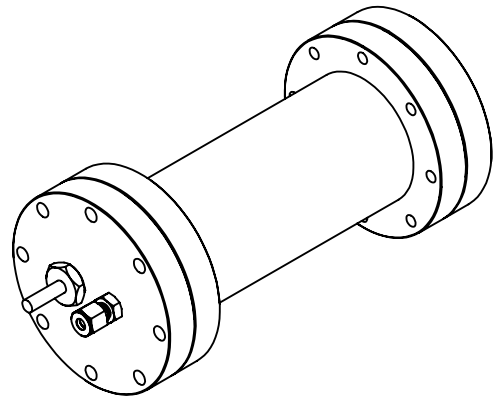
COMMENTS:

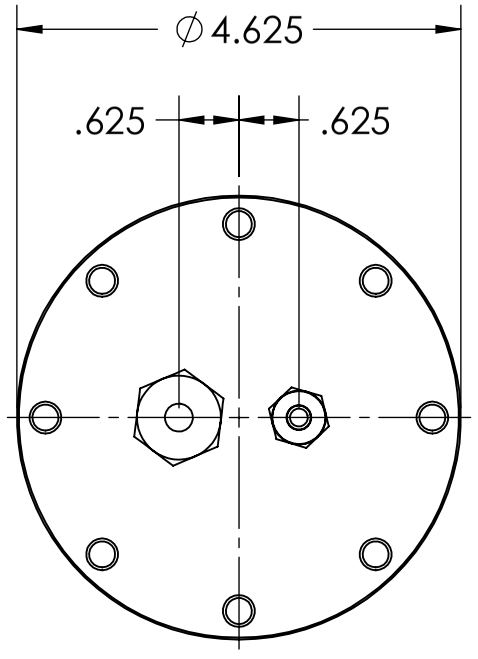
TITLE:

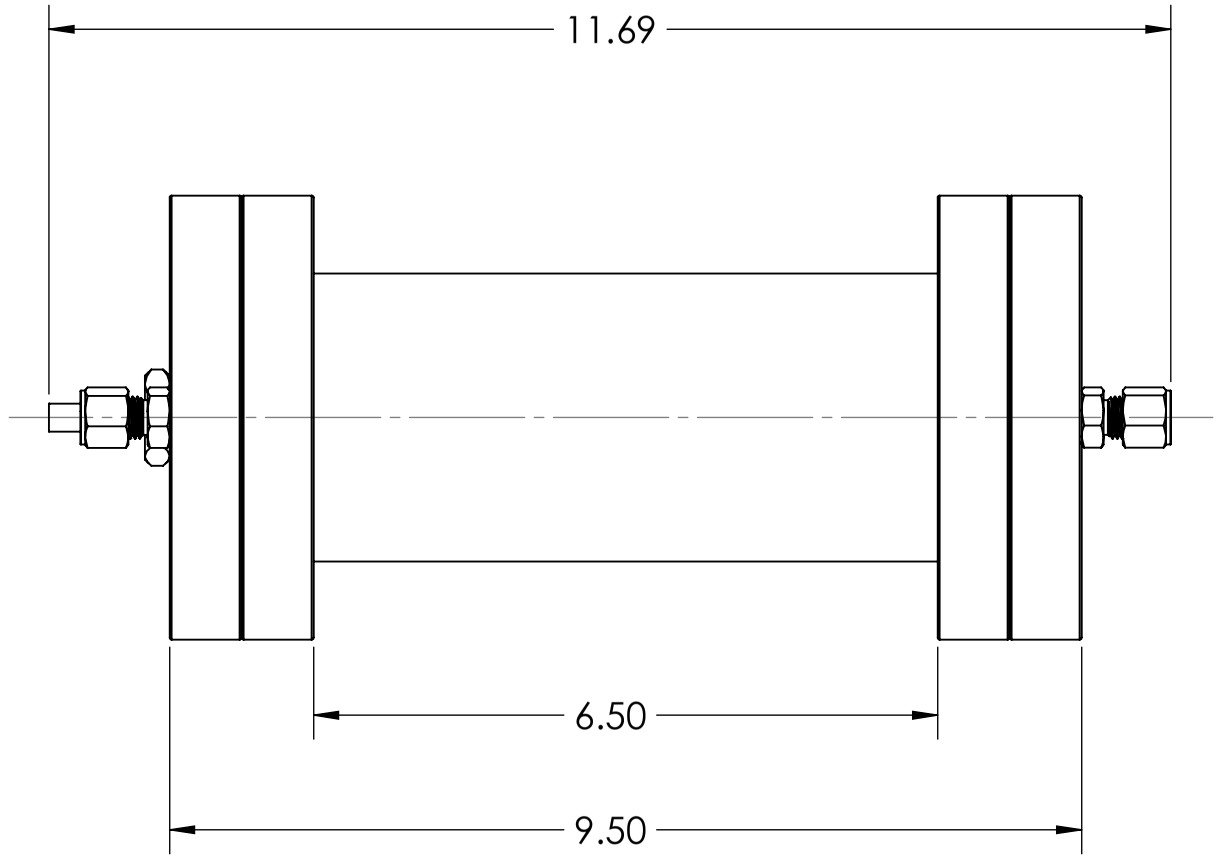
MIXING CHAMBER ASSEMBLY

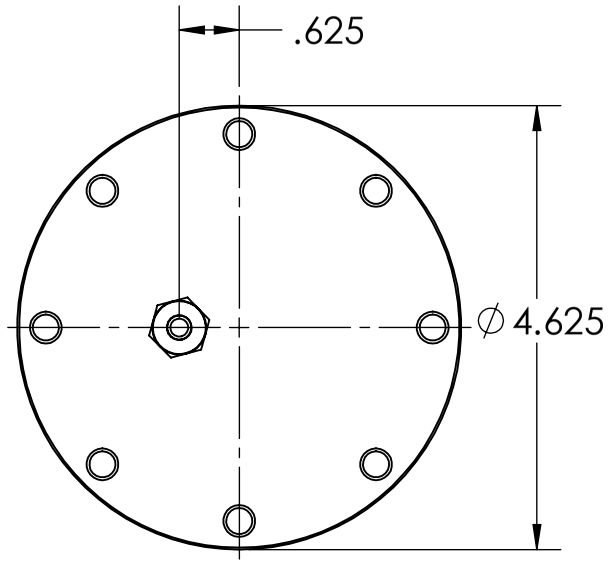
SIZE	DWG. NO.	REV
B		

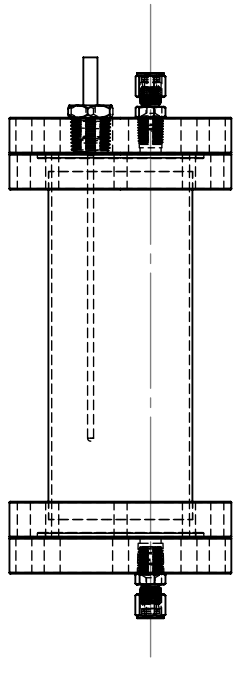
SCALE: 1:4 | WEIGHT: | SHEET 25 OF 32











PROPRIETARY AND CONFIDENTIAL

THE INFORMATION CONTAINED IN THIS DRAWING IS THE SOLE PROPERTY OF <INSERT COMPANY NAME HERE>. ANY REPRODUCTION IN PART OR AS A WHOLE WITHOUT THE WRITTEN PERMISSION OF <INSERT COMPANY NAME HERE> IS PROHIBITED.

NEXT ASSY	USED ON
APPLICATION	

UNLESS OTHERWISE SPECIFIED:

DIMENSIONS ARE IN INCHES
TOLERANCES:
FRACTIONAL ±
ANGULAR: MACH ± BEND ±
TWO PLACE DECIMAL ±
THREE PLACE DECIMAL ±

INTERPRET GEOMETRIC TOLERANCING PER:

MATERIAL

FINISH

DO NOT SCALE DRAWING

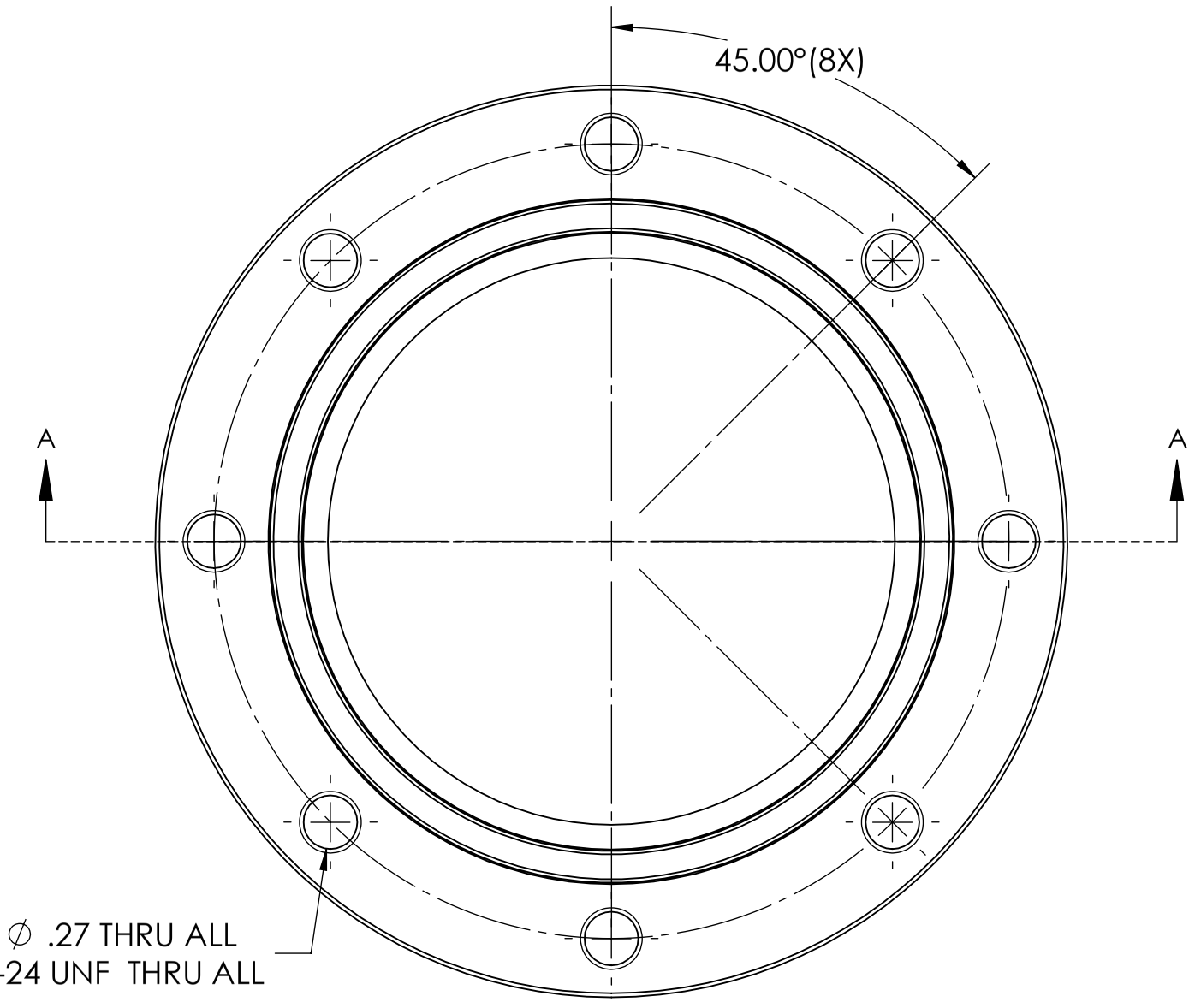
	NAME	DATE
DRAWN	F.K. SULEIMAN	
CHECKED		
ENG APPR.		
MFG APPR.		
Q.A.		

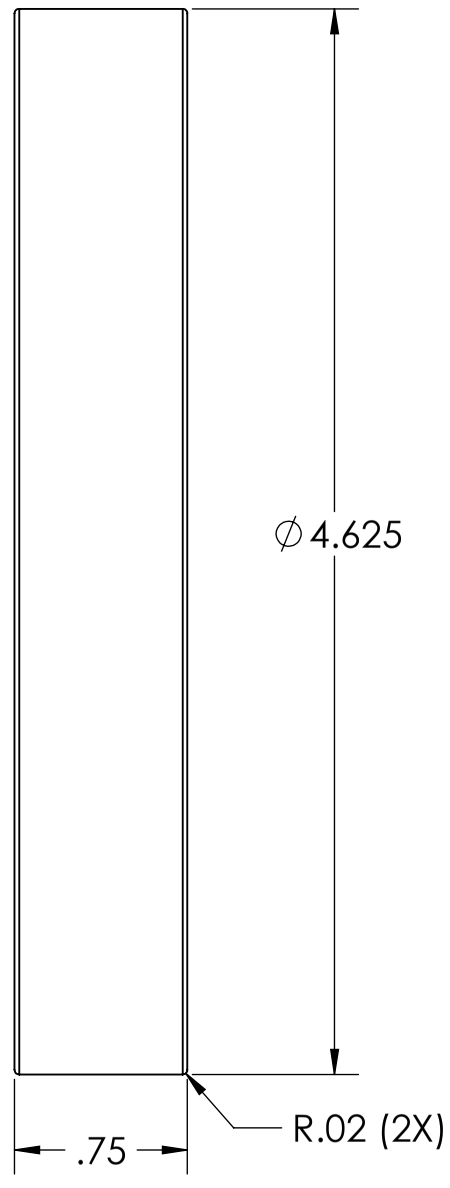
COMMENTS:

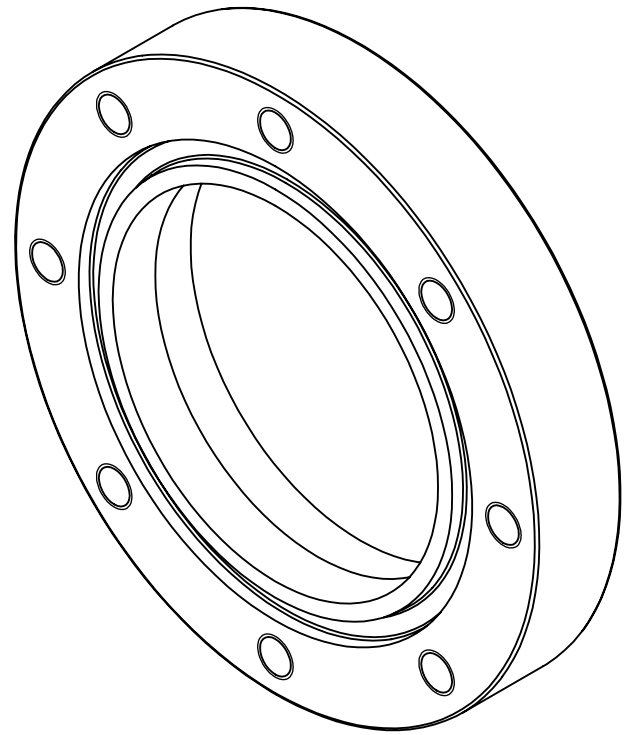
TITLE:
WATER CHAMBER ASSEMBLY

SIZE	DWG. NO.	REV
B		

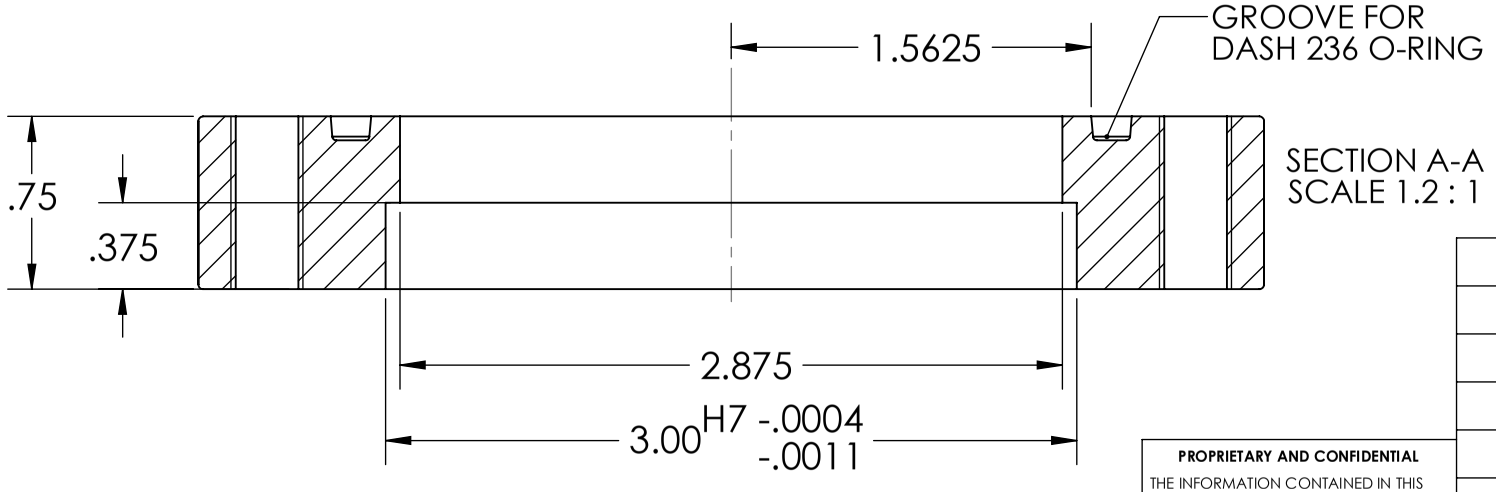
SCALE: 1:4 | WEIGHT: | SHEET 26 OF 32







NOTE:
CLEARANCE FIT: THE HOLE BASIS LIMIT (**3" H7**) IS DEFINED TO ACCOMODATE A STANDARD MASS PRODUCED 3" 16 GAUGE (0.065" Wall Thickness) TUBING. HOWEVER, THE DIAMETER OF THE PURCHASED TUBING MIGHT DIFFER SLIGHTLY FROM THE NOMINAL VALUES STATED HERE.



SECTION A-A
SCALE 1.2 : 1

PROPRIETARY AND CONFIDENTIAL
THE INFORMATION CONTAINED IN THIS DRAWING IS THE SOLE PROPERTY OF <INSERT COMPANY NAME HERE>. ANY REPRODUCTION IN PART OR AS A WHOLE WITHOUT THE WRITTEN PERMISSION OF <INSERT COMPANY NAME HERE> IS PROHIBITED.

		UNLESS OTHERWISE SPECIFIED:
		DIMENSIONS ARE IN INCHES TOLERANCES: FRACTIONAL ± ANGULAR: MACH ± BEND ± TWO PLACE DECIMAL ± THREE PLACE DECIMAL ±
		INTERPRET GEOMETRIC TOLERANCING PER:
		MATERIAL 304 STAINLESS STEEL
NEXT ASSY	USED ON	FINISH
APPLICATION		DO NOT SCALE DRAWING

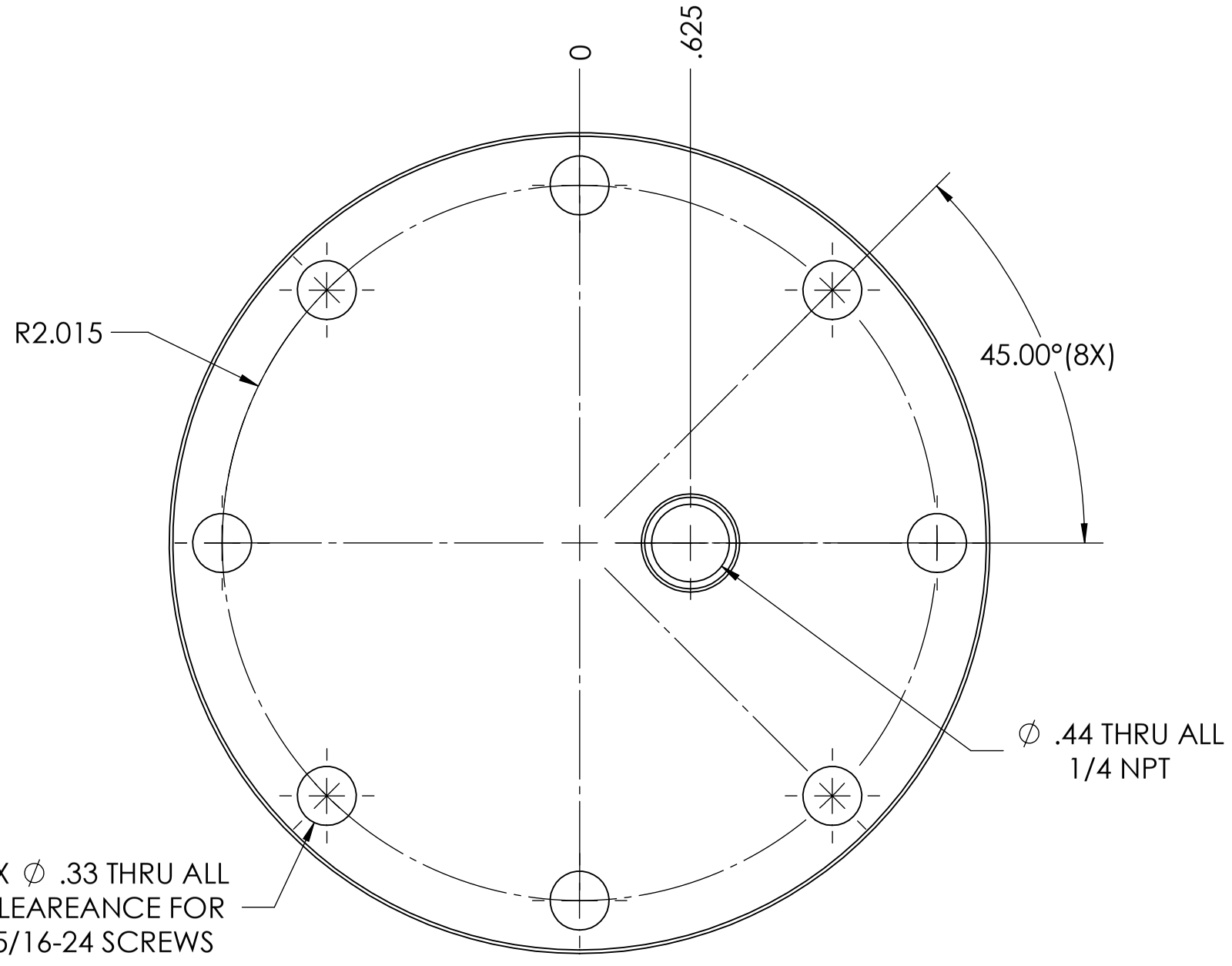
	NAME	DATE
DRAWN	F.K. SULEIMAN	
CHECKED		
ENG APPR.		
MFG APPR.		
Q.A.		

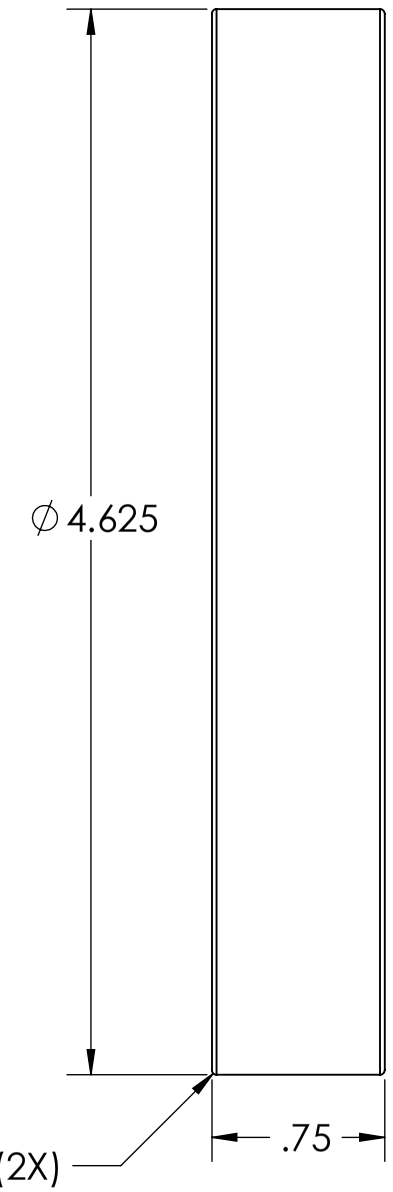
COMMENTS:

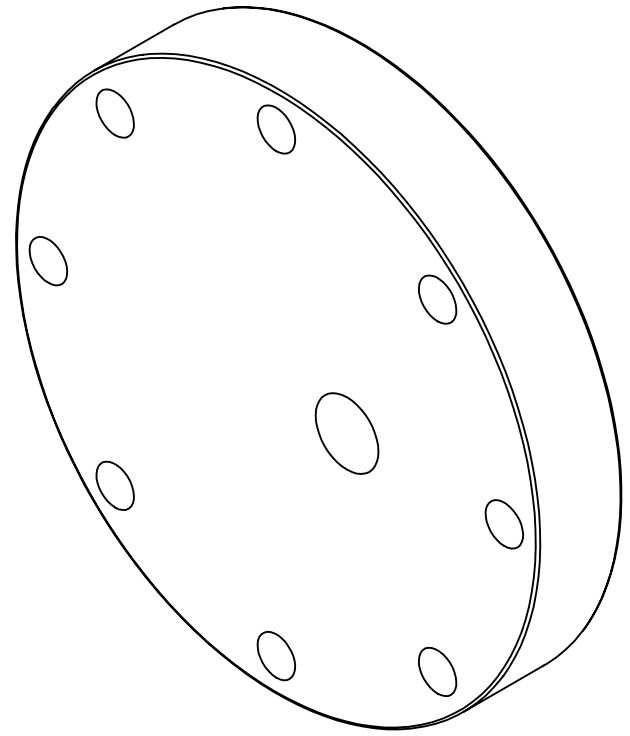
TITLE:
BORED FLANGE WITH TAPPED HOLES

SIZE	DWG. NO.	REV
B		

SCALE: 1:1 | WEIGHT: | SHEET 27 OF 32







218

		UNLESS OTHERWISE SPECIFIED:		NAME	DATE
		DIMENSIONS ARE IN INCHES TOLERANCES: FRACTIONAL ± ANGULAR: MACH ± BEND ± TWO PLACE DECIMAL ± THREE PLACE DECIMAL ±	DRAWN	F.K. SULEIMAN	
			CHECKED		
			ENG APPR.		
			MFG APPR.		
		INTERPRET GEOMETRIC TOLERANCING PER:	Q.A.		
		MATERIAL 304 STAINLESS STEEL	COMMENTS:		
NEXT ASSY	USED ON	FINISH			
APPLICATION		DO NOT SCALE DRAWING			

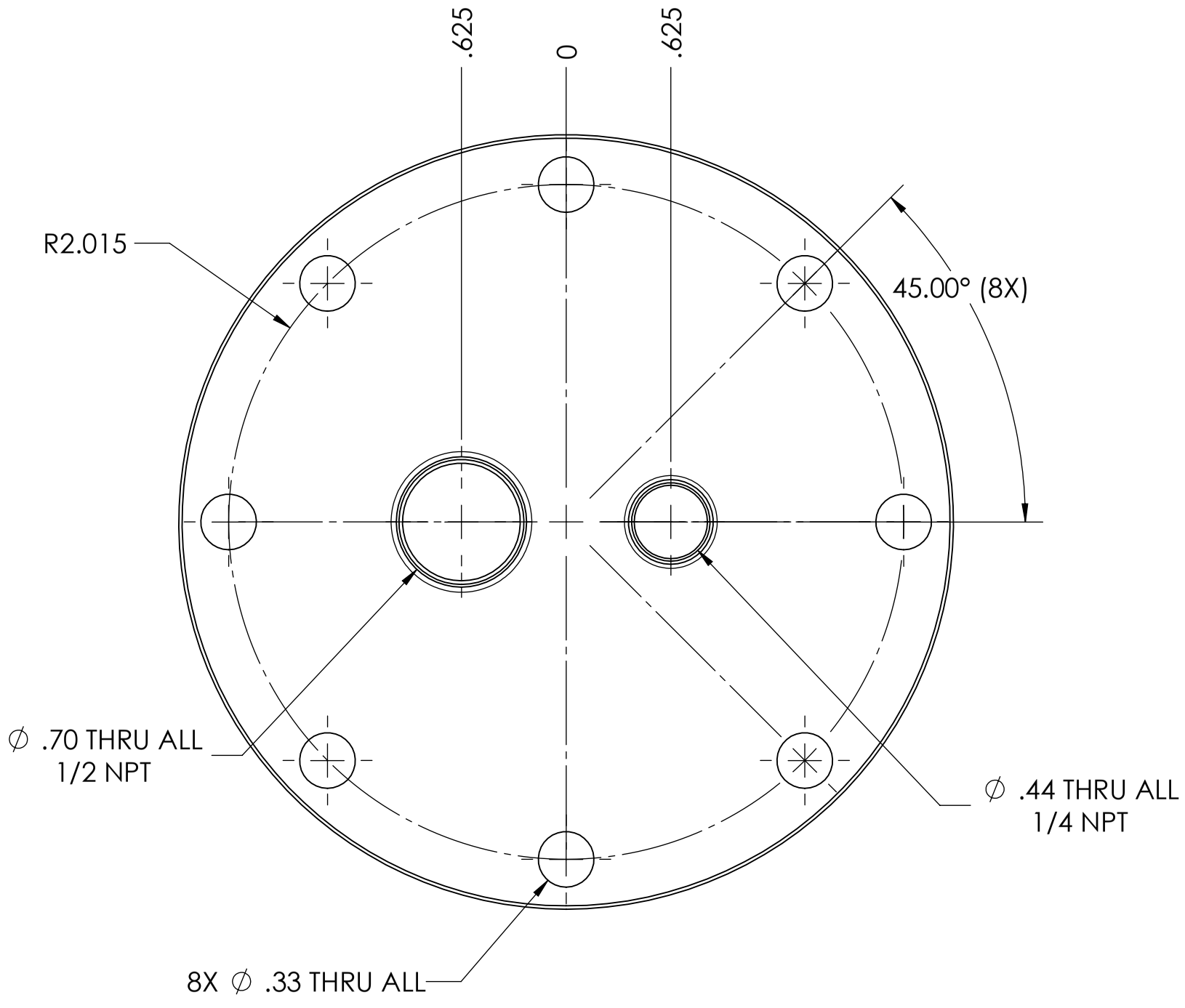
PROPRIETARY AND CONFIDENTIAL

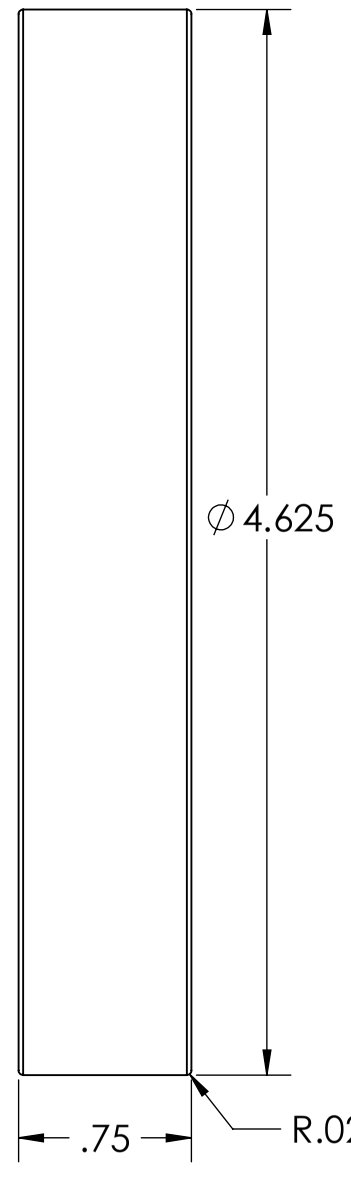
THE INFORMATION CONTAINED IN THIS DRAWING IS THE SOLE PROPERTY OF <INSERT COMPANY NAME HERE>. ANY REPRODUCTION IN PART OR AS A WHOLE WITHOUT THE WRITTEN PERMISSION OF <INSERT COMPANY NAME HERE> IS PROHIBITED.

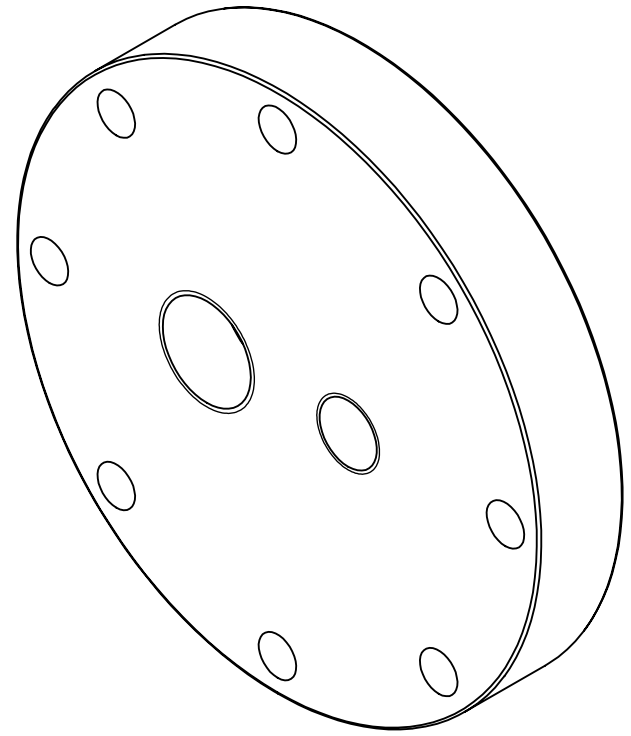
TITLE:
BLANK FLANGE WITH THROUGH HOLES - NPT INLET

SIZE	DWG. NO.	REV
B		

SCALE: 1:1 | WEIGHT: | SHEET 28 OF 32







PROPRIETARY AND CONFIDENTIAL

THE INFORMATION CONTAINED IN THIS DRAWING IS THE SOLE PROPERTY OF <INSERT COMPANY NAME HERE>. ANY REPRODUCTION IN PART OR AS A WHOLE WITHOUT THE WRITTEN PERMISSION OF <INSERT COMPANY NAME HERE> IS PROHIBITED.

NEXT ASSY	USED ON
APPLICATION	

UNLESS OTHERWISE SPECIFIED:

DIMENSIONS ARE IN INCHES
TOLERANCES:
FRACTIONAL ±
ANGULAR: MACH ± BEND ±
TWO PLACE DECIMAL ±
THREE PLACE DECIMAL ±

INTERPRET GEOMETRIC TOLERANCING PER:

MATERIAL
304 STAINLESS STEEL

FINISH

DO NOT SCALE DRAWING

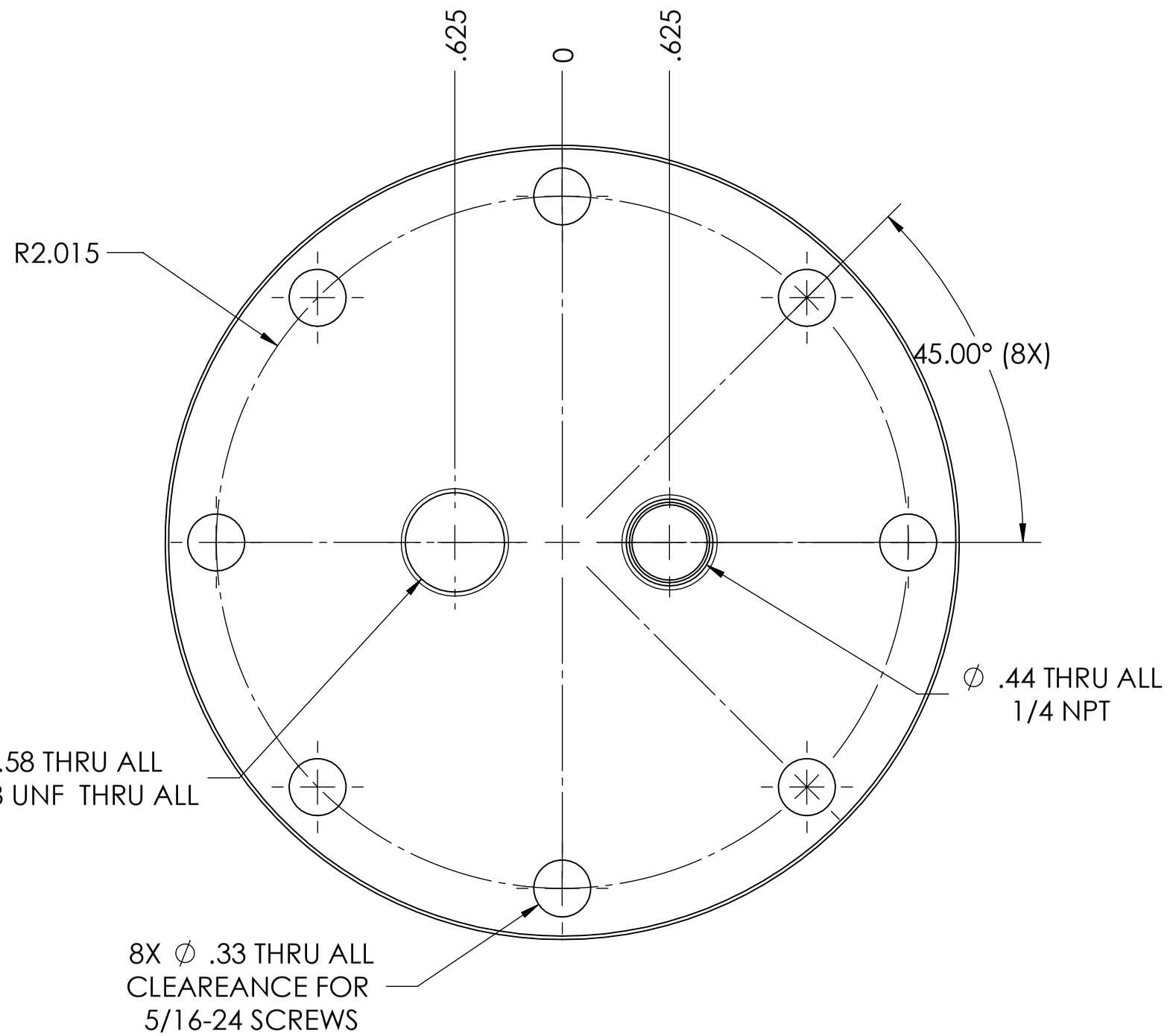
	NAME	DATE
DRAWN	F.K. SULEIMAN	
CHECKED		
ENG APPR.		
MFG APPR.		
Q.A.		

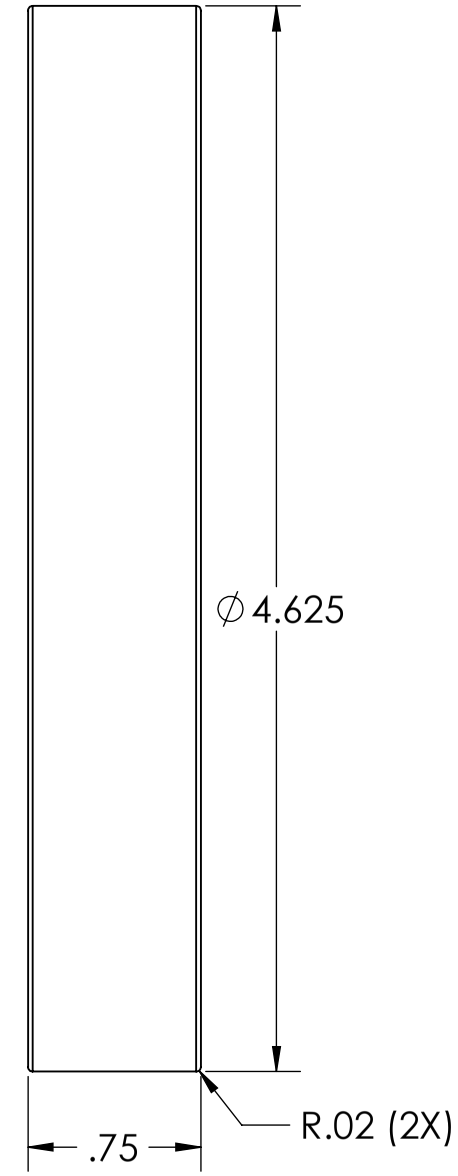
COMMENTS:

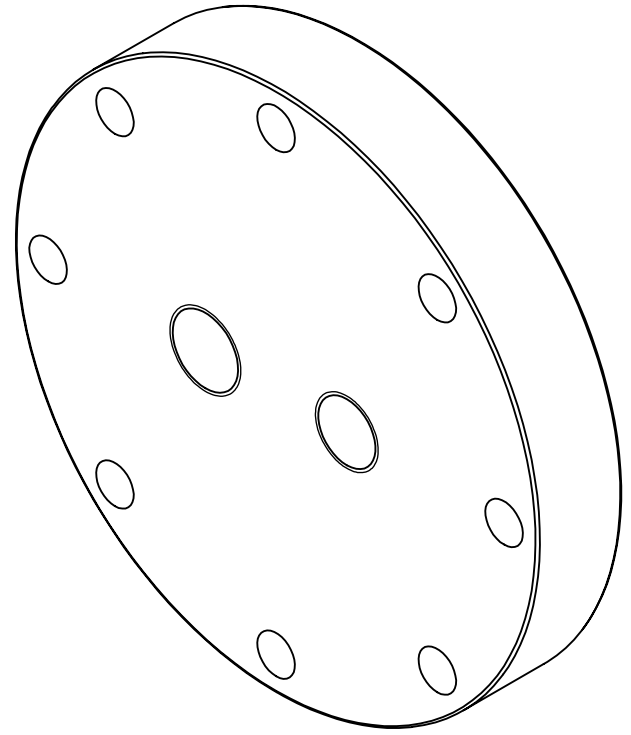
TITLE:
BLANK FLANGE WITH THROUGH HOLES - NPT & THERMOCOUPLE

SIZE	DWG. NO.	REV
B		

SCALE: 1:1 | WEIGHT: | SHEET 29 OF 32







NOTE:
MATERIAL: 304 SS

PROPRIETARY AND CONFIDENTIAL
THE INFORMATION CONTAINED IN THIS DRAWING IS THE SOLE PROPERTY OF <INSERT COMPANY NAME HERE>. ANY REPRODUCTION IN PART OR AS A WHOLE WITHOUT THE WRITTEN PERMISSION OF <INSERT COMPANY NAME HERE> IS PROHIBITED.

NEXT ASSY	USED ON
APPLICATION	

UNLESS OTHERWISE SPECIFIED:
DIMENSIONS ARE IN INCHES
TOLERANCES:
FRACTIONAL ±
ANGULAR: MACH ± BEND ±
TWO PLACE DECIMAL ±
THREE PLACE DECIMAL ±
INTERPRET GEOMETRIC TOLERANCING PER:
MATERIAL
FINISH
DO NOT SCALE DRAWING

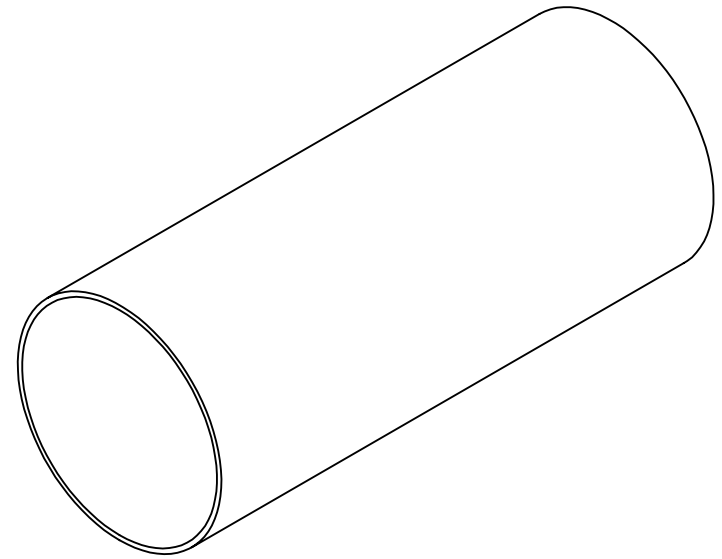
	NAME	DATE
DRAWN	F.K. SULEIMAN	
CHECKED		
ENG APPR.		
MFG APPR.		
Q.A.		

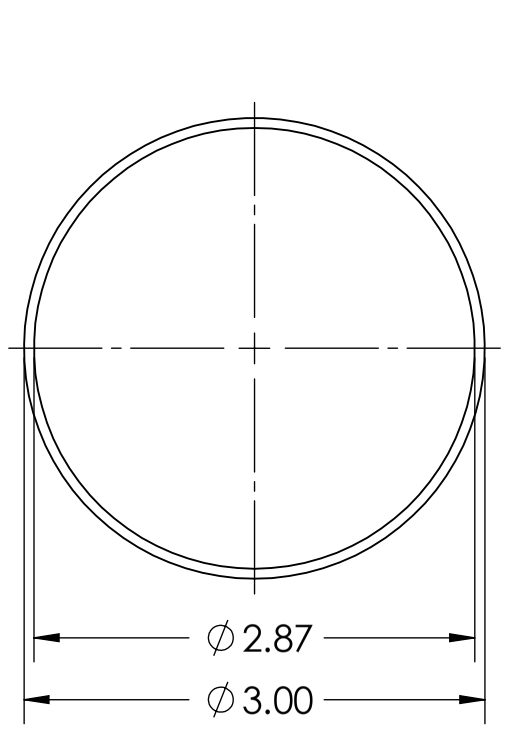
COMMENTS:

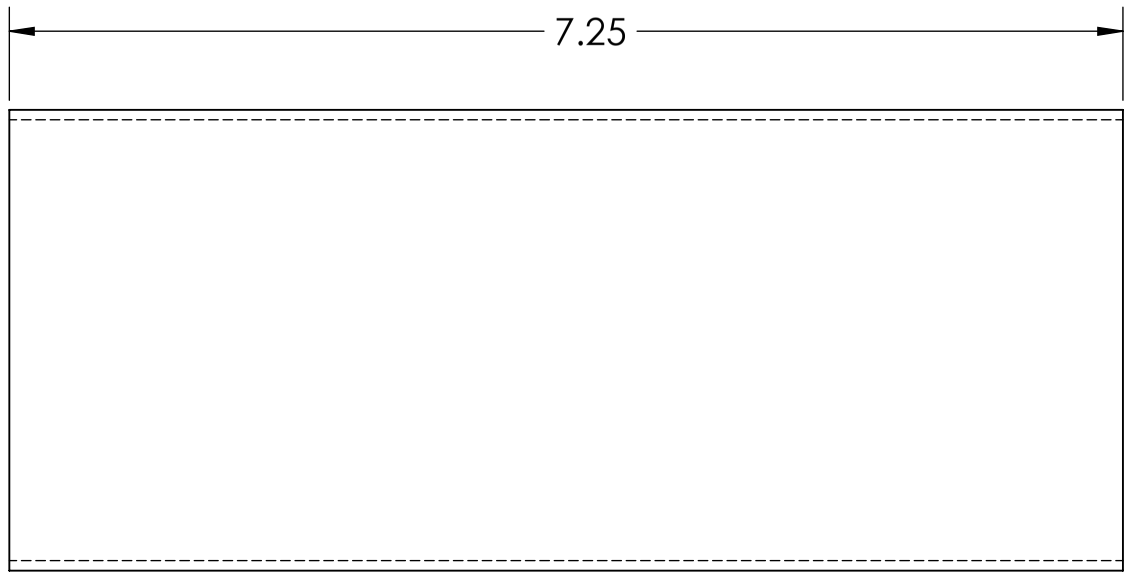
TITLE:
BLANK FLANGE WITH THROUGH HOLES - NPT & DEW POINT

SIZE	DWG. NO.	REV
B		

SCALE: 1:1 | WEIGHT: | SHEET 30 OF 32







PROPRIETARY AND CONFIDENTIAL

THE INFORMATION CONTAINED IN THIS DRAWING IS THE SOLE PROPERTY OF <INSERT COMPANY NAME HERE>. ANY REPRODUCTION IN PART OR AS A WHOLE WITHOUT THE WRITTEN PERMISSION OF <INSERT COMPANY NAME HERE> IS PROHIBITED.

NEXT ASSY	USED ON	
APPLICATION		DO NOT SCALE DRAWING

UNLESS OTHERWISE SPECIFIED:

DIMENSIONS ARE IN INCHES
TOLERANCES:
FRACTIONAL ±
ANGULAR: MACH ± BEND ±
TWO PLACE DECIMAL ±
THREE PLACE DECIMAL ±

INTERPRET GEOMETRIC TOLERANCING PER:

MATERIAL
304 STAINLESS STEEL

FINISH

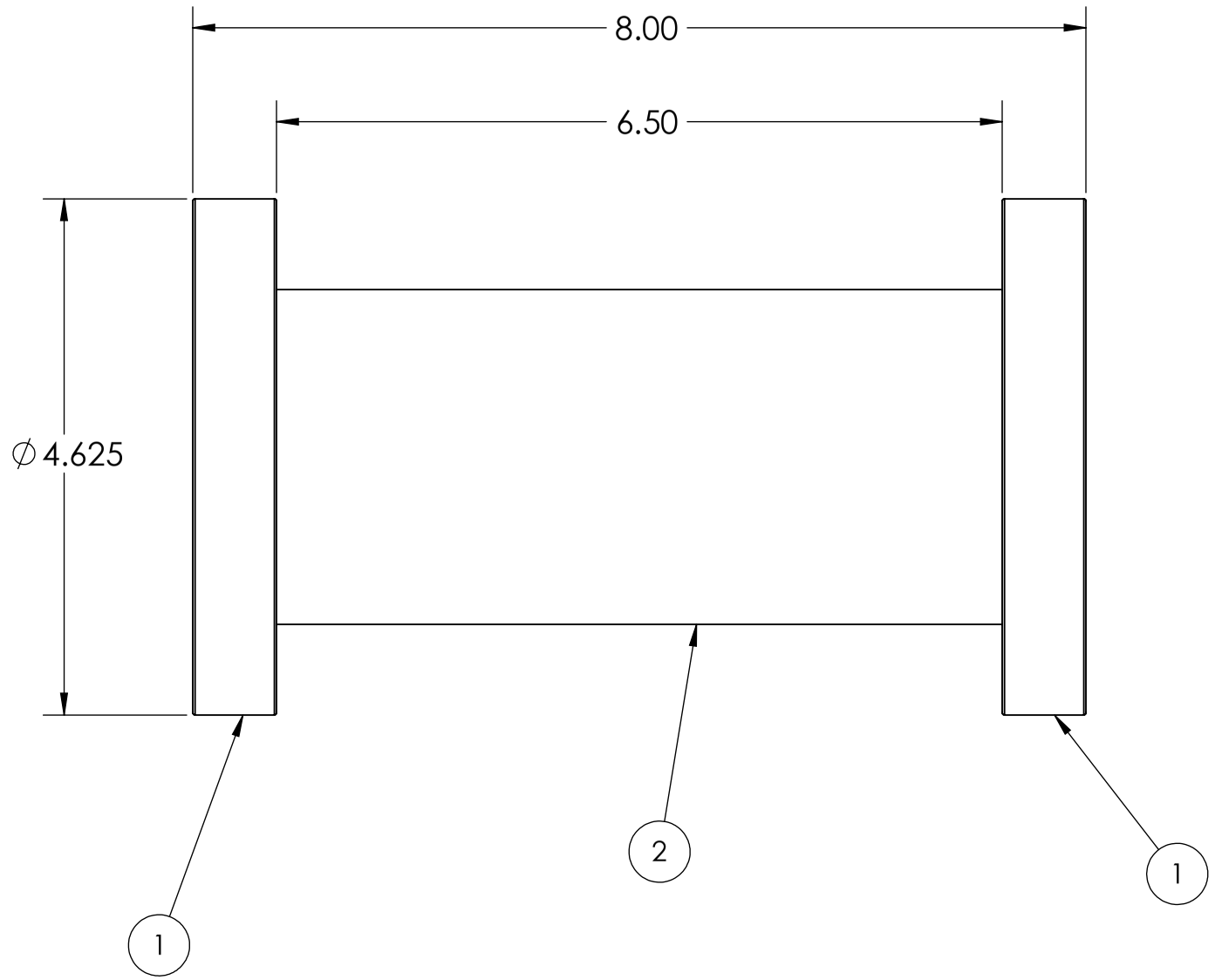
	NAME	DATE
DRAWN	F.K. SULEIMAN	
CHECKED		
ENG APPR.		
MFG APPR.		
Q.A.		

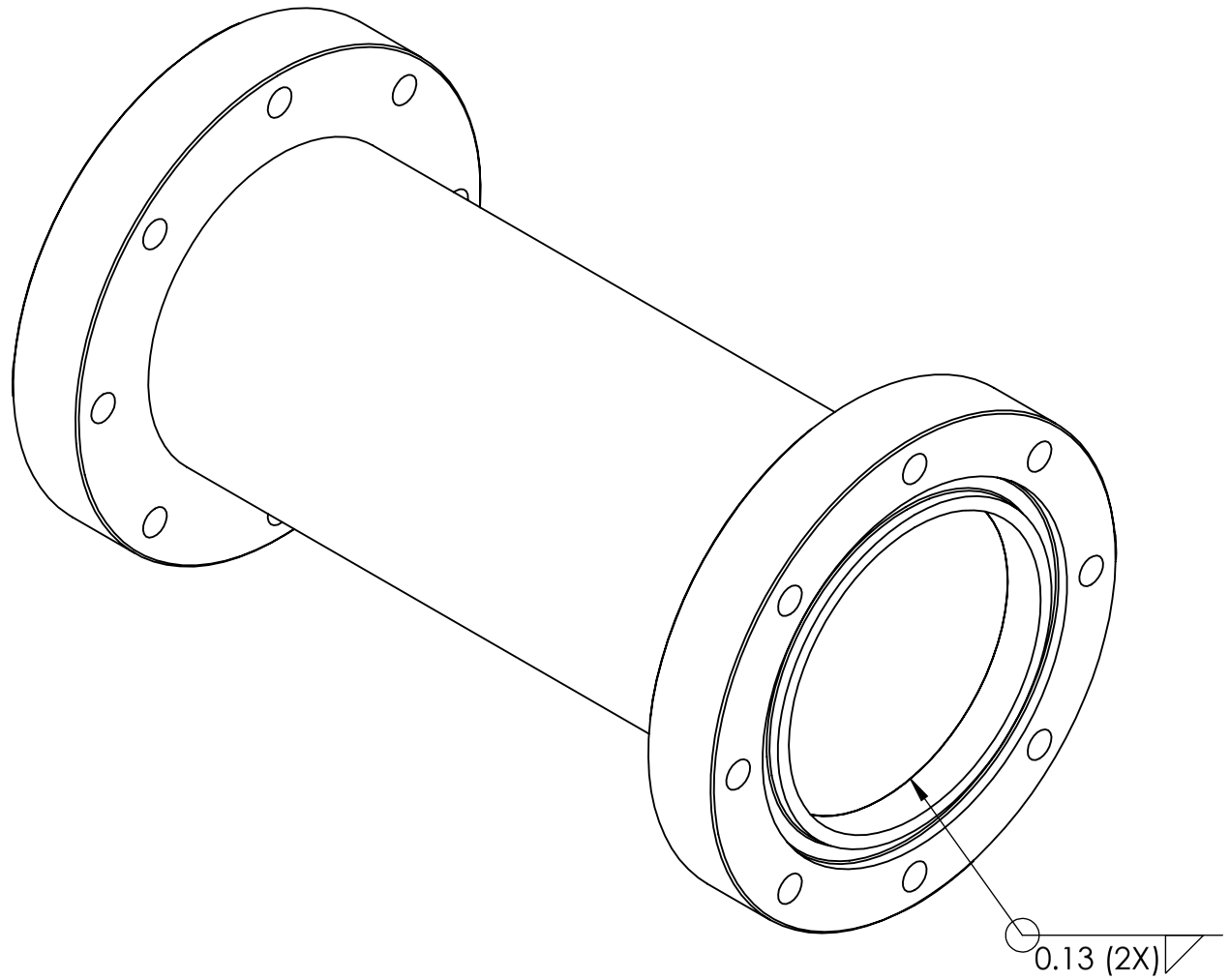
COMMENTS:

TITLE:
3" OD, 16-GAUGE (0.065") TUBING

SIZE	DWG. NO.	REV
B		

SCALE: 1:2 | WEIGHT: | SHEET 31 OF 32





NOTE:
THE FILLET WELD BEAD SIZE SPECIFIED FOR EACH WELD IN THIS DRAWING = 2 x TUBE THICKNESS.
PLEASE FEEL FREE TO SPECIFY AN ALTERNATIVE BEAD SIZE IF THIS VALUE IS NOT THE MOST APPROPRAITE

PROPRIETARY AND CONFIDENTIAL
THE INFORMATION CONTAINED IN THIS DRAWING IS THE SOLE PROPERTY OF <INSERT COMPANY NAME HERE>. ANY REPRODUCTION IN PART OR AS A WHOLE WITHOUT THE WRITTEN PERMISSION OF <INSERT COMPANY NAME HERE> IS PROHIBITED.

NEXT ASSY	USED ON	FINISH
APPLICATION		DO NOT SCALE DRAWING

UNLESS OTHERWISE SPECIFIED:
DIMENSIONS ARE IN INCHES
TOLERANCES:
FRACTIONAL ±
ANGULAR: MACH ± BEND ±
TWO PLACE DECIMAL ±
THREE PLACE DECIMAL ±
INTERPRET GEOMETRIC TOLERANCING PER:
MATERIAL

	NAME	DATE
DRAWN	F.K. SULEIMAN	
CHECKED		
ENG APPR.		
MFG APPR.		
Q.A.		

COMMENTS:

TITLE:
FULL NIPPLE FLANGE WELD ASSEMBLY

SIZE	DWG. NO.	REV
B		

SCALE: 1:4 | WEIGHT: | SHEET 32 OF 32